Dissertation zur Erlangung des Doktorgrades
der Fakultät für Chemie und Pharmazie
der Ludwig-Maximilians-Universität München

Connecting Excited State Lifetime and Intensity Correlations for Quantitative Analysis of Chromophore Interactions

Tim Schröder

aus

Salzgitter, Deutschland

2022

Erklärung

Diese Dissertation wurde im Sinne von § 7 der Promotionsordnung vom 28. November 2011 von Herrn Prof. Dr. Philip Tinnefeld betreut.

Eidesstattliche Versicherung

Diese Dissertation wurde eigenständig und ohne unerlaubte Hilfe erarbeitet.
München, 22.03.2022

Tim Schröder

Dissertation eingereicht am:	28.03.2022
1. Gutachter:	Prof. Dr. Philip Tinnefeld
2. Gutachter:	PD Dr. Jan Vogelsang
Mündliche Prüfung am:	05.05.2022

0 Summary

Intensity correlation is a powerful tool to study intensity fluctuations on various time scales. Fluorescence correlation spectroscopy (FCS) is a popular representative to monitor spontaneous intensity fluctuations caused by the deviation of the system from thermal equilibrium at nanomolar concentrations. FCS is frequently used to determine local concentrations, diffusion coefficients and intermolecular interactions of fluorescently labeled biomolecules. However, determination of the forward and backward transition rate constants and thereby also the equilibrium constant is not possible when two intensity levels are involved e.g. in a Förster resonance energy transfer (FRET) experiment. The idea of combining the fluorescence lifetime information (microtime) with the intensity information (macrotime) lead to the development of fluorescence lifetime FCS (FLCS). However, FLCS requires prior knowledge of the fluorescence lifetime components and suffers in experiments from inaccurate bunching amplitudes.

Therefore, it is the aim of this work to develop a model free connection between the microtime information and the macrotime information. To this end, shrinking-gate FCS (sg-FCS) is presented which enables the extraction of microscopic transition rate constants without prior knowledge by correlating photon subsets according to their arrival time after pulsed laser excitation. sg-FCS is demonstrated in simulations and in surface- and solution-experiments with a DNA based model system. Without prior knowledge, the equilibrium constant is recovered over two and a half orders of magnitude. Additionally, sg-FCS identifies dynamic bunching amplitudes in the intensity correlation as they come with a change in the fluorescence lifetime which is not the case for on-off switching processes.

Beyond the analysis of photon bunching on long timescales, the degree of photon antibunching on short timescales is used as a metric for the number of emitters in a multichromophoric system. So far, the interpretation of antibunching has been hampered by exciton annihilation processes. On the one hand, singlet-singlet annihilation (SSA) increases the degree of photon antibunching. On the other hand, singlet-triplet annihilation (STA) results in photon bunching on longer timescales and the interpretation of photon antibunching in presence of photon bunching was not discussed in literature yet.

Here, it is demonstrated in simulations and experiments with DNA origami-based model systems, how photon antibunching is affected by independent and collective chromophore blinking. Additionally, universal guidelines for correct interpretation of photon antibunching are identified. Thereby, the time dependence of the STA process is used to identify collective blinking chromophores by applying the sg-FCS analysis which in addition recovers the STA rate constant.

In a similar approach, picosecond time resolved antibunching (psTRAB) also utilizes the excited state lifetime information which is then used to recover the true number of chromophores in a multichromophoric system which is subject to SSA. It is demonstrated in simulations and experiments, that psTRAB can recover the true number of emitters on a DNA origami structure besides efficient SSA. Additionally, the analysis reveals the dimensionality of exciton diffusion in mesoscopic H- and J-type conjugated polymer aggregates.

At last, the potential for bright and small point light sources based on DNA origami is evaluated. State of the art dye loaded polymer beads suffer from inhomogeneous fluorescence properties and size. DNA origami provides stoichiometric and spatial control over the dye modifications and is a promising candidate to overcome the drawbacks of polymer beads. To obtain the highest labeling density on DNA origami structures the distance dependency of dye-dye interaction is systematically examined. At small distances, fluorescence lifetime and fluorescence intensity are quenched due to static and dynamic quenching which becomes less for larger distances until the dyes are permanently separated at ~ 3 nm distance. However, the dyes are not independent at this distances and resonant coupling like SSA as well as STA can affect the fluorescence intensity, photoblinking and photostability.

All in all, the findings and algorithms described above are easy to apply in many laboratories around the world which are already using TCSPC and will contribute to the quantitative analysis of switching kinetics between intensity states by sg-FCS and the change of independent chromophore numbers over time psTRAB. At last, further consideration of weak and strong coupling effects between organic dyes in close proximity will pave the way to bright and unprecedented homogeneous DNA origami-based point light sources for biophysics experiments and super resolution microscopy.

Table of Contents

1 Introduction

"Correlation does not imply causality" is a common phrase describing the fallacy of linking random occurrences to a causal relation. A famous example is the correlation of the number of sunspots with flu pandemics. This correlation was even printed two times in the prestigious journal Nature.[1,2] But only due to filtering, transcription mistakes and artificial binning, the data shows a correlation. However, the complete and unbinned dataset yields a null result.[3] Unfortunately, also life sciences are not immune to spurious relationships either. Recently, a catalysis induced diffusion enhancement of alkaline phosphatase was reported and measured with Fluorescence Correlation Spectroscopy (FCS).[4] In FCS experiments, the fluorescence intensity fluctuations caused by entering and leaving the confocal observation volume by a fluorescent organic dye due to Brownian motion are measured.[5–9] But instead of enhanced enzyme diffusion, the faster intensity fluctuations had their origin in substrate induced photophysics of the reporter dye. The dye entered a long living dark state after few excitation cycles in the confocal observation volume.[10] This example demonstrates how easy it is to misinterpret the data. Therefore, not only a careful experimental planning and execution is necessary, but also easy and reliable control experiments as well as careful data analysis is mandatory.
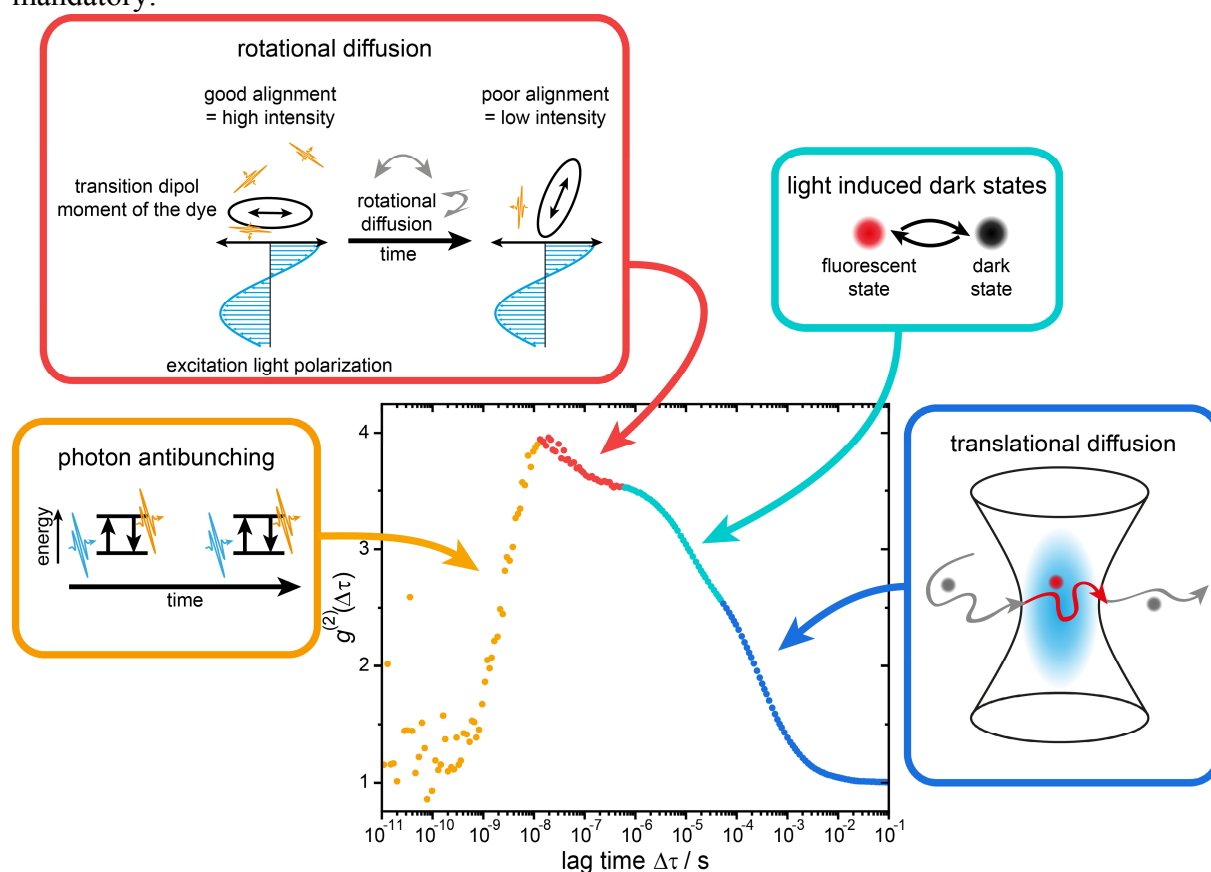
Figure 1.1: Timescales for various processes of free diffusion ATTO647N dyes linked to a single stranded oligonucleotide of 30 bases monitored by FCS in an aqueous solution and excited with a continues wave laser. Photon bunching can have different origins and is observed on different timescales. The photon antibunching (orange box) occurs on short timescales because after photon emission the dye needs to be excited again before it can emit a second photon which separates the photons in time. Photon bunching can be observed due to slow rotation (red box), photo-induced dark states (cyan box) and translational diffusion (blue box).

Besides the misinterpretation of the diffusion enhancement of the alkaline phosphatase, FCS is a widely applied and powerful method to quantify intensity fluctuations in fluorescence signals on various time scales as depicted in figure 1.1. Thereby, the excitation laser is focused into the sample by a high numerical objective. The fluorescence, which usually is emitted by organic dyes or fluorescent proteins, is collected by the same objective and guided through a pinhole to block all fluorescence that is not emitted in the focal plane of the objective. The fluorescence is detected by single photon sensitive detectors. In an autocorrelation, the intensity signal is processed and gives a measure for the self-similarity of the intensity signal. With high temporal data acquisition various processes on different timescales can be monitored by FCS as long as they induce intensity fluctuations. On very short timescales ($\sim 10^{-9}$ s = 1 ns) the excited state lifetime of an organic dye limits the probability to detect two consecutive photons within this timescale (figure 1.1 orange section). The result is an absence of correlation amplitude which is referred to as photon antibunching. On a timescale of tenth of nanoseconds the rotation of the dye is revealed (figure 1.1 red section). Rotation induces intensity fluctuation if the alignment of the dye's transition dipole moment to the polarization of the excitation light changes. Thus, the photos appear "bunched" on this time scale. Usually, the rotation of a free dye is two orders of magnitude faster and not observable in FCS because it is faster than the relaxation from the excited state lifetime.[11,12] However, sticking to a larger object slows the rotational diffusion of the transition dipole moment down. The observed rotation in figure 1.1 is most likely a ball made of the dye and the attached single-stranded deoxyribonucleic acid (ssDNA).[13] Intensity fluctuation from the dye's photophysics by transitions into a non-fluorescent triplet- or radical ion-state become probable which show a lifetime usually on the tenth of microsecond timescale (figure 1.1 cyan section).[14,15] But also protonation processes or light-induces photoisomerization can be studied with FCS.[16–18] Finally the slowest intensity fluctuation in a solution experiment is the dye entering and leaving the focal volume itself, which is observed close to the millisecond timescale (figure 1.1 blue section).[8]

In an experiment, the fluorescence signal is collected with single-photon sensitivity and each detection event is stored with a time stamp of picosecond precision. This is the starting point for the autocorrelation which therefore can have down to picoseconds time resolution. The autocorrelation monitors thereby fluctuation in the intensity signal like the entering and leaving of a single fluorescence molecule into and out of the observation volume. Thus, the correlation has a wealth of information which can be quantitatively analyzed with suitable models. The rotational and translational diffusion of a molecule depends on the size of its hydrodynamic radius.[5,19–21] The larger the hydro dynamic radius, the slower the rotational and translational diffusion. Therefore, FCS is widely applied to study molecular interactions between a small ligand, labeled with a fluorescence dye, and a larger counterpart. By monitoring the fluorescence signal continuously but analyzing shorter timeframes, the fraction of unbound ligand can be monitored until the reaction reached thermal equilibrium.[22,23] Such experiments have first been used to study DNA binding kinetics and nowadays to study ligand-receptor systems such as the binding of transferrin to the transferrin receptor which mediates the iron uptake in cells.[24] Beyond the study of the diffusion rate, FCS is also capable of measuring e.g. concentrations by the correlation amplitude which reflects the intensity fluctuation strength. Therefore, each molecule which enters or leaves the confocal volume has to contribute substantially to the measured signal in order to provide a significant correlation amplitude. A

dye concentration in the nano- to pico-molar range is sufficient, to study e.g. labeled proteins inside cells or on cell membranes.[25,26]
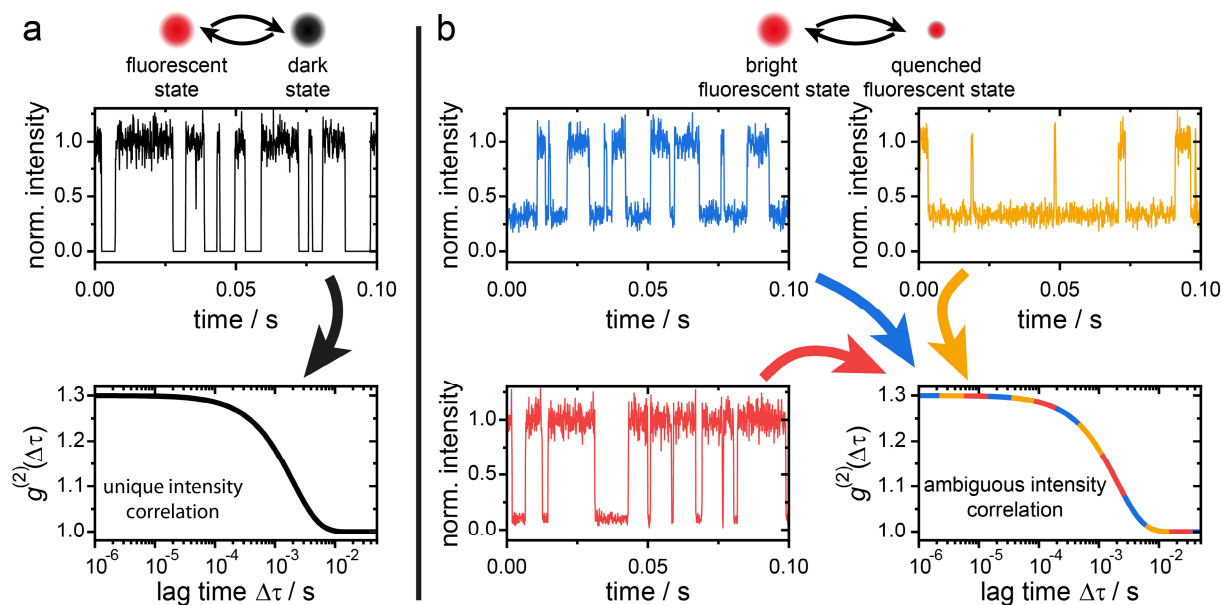

Figure 1.2: Simulated blinking intensity trajectories with their corresponding modeled intensity correlation. All intensity trajectories are normalized to the average intensity of the bright state. a) The on-off trajectory has a unique solution of the intensity correlation and the microtime switching rate constants can be recovered reliably. b) Three intensity trajectories (blue, orange and red) which show intensity fluctuations between two intensity states. The blue and orange trajectory have the same intensity contrast but different switching rate constants. The red trajectory shows a lager intensity contrast and longer dwell times in the bright intensity-state compared to the other two trajectories. However, all three intensity trajectories have identical intensity correlation (bottom right) and recovery of the switching rate constants is impossible without further knowledge of the equilibrium constant.

Beyond the study of molecular interactions, FCS is used to study the intensity fluctuations of organic dyes which can have their origin in e.g. photophysics[14,27,28] or photoisomerization.[18] The otherwise constant fluorescence signal of an organic dye is intermitted by transitions into a non-fluorescence dark state (see figure 1.2a black intensity trajectory). The transition from the first excited singled to the triplet state is quantum mechanically forbidden in the dipole-approximation which results in a small intersystem crossing rate (ISC) constant. For the time spent in the triplet state, which is usually three to four orders of magnitude larger than the excited state lifetime of the first excited singlet state, the fluorescence signal is intermitted. Even if the transitions into and out of the dark state are too fast to be monitored in a binned intensity trajectory, the autocorrelation analysis recovers the transition rates between the fluorescent and dark state. The bunching amplitude provides information about the equilibrium constant, which is the ratio of the time spent in the dark state to the time spent in the fluorescent state. The correlation relaxation time provides information about the sum of transition rate constants into the fluorescent- and into the dark-state. Therefore, FCS contributed to the optimization of the fluorescence properties of organic dyes e.g. by suppressing cis-trans isomerization of cyanine dyes by synthesis,[29,30] and changing the dark state population by buffer additives. Such buffer additives as ascorbic acid, trolox or methylviologen can be used in a reducing and oxidizing buffer system (ROXS) to depopulate triplet states by electron transfer

3

reactions.[31,32] To this end, the blinking kinetics of organic dyes can be tuned according to the experimental needs. By minimizing photo blinking, the organic dye can become a stable long-lasting fluorescent reporter to track e.g. transmembrane proteins or the buffer system can be changed to induce long living dark states which is sufficient for stochastic optical reconstruction microscopy to map e.g. microtubules with sub diffraction resolution.[33–35]

In addition to the on-off intensity fluctuation, the signal of an organic dye can also switch between different intensity levels as depicted in figure 1.2b. This was first observed for single molecules at low temperatures by spectral jumps and is nowadays frequently measured in experiments with dye-labeled proteins,[36–38] involving Förster resonance energy transfer (FRET) between a donor and acceptor dye.[39] Here, the donor dye transfers its excited state energy to the acceptor dye non-radiative. The energy transfer-efficiency scales inversely with the sixth power of the inter-dye distance and conformational changes of the protein result in a change of the inter dye distance and hence the donor and acceptor signal intensities change.[39,40] Such rapid dynamics are often measured and are monitored in the intensity correlation but are commonly not quantitatively utilized due to an ambiguity of the photon bunching amplitude in the correlation function.[36,38,41–43] For fluorescence trajectories, which alternate between two fluorescence intensities, the correlation amplitude does not hold a unique solution for the equilibrium constant. The trajectories in figure 1.2b differ in switching rate constants and intensity contrast, but the bunching amplitudes in the autocorrelation are identical. The bunching amplitudes are "convoluted" with the fractional intensity difference of the two states.[36,38,42,43] Hence quantitative analysis requires prior knowledge of the equilibrium constant.

The equilibrium constant is accessible in ensemble experiments, but is often difficult to obtain, e.g. due to imperfect protein labeling which limits the application of ensemble experiments. However, single-molecule experiments can filter data of imperfect labeled molecules out. Confocal data acquisition also can provide excited state lifetime information by time-correlated single-photon counting (TCSPC) which provides the arrival time of the photon with respect to the laser pulse, hence the excited state lifetime, and the macroscopic arrival time with respect to the beginning of the experiment. If the donor dye is quenched by FRET, the excited state lifetime is shortened due to the additional energy transfer rate constant which depopulates the donor's excited sate. This information is used in fluorescence lifetime correlation spectroscopy (FLCS) which defines species according to the excited state lifetime.[44] By defining lifetime filter for the expected species, the photons are weighted according to their arrival time after pulsed excitation for the autocorrelation. FLCS can provide the equilibrium constant on the condition, that the filter parameters are provided correctly. This may be achieved by measuring the lifetimes for each species isolated, or by a multi-exponential fit of the total excited lifetime decay of the sample with dynamics. However, the number of states and their excited state lifetimes have to be provided with high accuracy. Otherwise crosstalk between the species will distort the amplitude and cannot be used for quantitative analysis, which is usually the case in real experiments.[45] Additionally, the approach is not applicable to e.g. continuous excited state lifetime changes of the donor dye. Hence, FLCS is also not able to isolate the dynamic intensity fluctuation component from on- off-fluctuations, which do not change the fluorescence lifetime, when they appear on the same timescale.

The high-low intensity fluctuations of a single dye and the ambiguous interpretation of the correlation amplitude is very similar to the problem of interpreting the photophysics of multichromophoric systems by intensity correlation. Multichromophoric systems such as light

harvesting complexes,[46–48] dye loaded nanoparticles,[49] organic semiconductor aggregates or dye labeled biomolecules,[50–53] undergo intensity fluctuations as well. A quantitative interpretation of the excited state processes of important classes of materials like organic semiconductors is vitally needed. Such materials are used as active elements in devices like organic light emitting diodes or organic solar cells. However, the photophysics in multichromophoric systems is even more complicated. An organic semiconductor is a chain of a conjugated pi-System and the number of emitting units are referred to as chromophores (an organic dye also hosts a chromophore). On the one hand, the chromophores can interact with each other by coherent electronic coupling resulting in a change of several properties like quantum yield, fluorescence lifetime and emission- as well as absorption-spectrum.[54–57] On the other hand, the Frenkel-excitons can annihilate each other by incoherent resonant energy transfer within the multichromophoric system.[58–60] Such annihilation processes affect key parameters of conjugated polymers like brightness,[61] exciton harvesting efficiency,[62] and photostability.[63] The number of chromophores, and their interaction by exciton diffusion and consecutive exciton-exciton annihilation needs to be understood to develop design principles for e.g. super bright and stable nanoparticles for diagnostic applications, or to optimize charge separation for efficient organic solar cells.

Nevertheless, counting the number of chromophores in an ill-defined multichromophoric system is challenging because the chromophores cannot be resolved in space due to the diffraction limit.[64] Therefore, intensity- or localization-based chromophore counting techniques have been developed. Counting the number of chromophores by the detected fluorescence intensity and comparing it to the brightness of a single chromophore is maybe the simplest approach to count chromophores. It is applied for counting the number of dye labeled proteins in an aggregate.[65] However, for ill-defined multichromophoric nanoparticles (mcNP), such as conjugated polymers (CP), the brightness of a single chromophore is unknown and might vary. Therefore, intensity-based methods are not applicable for ill-defined mcNPs. Another approach uses stochastic activation of the chromophores, which is used in optical reconstruction microscopy to count e.g. the expression of transmembrane proteins as a target for cancer treatment,[66] or to study the size of protein complexes.[67] However, the stochastic activation of chromophores is only applicable for independently emitting organic dyes,[52] but the chromophores of a mcNP can neither be stochastically activated nor are they independent of each other.

Therefore, one turns to measure the photon statistics of the emitted photons from a mcNP. A single chromophore can emit at maximum one single photon per excitation cycle and the emitted photons are always separated in time. This is the trade mark signature of single photon sources like ions,[68–70] organic dyes,[71–74] and nitrogen vacancy centers in diamonds.[75,76] The degree of single photon emission is measured by two single photon detectors in a Hanbury Brown-Twiss (HBT) configuration.[77–79] With this configuration, the probability of two photon events is measured. A single photon source has zero chance to emit two photons at the same time, which is reflected in an absence of a correlation amplitude for zero lag time in the intensity cross correlation of both detector signals. This phenomenon is referred to as photon antibunching. The degree of photon antibunching is related to the number of chromophores in the sample.[80] A multichromophoric system has a finite probability to emit two photons at the same time. In a classic HBT setup, intensity correlations were used to measure up to eight chromophores.[81] For more chromophores, the photon antibunching contrast of two photon events becomes too weak since it scales inversely with the chromophore number. That's why

the group of Dirk P. Herten extended the HBT setup by two additional single photon detectors to make the setup sensitive for up to four photon events.[80] Counting by Photon Statistics (CoPS), is based on determining the probabilities of zero to four photon events under pulsed laser excitation which is used to extract the brightness and number of chromophores of the sample.[82] With CoPS, they therefore extended the reliable range for chromophore counting to ~ 36,[83] which is sufficient to count the organization of dye-labeled protein clusters.[84] However, CoPS assumes constant chromophore emission without any dark states or exciton annihilation processes which are expected in mcNPs.

Exciton-exciton annihilation processes in mcNP can be observed on many timescales.[85] The annihilation of two singlet excitons, which is referred to as singlet-singlet annihilation (SSA), occurs on the timescale of the singlet exciton lifetime. After the annihilation of two excitons, only a single exciton remains. The consequence of SSA is a higher degree of photon antibunching which results in a smaller number of apparent chromophores in the photon statistics as depicted in figure 1.3a.[58–60] The degree of photon antibunching in figure 1.3a implies 1.25 chromophores making it obvious, that some kind of annihilation is present, as chromophores come in discrete units. However, the SSA efficiency would not only affect the apparent number of chromophores in the system but it is also connected to the exciton diffusion in the mcNP. SSA is seen as long-range interaction,[86,87] because the excitons have to get into "contact range", i.e. come within their FRET radius by exciton diffusion. In this case, the excitons hop from chromophore to chromophore until they dissipate radiative, non-radiative or by annihilation.
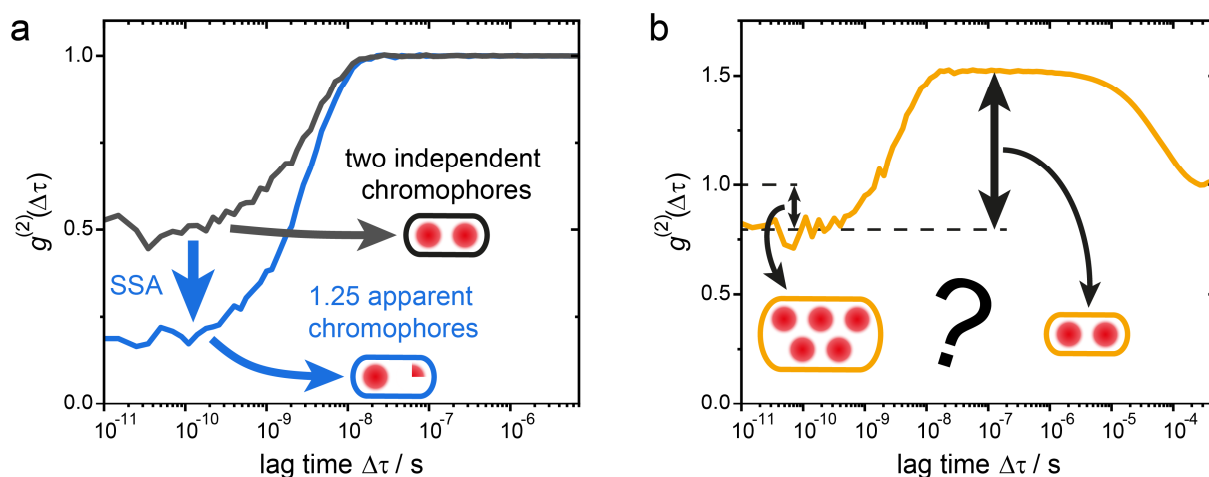

Figure 1.3: Intensity correlations of simulated photon streams of two chromophores under continuous wave excitation. a) Intensity correlation of a simulated photon stream of two independent chromophores (black) shows photon antibunching in the ns-time regime. Two chromophores undergoing singlet-singlet annihilation (SSA) results in a higher degree of photon antibunching (blue) and therefore a smaller number of apparent chromophores. b) Intensity correlation of a simulated photon stream with triplet-blinking. Two possible normalizations for the degree of photon antibunching are depicted which result either in two or five chromophores.

A striking example for the SSA efficiency can be found in the aggregation of conjugated polymer chains (CP) and was presented by Stangl et al.[51] A single CP chain in a host matrix holds multiple chromophores which is reflected in the degree of photon antibunching which is close to the expected value of two chromophores.[51] By solvent vapor annealing, the chains can

diffuse in the host matrix, enabling them to aggregate. Chromophore-chromophore interactions become visible by a spectral red-shift and a longer excited state lifetime due to a weaker oscillation strength of the chromophores in the aggregate. However, the degree of photon antibunching shows almost perfect single photon emission although an aggregate of 12 CP chains is expected to hold more chromophores than one single chain. Studies by Eder et al. suggest that the exciton diffusion depends on the morphological order of the aggregate and can therefore be controlled by modifying the side chains.[55] As a result, anisotropic exciton diffusion can be generated where the excitons diffuse primarily along one chain but hardly between them which affects the probability of SSA and thus the degree of single photon emission. But so far these models are only phenomenologically described.

Besides annihilation between singlet excitons, also singlet-triplet annihilation (STA) is expected in mcNPs which is considered as a main loss mechanism in lasers based on organic thin films and organic light-emitting diodes.[61,88,89] In STA, a long living triplet exciton annihilates multiple singlet excitons and a quenched intensity state of the mcNP is observed for the lifetime of the triplet exciton.[61,85] For this reason, mcNPs also show triplet blinking which results in photon bunching on long time scales even if the photons are mainly antibunched on short timescales as depicted in figure 1.3b.[85] Here, a fundamental question arises: How does photon bunching affect the interpretation of the degree of photon antibunching? So far, this question has not been addressed in the literature. If photon bunching affects the degree of photon antibunching, it has to be considered in the quantitative interpretation of the chromophore numbers and the exciton interactions. As seen in figure 1.3b, the normalization with respect to the average intensity would suggests a five chromophore system. On the other hand, the normalization with respect to the bunching amplitude results in a two chromophore system. Additionally, different mechanisms of photo blinking should be considered. A dye labeled protein aggregate may show independent photo blinking of the organic dyes as they are probably separated in space and out of the FRET range, whereas the mcNP shows collective photo blinking by STA due to exciton diffusion.[49,50] As for the independent blinking dyes, the intensity correlation's bunching amplitude should hold the formation- and lifetime-rate constants of the triplet exciton as well as the STA rate constant which includes exciton diffusion. But this information cannot be utilized due to the ambiguous bunching amplitude which arises from a two-intensity system as discussed before.

To utilize the excited lifetime information TCSPC data acquisition is required. TCSPC data holds the information of the photon detection time with respect to the beginning of the experiment (macrotime), and with respect to the excitation laser pulse (microtime). The macrotime gives information of the intensity fluctuations and is used for creating intensity trajectories or intensity correlation. As mentioned before, some intensity fluctuations come with a change in excited state lifetime like dynamic changes of distance between a donor and acceptor dye-pair in a FRET experiment. But also annihilation processes shorten the exciton lifetime if two excitons are present in a mcNP and a fingerprint of these processes must be conserved in the photon stream. So far FLCS utilizes the microtime information for FCS analysis by weighting the photons according to their arrival time with species filters. However, the fluorescence lifetimes for these filters have to be provided with high accuracy as discussed before. Another approach is microtime-gating, which can be used to isolate the species of interest. For microtime gating, only photons which are detected within a certain microtime window (microtime gate) are considered for FCS analysis. Thereby, the bunching amplitude only corresponds to the species of interest and quantitative concentrations can be provided for

an FCS experiment which can otherwise be compromised by laser scattering or species with shorter fluorescence lifetime.[42,90]

In this thesis, microtime gating is applied beyond the diffusion analysis of autocorrelations. Systematic microtime gating exploits so far unused information about the dynamics of a system which shows correlated intensity and lifetime changes. For FRET experiment with dynamic switching between two FRET states, microtime gating will, for example, isolate the low-FRET species of the donor signal due to its longer fluorescence lifetime. If the low-FRET signal is isolated, the intensity fluctuation of the donor dye is maximized and so is the bunching amplitude of the autocorrelation which then equals the equilibrium constant. In addition, microtime gating reveals intensity fluctuations with correlated lifetime changes without any assumptions by changing the bunching amplitude which scales with the intensity fluctuation strength. In chapter 4.4, it is demonstrated by theory, simulation and experiment, that systematic microtime gating recovers the needed equilibrium constant of a two level system. To proof the approach in experiment a robust model system is used based on the DNA origami technique, which enables spatial and stoichiometric control over the arrangement of organic dyes on the structure.[91,92] The DNA origami structure provides stochastic switching between two FRET-intensities and the switching kinetics are tuned by changing the stability of the FRET state. Further, it is shown, that the dynamic component in the autocorrelation can be isolated from intensity fluctuation which do not affect the fluorescence lifetime like photo induced blinking.

In a mcNP intensity fluctuations will be correlated with a change of the fluorescence lifetime as well as due to STA. The intensity contrast of the intensity state with and without the triplet-exciton will change by microtime gating as the bunching amplitude depends on the intensity contrast of the two intensity states. By applying microtime gating, the intensity contrast changes with the speed of the STA rate constant, which is the additional decay rate constant of a singlet-exciton in presence of a triplet-exciton. In chapter 4.3 it is demonstrated, by simulation and experiment, that the STA rate constant can be recovered with microtime-gated intensity correlation analysis. The experiments are again utilizing the spatial and stoichiometric control of DNA origami structures to place different types of organic dyes at designed positions.

The degree of photon antibunching is a metric to "count" the apparent number of emitting units in a mcNP.[51] Knowledge of its magnitude is vital to understand the underlying excited state processes. However, intensity fluctuations of a mcNP show up as bunching amplitude in the intensity correlation due to triplet-exciton formation and consecutive annihilation of singlet excitons.[61] So far, the effect on the interpretation of photon antibunching was not discussed in literature before. The degree of photon antibunching can be determined either by the value at $g^{(2)}(0)$, which normalizes the correlation amplitude with respect to the average intensity, or by the ratio of central to lateral correlation $\frac{N_C}{N_L}$ events. However, both procedures yield different results for the number of emitters in the presence of additional bunching amplitudes. In chapter 4.3, independent and collective chromophore blinking is modeled in simulation and experiment. Therefore, dyes are arranged on an DNA origami structure to either show independent blinking induced by a buffer holding reducing agent only, or to show collective blinking by a FRET-switch[93] which is placed between them to avoid SSA.

Besides STA processes, SSA is also a key process that affects the brightness[94] and photostability of a mcNP.[63] The degree of photon antibunching, and with that the apparent number of emitters, are significantly affected by this process.[58,60] As in STA processes, the

singlet exciton's lifetime is shortened if two singlet-excitons are present in a mcNP at the same time. Therefore, microtime gating will be applied in chapter 4.2 to monitor the SSA process in simulation and experiment as a change in the degree of photon antibunching. Because the annihilation is a time dependent rate process, the number of emitting units can be recovered as well as the SSA rate constant. Thereby, the SSA-rate constant is a combination of the annihilation process and the rate to bring the excitons into annihilation range, i.e. exciton hopping. The approach to extract both, numbers of chromophores and annihilation kinetics, is demonstrated on DNA origami model structures with up to five organic dyes and further applied to mesoscopic conjugated polymer aggregates to demonstrate the effect of dimensionality on exciton diffusion and subsequently on the SSA process.

Beyond the application in photovoltaic and display devise, mcNP are also of interest for the life science community. mcNP can be used as labels to localize or track biomolecules in a cell, or they can be used as point light source to determine the point spread function of a microscope.[95] In this context, a point light source should be as small as possible and as bright as possible. Additionally, for biological applications the labels should not affect the properties of the biomolecule of interest. Moreover, it should be biocompatible and non-toxic. The smallest fluorescent label used is a single organic dye. Even though its fluorescence signal is detectable,[28] the application of single dye labels is compromised by a need of equipment with high photon detection efficiency and a poor signal to background ratio in complex environments like cells. Therefore, brighter labels are expected to improve the signal to background ratio which leads to better localizations or higher time resolution for tracking of the labeled biomolecule. Additionally, the photon budged is expected to be higher which leads to longer observation times.[96]

Alternatives to a single organic dye are dye loaded nanoparticles or quantum dots. However, on one the hand, the biological applicability of quantum dots suffers from their toxicity and size.[97] On the other hand, dye loaded small nanoparticles suffer from inhomogeneity due to the stochastic dye loading and the formation of imperfect dye-dye aggregates.[98–101] The result is a broad fluorescence intensity distribution and fluorescence lifetime distribution among the particles.[102] Other alternatives such as conjugated polymer dots[103,104] and organic nanoparticles show more homogeneous fluorescence properties,[105,106] but are difficult to modify for biocompatibility. Hence, new biocompatible labels are needed which can be made with DNA nanotechnology as it gives control over the stoichiometry and position of the organic dyes to preserve their fluorescent properties. In chapter 4.1 a rigid DNA origami model system is used to study the dye interactions for different distances in order to find the optimal labeling density for DNA based mcNP. Therefore, the inter dye distance is varied on the single base pair level and strong and weak coupling effects between the dyes are investigated as well as the impact of dynamics in the DNA model structure on the fluorescence signal of the dyes itself. Thereby the initial step for a new generation of DNA based small and bright mcNP is made to path the way into a bright future.

2 Theory

This work is about dye interactions in well-defined multi chromophoric samples. Therefore, the basics of the luminescence and photophysics of organic dyes is introduced in this chapter. A simple model of singlet, triplet and radical states is presented. For long and bright fluorescence trajectories, a reducing and oxidizing buffer system (ROXS) was used to either minimize or cause photo blinking according to the experimental needs. Furthermore, the interaction between several identical dyes, coherent and particularly resonant coupling between dyes is examined as well as the theory for the analysis of intensity correlation.

2.1 Photophysics of Organic Dyes

The organic dyes used in this work are small molecules with a diameter of 1 - 2 nm, mostly composed out of carbon and hydrogen atoms. All organic dyes have a section of unsaturated carbon bonds which form the chromophore. The electrons are delocalized on the resulting conjugated π-system and can absorb light, mostly from the visible range. The emitted fluorescent light has a lower energy than the absorbed and can therefore spectrally separated from the excitation source. The fluorescence properties can be influenced by the chemical structure of the dye. The spectrum of the absorbed and emitted light can be changed with the length of the conjugated π-system. Heteroatoms, like oxygen or nitrogen, can either push or withdraw electron density from the π-system and thus change the energy gap between the highest occupied molecular orbital (HOMO) and the lowest unoccupied molecular orbital (LUMO). Furthermore, the stiffness of the chromophore can be tuned to increase the quantum yield[29,107] and even photo induced spectral shifts by reactions with oxygen can thus be prevented.[108] The naturally very hydrophobic dyes can be made hydrophilic e.g. with sulfonic groups.[109]
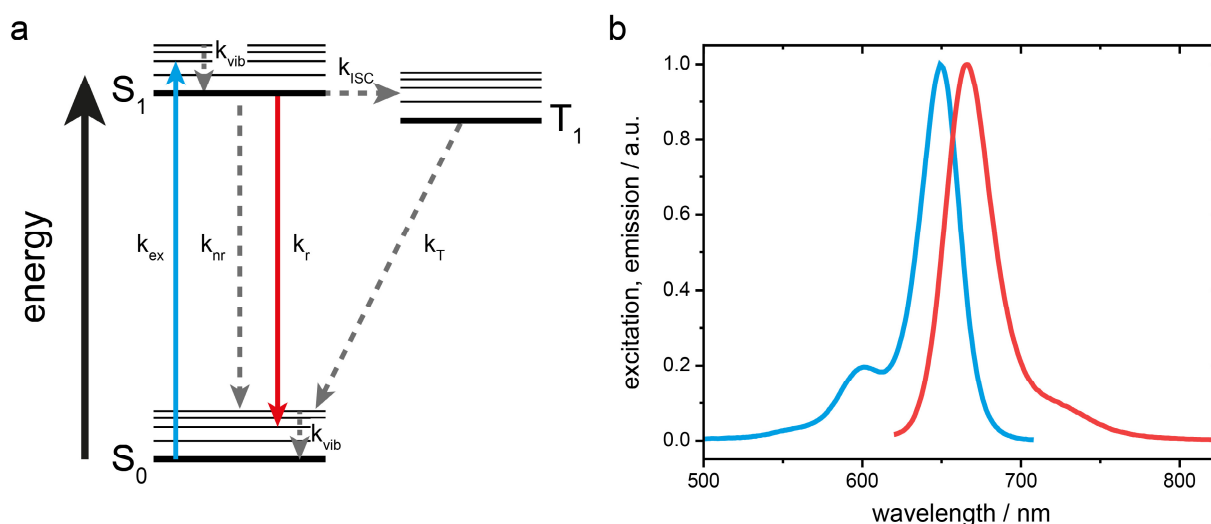

Figure 2.1: a) Schematic representation of a Jabłoński-diagram for organic dyes. Electronic levels are indicated with bold lines and vibronic levels with thin lines. Rotational levels are excluded for the sake of clarity. Radiative transitions are highlighted in blue and red; non-radiant transitions are highlighted with gray dashed lines. b) Absorption (blue line) and fluorescence (red line) spectrum of ATTO647N attached to deoxyribonucleic acid in phosphate buffered saline.

A Jabłoński-diagram depicted in Figure 2.1a gives a comprehensive overview of the possible electronic processes in an organic dye after a photon has been absorbed by the singlet ground state S_0. The dye has several electronically excited singlet states S_N (with N = 1,2,3 ...) and triplet states T_N (with N = 1,2,3 ...). Each electronic state has several vibration levels and each vibration level has several rotational levels which are not shown in Figure 2.1a for the interest of clarity. At room temperature, at which all experiments in this work were carried out, almost all dyes occupied the zero-vibration level of the S_0 state. A photon of the excitation laser (excitation rate, k_{ex}) can be absorbed if the photon corresponds to the energy difference between S_0 and S_N transition. This work features $S_0 \rightarrow S_1$ excitation transitions. k_{ex} is proportional to the laser's excitation intensity I_{ex} and the absorption cross section σ of the dye.

$$k_{ex} = I_{ex}\sigma$$

(2.1)

The absorption cross section reflects the probability of the electronic excitation which is explained by the Franck-Condon principle[110] and depends on the overlap of the vibrational wave functions of the S_0 and the S_1 state. After excitation the system returns to the lowest vibration level of the S_1 state within femtoseconds (vibrational relaxation rate, k_{vib}). From there, it can return to the electronic ground state S_0 either by heat dissipating (non-radiative rate, k_{nr}) or by photon emission (radiative rate, k_r). Due to the vibrational relaxation and solvent reorganization the emitted photon is red-shifted to the absorbed photon (as depicted in figure 2.1b). The relaxation to the ground state usually results in an excited vibrational level from which it relaxes to the vibrational ground level (k_{vib}). The emitted photon has a lower energy than the absorbed photon (indicated by the shorter arrow length). This red shift is called the Stokes shift and allows the spectral separation between excitation light and emitted light. From the S_1 state the system can undergo an inter system crossing (ISC) transition into the excited triplet state T_1. From there, the system can also return to the S_0 state by either emitting a photon (phosphorescence) or dissipating the energy as heat. Both paths are combined with the reverse ISC rate k_T.

The transitions between the electronic states are rate processes. Characteristic quantities of a dye, such as its fluorescence lifetime τ_{fl} or quantum yield Φ, can thus be described. The lifetime of an electronic state is inversely proportional to the sum of all depopulating rates of the state. Therefore, the average lifetime of the S_1 state, referred to as fluorescence lifetime τ_{fl}, is defined as:

$$\tau_{fl} = \frac{1}{k_r + k_{nr} + k_{ISC}}$$

(2.2)

For organic dyes τ_{fl} is in the nanosecond range. The lifetime of the triplet state is given as:

$$\tau_T = \frac{1}{k_T}$$

(2.3)

τ_T is in the microseconds to milliseconds range. The quantum yield Φ indicates the ratio between absorbed and emitted photons. Expressed in rates, this results in:

$$\Phi = \frac{k_r}{k_r + k_{nr} + k_{ISC}}$$

(2.4)

11

The ISC yield is equally calculated:

$$\Phi_{ISC} = \frac{k_{ISC}}{k_r + k_{nr} + k_{ISC}} \qquad (2.5)$$

Although the ISC yield for organic dyes is very small, for rhodamine dyes it is between 0.2-1%,[111,112] it leads to interruptions of the fluorescence signal due to the long T_1 lifetime. These interruptions are referred to as blinking. All electronically excited states have a higher reactivity than the ground state and can thus irreversibly photo beach, e.g. through oxidation by molecular oxygen.[113,114] The bleaching rate constant depends on the one hand on the reactivity of the excited electronic state but also on its occupation time. Although the T_1 state has a low formation rate, photo bleaching is most likely to occur from this state due to its long excited state lifetime τ_T.[115]

Therefore, the requirements for a fluorescent dye can be described with the characteristic quantities mentioned before. A reporter dye in a tracking experiment should have a large absorption cross section and high quantum yield for a strong fluorescence signal. In addition, the triplet state should only be occupied briefly and rarely. This is not only advantageous for a fluorescence trajectory with minimal blinking, but also for high photo stability.

2.2 Tuning the Blinking Kinetics with the Reducing and Oxidizing System

In order to increase the photo stability of organic dyes, various additives such as ascorbic acid (AA), methyl viologen (MV) or trolox (TX) and its quinone (TQ) were added[15,116] to buffers in order to scavenge reactive oxygen species. Another approach was the introduction of an oxygen scavenging system. Even though the photo stability was improved it came off the cost of pronounced triplet blinking because oxygen is an excellent triplet quencher as well due to its paramagnetic ground state. Therefore, the idea that additives can undergo electron transfer reactions with electronic excited organic dyes opened the door for controlling the blink kinetic of organic dyes. The concept of the reducing and oxidizing system (ROXS) was introduced by Vogelsang et al in 2008.[31]

The ROXS extends the Jabłoński diagram for an organic dye from figure 2.1 with a radical anionic state $R^{\cdot-}$ and a radical cationic state $R^{\cdot+}$ as shown in figure 2.2. These radical states are populated predominantly via the T_1 state by photoinduced electron transfer (PET) reactions which lead to a charge separation between the donor and acceptor molecule. By a reverse reaction the chromophore's S_0 ground state can be repopulated again. The reverse reaction does not happen with the same molecule because the electron spins are still correlated after the charge transfer.[117] However, molecules providing a high spin orbit coupling like β-mercaptoethanol can undergo a geminate recombination[117,118] and can therefor repopulate the S_0 state very efficiently. The reactions are diffusion-limited and the depopulation of the states, S_1, T_1, $R^{\cdot-}$ and $R^{\cdot+}$ can be controlled by the concentrations of the oxidizing or reducing species.
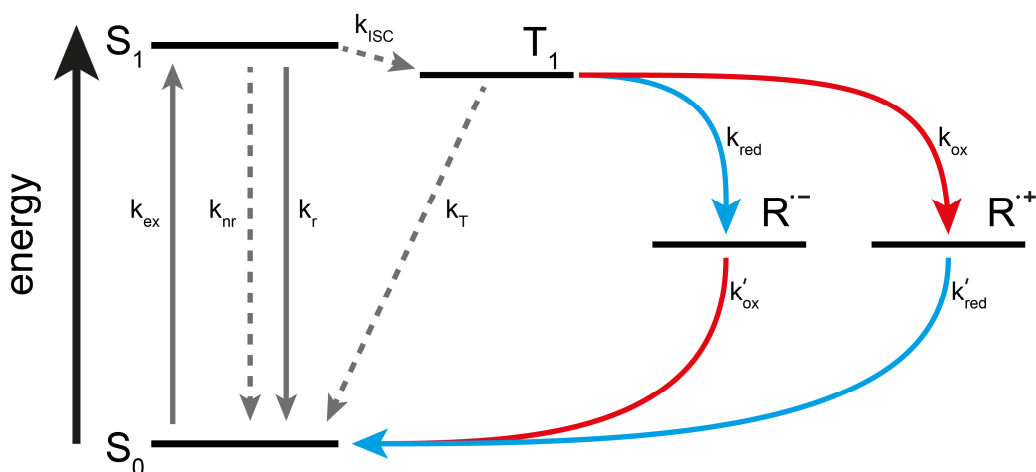
Figure 2.2: Simplified Jabłoński-diagram for organic dyes expanded with anionic ($R^{\cdot-}$) and cationic ($R^{\cdot+}$) radical states. The photo-induced electron transfer of the dye occurs mainly from the T_1 state. The reduction pathways are marked with blue arrows and the oxidation pathways with red arrows.

The efficiency of T_1 depletion depends on the redox potential of the electronically excited states of the dyes. E.g. cyanine and carborhodamine dyes, do not show any measurable triplet blinking with 1.75 mM TX and 0.25 mM TQ and an enzymatic oxygen scavenging system. However, 1,4-oxazine dyes, like ATTO 655 or ATTO 700, have an energetic low radical anionic state which is no longer effectively reoxidized with TQ, which results in radical blinking. This proved very useful in Chapter 4.3.

2.3 Strong Coupling of Organic Dyes

If multiple organic dyes come in contact range they are no longer independent of each other and can undergo strong coupling in an aggregate. Strong coupling has a particular effect on the electronically excited states, because assignment of the exciton to a single chromophore is no longer possible. The coupling results in a delocalization of the exciton between the aggregated dyes. The transition dipole phase relation becomes very important for the spectral properties of the aggregate and was first theoretical described by Kasha et al.[56] In an aggregate of two molecules van der Waals interactions lower the ground state energy, as shown in Figure 2.3a. The electronically excited state, however, splits up into two separate states. In one state the transition dipole moments interfere constructively (bold line) and in the second case the transition dipole moments interfere destructively and cancel out (dotted line). Which case is the most energetically favorable and dominates the luminescence of the aggregate depends on the relative transition dipole orientation.

In an J-aggregate, named after E. E. Jelly's work,[119] the chromophores form a head-to-tail alignment. The exited state where the transition dipole moments add up is energetic more favorable. The rise in oscillator strength increases the radiative rate, which is reflected in a higher quantum efficiency and a shorter fluorescence lifetime of the aggregate. The absorption and emission spectrum is red-shifted and the spectrum shows narrower peaks with a well-defined vibronic progression due to the strong coherence of the excited state which reduces vibrational couplings.
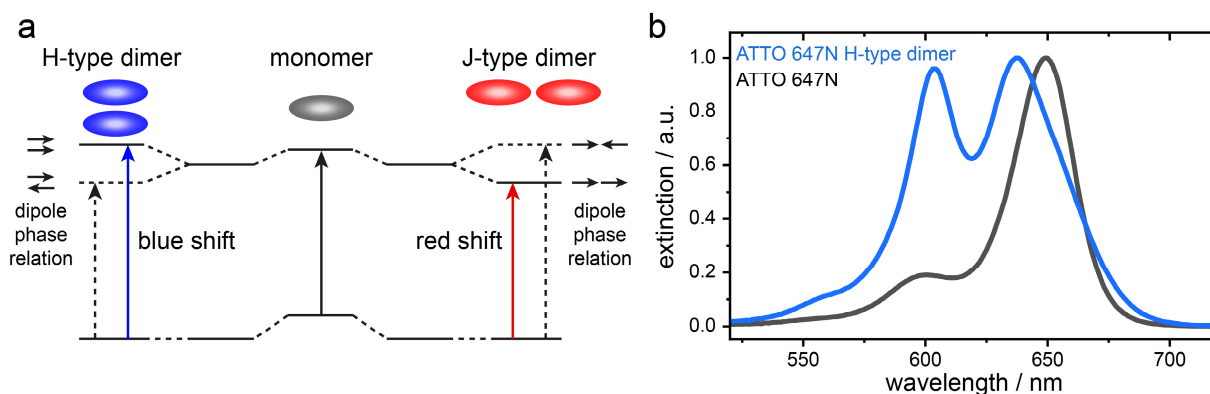
Figure 2.3: a) Exciton band energy diagram for molecular H- and J-type dimers. Radiative favored transitions are marked with solid lines. The phase relation of the transition dipole moments is indicated by the arrows next to the excited states. b) Absorption spectra of a single ATTO 647N dye attached to Deoxyribonucleic Acid (DNA) (black) and two ATTO 647N dyes separated by a single base pair distance forming a H-type dimer (blue).

The H-aggregate, named after the hypsochromic shift in the absorption spectrum, occurs much more frequently with rhodamine based dyes. The chromophores align in a face-to-face arrangement and the transition dipole moment phases cancel each other out in the energetically favored state. Electronic excitation in the energetic higher state is possible (the hypsochromic shift's origin, see figure 2.3b), but internal conversion (IC) quickly depopulates the state. If fluorescence is observed due to imperfect H-aggregates the quantum yield is drastic reduced and the fluorescence lifetime increases due to the diminished radiative rate. The emission spectrum is red-shifted and greatly broadened due to increased vibrational coupling. If organic dyes form an H-dimer, no fluorescence is usually observed. According to Stern and Vollmer, the loss of the fluorescence intensity for organic dyes is called static- or contact-quenching.[120]

2.4 Weak Coupling of Organic Dyes

If the chromophores are spatially separated, they are not completely independent of one another and can undergo resonant dipole-dipole coupling in the form of Förster Resonance Energy Transfer (FRET) up to a distance of $\sim 10\,nm$. The exciton of the donor molecule can be transferred non-radiativly to the acceptor molecule as depicted in figure 2.4.1a. The fact that the fluorescence lifetime is shortened by the energy transfer rate constant k_{ET} proves that FRET is not an uncorrelated donor-emission and random acceptor-absorption process but rather a S_1 depopulating rate process of the donor.[121] FRET between two different dyes is called hetero-FRET and is often used in life sciences to measure distances[122] and dynamic processes e.g. in proteins.[40] The absorption spectrum of the acceptor dye is red-shifted to the fluorescence spectrum of the donor dye (see figure 2.4.1b) and the emission of the dyes can be spectrally separated.
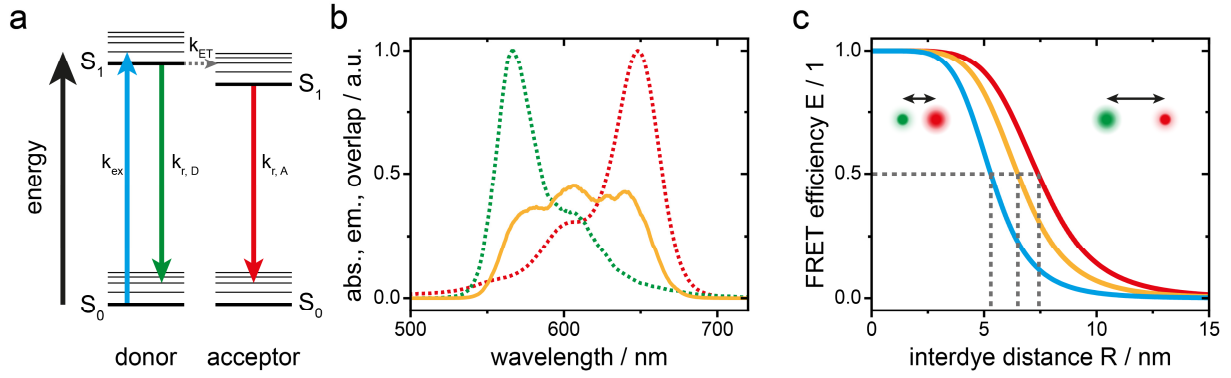
Figure 2.4.1: a) Jabłoński-diagram of a FRET-process between a donor and an acceptor molecule. b) Fluorescence spectrum of Cy3 (green, donor) and absorption spectrum of Cy5 (red, acceptor). Spectral overlap density $J(\lambda)$ of the FRET pair is depicted in orange. c) Distance-dependent FRET efficiency E for three different FRET pairs. The Förster radii R_0 are marked with dashed lines and correspond to 5.3 nm (blue, Cy3 - Cy5), 6.5 nm (orange, Cy3B - ATTO 647N) and for the FRET pair from this work 7.4 nm (red, ATTO 647N - ATTO 700).

The FRET efficiency E and the energy transfer rate constant k_{ET} scales with an inverse six power law of the interdye distance R.

$$E = \frac{k_{ET}}{k_r + k_{nr} + k_{ET}} = \frac{1}{1 + \left(\frac{R}{R_0}\right)^{-6}} \tag{2.6}$$

The Förster-radius R_0 is the characteristic for each FRET-pair and indicates the distance where the transfer efficiency is $E = 0.5$ (see figure 2.4.1c). Consequently, a typical R_0 value of 5 nm indicates that FRET between organic dyes can only be observed in a range between 2 and 10 nm. Various factors such as the overlap integral between the normalized emission spectrum $I_D(\lambda)$ of the donor and the absorption spectrum $\varepsilon_A(\lambda)$ of the acceptor are included. The overlap integral also scales with the fourth power of the wavelength λ and describes how well the acceptor molecule can couple to the nearfield of the excited donor. Furthermore, the relative orientation of the transition dipole moments to one another is decisive. Since it is a near field interaction, a collinear alignment is most efficient. For two freely rotating dyes, the orientation factor is $\kappa^2 = {}^2/_3$.

$$R_0 = \frac{9 \, ln10 \, \kappa^2 \, \Phi_D}{128 \, \pi^5 N_A \, n^4} \int_0^\infty I_D(\lambda)\varepsilon_A(\lambda)\lambda^4 d\lambda \tag{2.7}$$

Homo-FRET, on the other hand, describes the energy transfer between identical dyes. The energy-transfer shows in a faster loss of anisotropy and does not shorten the observed fluorescence lifetime nor lower the fluorescence intensity. Even if it is rarely used in designed FRET experiments, it is of particular importance when it comes to exciton diffusion in artificial light-harvesting complexes[123,124] and conjugated polymers (CP).[125]
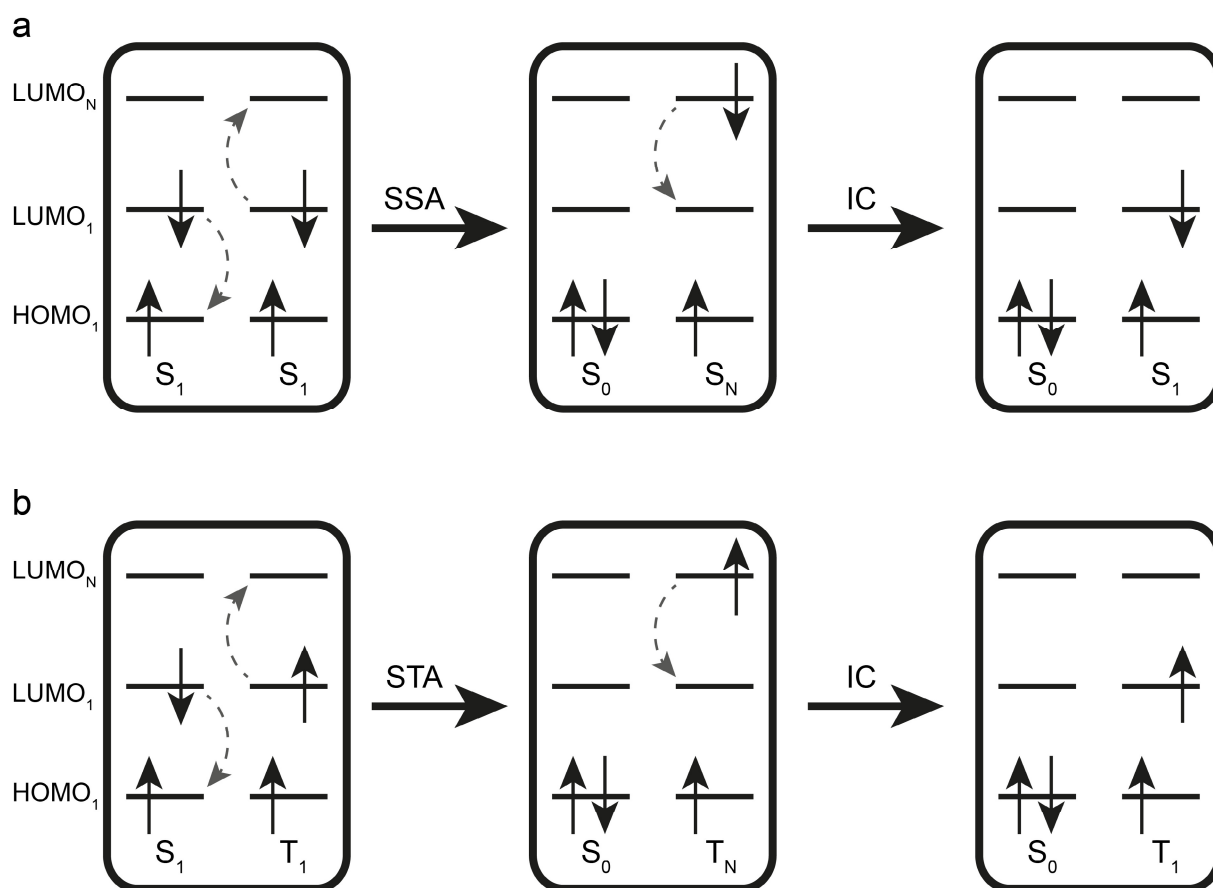
a

b

Figure 2.4.2: a) Principal of singlet-singlet annihilation (SSA). Two chromophores are in the electronically excited singlet state S_1. By resonant coupling, the left chromophore transfers its energy to the second chromophore and thus reaches the S_0 state. The second chromophore gets excited to an S_N state from which it quickly returns to the S_1 state by IC. b) Principal of singlet-triplet annihilation (STA). The left chromophore is in the S_1 state and the right chromophore in the T_1 state. By resonant coupling, the left chromophore transfers its energy to the chromophore in the T_1 state. The left one relaxes thereby into the S_0 state and the right chromophore gets excited into the T_N state. From there it relaxes again to the T_1 state.

FRET does not only occur between an electronically excited donor molecule and an acceptor molecule in the ground state. It can also occur if two molecules are in an electronically excited state. The mechanism is depicted in Figure 2.4.2a. By resonant coupling the energy is transferred from the donor molecule to the acceptor molecule, which is promoted to a higher electronic state S_N. From there it returns into the S_1 state by IC, from which it can fluoresce. This process is called singlet-singlet annihilation (SSA) and for low excitation powers it can only be observed in the photon statistics (see Chapter 4.2, 4.3). If two identical dyes are present, there is a chance that two photons can be detected simultaneously from one excitation laser pulse. By comparing the probability of a two-photon detection event to the probability to detect two photons from consecutive laser pulses the degree of single photon emission is determent (photon antibunching). But if a multi-chromophoric system never shows two detection events from the same excitation laser pulse, this high degree of photon antibunching in itself is evidence for SSA processes occurring. For high excitation powers, SSA results in a loss of fluorescence intensity.[94]

In addition to SSA, singlet-triplet annihilation (STA) between two identical chromophores can also occur (Figure 2.4.2b). The triplet exciton is as a quenching moiety and acts like a dark FRET acceptor in a hetero FRET experiment. In addition, radical states can also serve as FRET acceptors. If the electronic state of the acceptor is not known, one can speak of singlet dark-state annihilation (SDA). SDA shortens the fluorescence lifetime and lowers the fluorescence intensity of the donor dye where as SSA is only revealed in the photon correlation for low excitation rates.

For the sake of completeness, it should be mentioned that triplet-triplet annihilation (TTA) of dyes, which have a singlet ground state, is not subject to a FRET mechanism because a spin reversion is required. TTA can only occur through a collision enabling a double electron exchange (Dexter mechanism).

2.5 Intensity Correlation

The intensity correlation used in the life- and material-sciences has its origin in astronomy and was introduced in the 1950s. Hanbury-Brown and Twiss (HBT) measured the correlation of two detectors pointing to a star in order to determine its size.[77–79] They measured the decrease of correlation in the detected intensity as a function of the distance between two detectors. In a confocal HBT setup, like depicted in figure 2.5a, the fluorescence is distributed onto two single photon counting modules and a time correlated single photon counting (TCSPC) unit records the detected events.

Intensity correlations are very sensitive to intensity fluctuations. The correlations of the recorded intensities $I_1(t)$ and $I_2(t)$ are calculated for different delay times $\Delta\tau$.

$$g^{(2)}(\Delta\tau) = \frac{\langle I_1(t) \cdot I_2(t + \Delta\tau)\rangle}{\langle I_1(t)\rangle \cdot \langle I_2(t)\rangle} \tag{2.8}$$

The brackets denote temporal averaging. The normalized correlation function $g^{(2)}(\Delta\tau)$ indicates the probability of detecting a photon on channel 2 at a delay time $\Delta\tau$ if a photon was detected in channel 1 at time $\Delta\tau = 0$. In the life sciences, the $g^{(2)}(\Delta\tau)$ correlation is known as fluorescence correlation spectroscopy (FCS) which is used to study diffusion dynamics of dye labeled proteins or scattering nanoparticles.[8,126]
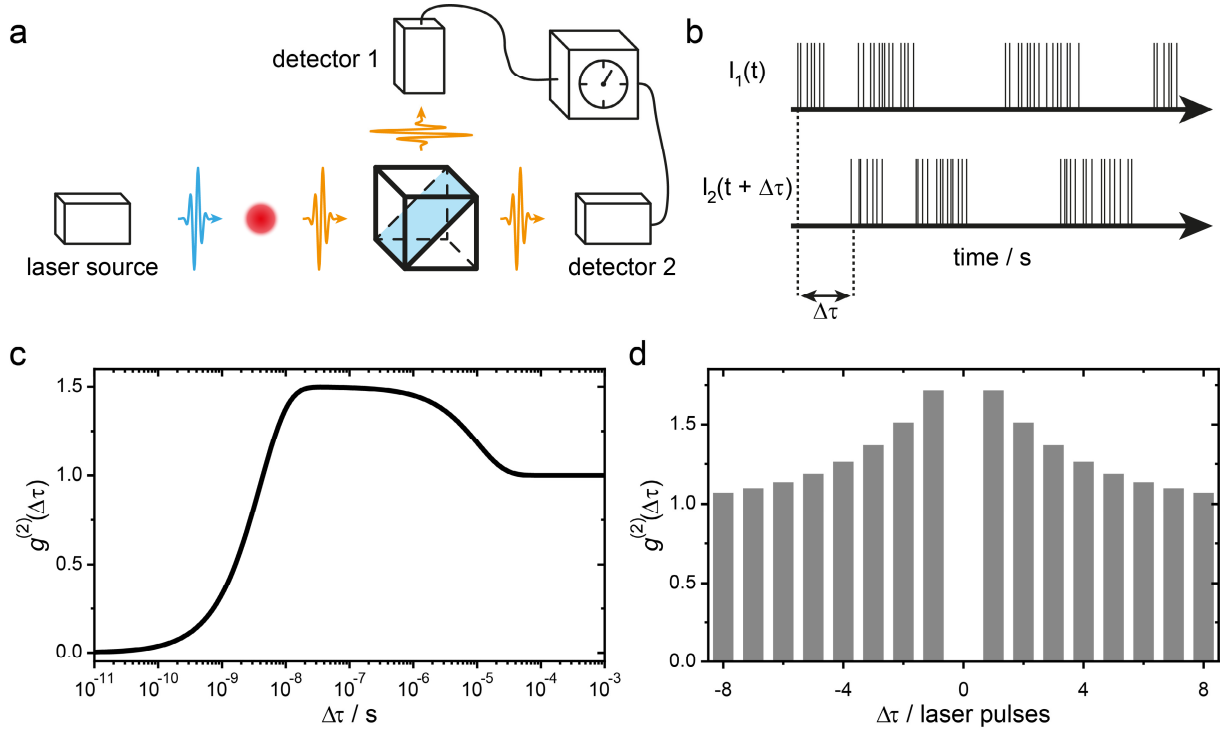
Figure 2.5: a) Simplified representation of an experimental setup. An organic dye (red dot) is electronically excited by a laser source (blue wave package). The fluorescence (orange wave package) is detected in an HBT photon correlator with a beam splitter and two single photon detectors. The photon arrival times are recorded by a time correlator. b) Detected photon stream with photo blinking of detector 1 and 2. Each line represents a single photon detection event. The photon stream I_2 is shifted by $\Delta\tau$ to I_1. c) Full $g^{(2)}(\Delta\tau)$ correlation plotted on a logarithmic time scale of a blinking single-photon source under continuous wave excitation. At small time scales the $g^{(2)}(\Delta\tau)$ correlation approaches zero because consecutive photon events in this time interval become impossible due to the finite exited state lifetime (in this example $\tau_{fl} = 4\ ns$) at low excitation rates. The correlation relaxation time (CRT) of the photo blinking equals $\tau_{CRT} = 10\ \mu s$ and the bunching amplitude equals $A = 0.5$. d) Photon correlation plotted on a linear time scalar of a blinking single-photon source under pulsed laser excitation. The CRT equals $\tau_{CRT} = 3$ laser repetition rate^{-1} and the bunching amplitude equals $A = 1.0$.

In this work, however, the intensity correlation of immobilized multi chromophoric nanoparticles is of interest. Here, intensity fluctuations occur mainly due to photophysics. The stochastic switching between a fluorescent and a dark state (see figure 2.5b), e.g. triplet or radical state, leads to photon bunches and shows in the $g^{(2)}(\Delta\tau)$ correlation as a mono-exponential decay:

$$g^{(2)}(\Delta\tau) = 1 + Ae^{-\tau/\tau_{CRT}} \tag{2.9}$$

The correlation relaxation time (CRT) is inverse proportional to the sum of intensity transition rate constants where k_{on} denotes the transition into the fluorescent and k_{off} denotes the transition out of the fluorescent state.

$$\tau_{CRT} = \frac{1}{k_{on} + k_{off}} \tag{2.10}$$

18

The bunching amplitude A equals the equilibrium constant K and derives from the ratio of the transition rate constants if the chromophore shows on-off switching.

$$A = K = \frac{k_{off}}{k_{on}}$$

(2.11)

If, on the other hand, the molecule does not go into a dark state, but only transitions into a quenched intensity state (weak fluorescence can still be observed), the intensity difference between the bright state I_A and the quenched state I_B must be taken into account.[36,38,42,43]

$$A = \frac{k_{off}}{k_{on}} \left(\frac{I_A - I_B}{I_A + \frac{k_{off}}{k_{on}} I_B} \right)^2$$

(2.12)

Thus there is no longer a unique solution for the transition rate constants k_{on} and k_{off}.

Photon bunching shows on the μs to ms timescales where triplet- and radical-states are observed. But on the timescale of an organic dye's fluorescence lifetime, photon antibunching is observed. Photon antibunching is a trademark signature of the quantum nature of a single photon source like organic dyes,[71,72] single ions[69,70] or single nitrogen vacancies in diamonds.[75,76] A single photon source can emit at maximum one single photon per excitation cycle resulting in a lack of zero delay times between two consecutive photons. The result is an absence of correlation events for zero delay time showing as anti-correlation in figure 2.5c for continuous wave excitation. In order to detect a second photon, the single photon source has to be re-excited before emitting the next photon. However, continuous wave excitation is usually not the first choice if photon antibunching is of interest. With an average inter-photon time of $10\ \mu s$ for a $100\ kHz$ countrate trajectory, consecutive photon events in the ns time range are rarely observed. More photon efficient is the $g^{(2)}(\Delta\tau)$ intensity correlation with pulsed excitation if photon antibunching is of interest like depicted in figure 2.5d.

If several single photon sources are present, two photons can be detected at the very same time. The number of independent emitters n can be deduced from the degree of photon antibunching at $g^{(2)}(0)$. In theory $g^{(2)}(0)$ is calculated from the ratio of independent emitters n and the number of independent emitters that can carry a second exciton $(n-1)$ independently.

$$g^{(2)}(0) = \frac{n-1}{n}$$

(2.13)

However, the interpretation of $g^{(2)}(0)$ in multi-chromophoric nanoparticles like conjugated polymer aggregates becomes challenging due to SSA, SDA processes and the resulting photon bunching.[51,55] The problems and solutions are discussed in detail in chapter 4.2 and 4.3.

2.6 DNA Origami

Deoxyribonucleic acid (DNA) nanotechnology uses designed synthetic DNA strands to build nanometer size structures for technical or scientific purposes. Nadrian (he wished to be named Ned) C. Seeman founded the field in the 80s with his idea to build two and three-dimensional networks from holiday connections.[127]
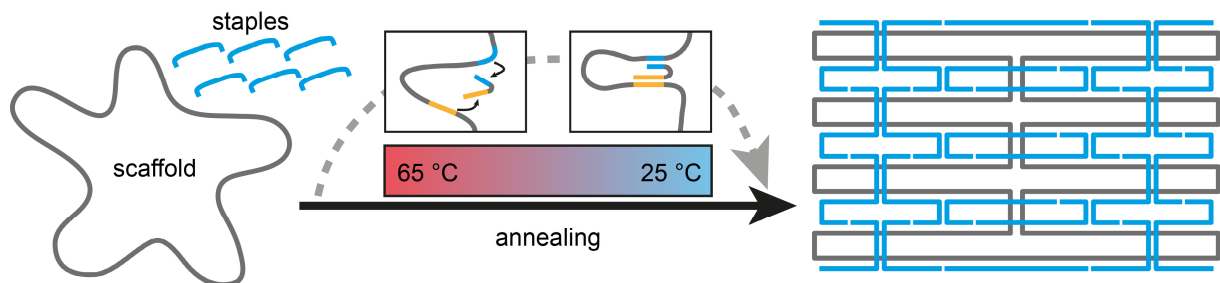

Figure 2.6: Principle of DNA origami folding. The circular scaffold (black) is mixed with hundreds of shorter staples (blue). During the annealing process, each staple binds to its designed scaffold positions (blue and orange staple sequence bind to the blue and orange scaffold sequence) and thus forms the flat rectangular DNA origami structure.

DNA origami is a branch of DNA nanotechnology and was invented by Paul Rothemund in 2006.[91] DNA origami enables the design of megadalton DNA structures in combination with bottom-up self-assembly. A $7000 - 8000$ base long single-stranded (ss) circular virus DNA is used as a scaffold. With approximately 200 shorter ssDNA staples strand, the scaffold is folded into the designed shape. The structure can be designed with an open source software such as caDNAno.[128] For the production of the DNA origami structure, the staples and the scaffold are mixed in a magnesium containing buffer and annealed over a temperature ramp from $65\,°C$ to $25\,°C$. Simple two-dimensional structures can be annealed within an hour, complex three-dimensional structures can take up to 17 hours. By this procedure, billions of identical structures are produced in one batch.

Each staple has a unique sequence and thanks to the specific Watson-Crick base pairing, it has a defined position in the DNA origami structure. Furthermore, the DNA can be chemically modified with various molecules such as organic dyes, vitamin B7 (Biotin) or functional groups like dibenzocyclooctyne (DBCO) for coupling reactions. Therefore, multiple molecules or nanoparticles can be positioned to each other with nanometer accuracy on a DNA origami structure. This capability is unique to the DNA origami technique and is instrumental for its success. Over the past years more and more complicated DNA origami structures were realized like a molecular DNA force clamp to study force effects on DNA-protein interactions[129,130] or icosahedral DNA based shell system for virus trapping[131] to mention just two of many milestones. On the other hand, a DNA origami structure can be used as a molecular breadboard to study interactions of plasmonic nanoparticles and chromophores with respect to the change in the non-radiative and radiative rate constants[132,133] and the superposition of emission.[134] In this work, organic dyes are spaced to another with nanometer precession in order to develop and validate new analysis methods for the photon correlation of resonant interacting chromophores.

3 Materials and Methods

To study dye-dye interactions in the strong and weak coupling regime fluorescent trajectories from individual immobilized DNA origami structures were required. The home build microscope and the associated measurement techniques as well as the principles of sample preparation and the concept of data analysis are described in this chapter.

3.1 Confocal Microscopy

All single particle measurements were performed on a home-built confocal microscope sketched in figure 3.1. The setup was based on an Olympus IX-71 inverted microscope. DNA-origami structures were excited by a pulsed laser either at 637 nm (LDH-D-C-640; PicoQuant GmbH) or 532 nm (LDH-P-FA-530B; PicoQuant GmbH). For most experiments the lasers operated at 40 MHz repetition rate. Each laser power was adjusted with a neutral-density filter (ND06A, Thorlabs) according to the experiments needs. The lasers were combined by a dichroic mirror (640 LPXR, Chroma) and coupled into a polarization maintaining single mode fiber (P3-488PM-FC, Thorlabs GmbH) for perfect overlay of the lasers and to obtain a Gaussian beam profile. After the optical fiber circularly polarized light was obtained by aligning a linear polarizer (LPVISE100-A, Thorlabs GmbH) and a quarter-wave plate (AQWP05M-600, Thorlabs GmbH). In the microscope the light was focused to a diffraction limited spot by an oil-immersion objective (UPLSAPO100XO, NA 1.40, Olympus Deutschland GmbH). The sample was moved by a piezo stage (P-517.3CD, Physik Instrumente (PI) GmbH & Co. KG) controlled by a piezo controller (E-727.3CDA, Physik Instrumente (PI) GmbH & Co. KG). Inside the microscope body the emission was separated from the excitation beam by a dichroic beam splitter (zt532/640rpc, Chroma) and focused onto a 50 μm diameter pinhole (Thorlabs GmbH).

In a two-color experiment the emitted light was split by a dichroic beam splitter (640DCXR, Chroma) into a green (Brightline HC582/75, Semrock AG; RazorEdge LP 532, Semrock) and red (Shortpass 750 (FES0750), Thorlabs GmbH; RazorEdge LP 647, Semrock) detection channel. For an experiment where the degree of photon antibunching was of interest, the emitted light was first separated from scattered excitation light by a 647 nm long-pass filter (RazorEdge LP 647, Semrock). The filtered emission was split into two detection channels by a non-polarizing 50 : 50 beam splitter (CCM1-BS013/M, Thorlabs GmbH). In each detection channel, the afterglow luminescence of the avalanche photodiode was blocked by a 750 nm short-pass filter (FES0750, Thorlabs GmbH).

For each detection path the emission was focused onto avalanche photodiodes (SPCM-AQRH-14-TR, Excelitas Technologies GmbH & Co. KG) and the signals were registered by a multichannel picosecond event timer (HydraHarp 400, PicoQuant GmbH). The setup was controlled by a commercial software package (SymPhoTime64, Picoquant GmbH).
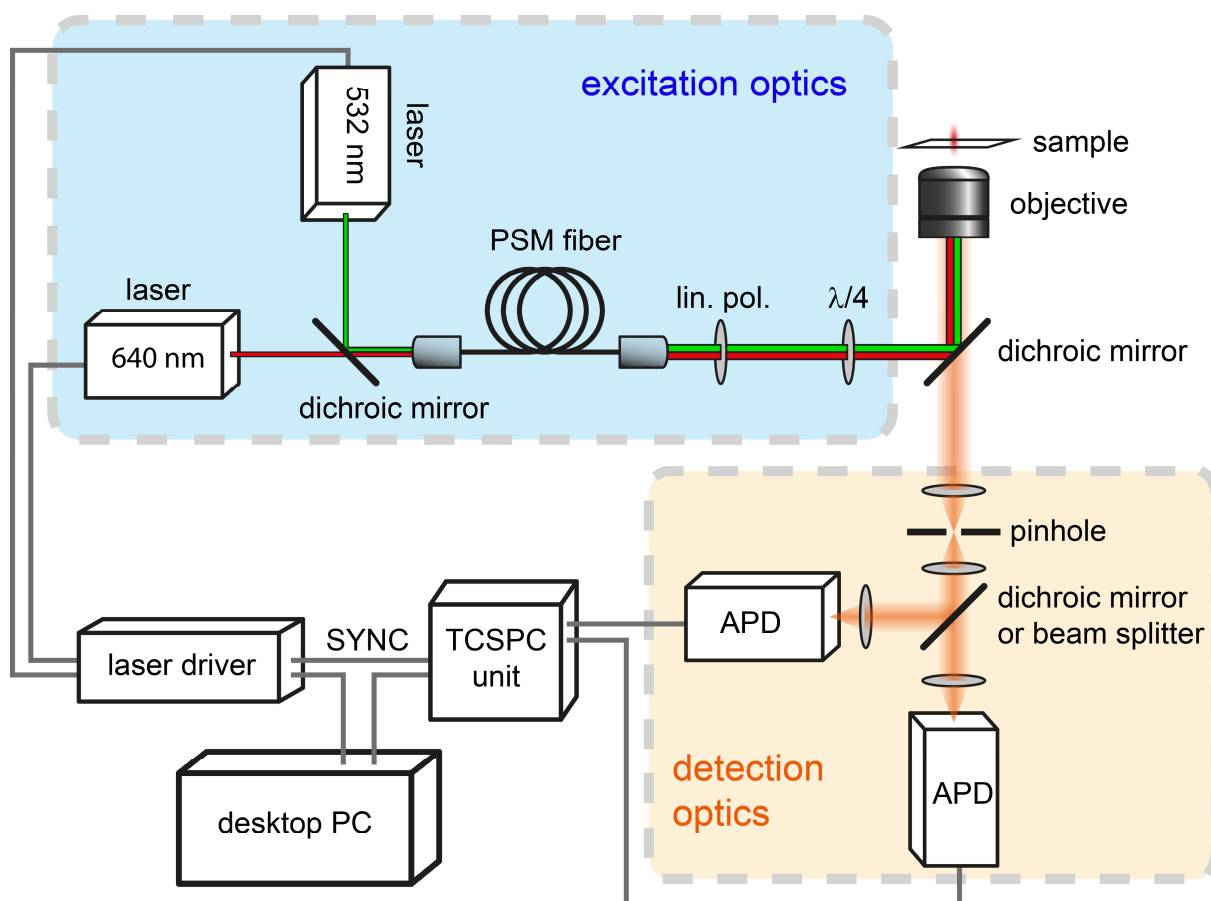
Figure 3.1: Simplified schematic drawing of the confocal microscope constructed for this work. Pulsed laser sources with wavelength of 532 nm and 640 nm are combined and coupled into a polarization maintaining single-mode fiber (PSM) in the excitation optics. The excitation light is focused by the objective onto the sample. The collected fluorescence emission is focused on a pinhole and detected by an avalanche photodiode (APD). The signals are correlated by a Time Correlated Photon Counting (TCSPC) unit. For details see the method section of the respective publication.

In this work the DNA origami structures were immobilized on the glass surface. The DNA origami structurers were identified in a line scan in order to record fluorescence trajectories. For this purpose, usually a 10 μm × 10 μm area was scanned by moving the sample by the piezo over the fixed objective (see example scan in figure 3.2.1a). The pixel size was 50 nm × 50 nm and the integration time was 2 ms / $pixel$. Single isolated structures could be selected in order to obtain fluorescence trajectories from their position.

3.2 Concept of TCSPC and Microtime Gating

Time Correlated Photon Counting (TCSPC) enables fluorescence lifetime measurements. If a photon is detected on an avalanche photodiode (APD), the time until the next laser pulse is measured by the TCSPC unit and the delay between excitation pulse and detected photon is calculated (microtime). Additionally, the time relative to the start of the experiment (macrotime) as well as the detector number (channel) is saved. Macrotime tags have the time

resolution of the laser repetition rate (typically $12.5\ ns - 50\ ns$) and are used to visualize fluorescence trajectories like in figure 3.2.1b or to calculate $g^{(2)}(\Delta\tau)$ intensity correlations. The microtime tag has a much higher time resolution (typically $1 - 50\ ps$) and from its histogram of the selected photons the fluorescent lifetime can be extracted. However, for fluorescence lifetime fitting the convolution of exponential fluorescence decay with the instrument response function (IRF) of the detection electronic has to be taken into account. An example TCSPC histogram of a fluorescence decay and the IRF is depicted in figure 3.2.1c.
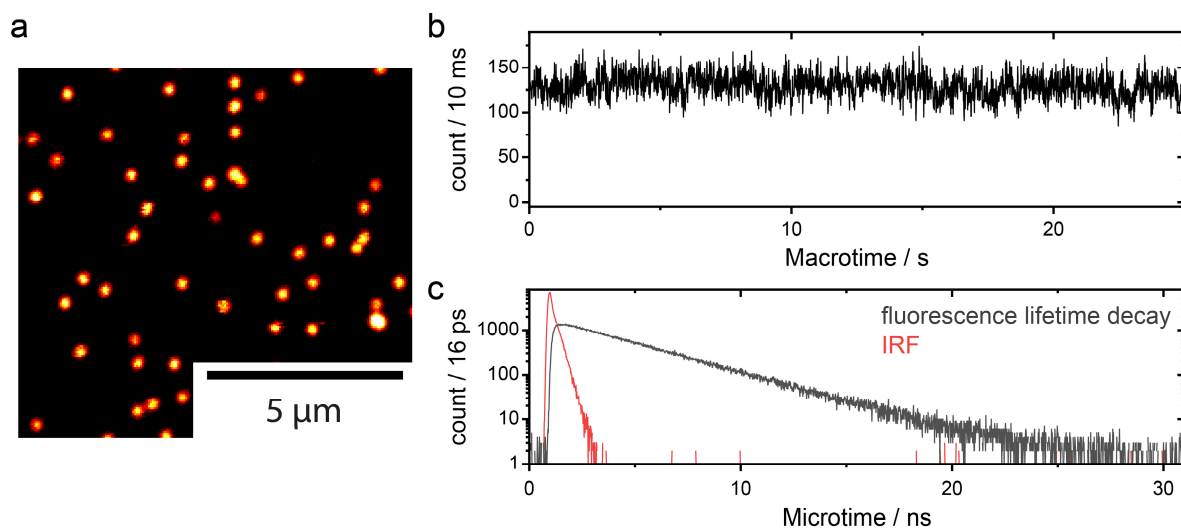

Figure 3.2.1: Example for single molecule data acquisition. a) A $10\ \mu m \times 10\ \mu m$ confocal scan image of immobilized DNA origami structures labeled with ATTO 542. Pixel size is $50\ nm \times 50\ nm$. b) From the macrotime stamps created fluorescence trajectory of a single DNA origami structure. c) Corresponding microtime histogram of the ATTO 542's fluorescence lifetime decay (black). The measured lifetime decay is convoluted with the IRF (red).

Macrotime and microtime tags can be used to sort photons. E.g. in fluorescence lifetime imaging (FLIM), all microtimes of a pixel are used in order to determine the average fluorescence lifetime of molecules in the corresponding pixel. A prominent target of FLIM is the enzymatic cofactor NADPH which changes its fluorescence lifetime once it gets bound by an enzyme.[135] Thus the free and bound NADPH fractions can be mapped in cells.[135]

However, photons sorting according to their microtime is of particular interest for this work. Microtime gating is frequently used e.g. in gated stimulated emission depletion (gSTED) experiment to exclude fluorescence from the doughnut area.[136] In a similar way microtime gating was used in the early days of FCS experiments to exclude the laser pulse scattering signal which adds uncorrelated macrotime stamps and thus reduces the correlation amplitude.[42,90] Also a weighting of the macrotime tags according to their microtime was introduced as Fluorescence Lifetime Correlation Spectroscopy (FLCS) to overcome electronic artifacts like after-pulsing.[137] With prior knowledge different species with the same spectral properties can be correlated.[138] However, the microtime dependent bunching amplitude for dynamic systems as well as the microtime dependent degree of photon antibunching was not explored in great detail yet.

Microtime gating affects the bunching amplitude of a dynamic system switching between an unquened state A and a quenched state B which is subject to FRET. Therefore, the quenched species B is subject to an additional quenching rate k_{ET}, thus its fluorescence lifetime τ_B is

23

shortened and the quantum yield Φ_B is reduced. A simulated blinking fluorescent trajectory is depicted in figure 3.2.2. The first trajectory switches stochastically between the bright I_A and the quenched intensity I_B and the $g^{(2)}(\Delta\tau)$ intensity correlation shows a bunching amplitude. However, the switching rates cannot be derived from the CRT and the correlation amplitude since the equilibrium constant K has no unique solution for two intensity levels (see equation 2.12). By only considering photons that were detected between $0.0 - 0.5 \, ns$ after excitation the fluorescent trajectory does not show any blinking, because the trajectory is dominated by the radiative rate k_r. Thus the $g^{(2)}(\Delta\tau)$ intensity correlation does not show any bunching (see figure 3.2.2c). For the microtime gate between $8.0 - 8.5 \, ns$ the fluorescence trajectory only contains photons from the slower decaying species A. The $g^{(2)}(\Delta\tau)$ intensity correlation is maximized because for this microtime gate the quenched intensity I_B is close to zero. This simple simulation demonstrates the microtime gate dependency of the bunching amplitude $A(t)$. The Bunching amplitude scales with the square of the intensity contrast between the two species (see equation 2.12) which is altered by microtime gating because the intensity of the two species decay at different rates.

$$I_A(t) = e^{-(k_r + k_{nr}) \cdot t}$$

(3.1)

$$I_B(t) = e^{-(k_r + k_{nr} + k_{ET}) \cdot t}$$

(3.2)

Therefor we can express the microtime dependent correlation amplitude $A(t)$ as:

$$A(t) = K \left(\frac{1 - e^{-k_{ET} \cdot t}}{1 + K \cdot e^{-k_{ET} \cdot t}} \right)^2$$

(3.3)

The microtime dependent correlation amplitude $A(t)$ is zero for $t = 0$ because at excitation there was no time for non-radiative processes. For later microtime gates $A(t)$ starts to rise because of the increasing intensity contrast between the two species. This is reflected in the exponential term of the expression 3.3. Late microtime gates provide a large intensity contrast and the correlation amplitude saturates at the equilibrium constant K. To give an example: The amplitude reaches 95% of K at an intensity contrast of $\frac{I_A(t)}{I_B(t)} = 78$. With an quenching rate of $k_{ET} = 1 \, ns^{-1}$ the intensity contrast is provided at an microtime gate of $t = 4.35 \, ns$. The extraction of the equilibrium constants was previously not possible when all photons were considered for the $g^{(2)}(\Delta\tau)$ intensity correlation.

By applying microtime gating with equal step size each $g^{(2)}(\Delta\tau, t)$ correlation can be fitted with a monoexponential model of equation 2.9. The extracted amplitudes can be fitted with equation 3.3 and yield the equilibrium constant K and the additional quenching rate k_{ET} of I_B. However, this microtime gating approach may be very intuitive but suffers from a low signal to noise level for late microtime gates. Late microtime gates give low fluorescence intensities due to the exponential intensity decay. The signal to noise ratio of a $g^{(2)}(\Delta\tau)$ intensity correlation scales linear with the intensity and thus $g^{(2)}(\Delta\tau, t)$ correlations from late microtime gates are noisy as depicted figure 3.2.2c. A more photon efficient approach of microtime gating is presented in chapter 4.3 and 4.4.
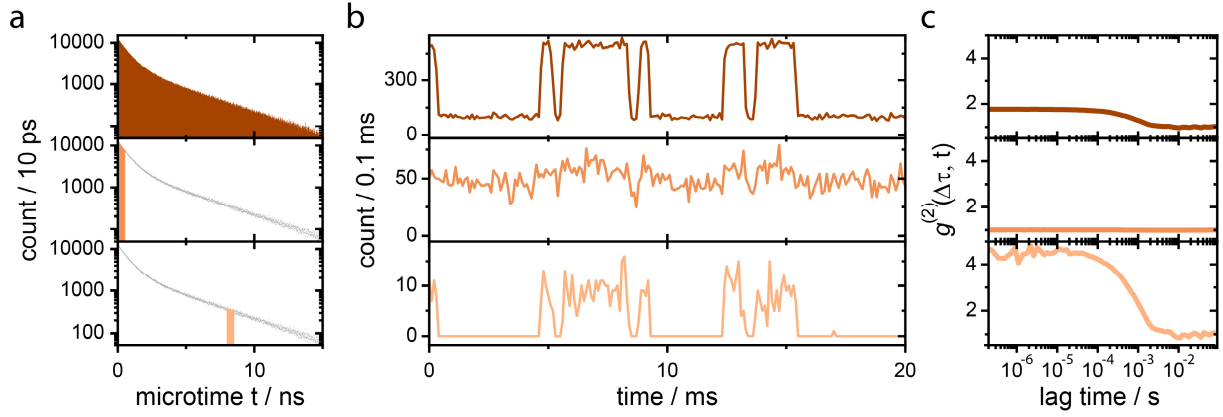
Figure 3.2.2: The Effect of microtime gating on the intensity trajectory and the corresponding intensity correlation $g^{(2)}(\Delta\tau, t)$. a) Histograms of simulated photon arrival times in a pulsed laser excitation experiment with different microtime gates. The colored area indicates the applied microtime gate. b) Extracted intensity trajectories according to the considered photons of the microtime gate. c) Corresponding $g^{(2)}(\Delta\tau, t)$ intensity correlation of the intensity trajectories. Simulation parameters: $k_a = 2150\ s^{-1}$, $k_b = 7820\ s^{-1}$, $\tau_A = 4.0\ ns$, $\tau_B = 0.8\ ns$, $\Phi_A = 0.5$, $\Phi_B = 0.1$, laser repetition rate $= 10\ MHz$, simulated laser pulses $= 10,000,000$.

SSA is also a rate process and reduces the probability of detecting two photons from a single excitation pulse. However, for low excitation rates SSA has no impact on the fluorescence trajectory, since two chromophores are only very rarely electronically excited at the same time. If on average every 1,000th laser pulse excites one of n chromophore in the system, statistically only every 1,000,000 laser pulses two of the n chromophores are excited within one laser pulse. Even very efficient SSA reduces the fluorescence intensity only by a per mil. To detect such rare double excitation events the HBT setup is used. But with SAA occurring, the probability of two photon events is reduced. Thus the $g^{(2)}(\Delta\tau)$ correlation shows a much higher degree of photon antibunching which underestimates the true number of chromophores in the sample. Furthermore, the probability of detecting two photons after a laser pulse excitation decays exponentially with the SSA rate k_{SSA}. This is why microtime gating can also take advantage of the time dependent SSA rate process. However, the direction of the annihilation is not specified. Each exciton can be quenched by another one with an energy transfer rate k_{ET}. Hence, the observed SSA rate k_{SSA} is the sum of the energy transfer rates $k_{SSA} = 2k_{ET}$.

In a system with n chromophores, $n-1$ chromophores can carry a second exciton. Let us detect the first photon at time t after laser excitation and the second photon at time $t + \tau$. The probability of a correlation event $N_C(t, t + \tau)$ from a single excitation pulse X can therefore be expressed as:

$$N_C(t, t + \tau) = P_X(t) \cdot P_X(t + \tau)$$

(3.4)

With the probability of detecting the first photon $P_X(t)$ and the probability of detecting the second photon $P_X(t + \tau)$. The probability $P_X(t)$ is subject to the radiative k_r, non-radiative k_{nr} and energy transfer rate k_{ET}:

$$P_X(t) = pne^{-(k_r + k_{nr} + k_{ET})t}$$

(3.5)

25

With p, the combined probability for chromophore excitation and photon emission detection. $P_X(t + \tau)$ is subject to the energy transfer rate k_{ET} until the first photon is emitted at time t. For later emission times τ the exciton is no longer subject to the annihilation process.

$$P_X(t + \tau) = p(n - 1)e^{-(k_r + k_{nr} + k_{ET})t}e^{-(k_r + k_{nr})\tau}$$

(3.6)

Integration over all delay times τ between the two photon detection events gives the number of correlation events $N_C(t)$.

$$N_C(t) = \int_0^\infty N_C(t, t + \tau)d\tau \Rightarrow p^2\tau_{fl}n(n - 1)e^{-2(k_r + k_{nr})t}e^{-k_{SSA}t}$$

(3.7)

The lateral correlation events, on the other hand, deal with the probability of detecting two photons at t and $t + \tau$ after excitation from different excitation pulses X and Y.

$$N_L(t, t + \tau) = P_X(t) \cdot P_Y(t + \tau)$$

(3.8)

At low excitation rates only a single of the n chromophores is excited by the laser excitation pulse hence the exciton is not subject to any annihilation processes. For non-blinking systems, the probability of detecting the first photon from the laser pulse X is given as:

$$P_X(t) = pne^{-(k_r + k_{nr})t}$$

(3.9)

And the probability for the second photon from laser pulse Y is:

$$P_Y(t + \tau) = pne^{-(k_r + k_{nr})(t + \tau)}$$

(3.10)

The correlation events independent of the delay time τ can also be obtained by integration:

$$N_L(t) = \int_0^\infty N_L(t, t + \tau)d\tau \Rightarrow p^2\tau_{fl}n^2e^{-2(k_r + k_{nr})t}$$

(3.11)

For non-blinking systems the ratio $\frac{N_C}{N_L}$ corresponds to the normalized intensity correlation $g^{(2)}(\Delta\tau = 0)$. Accordingly, the number of independent chromophores n at delay time t after excitation can be derived by the time dependent ratio $\frac{N_C(t)}{N_L(t)}$.

$$\frac{N_C(t)}{N_L(t)} = \frac{(n - 1)}{n}e^{-k_{SSA}t}$$

(3.12)

The question we are raising with this theory is: Was a second exciton present when the first photon was emitted? This method is called picosecond time resolved antibunching (psTRAB) and is presented in chapter 4.2 in more detail. The concept of the microtime gating is depicted in figure 3.2.3. As depicted in figure 3.2.3a and 3.2.3c only photons from a small microtime

gate of the first detector are considered (indicated in orange and blue). These photons are then correlated to all photons from the second detector that were detected in the same microtime gate or later. With this microtime gating approach we can observe the decaying probability of two photon detection events independent of the fluorescence lifetime. In the example in figure 3.2.3b the correlation of the early microtime gate gives a value of $\frac{N_C}{N_L} = 0.5$ which is expected for two chromophores. For late microtimes, the central correlation count drops in figure 3.2.3d compared to the lateral correlation counts and hence indicates SSA.
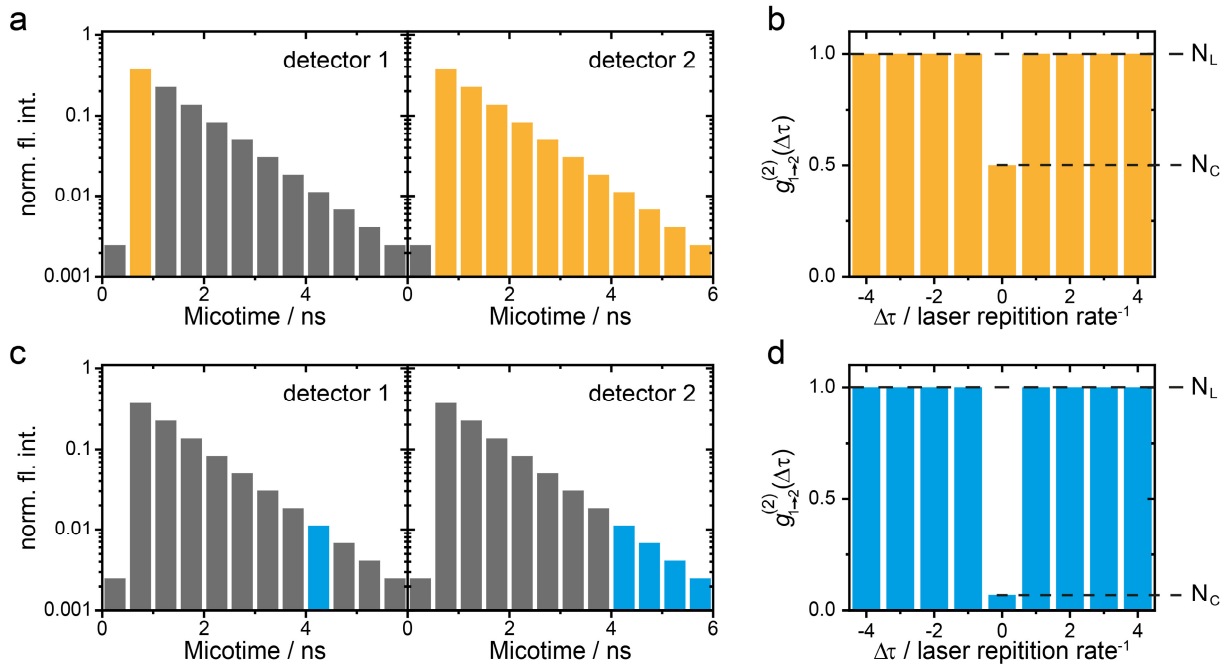
Figure 3.2.3: Gating principle of psTRAB. a) + c) Fluorescence lifetime histogram of two detectors in an HBT setup. For the cross correlation considered photons are indicated in orange or blue. b) + d) Correlation histograms of the cross correlations. The central correlation events N_C in d) drop relative to the lateral correlation events N_L due to SSA for later microtime gates.

3.3 Immobilization of DNA Origami Structures

In order to acquire long single particle trajectories, the DNA origami structures were immobilized. Their photophysics and their weak coupling interactions were of interest and were examined on different time scales. While dynamic quenching occurs on the *ns* time scale, simultaneous blinking occurs on the *second* time scale. Hence a ROXS buffer provides the desired photo stability.

Figure 3.3: Immobilization strategy of DNA origami structures by BSA-biotin-NeutrAvidin-biotin coupling.

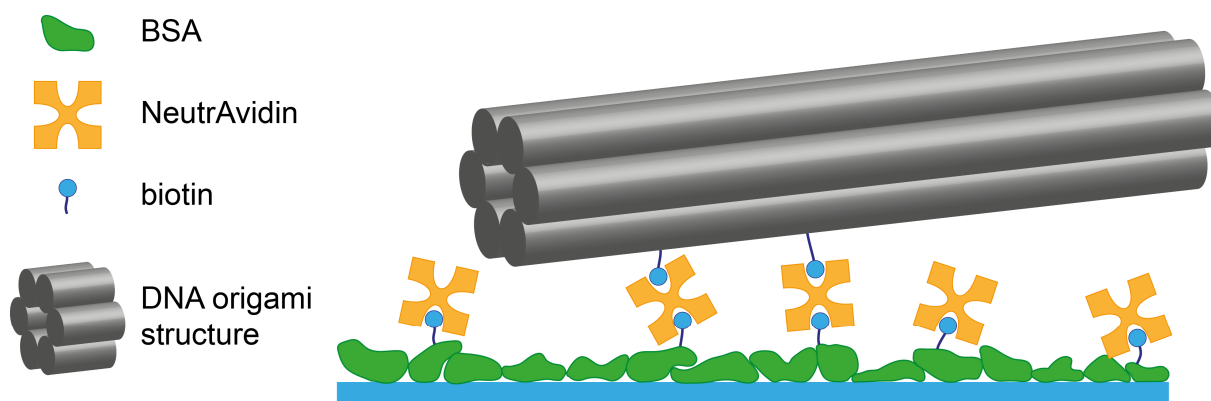The DNA origami structures were immobilized in a LabTek™ chamber and these chambers were cleaned beforehand to avoid contamination of the fluorescence signal with fluorescence from contaminated glass. Depending on the LabTek's™ contamination, they were either cleaned with 0.1 M hydrofluoric acid or with Hellmanex®. The immobilization on a bovine serum albumin (BSA) -biotin NeutrAvidin surface as depicted in figure 3.3 gives a homogeneous nano-environment and immobilizes the DNA origami structure on the surface. The BSA passivates the glass surface and is stochastically modified with biotin (vitamin B7). The NeutrAvidin has four biotin binding pockets and binds to the biotinylated-BSA on the surface and the DNA origami structures which are also modified with biotin labeled staples. In the immobilization process the origami solution was pipetted against a single LabTek™ chamber wall to create a gradient in the surface density of immobilized DNA origami structures. This is advantageous in order to find a suitable surface density in every prepared LabTek™ chamber. Ideally, $20 - 40$ individual structures can be picked to acquire single particle trajectories in a $10 \ \mu m \times 10 \ \mu m$ scan. Further details on the procedure like incubation time and concentrations are provided in the materials and methods sections of the corresponding publications.

4 Publications

4.1 Interchromophoric Interactions Determine the Maximum Brightness Density in DNA Origami Structures

Tim Schröder, Max B. Scheible, Florian Steiner, Jan Vogelsang, and Philip Tinnefeld

For optical characterization of microscopes and biomolecular imaging, the point light sources used should be as small, as bright and as homogeneous as possible. So far, dye-loaded nanoparticles have been used, but due to the uncontrolled dye-dye interactions and stochastic incorporation into the nanoparticle, their brightness and fluorescence properties are inhomogeneous.[102] In addition, their surface chemistry is only biocompatible to a limited extent. DNA origami, on the other hand, is ideal for controlling the stoichiometry and distances between the dyes. The aim of this work was to find out how densely a DNA origami structure can be labeled with organic dyes. Possible dye-dye interactions as well dynamics from the DNA structure were characterized in order to create the basis for the smallest possible but very bright point light source.

In this publication, I modified a simple flat and twist corrected rectangular DNA origami structure to investigate the distance dependence of two ATTO647N dyes in terms of their fluorescence properties and interactions. I changed the distance between the two dyes in single base pair (bp) steps, that is 0.34 nm steps. The gap between the dyes was filled by a spacer oligonucleotide bound to the adjacent helix in order to hybridize to the scaffold DNA between the dyes to separate them by dsDNA. In order to identify and analyze non-fluorescent ATTO 647N aggregates in the experiment, I attached up to 10 ATTO 542 dyes externally 60 nm away of the ATTO 647N dyes.

For confocal experiments I immobilized the model structures on the surface in LabTek^{TM} chambers. Fluorescence intensity and fluorescence lifetime were recorded by a TCSPC unit. In addition, all experiments were carried out under oxygen removal and ROXS conditions using TX/TQ in order to suppress photo-blinking of the ATTO 647N dyes due to triplet or radical states. At the 1-3 bp distance the samples showed only 10% of the expected fluorescence intensity in combination with a halved fluorescence lifetime. From 4-6 bp distance the samples showed blinking dynamics by switching between the expected fluorescence intensity and the quenched state. With increasing spacer length, the bright fluorescence state duration became longer and at 7 bp distance the expected fluorescence intensity and lifetime without blinking was reached.

From the fluorescence intensity and fluorescence lifetime data, I was able to conclude that two mechanisms were involved. First a non-fluorescent H-type dimer formation was reducing the

radiative rate by a factor of five. I also observed the H-type dimer in the absorption spectra of a dsDNA model structure. However, the complex is not thermally stable but even after dissociation of the H-type dimer the dyes could still undergo quenching dynamically through collision, which explains the shortening of the fluorescence lifetime. The quenched state was thus a combination of static and dynamic quenching.

In the second regime at 4-6 bp distance I observed dynamic blinking which had its origin in the temporary unbinding of the separating spacer oligonucleotide which was at this length thermally not stable. If the spacer was hybridized to the scaffold, the two dyes were separated and neither dynamic nor static quenching was observed. I was able to demonstrate that the blinking had its origin in the temporal unbinding of the spacer oligonucleotide by showing that quenching could still be observed in samples without the spacers up to a distance of 10 bp.

Although the dyes were spatially separated from one another at a distance of 7 bp, they did not necessarily have to be independent of one another. Resonant couplings could still occur. Weak coupling between one dye in the S_1 state and the second dye, which could be either in the S_1, T_1 or a radical state $R^{\cdot\pm}$, could still effect the fluorescence intensity by SSA or SDA.

First, I investigated if quenching of excited singlet states by SSA can occur. Therefore, I compared the $g^{(2)}(\tau)$ intensity correlation from single fluorescence trajectories of the 7 bp distance and 20 bp distance samples under ROXS conditions. I was able to show that the 7 bp distance sample was subject to very effective SSA with a mean ratio of $\frac{N_C}{N_L} = 0.12$. The 20 bp sample, on the other hand showed a ratio of $\frac{N_C}{N_L} = 0.48$, which was close to the theoretical value of 0.50 expected for two independent dyes. In addition, the samples were very homogeneous. To examine SDA, I did not use a ROXS buffer, but instead made the dyes blink by an enzymatic oxygen scavenger and a trolox buffer without the quinone to generate anionic radical states. The 20 bp sample showed independent blinking dyes. In contrast the 7 bp sample showed collective blinking dyes and greatly shortened off-times. The acceptor dye in the dark state got excited by SDA to a higher dark state level from which the rate back into a S_N state is increased.[63] As a result, the off-states were recovered faster and more effective SDA led to a more effective repopulation of the singled manifold. If the dyes were subject to SDA, they delivered on average five times more photons per second than two independent dyes without SDA.

All in all, I showed in the associated publication that DNA origami is an exciting tool to design densely dye labeled structures as point light sources. I elaborated rules to place dyes in a DNA origami structure. For maximal brightness of the structure there are four points of dye interactions to consider. If dyes are in close spacial proximity, they can be subject to static and dynamic quenching which compromises the brightness. If they are spatial separated, they can still interact by resonant coupling through SSA and SDA. The SDA can have advantages and disadvantages. The disadvantage is that a single dye in a dark state quenches the surrounding dyes and the system blinks collectively. The advantage of SDA on the other hand is the faster depopulation of the dark state. However, the data highlight the importance of avoiding dark state formation by stabilizing agents to prevent collective blinking dyes. SSA, on the other hand, can lead to saturation at high excitation rates. These findings pave the way to create small DNA origami structures with unprecedented brightness and homogeneity. According to your calculation, a DNA origami structure could carry up to 1,000 dyes by using a 5 nucleotide spacing and preserving the photophysical properties of the dyes. This study is the first to study

on the single-molecule level the interaction of two identical organic dyes and will help to design and interpret many biophysical single-molecule experiments.

Interchromophoric Interactions Determine the Maximum Brightness Density in DNA Origami Structures

Tim Schröder,[†] Max B. Scheible,[‡] Florian Steiner,[†] Jan Vogelsang,*,[†] and Philip Tinnefeld*,[†]

[†]Department Chemie and Center for NanoScience, Ludwig-Maximilians-Universitaet Muenchen, Butenandtstrasse 5-13 Haus E, 81377 Muenchen, Germany

[‡]GATTAquant GmbH, Am Schlosshof 8, 91355 Hiltpoltstein, Germany

Ⓢ *Supporting Information*

ABSTRACT: An ideal point light source is as small and as bright as possible. For fluorescent point light sources, homogeneity of the light sources is important as well as that the fluorescent units inside the light source maintain their photophysical properties, which is compromised by dye aggregation. Here we propose DNA origami as a rigid scaffold to arrange dye molecules in a dense pixel array with high control of stoichiometry and dye−dye interactions. In order to find the highest labeling density in a DNA origami structure without influencing dye photophysics, we alter the distance of two ATTO647N dyes in single base pair steps and probe the dye−dye interactions on the single-molecule level. For small distances strong quenching in terms of intensity and fluorescence lifetime is observed. With increasing distance, we observe reduced quenching and molecular dynamics. However, energy transfer processes in the weak coupling regime still have a significant impact and can lead to quenching by singlet-dark-state-annihilation. Our study fills a gap of studying the interactions of dyes relevant for superresolution microscopy with dense labeling and for single-molecule biophysics. Incorporating these findings in a 3D DNA origami object will pave the way to bright and homogeneous DNA origami nanobeads.

KEYWORDS: *DNA origami, single-molecule spectroscopy, interchromophoric interactions, photophysics, nanobeads*
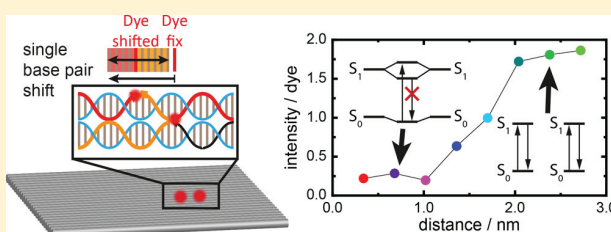
Fluorescence enables ultrasensitive detection down to single molecules. Nevertheless, the signal emitted from single molecules is often too weak to be detected with simple devices and in complex environments. As single organic dye molecules also suffer from photobleaching, the overall obtainable signal is too small for many applications and larger, often multichromophoric alternatives are required.[1] Brighter alternatives such as dye loaded nanoparticles and quantum dots are larger and more heterogeneous, limiting their usefulness as point light sources.[2−4] In optical characterizations such as the determination of a point-spread function of a STED microscope,[5] the small size of the light source is central. Similarly, optical setup characterizations of, for example, sensitivity require homogeneous, well characterized light sources. Moreover, for biomolecular imaging and molecular diagnostics the size of the light source negatively influences biocompatibility as well as diffusion and binding kinetics. Quantum dots have additional disadvantages of toxicity and size in bioapplicable formulations.

Bright fluorescent particles are commonly produced by embedding fluorescent dyes in a polymer particle of nanoscale dimensions. The density of dyes that can be embedded is limited by the dye's tendency to aggregate yielding low-fluorescent imperfect H-type aggregates.[6−10] Often it is also observed that dye interactions lead to broad brightness and fluorescence lifetime distributions especially for nanobeads

below 60 nm diameter.[11] Only recently were fluorescent nanoparticles with improved photophysical properties such as conjugated polymer dots[12,13] and fluorescent organic nanoparticles developed.[4,14,15] Still, these nanoparticles exhibit substantial heterogeneity in size and shape as well as limited control over surface chemistry. Moreover, these nanoparticles exhibit a limited linear dynamic range of emission versus excitation power and their brightness could yet also not be referenced to that of single dye molecules.

Here, we investigate DNA origami as scaffold for ultrabright point light sources. In DNA origami, a roughly 7000−8000 nucleotide long, single-stranded DNA (ssDNA) strand is folded into a programmed three-dimensional shape by ∼200 staple strands that have a length on the order of 32 nucleotides.[16,17] In DNA origami nanobeads, the DNA nanostructure provides a three-dimensional scaffold to which dye molecules can be attached in a predefined pattern. This predefined pattern could be a regular, two- or three-dimensional arrangement in which the dye molecule positions are representing voxels.
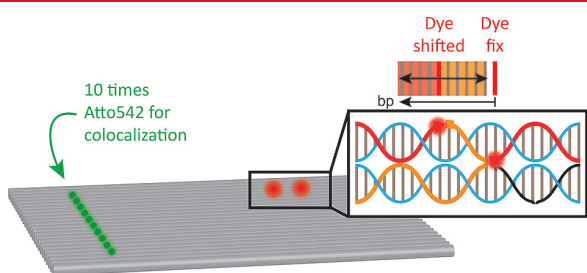
If staple strands are labeled at the end with a single dye molecule, usually a dye arrangement with interdye distance of

32

~6 nm can be obtained for a two-dimensional DNA origami structure as the one indicated in Figure 1. With these 6 nm

Figure 1. Model of the rectangular DNA origami labeled with up to ten green ATTO542 dyes for DNA nanostructure identification and two ATTO647N dyes for dye−dye-interaction studies. The spacer oligo (orange) hybridizes with the scaffold (light blue) to separate the dyes (red glowing dots) by a crossover from the neighboring helix. For every distance a different dye-labeled oligo was used together with an adjusted spacer length. The right oligo stays the same for every experiment and is labeled at the 5′ end. Other oligonucleotides are black. The magnified view shows a 6 bp distance between the ATTO647N dyes.

pixels, dye molecules can interact via Förster resonance energy transfer,[18] but the brightness and fluorescence lifetime of identical fluorescent dyes are not affected.[11,19] We note that the distance of 6 nm can be decreased by redesigning the 2D or 3D DNA origami structure or by considering additional internal labeling of the staple strands. Therefore, we set out to identify the highest brightness density that can be achieved with DNA origami and the optimal distance of placing fluorescent dyes, here ATTO647N, without quenching. Using single-molecule fluorescence spectroscopy, we reveal five distinct interaction processes and dynamics that have to be considered to satisfactorily describe the apparently simple two-dye system in DNA origami.

To study the distance dependence of the fluorescent properties of two dye molecules, we placed them in a two-dimensional rectangular DNA origami model structure, as schematically depicted in Figure 1 (see Supporting Information for AFM pictures in Figure S1 of the DNA origami, sample preparation and methods). We altered the distance of these two red emitting dyes on one helix in single-nucleotide steps. Green ATTO542 dyes were also incorporated into the DNA origami structure for identifying DNA origami structure locations. Single-molecule measurements were performed on a BSA-biotin coated glass surface (see Supporting Information for details). The signals were analyzed in terms of fluorescence intensity and fluorescence lifetime for each single DNA origami structure.

For placing the dye molecules in the DNA origami structure, we used commercially available dye chemistry. The first dye was attached at the 5′-end via a C6 amino linker to an oligonucleotide, which was used in every DNA origami structure in this study. To keep the environment similar, the second dye was attached to the next oligo at the 3′-end by a C7 amino linker. For each distance a different labeled oligo was used in the folding process. At the smallest possible distance, both dye-labeled ends face each other. This distance is referred to as 1 base pair (bp). For greater distances, e.g., 3 bps (the 3′ labeled oligo is two nucleotides shorter than the 1 bp oligo), we filled the two unpaired bases at the scaffold with a

complementary sequence attached to an oligo from the neighboring helix, as is shown in the magnified view in Figure 1. Forming double-stranded DNA (dsDNA) should rigidify the structure. At a distance 60 nm away from the ATTO647N dye couple we placed up to 10 ATTO542 dyes by external labeling to identify the location of DNA origami structures on the coverslip surface.[19]

The confocal fluorescence microscopy surface scans in Figure 2a with alternating laser excitation at 532 and 637 nm show strong intensity quenching for small (1−3 bp) distances between the red dyes (see Supporting Information for details on the setup). Dark pixels inside the diffraction-limited spots for the intermediate distances (4−6 bps) reveal pronounced blinking. For the 3−7 bp distance samples we introduced a so-called spacer strand, which binds to the single-stranded scaffold
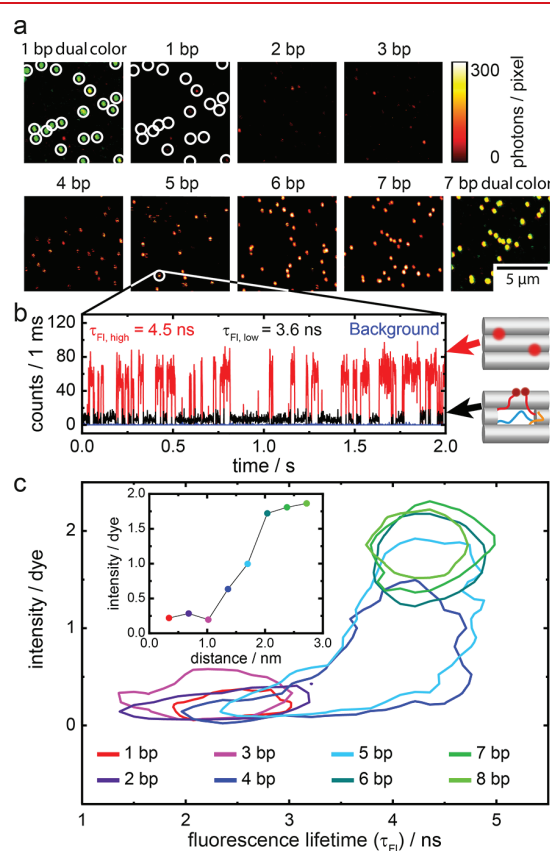
Figure 2. (a) Confocal fluorescence microscopy images of DNA origami nanostructures under oxygen removal and ROXS using trolox/troloxquinone.[20,34] The first image shows a false-color overlay image of the green reference channel and the red fluorescence from the 1 bp distance sample. The following images show the red spectral channel with increasing distance between the ATTO647N molecules. The last image is again an overlay of green and red channels to demonstrate perfect colocalization. Each pixel is 50 × 50 nm with an integration time of 1 ms for each color. (b) Representative transient of a blinking 5 bp distance sample. High intensity corresponds to a closed stem, and low-intensity states correspond to an open stem. Both states are depicted schematically on the right in panel (b). (c) Sample brightness normalized to the average brightness of one dye vs fluorescence lifetime for the 1−8 bp distance samples. Lines surround 90% of the overall population. The inset shows the mean intensity of each distribution versus the distance between both dyes in nanometers, assuming that 1 bp corresponds to ~0.34 nm.

33

domain between the two dyes to separate them by building a double helical filling (see Figure 1). The spacer is a ssDNA strand, which originates from the neighboring helix and binds into the gap between the two dyes. For the 3 bp distance sample, the spacer strand has therefore only two nucleotides to form a duplex, which is thermodynamically unstable at room temperature. Although the spacer strand has a high local concentration by being fixed to the adjacent helix, which should push the equilibrium toward the separation of the two dyes, the introduced spacer strand has no influence at the 3 bp distance sample due to the weak hybridization energy of only two nucleotides. At greater distances (4 and 5 bps), a stronger fluorescence signal was obtained with pronounced blinking. At 6 bps the blinking is largely vanished. Only a few spots demonstrate blinking. The blinking vanishes completely at 7 bps distances, indicating permanent separation of the dyes. Figure S2 in the Supporting Information further demonstrates that the blinking kinetics are slowed down by increasing the length of the spacer strand. The comparison with the dual color image, i.e., detecting ATTO542 and ATTO647N simultaneously, shows a perfect match of green and red spots without blinking. The assignment of the blinking to the hybridization and dehybridization of the spacer strand from the neighboring helix is confirmed by measurements without the spacer extension. In this case the DNA linker between the dyes is so floppy that quenching can even occur up to 10 nm (see Figure S3).

The adjustable blinking between an unquenched and a quenched state of the bichromophoric system allowed us to directly compare these two states with each other at the single-molecule level to reveal the nature of the quenched state. We recorded fluorescence transients as shown in Figure 2b for the 5 bp distance sample under oxygen removal and reducing and oxidizing (ROXS) conditions thus, blinking due to photophysics of the dyes themselves is successfully suppressed.[20] Hence, the fluorescence blinking can be solely attributed to dye−dye interactions. Two fluorescence intensity levels are observed, a high-intensity state with a mean intensity of 61 ± 12 kHz (marked in red) and a low-intensity state with 7 ± 3 kHz (marked in black). The background level (marked in blue) is below 0.5 kHz. We note that the high-intensity level corresponds to approximately two times the intensity of a single dye. Additionally, the fluorescence lifetimes $\tau_{Fl,high}$ and $\tau_{Fl,low}$ of the high- and low-intensity states are recorded by time-correlated single-photon counting (TCSPC), respectively, yielding $\tau_{Fl,high} = 4.5 \pm 0.1$ ns and $\tau_{Fl,low} = 3.6 \pm 0.1$ ns. The fluorescence lifetime of the high-intensity state corresponds to the lifetime of a single ATTO647N reference dye. As the high-intensity state resembles two completely unquenched ATTO647N dyes with a reported fluorescence quantum yield $QY_{Fl} = 65\%$ and by assuming that the low-intensity state is solely attributed to a drop in QY_{Fl} (as both two times the monomer and dimer spectra show similar extinction at the excitation wavelength of 637 nm, see Figure 3c), we could estimate the radiative, k_r, and nonradiative, k_{nr}, rate constants of both states.

For the high-intensity state we calculated $k_{r,high} = 1.4 \times 10^8$ s^{-1} and $k_{nr,high} = 0.77 \times 10^8$ s^{-1}, whereas the low-intensity state yielded $k_{r,low} = 0.2 \times 10^8$ s^{-1} and $k_{nr,low} = 2.6 \times 10^8$ s^{-1}. In conclusion, the radiative rate drops down by almost an order of magnitude whereas the nonradiative rate increases by a factor of ∼3.5 in the quenched state.
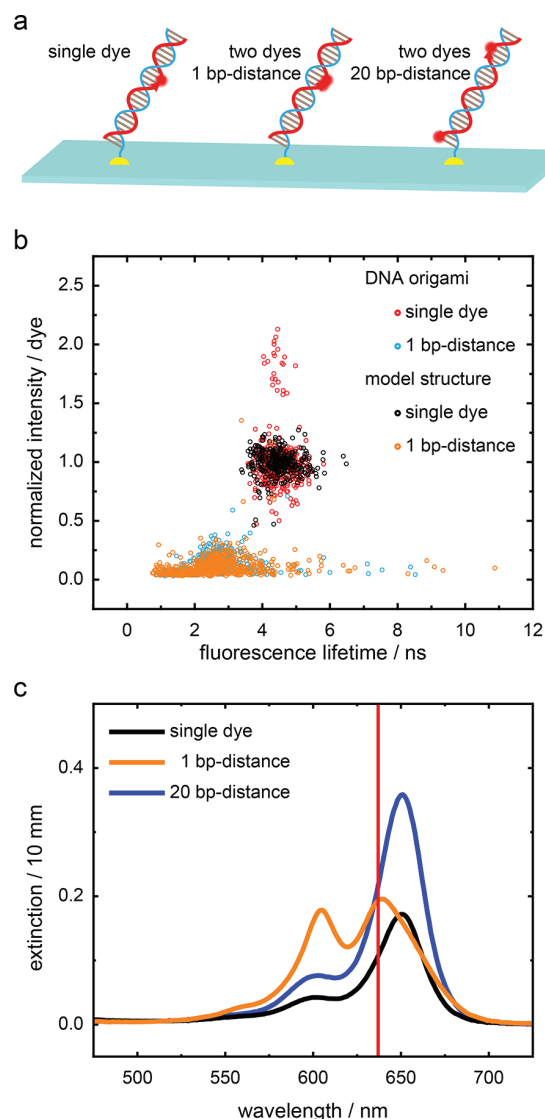
Figure 3. (a) Schematic overview of the immobilized model structures used to compare with the DNA origami structure and to measure the absorption spectrum of the dimer. (b) Scatterplot of fluorescence lifetime and fluorescence intensity. DNA origami and model structure are compared and show no difference at the single-molecule level for the single-dye samples and the two dyes at 1 bp distance samples. Spot finding was performed only on the red detection channel. A small population of dimers is observed for the 1 bp distance DNA origami, because DNA origami tend to blunt-end stack. (c) Absorption spectra of the 1 bp distance model (orange) and 20 bp distance model (blue) compared to a single Atto647N dye attached to dsDNA (black curve). All concentrations are set to 4.5 μM. The red line indicates the laser excitation wavelength of 637 nm at which all DNA origami samples are excited. We note that the extinction is very similar for the 1 bp and 20 bp distance sample.

For a statistical analysis regarding the change of rate constants, we extracted the fluorescence intensity and lifetime of each diffraction-limited spot. We note that the integration time per measured spot is approximately 100 ms and, therefore, the measured fluorescence lifetime is a temporal average. More than 400 spots were analyzed per sample and plotted in a scatter plot. Figure 2c shows weak fluorescence combined with a shortened fluorescence lifetime for the 1 bp

34

to 3 bp distance samples. The inset of Figure 2c demonstrates the decrease of the mean fluorescence brightness with decreasing distance between both dyes. We simplified that 1 bp corresponds to ∼0.34 nm, neglecting the impact of the dsDNA backbone on the distance. The fluorescence intensity is homogeneously ten times lower than expected for two unquenched dyes while the fluorescence lifetime is shorter by a factor of two compared to the unquenched 6 bps to 8 bps distance samples. The medium distances with 4 and 5 bps display a broad distribution, essentially connecting the unquenched and quenched populations. By extracting the mean brightness and fluorescence lifetime for the quenched populations, i.e., the 1−3 bps distance samples, and the unquenched populations, i.e., 6−8 bps distance samples, we can estimate the following representative mean rate constants for both populations: $\langle k_{r,high} \rangle = 1.5 \times 10^8 \; s^{-1}$, $\langle k_{nr,high} \rangle = 0.8 \times 10^8 \; s^{-1}$, $\langle k_{r,low} \rangle = 0.3 \times 10^8 \; s^{-1}$, and $\langle k_{nr,low} \rangle = 3.9 \times 10^8 \; s^{-1}$.

Both changes of k_r and k_{nr} indicate that two quenching mechanisms must be responsible for the strong decrease of the fluorescence, when the two dyes come too close to each other. The almost three-fold decrease of k_r can be associated with an H-type dimer formation, i.e., an imperfect H-aggregate, which is still fluorescent. A cofacial stacking of both dyes leads to a splitting of the excited state. Further, the transition dipole moment (TDM) of the higher lying excited state is enhanced whereas the TDM of the lower excited state is significantly reduced. For these reasons, the excitation of such a dimer is shifted to higher energies, known as a hypsochromic shift, which can be seen in the absorption spectrum of a comparable dsDNA model structure, which is shown in Figure 3. Further, the fluorescence from the lower lying state is slowed down. An absorption spectrum requires roughly 30 batches of DNA origami structures to reach the needed amount of substance. For this reason, we choose dsDNA as a model for two extreme distances of 1 bp and 20 bps. The model structures are shown in Figure 3a. Dye-labeled oligo sequences were maintained. Other distances need a spacer between the two dyes, and short nucleotides are thermally not stable. In the DNA origami structure a neighboring helix is present where the spacer oligo is attached, which leads to a high local concentration of the separating sequence when it is in an unbound state. The dsDNA 1 bp distance model structure matches the intensity and fluorescence lifetime distribution of the 1 bp distance DNA origami structure, when immobilized on the surface as shown in Figure 3b, which justifies the comparison. The absorption spectrum of the dsDNA 1 bp distance model structure shows the hypsochromic shift at 605 nm (Figure 3c). Similar results were obtained for cofacially stacked π-conjugated oligomers by Stangl et al.[7] However, the major difference here is given by the environment. Whereas the dimers in the work by Stangl et al. were embedded in poly(methyl methacrylate), i.e., solid state, we have a dynamic solution environment. The dimers can undergo rapid conformational changes due to the C6 and C7 linkers of the dyes, allowing for rotational diffusion. Such freedom leads to rapid collisions between both dyes, hence dynamic quenching and an increase of k_{nr}. The change of k_{nr}, $\Delta k_{nr} = 1.83 \times 10^8 \; s^{-1}$, corresponds to the collision frequency and relates to one collision per 5.5 ns, a similar time regime in which rotational diffusion of dyes attached to DNA takes place.[21]

Intensity and fluorescence lifetime distributions become very broad for the 4 bps and 5 bps distance samples. Low intensity always correlates with shortened fluorescence lifetime but it

does not scale linear but in a mirrored/reverse "L" shape (Figure 2c). This can be explained by the spacer separating the two dyes. The dyes are well separated while the spacer is hybridized to the scaffold (unquenched state) and therefore we observe the expected intensity and fluorescence lifetime of two dyes. But the sequence of the separation spacer is only 3 and 4 nt long and is not thermally stable. When the separating part of the spacer dissociates, the dyes are no longer separated and they can quench each other by the static and dynamic quenching mechanisms discussed above.

In the next step, we focus on the 7 bp distance sample, for which the spacer strand is stably incorporated. A distance of 7 bps between both dyes corresponds to a distance of ∼2.4 nm, which is typical for weak coupling effects, i.e., energy transfer in the Förster regime (FRET). Whereas FRET between identical dyes (Homo-FRET) might occur, it has no influence on the emitted fluorescence intensity at the here used excitation intensities as the emissive rate is independent of which of the identical dyes is in the excited state. Still, energy transfer processes might occur that limit the usefulness of dense labeling in the Förster regime through saturation of the emitted fluorescence.[22] Such energy transfer processes can lead to quenching of excited singlet states of one dye by light-absorbing states of other dyes in close proximity. These light-absorbing states can be associated with excited singlet states, S_1,[23] excited triplet states, T_1,[24,25] or radical states.[26] To test whether such quenching mechanisms play an important part for the here investigated system, we analyzed the photon stream of the 7 bp distance sample by photon correlation techniques and compare this sample with a single-chromophore sample and the 20 bp distance sample.

First, we investigate if quenching of excited singlet states by another chromophore in its excited singlet state, i.e., singlet−singlet annihilation, does play a significant role, which will lead to single-photon emission.[23,24] The quality of photon antibunching is therefore directly related to energy transfer between both chromophores. We measured the statistics of fluorescence photons of a single 7 bp distance sample by splitting the detection path onto two detectors that yield the coincidence counts in dependence of the lag time between the two detectors. Figure 3a plots the coincidence counts for a single 7 bp distance sample acquired with laser pulses separated by 25 ns. The ratio of the magnitude of the central peak at lag time equals zero, N_C, to that of the lateral peaks, N_L, provides a measure for the degree of photon antibunching. For two completely independent chromophores, a value of 0.5 for N_C/N_L is expected.[27] The example shown in Figure 4a displays an antibunching value, N_C/N_L, of ∼0.1, which translates to almost 100% singlet−singlet annihilation after considering the signal/background level.[28] N_C/N_L was determined for 56 single 7 bp distance samples plotted in a histogram in Figure 4b (black bars). The histogram shows a narrow distribution between 0 and 0.2. In comparison, the 68 single 20 bp distance samples have mainly antibunching values around 0.5 (gray bars). In conclusion, singlet−singlet annihilation plays a significant role in the 7 bp distance sample.

Long-lived dark states can be deliberately induced by simply removing oxygen, which leads either to long-lived triplet states or, depending on the environment, to long-lived radical states by a subsequent electron transfer. This is evidenced by strong blinking behavior of the dyes, which is shown in Figure 4c for a DNA origami structure bearing one ATTO647N dye under oxygen removal *without* stabilizing agents.[20] For such a

35
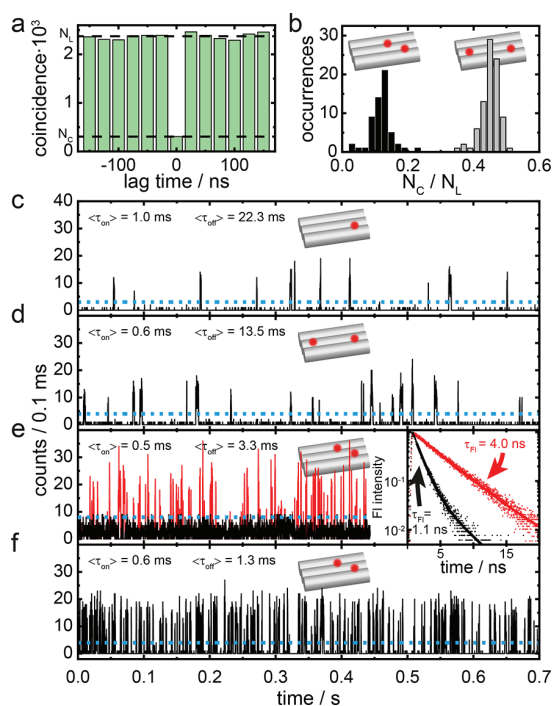
Figure 4. (a) Photon antibunching from a 7 bp distance sample under oxygen removal and ROXS. The sample was excited by laser pulses (40 MHz repetition rate). The photon statistics in emission are shown in terms of coincidence counts of two photodetectors per one pulse delay in the emission pathway. The ratio between the center peak, N_C, and lateral peaks, N_L, are stated by dashed lines, respectively. (b) Histograms of N_C/N_L values for the 7 bp distance (black bars, 56 measured spots) and 20 bp distance (gray bars, 68 measured spots) sample. (c)−(f) Representative transients of a DNA origami sample bearing only one ATTO647N dye (c), the 20 bp distance sample (d), and two examples of the 7 bp distance sample (e, f) under oxygen removal without stabilizing agents. The average on- and off-times, τ_{on} and τ_{off}, for which the molecule is in a fluorescent on-state or a nonfluorescent off-state are given for each transient. The blue dashed line is the threshold to separate the on- and off-states. We note that in (e) all intensity values corresponding to the (un)quenched state are color coded (red) black. From the corresponding photons the fluorescence decays and fluorescence lifetimes, τ_{Fl}, are given for the bright state (red curve) and dark state (black curve).

transient, the average time is extracted for which the molecule is in a fluorescent state, τ_{on}, or in a dark state, τ_{off} (longer transients are provided in the Supporting Information in Figure S4). The blue dashed line indicates the threshold, which was used to differentiate between a fluorescent or a dark state. τ_{on} (τ_{off}) was determined for each state by counting the number of consecutive time bins for which the intensity was above (below) the threshold. For a single ATTO647N dye, average τ_{on} = 1.0 ms and τ_{off} = 22.3 ms were measured. For ATTO647N dyes at 20 bp distance, τ_{off} is approximately halved to 13.5 ms and the fluorescence intensity of the bursts is similar to that of a single ATTO647N due to independent blinking of both dyes (see Figure 4d). However, the 7 bp distance sample shows an unexpected blinking behavior, because here the dark state of one dye is influencing the fluorescence properties of the neighboring dye. Panels e and f of Figure 4 show two representative transients of the 7 bp distance sample. A total of 95% of the transients can be sorted into these two types of blinking. In the first type (Figure 4e),

two fluorescence intensity levels are clearly distinguishable: one at ∼200−300 kHz (marked red) with a fluorescence lifetime of 4 ns (right panel, red curve) and a second with up to 60 kHz count rate (marked black) with a biexponential fluorescence lifetime decay (right panel, black curve), resulting in a long component with 4 ns and a short component of 1.1 ns. Further, τ_{off} is strongly reduced to 3.3 ms. This behavior is explained by strong singlet-dark-state annihilation (SDA), which also impacts the lifetime of the dark state itself. The transient in Figure 4e exhibits an example in which the energy transfer of one dye in its singlet manifold to the neighboring dye in its dark state is not 100%, hence the remaining fluorescence during the dark state periods with a quenched fluorescence lifetime of 1.1 ns. The remaining 4 ns contribution stems from the small on-time periods, in which both dyes are in the singlet manifold. Additionally, this energy transfer leads to higher excited states of the dark state, for example, higher triplet states, T_n, or excited radical states. Such higher excited dark states are more reactive, which can lead to a faster recovery to the ground state, S_0.[29,30] The transient in Figure 4f exhibits an example in which the energy transfer is almost 100%, because no remaining fluorescence above the background was detected during the off-time periods. For this reason, the off-time periods are even more reduced to τ_{off} = 1.3 ms, due to more efficient excitation and recovery of the dark state. We note that τ_{on} is very similar for all cases with values below 1 ms, indicating that the time the dyes spend in the singlet manifold is poorly effected by energy transfer between them. However, energy transfer between the dyes in excited states must be considered and has two effects: (i) the negative effect is that the dark state of one dye is capable of quenching the fluorescence of dyes nearby and (ii) the positive effect is that the dark state lifetime is reduced significantly, leading to a higher brightness of the sample. As a consequence, dark states are detrimental, especially in multichromophoric systems for achieving the highest brightness and can lead to saturation already at moderate excitation powers.[31] Singlet−singlet annihilation would only enhance saturation at high excitation powers.[32] Other transient dark states can fortunately be depopulated efficiently using the reducing and oxidizing system[20] so that a linear fluorescence response of a multichromophoric DNA origami structure can be obtained over more than an order of magnitude excitation power range and up to a count rate of 1 MHz for fluorescence detection (see Figure S5).

In summary, DNA origami are exciting scaffolds for dense dye arrangements to obtain bright point light sources. We here elaborated the rules to optimally place dyes in bright DNA origami constructs. The distance between two ATTO647N dyes was altered with a single-nucleotide step size. We revealed five relevant levels of interaction using single-molecule spectroscopy. Small distances show halved fluorescence lifetime and a ten-fold decrease in intensity due to dynamic quenching and static quenching by H-type dimer formation. This contact related quenching is avoided when the dyes are separated by 7 bps when the spacer stems from the neighboring helix. With dye labels in the middle of the sequence, our data indicate that 5 bp separation would be sufficient to avoid physical contact between the dyes. For the larger distances (e.g., 7 bps), weak coupling effects between dyes including singlet−singlet annihilation, singlet−triplet annihilation, and singlet-radical-state annihilation have to be taken into account. Depending on the properties of the dyes

36

used, the energy transfer between dyes can have beneficial or detrimental aspects on the fluorescence, e.g., by leading to saturation or by opening new photophysical pathways for dark-state depopulation. The data shown also highlight the importance of avoiding dark state formation by using stabilizing agents.[20] This knowledge will pave the way to create small DNA origami nanobeads with unprecedented brightness density by preserving the photophysical properties of the dyes used. On the basis of the finding of a minimal spacing of 5 nucleotides between two dyes, we estimate that more than 1000 dyes could be placed within one DNA origami structure as used here without substantial perturbation of the photophysical properties. Despite interesting applications,[33] a detailed single-molecule study of fluorescence interactions of identical dyes had been lacking and will help in the design and interpretation of many biophysical single-molecule experiments.

■ ASSOCIATED CONTENT

ⓢ Supporting Information

The Supporting Information is available free of charge on the ACS Publications website at DOI: 10.1021/acs.nanolett.8b04845.

> Details of the confocal fluorescence microscope, DNA origami folding, surface preparation and immobilization, absorption spectra, data analysis, AFM imaging, blinking kinetic data, quenching data, extended transient plots, fluorescence intensity dependence graphics, DNA origamis, and DNA sequences (PDF)

■ AUTHOR INFORMATION

Corresponding Authors
*E-mail: Philip.Tinnefeld@cup.lmu.de.
*E-mail: Jan.Vogelsang@cup.lmu.de.
ORCID ⓘ
Jan Vogelsang: 0000-0001-7952-9342
Philip Tinnefeld: 0000-0003-4290-7770

Author Contributions

The manuscript was written through contributions of all authors. All authors have given approval to the final version of the manuscript.

Notes

The authors declare no competing financial interest.

■ ACKNOWLEDGMENTS

■ REFERENCES

(1) De Schryver, F. C.; Vosch, T.; Cotlet, M.; Van der Auweraer, M.; Müllen, K.; Hofkens, J. Energy dissipation in multichromophoric single dendrimers. *Acc. Chem. Res.* **2005**, *38* (7), 514−522.

(2) Bruchez, M.; Moronne, M.; Gin, P.; Weiss, S.; Alivisatos, A. P. Semiconductor nanocrystals as fluorescent biological labels. *Science* **1998**, *281* (5385), 2013−2016.

(3) Reisch, A.; Klymchenko, A. S. Fluorescent Polymer Nanoparticles Based on Dyes: Seeking Brighter Tools for Bioimaging. *Small* **2016**, *12* (15), 1968−1992.

(4) Trofymchuk, K.; Reisch, A.; Didier, P.; Fras, F.; Gilliot, P.; Mely, Y.; Klymchenko, A. S. Giant light harvesting nano-antenna for single-molecule detection at ambient light. *Nat. Photonics* **2017**, *11*, 657.

(5) Hell, S. W. Far-field optical nanoscopy. *Science* **2007**, *316* (5828), 1153−1158.

(6) Spano, F. C.; Silva, C. H- and J-Aggregate Behavior in Polymeric Semiconductors. *Annu. Rev. Phys. Chem.* **2014**, *65*, 477−500.

(7) Stangl, T.; Wilhelm, P.; Schmitz, D.; Remmersen, K.; Henzel, S.; Jester, S. S.; Höger, S.; Vogelsang, J.; Lupton, J. M. Temporal Fluctuations in Excimer-Like Interactions between pi-Conjugated Chromophores. *J. Phys. Chem. Lett.* **2015**, *6* (8), 1321−1326.

(8) Hernando, J.; van der Schaaf, M.; van Dijk, E.; Sauer, M.; Garcia-Parajo, M. F.; van Hulst, N. F. Excitonic behavior of rhodamine dimers: A single-molecule study. *J. Phys. Chem. A* **2003**, *107* (1), 43−52.

(9) Marme, N.; Friedrich, A.; Denapaite, D.; Hakenbeck, R.; Knemeyer, J. P. Single nucleotide polymorphism analysis using different colored dye dimer probes. *Chem. Phys. Lett.* **2006**, *428* (4−6), 440−445.

(10) Nicoli, F.; Roos, M. K.; Hemmig, E. A.; Di Antonio, M.; de Vivie-Riedle, R.; Liedl, T. Proximity-Induced H-Aggregation of Cyanine Dyes on DNA-Duplexes. *J. Phys. Chem. A* **2016**, *120* (50), 9941−9947.

(11) Schmied, J. J.; Gietl, A.; Holzmeister, P.; Forthmann, C.; Steinhauer, C.; Dammeyer, T.; Tinnefeld, P. Fluorescence and super-resolution standards based on DNA origami. *Nat. Methods* **2012**, *9* (12), 1133−1134.

(12) Kim, B. S.-I.; Jin, Y.-J.; Lee, W.-E.; Byun, D. J.; Yu, R.; Park, S.-J.; Kim, H.; Song, K.-H.; Jang, S.-Y.; Kwak, G. Highly Fluorescent, Photostable, Conjugated Polymer Dots with Amorphous, Glassy-State, Coarsened Structure for Bioimaging. *Adv. Opt. Mater.* **2015**, *3* (1), 78−86.

(13) Wu, C.; Bull, B.; Szymanski, C.; Christensen, K.; McNeill, J. Multicolor conjugated polymer dots for biological fluorescence imaging. *ACS Nano* **2008**, *2* (11), 2415−23.

(14) Genin, E.; Gao, Z.; Varela, J. A.; Daniel, J.; Bsaibess, T.; Gosse, I.; Groc, L.; Cognet, L.; Blanchard-Desce, M. "Hyper-bright" near-infrared emitting fluorescent organic nanoparticles for single particle tracking. *Adv. Mater.* **2014**, *26* (14), 2258−61 2257 .

(15) Acuna, G. P.; Tinnefeld, P. Molecule detection with sunlight. *Nat. Photonics* **2017**, *11* (10), 616−618.

(16) Rothemund, P. W. Folding DNA to create nanoscale shapes and patterns. *Nature* **2006**, *440* (7082), 297−302.

(17) Douglas, S. M.; Dietz, H.; Liedl, T.; Hogberg, B.; Graf, F.; Shih, W. M. Self-assembly of DNA into nanoscale three-dimensional shapes. *Nature* **2009**, *459* (7245), 414−8.

(18) Hemmig, E. A.; Creatore, C.; Wunsch, B.; Hecker, L.; Mair, P.; Parker, M. A.; Emmott, S.; Tinnefeld, P.; Keyser, U. F.; Chin, A. W. Programming Light-Harvesting Efficiency Using DNA Origami. *Nano Lett.* **2016**, *16* (4), 2369−74.

(19) Schmied, J. J.; Raab, M.; Forthmann, C.; Pibiri, E.; Wunsch, B.; Dammeyer, T.; Tinnefeld, P. DNA origami-based standards for quantitative fluorescence microscopy. *Nat. Protoc.* **2014**, *9* (6), 1367−91.

(20) Vogelsang, J.; Kasper, R.; Steinhauer, C.; Person, B.; Heilemann, M.; Sauer, M.; Tinnefeld, P. A reducing and oxidizing system minimizes photobleaching and blinking of fluorescent dyes. *Angew. Chem., Int. Ed.* **2008**, *47* (29), 5465−5469.

(21) Unruh, J. R.; Gokulrangan, G.; Lushington, G. H.; Johnson, C. K.; Wilson, G. S. Orientational dynamics and dye-DNA interactions in a dye-labeled DNA aptamer. *Biophys. J.* **2005**, *88* (5), 3455−3465.

(22) Di Fiori, N.; Meller, A. The Effect of Dye-Dye Interactions on the Spatial Resolution of Single-Molecule FRET Measurements in Nucleic Acids. *Biophys. J.* **2010**, *98* (10), 2265−2272.

(23) Hofkens, J.; Cotlet, M.; Vosch, T.; Tinnefeld, P.; Weston, K. D.; Ego, C.; Grimsdale, A.; Müllen, K.; Beljonne, D.; Brédas, J. L.; Jordens, S.; Schweitzer, G.; Sauer, M.; De Schryver, F. Revealing competitive Forster-type resonance energy-transfer pathways in single

37

bichromophoric molecules. *Proc. Natl. Acad. Sci. U. S. A.* **2003**, *100* (23), 13146−13151.

(24) Hübner, C. G.; Zumofen, G.; Renn, A.; Herrmann, A.; Müllen, K.; Basché, T. Photon antibunching and collective effects in the fluorescence of single bichromophoric molecules. *Phys. Rev. Lett.* **2003**, *91* (9), 093903.

(25) Steiner, F.; Vogelsang, J.; Lupton, J. M. Singlet-Triplet Annihilation Limits Exciton Yield in Poly(3-Hexylthiophene). *Phys. Rev. Lett.* **2014**, *112* (13), 137402.

(26) Kandori, H.; Kemnitz, K.; Yoshihara, K. Subpicosecond Transient Absorption Study of Intermolecular Electron-Transfer between Solute and Electron-Donating Solvents. *J. Phys. Chem.* **1992**, *96* (20), 8042−8048.

(27) Tinnefeld, P.; Müller, C.; Sauer, M. Time-varying photon probability distribution of individual molecules at room temperature. *Chem. Phys. Lett.* **2001**, *345* (3−4), 252−258.

(28) Weston, K. D.; Dyck, M.; Tinnefeld, P.; Müller, C.; Herten, D. P.; Sauer, M. Measuring the number of independent emitters in single-molecule fluorescence images and trajectories using coincident photons. *Anal. Chem.* **2002**, *74* (20), 5342−5349.

(29) Tinnefeld, P.; Hofkens, J.; Herten, D. P.; Masuo, S.; Vosch, T.; Cotlet, M.; Habuchi, S.; Mullen, K.; De Schryver, F. C.; Sauer, M. Higher-excited-state photophysical pathways in multichromophoric systems revealed by single-molecule fluorescence spectroscopy. *ChemPhysChem* **2004**, *5* (11), 1786−1790.

(30) Haimerl, J.; Ghosh, I.; König, B.; Vogelsang, J.; Lupton, J. M. Single-molecule photoredox catalysis. *Chem. Sci.* **2019**, *10*, 681.

(31) Reisch, A.; Didier, P.; Richert, L.; Oncul, S.; Arntz, Y.; Mely, Y.; Klymchenko, A. S. Collective fluorescence switching of counterion-assembled dyes in polymer nanoparticles. *Nat. Commun.* **2014**, *5*, 4089.

(32) Becker, K.; Lagoudakis, P. G.; Gaefke, G.; Höger, S.; Lupton, J. M. Exciton accumulation in pi-conjugated wires encapsulated by light-harvesting macrocycles. *Angew. Chem., Int. Ed.* **2007**, *46* (19), 3450−3455.

(33) Zhou, R. B.; Kunzelmann, S.; Webb, M. R.; Ha, T. Detecting Intramolecular Conformational Dynamics of Single Molecules in Short Distance Range with Subnanometer Sensitivity. *Nano Lett.* **2011**, *11* (12), 5482−5488.

(34) Cordes, T.; Vogelsang, J.; Tinnefeld, P. On the Mechanism of Trolox as Antiblinking and Antibleaching Reagent. *J. Am. Chem. Soc.* **2009**, *131* (14), 5018−5020.

38

Interchromophoric Interactions Determine the Maximum Brightness Density in DNA Origami Structures

Tim Schröder, Max B. Scheible, Florian Steiner, Jan Vogelsang*, Philip Tinnefeld*

Department Chemie and Center for NanoScience, Ludwig-Maximilians-Universitaet Muenchen, Butenandtstr. 5-13 Haus E, 81377 Muenchen, Germany.

1. Materials and Methods

Confocal setup

A home built confocal microscope based on an Olympus IX-71 inverted microscope was used. Two pulsed lasers (637 nm, 80 MHz, LDH-D-C-640; 532 nm, 80 MHz, LDH-P- FA-530B; both PicoQuant GmbH) were altered through an acousto optical tunable filter (AOTFnc-VIS, AA Opto Electronic). Circular polarized light was obtained by a linear polarizer (LPVISE100-A, Thorlabs GmbH) and a quarter-wave plate (AQWP05M- 600, Thorlabs GmbH). The light was focused by an oil-immersion objective (UPLSAPO100XO, NA 1.40, Olympus Deutschland GmbH) onto the sample. The sample was moved by a piezo stage (P-517.3CD, Physik Instrumente (PI) GmbH & Co. KG) controlled by a E-727.3CDA piezo controller (Physik Instrumente (PI) GmbH & Co. KG). The emission was separated from the excitation beam by a dichroic beam splitter (z532/633, AHF analysentechnik AG) and focused onto a 50 μm pinhole (Thorlabs GmbH). The emission light was split by a dichroic beam splitter (640DCXR, AHF analysentechnik AG) into a green (Brightline HC582/75, AHF analysentechnik AG; RazorEdge LP 532, Laser 2000 GmbH) and red (Shortpass 750, AHF analysentechnik AG; RazorEdge LP 647, Laser 2000 GmbH) detection channel. Emission was focused onto avalanche photo diodes (SPCM-AQRH-14-TR, Excelitas Technologies GmbH & Co. KG) and signals were registered by a time-correlated single photon counting (TCSPC)-unit (HydraHarp400, PicoQuant GmbH). The setup was controlled by a homemade LabVIEW software or a commercial software package (SymPhoTime64, Picoquant GmbH). For cross correlation experiments the dichroic beam splitter in the detection path was substituted by a non-polarizing 50:50 beam splitter cube (CCM1-BS013/M, Thorlabs GmbH).

DNA origami sample preparation

The flat rectangular DNA origami [1] was modified using caDNAno (version 0.2.2, design schematics in Fig. S6-S16). The 7249 nucleotide long scaffold was extracted from M13mp18 bacteriophages. All staple strands were purchased from Eurofins Genomics GmbH as well as the ATTO 647N modified oligos. The ATTO 542 modified oligos were purchased from biomers.net. For DNA origami folding oligos and scaffold from Table S1 were mixed for given final concentrations. As folding buffer (FB) 1x TAE with additional 12 mM $MgCl_2$ was used. For folding a nonlinear thermal annealing ramp over 16 hours was used [2]. After annealing the excess staples were removed by polyethylene glycol (PEG) precipitation [3]. The samples were mixed with an equal volume of PEG precipitation buffer (1x TAE, 15 % (w/v) PEG-8000, 500 mM NaCl, 12 mM $MgCl_2$) and centrifuged at 16 krcf for 30 min at 4°C. The pellet was suspended in 1x FB. Afterwards the DNA origami was externally labeled with ATTO 542 modified oligos. A three times excess respectively the extended staples was used and incubated overnight in a wet chamber. The DNA origami structures were purified via a gel electrophoresis. Therefor a 1.5 % agarose gel containing 0.5x TAE and 11 mM $MgCl_2$ was used at 70 V for 2 hours in a gel box cooled in an ice water bath. The gel was not stained to avoid unwanted staining reagent-dye interaction. DNA origami structures could be seen on a blue illuminated table due to the numerous ATTO 542 dyes. The target band was cut out and the DNA origami structures were recovered from the gel. The samples were stored at -26 °C until further use.

Folding Table

Final concentration for DNA origami folding are given in Table S1. Meaning of the reagents is described below:

Table S1. Folding reagents with final concentrations.

Reagent	Final concentration / nM
scaffold	30
core staples	240
biotin staples	300
extended staples	240
dye used in every DNA origami	450
refill for 10bp	240
dye with different distance	450

scaffold: single stranded viral DNA from M13mp18.

core staples: Contains every unmodified staples of the rectangular DNA origami. The wild structure is given in reference [1].

biotin staples: Six Biotin modified staples. Modifications are placed at the 5' end.

extended staples: Ten staples extended at the 3' end for external labeling. The extended sequence is: 5' TTTTCCTCTACCACCTACATCAC 3'

dye used in every DNA origami: Oligo labeled at the 3' end with ATTO647N. This oligo is used in every DNA Origami.

refill for 10bp: For the 10bp sample the DNA origami was slightly modified to granite a stable incorporation of the 10bp oligo. This oligo is missing in the 10bp sample. For a 10bp sample replace it with H_2O.

dye with different distances: This stock contains the oligo labeled at the 5' end with its corresponding spacer.

The listed reagents were mixed and the folding buffer (FB) was added to 1xFB concentration.

Surface preparation and immobilization

Measurements were performed in LabTek^{TM} chamber slides (Thermo Fisher Scientific Inc.) which were cleaned two times for 20 minutes with 0.1 M hydrofluoric acid (AppliChem GmbH) and washed afterwards three times with ultrapure water. The glass surface was coated with biotin labeled bovine serum albumin (BSA) (Sigma-Aldrich Chemie GmbH). The DNA origami structure was immobilized through NeutrAvidin (Sigma-Aldrich Chemie GmbH) and six biotin labeled oligos to the BSA coated surface. dsDNA model structures were used likewise.

Single molecule measurements

Surface scans were performed after DNA origami structure immobilization. An oxidizing and reducing buffer system (1x TAE, 12 mM $MgCl_2$, 2 mM Trolox/Troloxquinone, 1 % (w/v) D-(+)-Glycose) [4] was used in combination with an oxygen scavenging system (1 mg mL−1 glucose oxidase, 0.4 % (v/v) catalase (50 μg mL−1), 30 % glycerol, 12.5 mM KCl in 50 mM TRIS) to suppress blinking and photo bleaching. The oxygen scavenging system was added to the oxidation and reducing buffer at a

concentration of 10 % (v/v) in the LabTek^{TM}. For surface scans a 10×20 μm^2 area size was used with a pixel size of 50×50 nm and alternating laser excitation. The integration time was 2 ms (1 ms for each color) and the laser power was adjusted to 9 μW at 639 nm and 1 μW at 532 nm.

Blinking kinetics under oxygen depletion without ROXS were performed by using glucose oxidase and catalase as described above. The measuring buffer was a 1xTEA buffer with 12 mM MgCl$_2$ and 1 % (w/v) D-(+)-Glycose.

Absorption spectrum

For absorption spectra a higher concentration and amount of mass was needed than DNA origami structure folding could provide. Therefor a model structure was designed. Oligos, that are used in the DNA origami structure were hybridized to a complementary sequence (1bp: 5'- Biotin TTAATGAAACTTGATTCTGTCGCTACTGATTACGGTGCTGCTATCGATGGTTTCTGA, 20bp: 5'- Biotin TTAATGAAACTTGATTCTGTCGCTACTGATTACGGTGCTGCTATCGTGGTTTCTGAGGGTGG TGGCTCTTCAAGGCC). The spacer was the same as in the DNA origami structure. For hybridization equal amounts of substance were mixed and the solution was adjusted to the 1x FB concentration of TAE and MgCl$_2$. The solution was heated to 70 °C for 5 min and subsequently cooled down at a linear ramp to 25 °C by 1 K per minute. The absorption measurements were performed using a 10 mm path length cuvette (UVette, Eppendorf AG) and an Evolution 201 spectrometer (ThermoFisher Scientific Inc.) with 1 nm resolution and 1 s point integration time.

Data analysis

Each scan image has a 10×20 μm² size with a pixel size of 50×50 nm². Each pixel has a total integration time of 2 ms (1 ms per color). We use a home-build LabVIEW software with a spot finding algorithm to analyze the scans. DNA origami structures were marked with up to ten ATTO 542 dyes. Therefor the spot finding algorithm uses the green excitation green emission channel to find spots.

To define a spot, we used three different filters. The first one discriminates the pixels that we take into account. If a pixel has less or equal than 10 photons the algorithm does not take this pixel into account. The second filter discriminates by spot size. If an area of neighboring pixels, that were taken into account, is between 10 and 60 pixels we used them for further analysis. This is the expected area size of our PSFs. If an area is smaller, it is probably due to scattering dirt. A bigger area refers to two overlapping or close by DNA origami structures. The third parameter is the Heywood circular factor. Areas with a factor between 1.00 and 1.22 were taken into account. We use the last filter to get rid of PSFs which are cut in half because they are located at the edge of a scan. The remaining spots are analyzed. The program sums up the photons that are in range of a seven-pixel radius from the center of the spot for each channel. Red excitation, red emission channel was used to obtain the intensity per spot and fluorescence lifetime data of the ATTO 647N dyes.

For the dsDNA model a green dye was not attached to the dsDNA. The red channel was analyzed with following parameters. A pixel was taken into account when it had more than 5 photons and a PSF was recognized when it had more than 10 and less than 80 pixels. The Heywood circular factor was not used due to the blinking characteristic of the dye dimer that leads to rough shaped spots.

When analyzing cross correlation measurements, the first three million photons were used to calculate the coincidence histogram. This gives a lateral count of roughly 2000 coincidences with little shot noise. Signal to background ratio for one dye experiments was always above 170 and for two dyes above 340. For calculation the coincidence ratio the central peak was divided by the average of the six lateral peaks.

2. AFM

AFM imaging was performed on a NanoWizard® 3 ultra AFM (JPK Instruments AG) in solution using 1xFB. The DNA origami structures were immobilized on a freshly cleaved mica surface (Quality V1, Plano GmbH) by Ni^{2+} ions which were incubated on the mica for 5 minutes with a 10 mM $NiCl_2$ solution. Afterwards the mica was washed three times with ultra-pure water and dried by dry air. The origami structures were incubated for 5 minutes by a 1 nM solution. Measurements were performed with a USC-F0.3-k0.3-10 cantilever from NanoWorld AG.
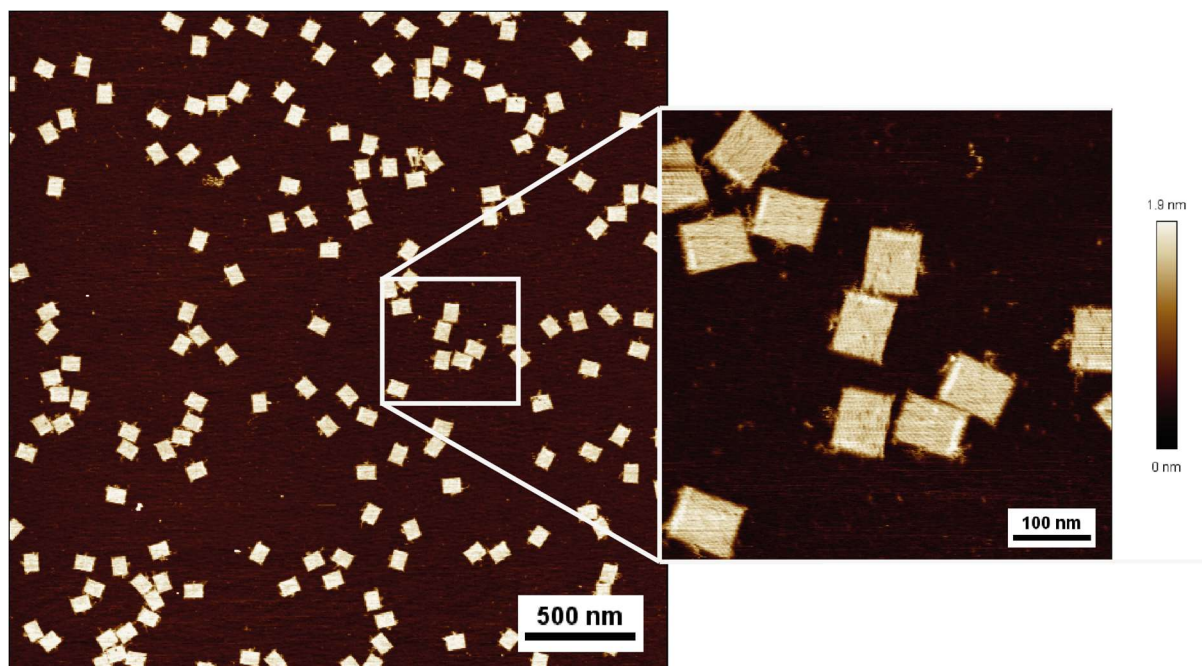
Figure S1. AFM image of a 1-bp distance sample. Magnification of the indicated area on the right. The bright lines on the DNA origamis indicate the external labeling due to an additional layer of dsDNA.

2. Blinking kinetics in the 4 bp- to 6 bp-distance samples
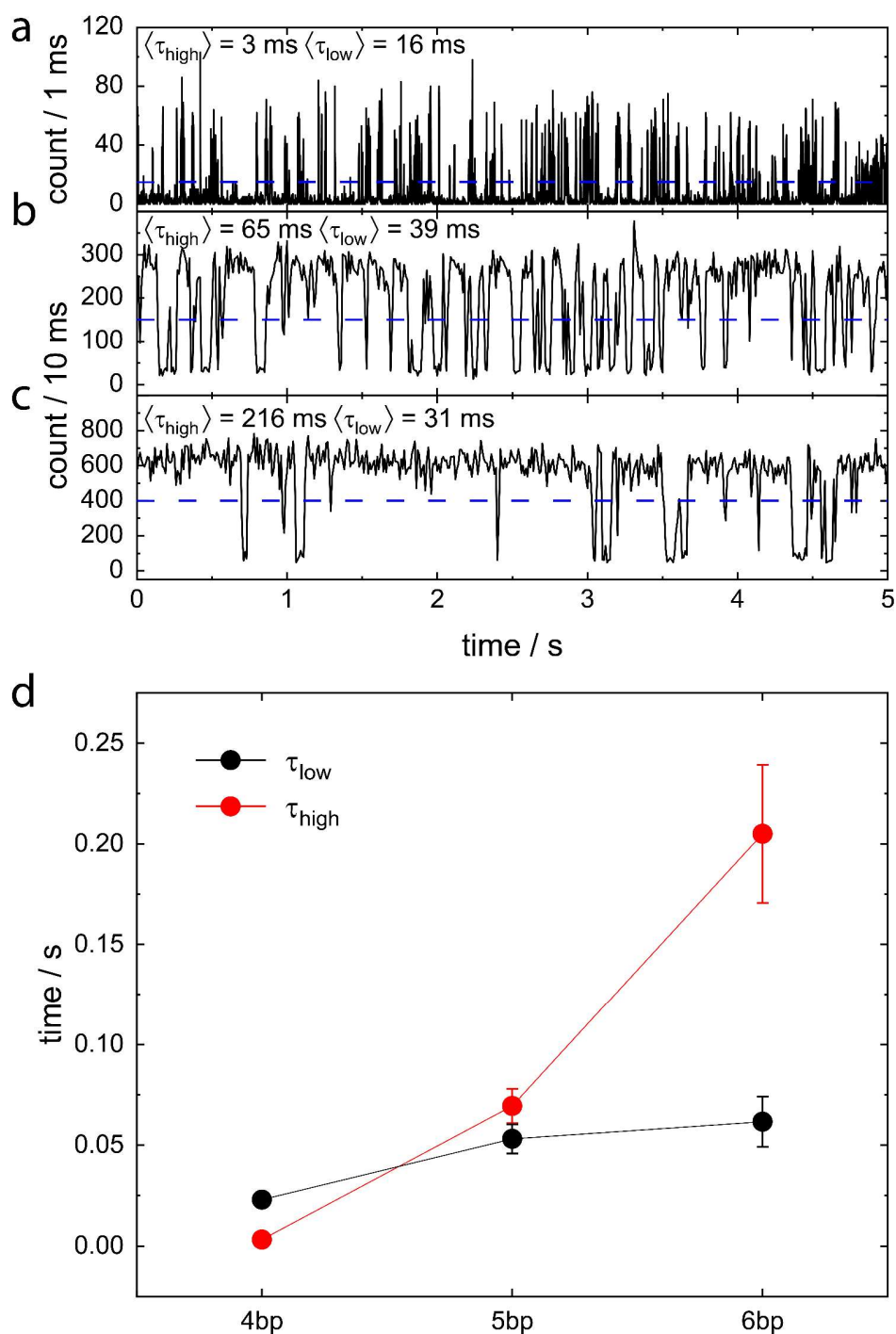
**Figure S2.** Representative transients from a) 4bp- b) 5bp- and c) 6bp-distance samples. Average dwell times for the high and low fluorescence state for each transient were extracted by using the threshold indicated as blue dashed lines. d) Mean dwell times are shown for each fluorescent state with standard error of the mean of 55, 47 and 32 DNA origami structures for the 4bp-, 5bp- and 6bp-distance samples, respectively. The lifetime of the high fluorescent state becomes longer with increasing spacer length, because additional nucleotides increase the hybridization energy of double stranded DNA. The lifetime of the low fluorescent state stays roughly the same, because the chance of hybridization is limited by the local concentration of the single stranded spacer sequence which is approximately the same for all samples. We note that the blinking kinetic is inhomogeneous throughout the samples due to different nano environments. Different nano environments mainly arises by magnesium ion which clip tow neighboring helices and can therefor stabilize the high fluorescent state.[5]

3. Quenching in the 1 bp- to 10 bp-distance samples without a spacer strand
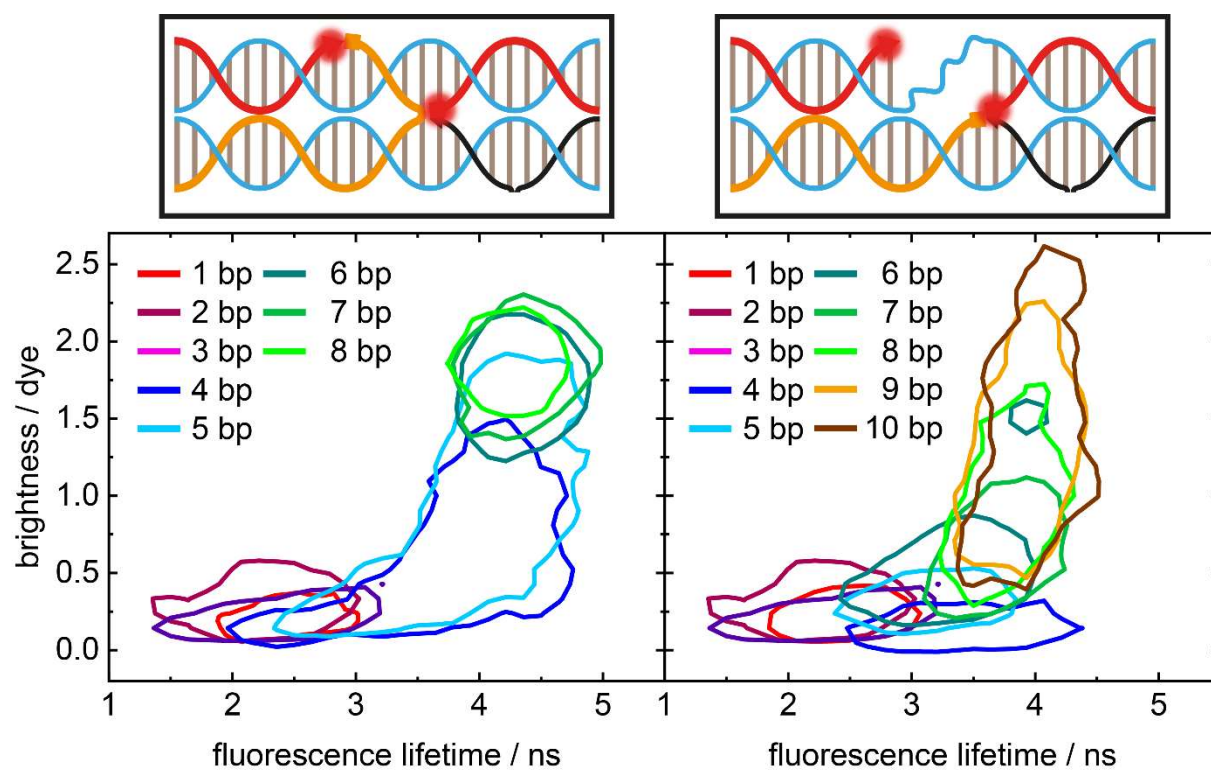
Figure S3. Sample brightness normalized to the average brightness of one dye vs. fluorescence lifetime for the 1 bp- to 10 bp-distance samples with (left panel) and without (right panel) a spacer strand. Lines surround 90 % of the overall population. No pure high intensity and long lifetime population is visible in the samples without a spacer strand.

4. Transients of the 7 bp-distance sample
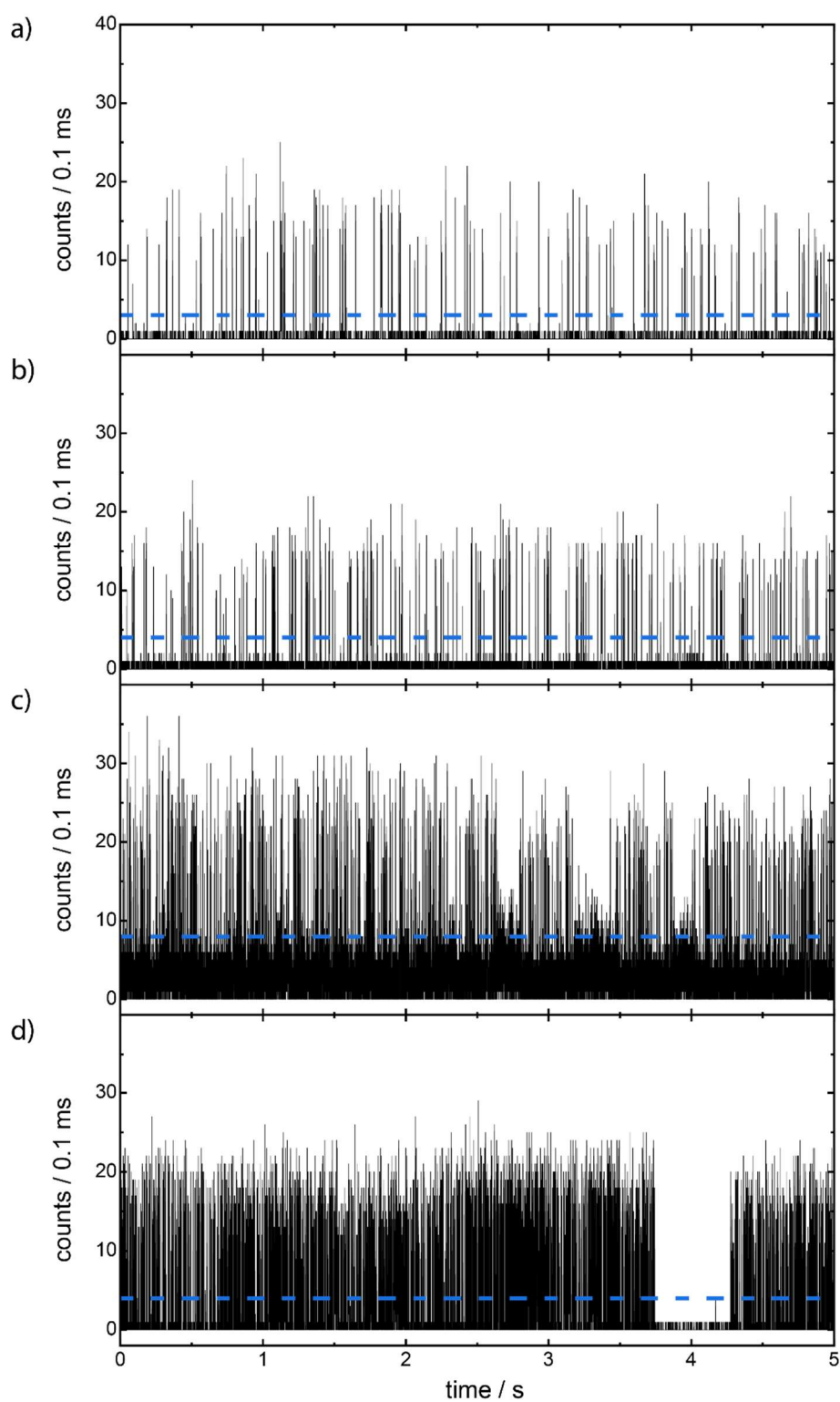
Figure S4. Extended transients from Figure 3 c)-f) with oxygen scavenging and without further stabilization. Blue lines indicate threshold for the determination of on- and off-times, respectively. a) DNA origami sample with one ATTO647N dye, b) 20 bp-distance sample, c) 7 bp-distance sample with background fluorescence and d) without background fluorescence.

5. Fluorescence intensity dependence of the 7 bp-distance sample
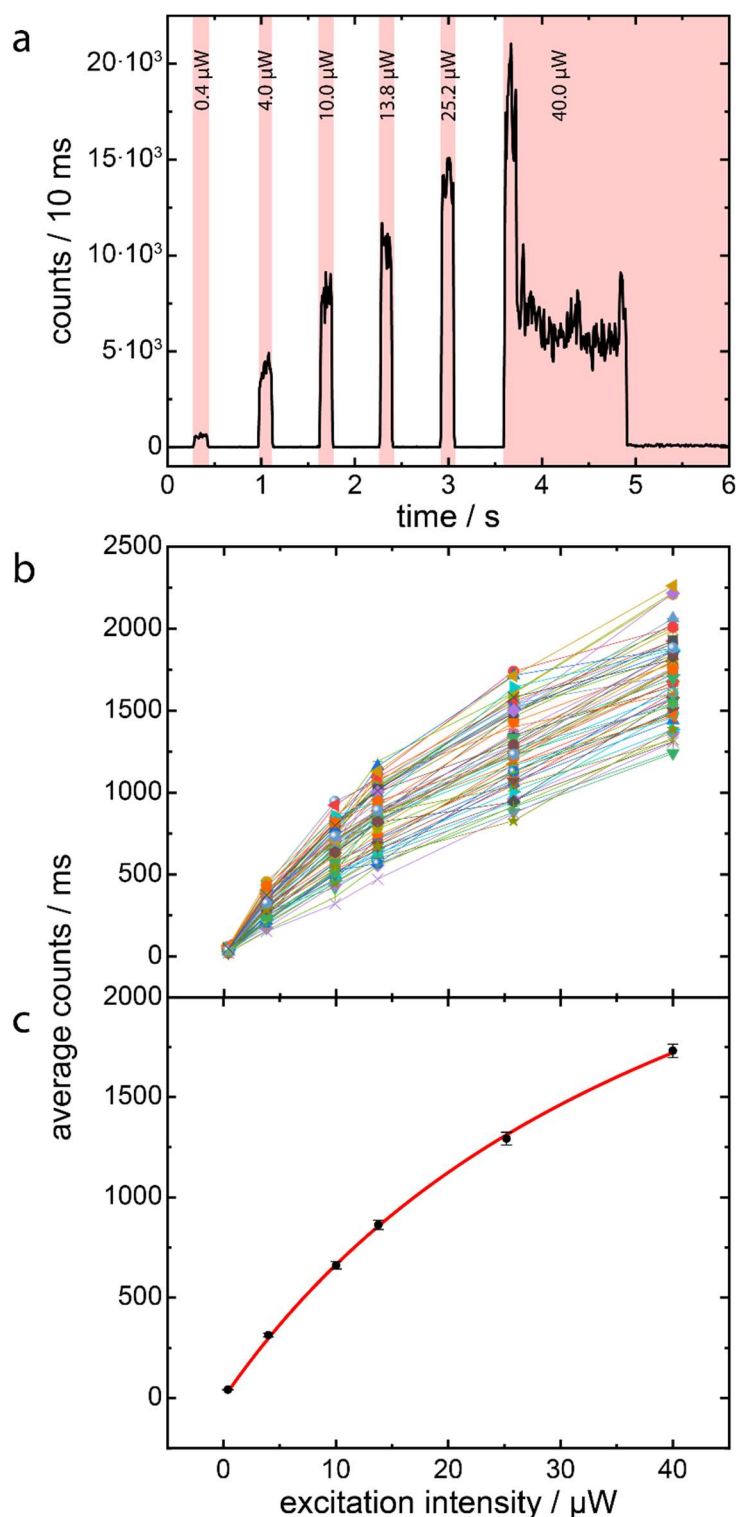
Figure S5. a) Fluorescence transient of a 7 bp-distance sample with increasing laser excitation intensities as stated in the panel. Red areas highlight laser excitation. Two bleaching steps at the end confirm the presence of two dyes. The count rate was extracted at each excitation intensity. b) Count rate at the set excitation powers of 61 transients. c) Averaged count values obtained from the 61 transients shown in (b) with standard error of the mean. A saturation curve in red is fitted to the data points to obtain the maximum count rate = $3.6 \cdot 10^6$ Hz. The following model was used:[6] $N = \frac{N_{max} \cdot \frac{I_{ex}}{I_{sat}}}{1 + \frac{I_{ex}}{I_{sat}}}$ where N is the count rate, N_{max} the maximum count rate, I_{ex} the excitation intensity and I_{sat}

represents the excitation intensity where half of N_{max} is reached. An almost linear fluorescence dependence is demonstrated up to an average count rate of ~ 1 MHz. An optical density filter of OD1 was placed in the detection path and corrected for to avoid saturation due to the dead time of the avalanche photo detector. The maximum count rate of $3.6 \cdot 10^6$ Hz translates to an emission rate ~$3.6 \cdot 10^7$ Hz under the assumption that the confocal microscope provides a detection efficiency of ~10 %. This count rate leads to a maximum off-time of ~ 28 ns, which can be well attributed to a diffusion-limited quenching process of the triplet state by the reducing and oxidizing system at 1 mM concentration.

6. DNA origamis

Two exemplary caDNAno designs are shown below. Previously used staples are colored in black. Green staples are labeled at the 5' end with biotin. Yellow marked staples are extended at the 3' end with following sequence: 5' TTTTCCTCTACCACCTACATCAC 3'. Red staples are labeled with ATTO647N either at the 3' or 5'. Blue staples are staples around the ATTO647N labeled staples to stabilize the structure.
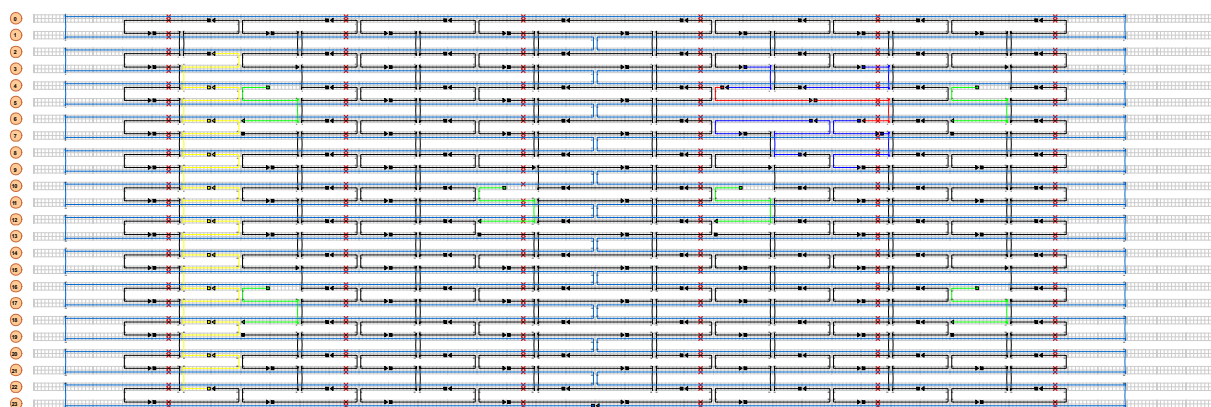
Figure S6: Design of the 1bp sample.
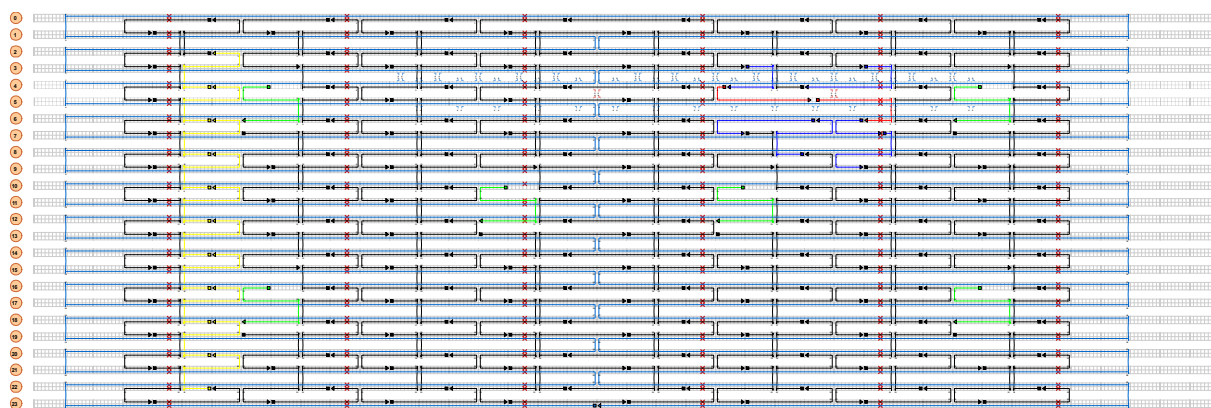
Figure S7: Design of the 2bp sample.
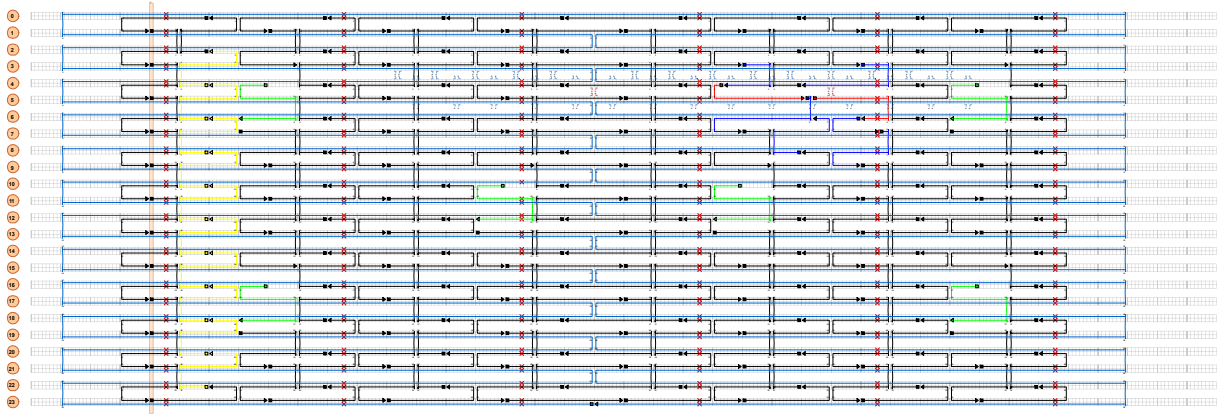
Figure S8: Design of the 3bp sample.
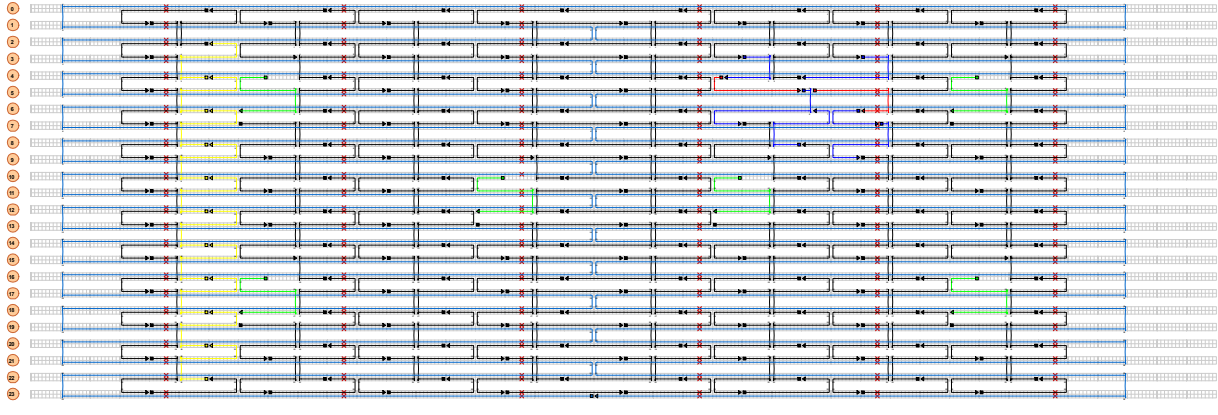
Figure S9: Design of the 4bp sample.
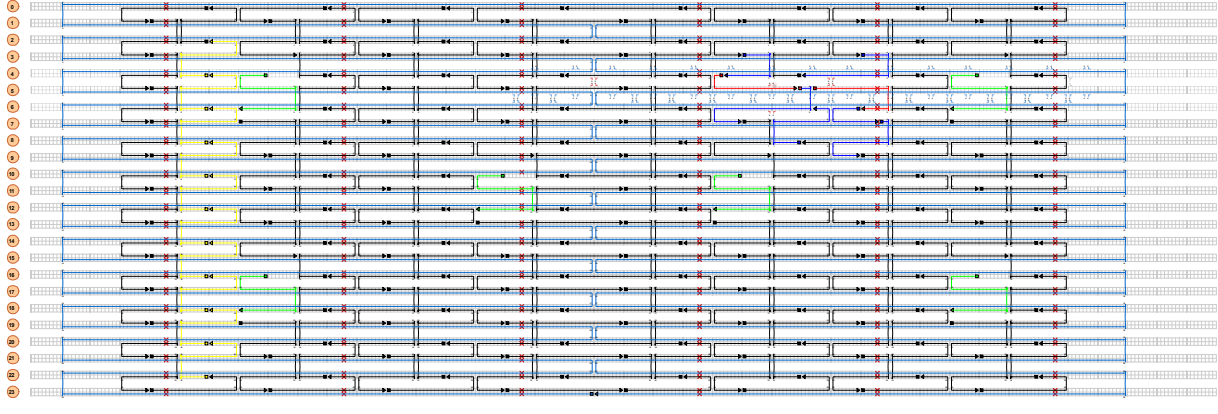
Figure S10: Design of the 5bp sample.
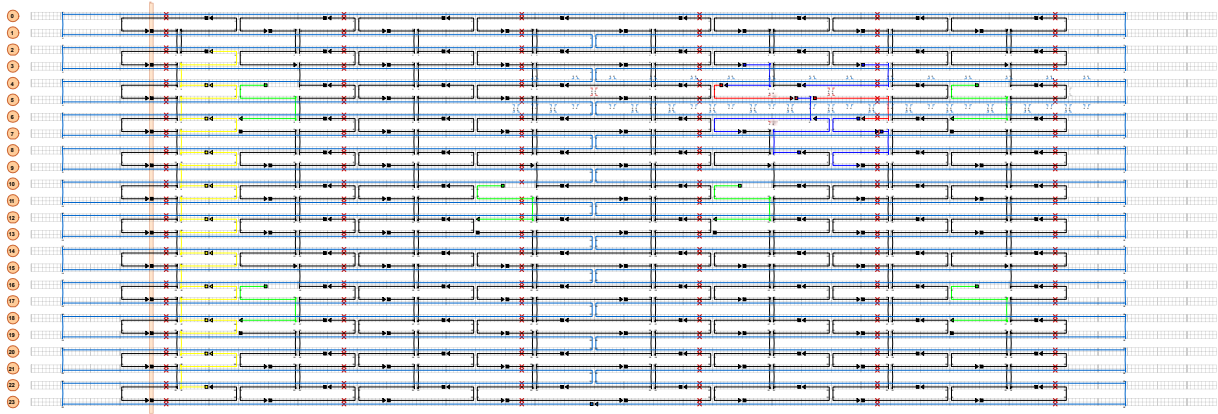
Figure S11: Design of the 6bp sample.
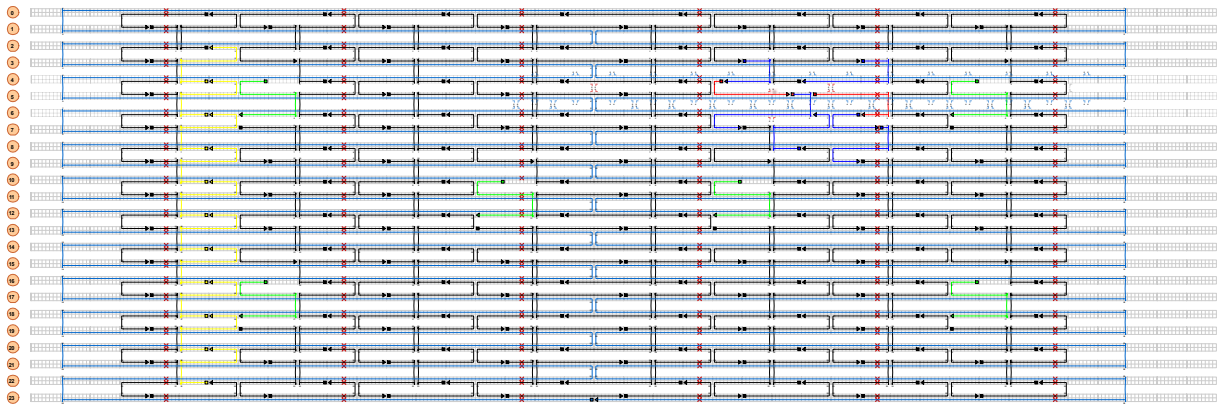
Figure S12: Design of the 7bp sample.
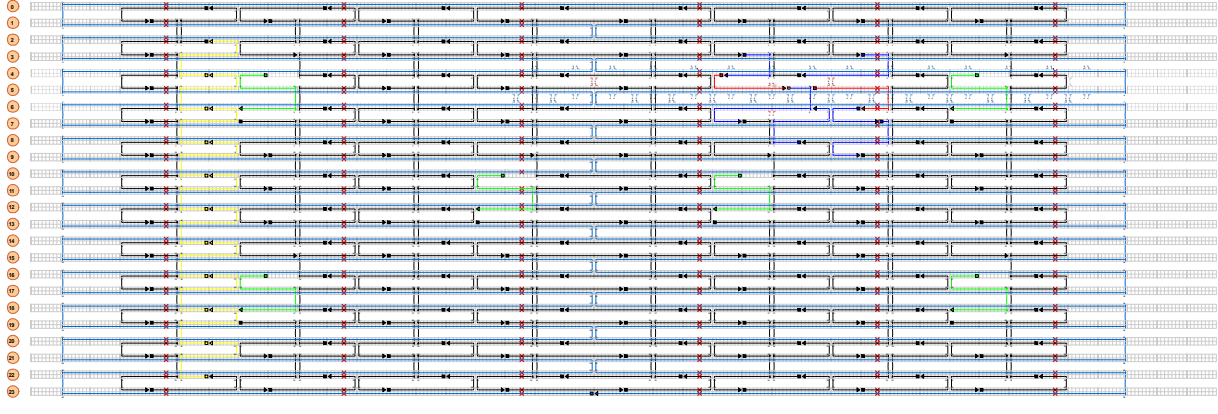
Figure S13: Design of the 8bp sample.
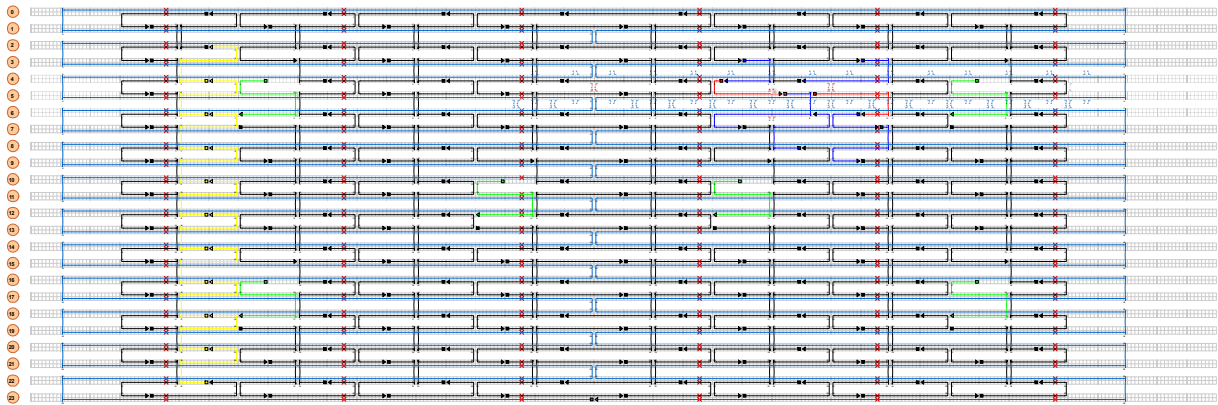
Figure S14: Design of the 9bp sample.
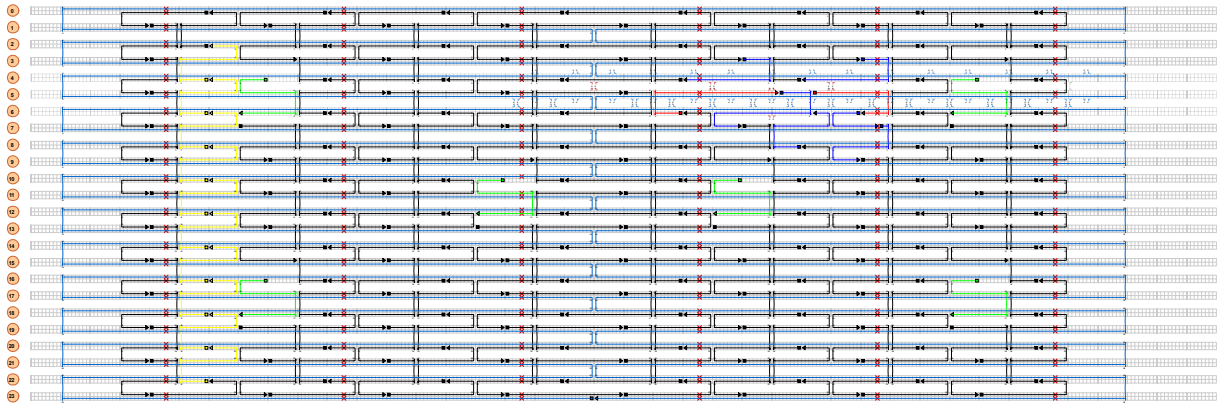
Figure S15: Design of the 10bp sample.
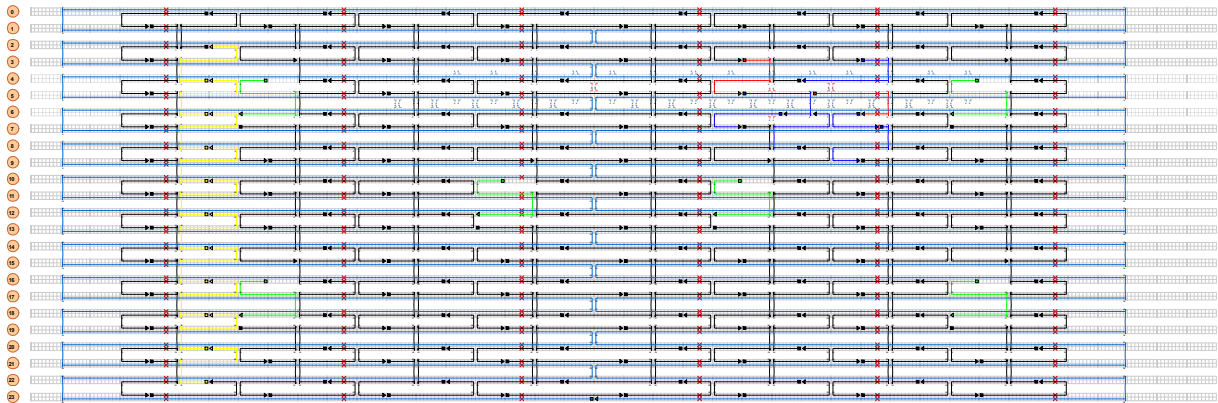
Figure S16: Design of the 20bp sample.

Table S2: Sequences of staples

5' position	Sequence	Comment
5[211]	AGTAGCGACAGAATCAAGTTTCATTAA	5' labeled ATTO647N
4[186]	TCAGAAACCATCGATAGCAGCACCGTAATC	3' labeled ATTO647N 1bp
4[186]	TCAGAAACCATCGATAGCAGCACCGTAAT	3' labeled ATTO647N 2bp
4[186]	TCAGAAACCATCGATAGCAGCACCGTAA	3' labeled ATTO647N 3bp
4[186]	TCAGAAACCATCGATAGCAGCACCGTA	3' labeled ATTO647N 4bp
4[186]	TCAGAAACCATCGATAGCAGCACCGT	3' labeled ATTO647N 5bp
4[186]	TCAGAAACCATCGATAGCAGCACCG	3' labeled ATTO647N 6bp
4[186]	TCAGAAACCATCGATAGCAGCACC	3' labeled ATTO647N 7bp

4[186]	TCAGAAACCATCGATAGCAGCAC	3' labeled ATTO647N 8bp
4[186]	TCAGAAACCATCGATAGCAGCA	3' labeled ATTO647N 9bp
4[186]	CAGCAAAAGGAAACGTCACCAATGAAACCATCGATAGCAGC	3' labeled ATTO647N 10bp
3[192]	GGCCTTGAAGAGCCACCACCCTCAGAAACCAT	3' labeled ATTO647N 20bp
6[210]	CCGTCACCGACTTGAGCCATTTGGGAACGTAGAAA	spacer 1bp
6[210]	TCCCGTCACCGACTTGAGCCATTTGGGAACGTAGAAA	spacer 3bp
6[210]	ATCCCGTCACCGACTTGAGCCATTTGGGAACGTAGAAA	spacer 4bp
6[210]	AATCCCGTCACCGACTTGAGCCATTTGGGAACGTAGAAA	spacer 5bp
6[210]	TAATCCCGTCACCGACTTGAGCCATTTGGGAACGTAGAAA	spacer 6bp
6[210]	GTAATCCCGTCACCGACTTGAGCCATTTGGGAACGTAGAAA	spacer 7bp
6[210]	CGTAATCCCGTCACCGACTTGAGCCATTTGGGAACGTAGAAA	spacer 8bp
6[210]	CCGTAATCCCGTCACCGACTTGAGCCATTTGGGAACGTAGAAA	spacer 9bp
6[175]	ACCGTAATCCCGTCACCGACTTGAGCCATTTGGGAACGTAGAAA	spacer 10bp
7[229]	CAAAGATAGCCGAACAAACCCTGAAC	stabilizer
6[223]	AGGTGAATATAAAAGAAACG	stabilizer
3[224]	TTAAAGCCAGAGCCGCCACCCTCAGAACCG	stabilizer
8[207]	AAGGAAACATAAAGGTGGCAACATTATCA	stabilizer
3[192]	GGCCTTGAAGAGCCACCACCC	stabilizer
18[47]	CCAGGGTTGCCAGTTTGAGGGGACCCGTGGGA	for external labeling
12[47]	TAAATCGGGATTCCCAATTCTGCGATATAATG	for external labeling
22[47]	CTCCAACGCAGTGAGACGGGCAACCAGCTGCA	for external labeling
16[47]	ACAAACGGAAAAGCCCCAAAAACACTGGAGCA	for external labeling
8[47]	ATCCCCCTATACCACATTCAACTAGAAAAATC	for external labeling
4[47]	GACCAACTAATGCCACTACGAAGGGGGTAGCA	for external labeling
10[47]	CTGTAGCTTGACTATTATAGTCAGTTCATTGA	for external labeling
14[47]	AACAAGAGGGATAAAAATTTTTAGCATAAAGC	for external labeling
6[47]	TACGTTAAAGTAATCTTGACAAGAACCGAACT	for external labeling
20[47]	TTAATGAACTAGAGGATCCCCGGGGGGTAACG	for external labeling
10[191]	GAAACGATAGAAGGCTTATCCGGTCTCATCGAGAACAAGC	biotin
10[127]	TAGAGAGTTATTTTCATTTGGGGATAGTAGTAGCATTA	biotin
16[255]	GAGAAGAGATAACCTTGCTTCTGTTCGGGAGAAACAATAA	biotin
4[255]	AGCCACCACTGTAGCGCGTTTTCAAGGGAGGGAAGGTAAA	biotin
4[63]	ATAAGGGAACCGGATATTCATTACGTCAGGACGTTGGGAA	biotin
16[63]	CGGATTCTGACGACAGTATCGGCCGCAAGGCGATTAAGTT	biotin
6[175]	CAGCAAAAGGAAACGTCACCAATGAGCCGC	for 10bp not needed
15[128]	TAAATCAAAATAATTCGCGTCTCGGAAACC	
14[271]	TTAGTATCACAATAGATAAGTCCACGAGCA	
17[224]	CATAAATCTTTGAATACCAAGTGTTAGAAC	
8[175]	ATACCCAACAGTATGTTAGCAAATTAGAGC	
19[248]	CGTAAAACAGAAATAAAAATCCTTTGCCCGAAAGATTAGA	
5[96]	TCATTCAGATGCGATTTTAAGAACAGGCATAG	
0[79]	ACAACTTTCAACAGTTTCAGCGGATGTATCGG	
12[79]	AAATTAAGTTGACCATTAGATACTTTTGCG	
6[111]	ATTACCTTTGAATAAGGCTTGCCCAAATCCGC	

51

11[224]	GCGAACCTCCAAGAACGGGTATGACAATAA	
16[111]	TGTAGCCATTAAAATTCGCATTAAATGCCGGA	
13[120]	AAAGGCCGGAGACAGCTAGCTGATAAATTAATTTTTGT	
16[271]	CTTAGATTTAAGGCGTTAAATAAAGCCTGT	
11[96]	AATGGTCAACAGGCAAGGCAAAGAGTAATGTG	
22[143]	TCGGCAAATCCTGTTTGATGGTGGACCCTCAA	
5[128]	AACACCAAATTTCAACTTTAATCGTTTACC	
20[271]	CTCGTATTAGAAATTGCGTAGATACAGTAC	
15[224]	CCTAAATCAAAATCATAGGTCTAAACAGTA	
21[96]	AGCAAGCGTAGGGTTGAGTGTTGTAGGGAGCC	
1[224]	GTATAGCAAACAGTTAATGCCCAATCCTCA	
2[143]	ATATTCGGAACCATCGCCCACGCAGAGAAGGA	
4[79]	GCGCAGACAAGAGGCAAAAGAATCCCTCAG	
13[184]	GACAAAAGGTAAAGTAATCGCCATATTTAACAAAACTTTT	
6[239]	GAAATTATTGCCTTTAGCGTCAGACCGGAACC	
14[111]	GAGGGTAGGATTCAAAAGGGTGAGACATCCAA	
19[96]	CTGTGTGATTGCGTTGCGCTCACTAGAGTTGC	
23[192]	ACCCTTCTGACCTGAAAGCGTAAGACGCTGAG	
18[111]	TCTTCGCTGCACCGCTTCTGGTGCGGCCTTCC	
4[111]	GACCTGCTCTTTGACCCCCAGCGAGGGAGTTA	
18[239]	CCTGATTGCAATATATGTGAGTGATCAATAGT	
21[224]	CTTTAGGGCCTGCAACAGTGCCAATACGTG	
16[239]	GAATTTATTTAATGGTTTGAAATATTCTTACC	
7[32]	TTTAGGACAAATGCTTTAAACAATCAGGTC	
7[248]	GTTTATTTTGTCACAATCTTACCGAAGCCCTTTAATATCA	
2[239]	GCCCGTATCCGGAATAGGTGTATCAGCCCAAT	
12[271]	TGTAGAAATCAAGATTAGTTGCTCTTACCA	
15[160]	ATCGCAAGTATGTAAATGCTGATGATAGGAAC	
10[207]	ATCCCAATGAGAATTAACTGAACAGTTACCAG	
10[271]	ACGCTAACACCCACAAGAATTGAAAATAGC	
18[79]	GATGTGCTTCAGGAAGATCGCACAATGTGA	
13[160]	GTAATAAGTTAGGCAGAGGCATTTATGATATT	
20[207]	GCGGAACATCTGAATAATGGAAGGTACAAAAT	
23[256]	CTTTAATGCGCGAACTGATAGCCCCACCAG	
17[128]	AGGCAAAGGGAAGGGCGATCGGCAATTCCA	
4[207]	CCACCCTCTATTCACAAACAAATACCTGCCTA	
21[192]	TGAAAGGAGCAAATGAAAAATCTAGAGATAGA	
7[160]	TTATTACGAAGAACTGGCATGATTGCGAGAGG	
10[111]	TTGCTCCTTTCAAATATCGCGTTTGAGGGGGT	
22[175]	ACCTTGCTTGGTCAGTTGGCAAAGAGCGGA	
10[239]	GCCAGTTAGAGGGTAATTGAGCGCTTTAAGAA	
1[64]	TTTATCAGGACAGCATCGGAACGACACCAACCTAAAACGA	
14[143]	CAACCGTTTCAAATCACCATCAATTCGAGCCA	
1[96]	AAACAGCTTTTTGCGGGATCGTCAACACTAAA	
6[143]	GATGGTTTGAACGAGTAGTAAATTTACCATTA	
14[239]	AGTATAAAGTTCAGCTAATGCAGATGTCTTTC	

16[175]	TATAACTAACAAAGAACGCGAGAACGCCAA	
12[175]	TTTTATTTAAGCAAATCAGATATTTTTTGT	
2[175]	TATTAAGAAGCGGGGTTTTGCTCGTAGCAT	
21[64]	GCCCTTCAGAGTCCACTATTAAAGGGTGCCGT	
9[160]	AGAGAGAAAAAAATGAAAATAGCAAGCAAACT	
12[207]	GTACCGCAATTCTAAGAACGCGAGTATTATTT	
19[192]	ATTATACTAAGAAACCACCAGAAGTCAACAGT	
0[175]	TCCACAGACAGCCCTCATAGTTAGCGTAACGA	
1[128]	TGACAACTCGCTGAGGCTTGCATTATACCA	
14[175]	CATGTAATAGAATATAAAGTACCAAGCCGT	
7[56]	ATGCAGATACATAACGGGAATCGTCATAAATAAAGCAAAG	
22[79]	TGGAACAACCGCCTGGCCCTGAGGCCCGCT	
17[96]	GCTTTCCGATTACGCCAGCTGGCGGCTGTTTC	
21[32]	TTTTCACTCAAAGGGCGAAAAACCATCACC	
13[32]	AACGCAAAATCGATGAACGGTACCGGTTGA	
6[271]	ACCGATTGTCGGCATTTTCGGTCATAATCA	
2[47]	ACGGCTACAAAAGGAGCCTTTAATGTGAGAAT	
22[239]	TTAACACCAGCACTAACAACTAATCGTTATTA	
11[32]	AACAGTTTTGTACCAAAAACATTTTATTTC	
1[160]	TTAGGATTGGCTGAGACTCCTCAATAACCGAT	
23[64]	AAAGCACTAAATCGGAACCCTAATCCAGTT	
19[56]	TACCGAGCTCGAATTCGGGAAACCTGTCGTGCAGCTGATT	
19[160]	GCAATTCACATATTCCTGATTATCAAAGTGTA	
15[32]	TAATCAGCGGATTGACCGTAATCGTAACCG	
17[192]	CATTTGAAGGCGAATTATTCATTTTTGTTTGG	
11[256]	GCCTTAAACCAATCAATAATCGGCACGCGCCT	
23[224]	GCACAGACAATATTTTTGAATGGGGTCAGTA	
0[239]	AGGAACCCATGTACCGTAACACTTGATATAA	
9[64]	CGGATTGCAGAGCTTAATTGCTGAAACGAGTA	
0[143]	TCTAAAGTTTTGTCGTCTTTCCAGCCGACAA	
4[239]	GCCTCCCTCAGAATGGAAAGCGCAGTAACAGT	
16[207]	ACCTTTTTATTTTAGTTAATTTCATAGGGCTT	
20[111]	CACATTAAAATTGTTATCCGCTCATGCGGGCC	
8[239]	AAGTAAGCAGACACCACGGAATAATATTGACG	
7[192]	ATACATACCGAGGAAACGCAATAAGAAGCGCATTAGACGG	
20[239]	ATTTTAAAATCAAAATTATTTGCACGGATTCG	
1[32]	AGGCTCCAGAGGCTTTGAGGACACGGGTAA	
23[96]	CCCGATTTAGAGCTTGACGGGGAAAAGAATA	
8[143]	CTTTTGCAGATAAAAACCAAAATAAAGACTCC	
12[239]	CTTATCATTCCCGACTTGCGGGAGCCTAATTT	
13[256]	GTTTATCAATATGCGTTATACAAACCGACCGTGTGATAAA	
12[111]	TAAATCATATAACCTGTTTAGCTAACCTTTAA	
6[79]	TTATACCACCAAATCAACGTAACGAACGAG	
13[224]	ACAACATGCCAACGCTCAACAGTCTTCTGA	
17[160]	AGAAAACAAAGAAGATGATGAAACAGGCTGCG	
11[160]	CCAATAGCTCATCGTAGGAATCATGGCATCAA	

1[256]	CAGGAGGTGGGGTCAGTGCCTTGAGTCTCTGAATTTACCG	
23[128]	AACGTGGCGAGAAAGGAAGGGAAACCAGTAA	
4[175]	CACCAGAAAGGTTGAGGCAGGTCATGAAAG	
19[224]	CTACCATAGTTTGAGTAACATTTAAAATAT	
10[143]	CCAACAGGAGCGAACCAGACCGGAGCCTTTAC	
23[160]	TAAAAGGGACATTCTGGCCAACAAAGCATC	
15[192]	TCAAATATAACCTCCGGCTTAGGTAACAATTT	
22[207]	AGCCAGCAATTGAGGAAGGTTATCATCATTTT	
5[160]	GCAAGGCCTCACCAGTAGCACCATGGGCTTGA	
21[256]	GCCGTCAAAAAACAGAGGTGAGGCCTATTAGT	
2[207]	TTTCGGAAGTGCCGTCGAGAGGGTGAGTTTCG	
15[96]	ATATTTTGGCTTTCATCAACATTATCCAGCCA	
3[160]	TTGACAGGCCACCACCAGAGCCGCGATTTGTA	
11[64]	GATTTAGTCAATAAAGCCTCAGAGAACCCTCA	
20[175]	ATTATCATTCAATATAATCCTGACAATTAC	
8[79]	AATACTGCCCAAAAGGAATTACGTGGCTCA	
4[143]	TCATCGCCAACAAAGTACAACGGACGCCAGCA	
22[111]	GCCCGAGAGTCCACGCTGGTTTGCAGCTAACT	
3[128]	AGCGCGATGATAAATTGTGTCGTGACGAGA	
0[111]	TAAATGAATTTTCTGTATGGGATTAATTTCTT	
7[96]	TAAGAGCAAATGTTTAGACTGGATAGGAAGCC	
23[32]	CAAATCAAGTTTTTTGGGGTCGAAACGTGGA	
8[111]	AATAGTAAACACTATCATAACCCTCATTGTGA	
4[271]	AAATCACCTTCCAGTAAGCGTCAGTAATAA	
16[143]	GCCATCAAGCTCATTTTTTAACCACAAATCCA	
0[47]	AGAAAGGAACAACTAAAGGAATTCAAAAAAA	
21[128]	GCGAAAAATCCCTTATAAATCAAGCCGGCG	
18[175]	CTGAGCAAAAATTAATTACATTTTGGGTTA	
0[207]	TCACCAGTACAAACTACAACGCCTAGTACCAG	
3[32]	AATACGTTTGAAAGAGGACAGACTGACCTT	
2[111]	AAGGCCGCTGATACCGATAGTTGCGACGTTAG	
0[271]	CCACCCTCATTTTCAGGGATAGCAACCGTACT	
9[32]	TTTACCCCAACATGTTTTAAATTTCCATAT	
9[96]	CGAAAGACTTTGATAAGAGGTCATATTTCGCA	
14[79]	GCTATCAGAAATGCAATGCCTGAATTAGCA	
18[143]	CAACTGTTGCGCCATTCGCCATTCAAACATCA	
18[207]	CGCGCAGATTACCTTTTTTAATGGGAGAGACT	
3[96]	ACACTCATCCATGTTACTTAGCCGAAAGCTGC	
17[32]	TGCATCTTTCCCAGTCACGACGGCCTGCAG	
7[128]	AGACGACAAAGAAGTTTTGCCATAATTCGAGCTTCAA	
8[271]	AATAGCTATCAATAGAAAATTCAACATTCA	
10[79]	GATGGCTTATCAAAAAGATTAAGAGCGTCC	
19[32]	GTCGACTTCGGCCAACGCGCGGGGTTTTTC	
19[128]	CACAACAGGTGCCTAATGAGTGCCCAGCAG	
13[64]	TATATTTTGTCATTGCCTGAGAGTGGAAGATTGTATAAGC	
5[32]	CATCAAGTAAAACGAACTAACGAGTTGAGA	

1[192]	GCGGATAACCTATTATTCTGAAACAGACGATT	
14[207]	AATTGAGAATTCTGTCCAGACGACTAAACCAA	
9[224]	AAAGTCACAAAATAAACAGCCAGCGTTTTA	
21[160]	TCAATATCGAACCTCAAATATCAATTCCGAAA	
13[96]	TAGGTAAACTATTTTTGAGAGATCAAACGTTA	
2[79]	CAGCGAAACTTGCTTTCGAGGTGTTGCTAA	
22[271]	CAGAAGATTAGATAATACATTTGTCGACAA	
2[271]	GTTTTAACTTAGTACCGCCACCCAGAGCCA	
20[143]	AAGCCTGGTACGAGCCGGAAGCATAGATGATG	
16[79]	GCGAGTAAAAATATTTAAATTGTTACAAAG	
10[175]	TTAACGTCTAACATAAAAACAGGTAACGGA	
18[271]	CTTTTACAAAATCGTCGCTATTAGCGATAG	
9[256]	GAGAGATAGAGCGTCTTTCCAGAGGTTTTGAA	
20[79]	TTCCAGTCGTAATCATGGTCATAAAAGGGG	
12[143]	TTCTACTACGCGAGCTGAAAAGGTTACCGCGC	

References

[1] J. J. Schmied, C. Forthmann, E. Pibiri, B. Lalkens, P. Nickels, T. Liedl, P. Tinnefeld, *DNA origami nanopillars as standards for three-dimensional superresolution microscopy*, Nano Lett., *13*, 781–785, **2013**.

[2] P. C. Nickels, B. Wunsch, P. Holzmeister, W. Bae, L. M. Kneer, D. Grohmann, P. Tinnefeld, T. Liedl, *Molecular force spectroscopy with a DNA origami-based nanoscopic force clamp*, Science (New York, N.Y.), *354*, 305–307, **2016**.

[3] E. Stahl, T. G. Martin, F. Praetorius, H. Dietz, *Facile and Scalable Preparation of Pure and Dense DNA Origami Solutions*, Angew. Chem., *53*, 12735-12740, **2014**.

[4] J. Vogelsang, R. Kasper, C. Steinhauer, B. Person, M. Heilemann, M. Sauer, P. Tinnefeld, *A reducing and oxidizing system minimizes photobleaching and blinking of fluorescent dyes*, Angew. Chem. Int. Ed., *47*, 5465–5469, **2008**.

[5] C. Hyeon, J. Lee, J. Yoon, S. Hohng, D. Thirumalai, *Hidden complexity in the isomerization dynamics of Holliday junctions*, Nature Chem., *4*, 907-914, **2012**.

[6] W. P. Ambrose, T. Basché, W. E. Moerner, *Detection and Spectroscopy of Single Pentacene Molecules in a P-Terphenyl crystal by means of Fluorescence Excitation*, J. Chem. Phys., *95*, 7150-7163, **1991**.

4.2 Picosecond Time-Resolved Photon Antibunching Measures Nanoscale Exciton Motion and the True Number of Chromophores

Gordon J. Hedley*, **Tim Schröder***, Florian Steiner, Theresa Eder, Felix Hofmann, Sebastian Bange, Dirk Laux, Sigurd Höger, Philip Tinnefeld, John M. Lupton & Jan Vogelsang

(* equal contribution)

Multichromophoric nanoparticle (mcNP) such as conjugated polymers, quantum dots, perovskite nano particles and light-harvesting complexes can carry several excitons at the same time. To optimize the performance of optoelectronic devices in terms of photoluminescence and photo-stability requires knowledge about the exciton number such system can carry and how the excitons interact with each other. Many mcNPs show good single photon emission in the photon statistics, which is interpreted as evidence for SSA and long-range interchomophore interactions thus making photon antibunching data hard to interpret. Therefore, we introduced picosecond time-resolved photon antibunching (psTRAB) in the publication P2, which makes use of the time dependence of the annihilation processes under pulsed laser excitation. To demonstrate the functionality of psTRAB we used DNA origami structures as model systems because this technique provides control over the inter dye distance and dye stoichiometry. In addition, the exciton diffusion in ordered and disordered conjugated polymers was investigated.

psTRAB uses the time dependency of rate processes. Under pulsed laser excitation, we sorted the photons according to their arrival time. We correlated only those photons within the selected microtime gate. E.g. the intensity correlation of photons detected directly after laser pulse excitation monitors the true number of chromophores that can carry an exciton, as SSA had no time to occur. If photons from a later microtime gate were selected, SSA and exciton diffusion (e.g. by homo FRET or exciton hopping) could have taken place thus reducing the number of independent chromophores that could carry a second exciton. The reduced number of independent chromophores showed in the photon statistics as a lower probability of two photon emission resulting in a greater degree of photon antibunching. The slope of this decrease yielded the SSA rate constant.

To demonstrate the psTRAB technique, I fabricated a total of seven different DNA origami structures, measured and analyzed them. The simplest structure contained only a single ATTO 647N dye to demonstrate the signal to background limit of psTRAB. As SSA is a FRET-based mechanism for the DNA origami model structure, a strong distance dependent annihilation efficiency was expected. Therefore, I measured three samples with two dyes with an interdye distance of either 3, 6 or 12 nm. As expected, the 12 nm sample showed no annihilation and consistently showed the expected degree of photon antibunching ~ 0.5 for two chromophores. The samples with 3 nm and 6 nm distance started in the psTRAB analysis at the degree of photon antibunching of the 12 nm sample but showed a decrease in the number of independent

chromophores for later microtime gates. I was able to extract the annihilation rate constants as well as the number of emitters with a monoexponential model. The annihilation rate constant in the 3 nm sample was ~19 times faster than in the 6 nm sample, which was expected as the FRET mechanism scales with an inverse six power law of the distance. Two samples with three dyes also started at the expected photon antibunching value for three dyes. The sample with a distance of 3 nm did not exhibit a mono-exponential decay because of the next-nearest neighbor interactions. These were linked to exciton diffusion, which first had to occur, in order to bring the two excitons to neighboring chromophores for efficient SSA. The same applied to the last sample with 5 dyes and 3 nm spacing. All origami structures that showed SSA were approaching single photon emission for late microtime gates indicating efficient exciton diffusion between the dyes.

Our collaboration partners in Regensburg applied psTRAB analysis to two types of conjugated polymer aggregates, well-ordered H-aggregates and unordered J-aggregates. Three phases of the annihilation process were identified in both types. Shortly after the laser pulse excitation, neighboring excitons annihilated within picoseconds. Later microtime gates showed different annihilation rate constants in H- and J-aggregates. A well-ordered H-aggregate enabled three-dimensional exciton diffusion and a J-aggregate mainly only two-dimensional diffusion along the chain, thus resulted in a smaller annihilation rate constant. Eventually, the curves saturated due to energy sinks in the conjugated polymer which inhibited SSA at later times.

In a nutshell, the associated publication introduced psTRAB as a new method which combines the intensity correlation information and fluorescence lifetime information. Thereby, psTRAB allowed for the first time the determination of the true number of chromophores in a mcNP and the study of annihilation processes without further assumptions. Despite the very efficient SSA, the true number of chromophores in DNA origami structures were reliably determined and the diffusion dependent annihilation processes were monitored in different kinds of conjugated polymer aggregates. My contribution was to design, fabricate and characterize the DNA origami structures with psTRAB. The idea and theory for psTRAB was developed by our collaboration partners from Regensburg, who also measured the conjugated polymers and provided the analysis software.

Picosecond time-resolved photon antibunching measures nanoscale exciton motion and the true number of chromophores

Gordon J. Hedley [1,5✉], Tim Schröder [2,5], Florian Steiner [2], Theresa Eder[3], Felix J. Hofmann[3], Sebastian Bange[3], Dirk Laux[4], Sigurd Höger[4], Philip Tinnefeld [2], John M. Lupton [3] & Jan Vogelsang [3✉]

The particle-like nature of light becomes evident in the photon statistics of fluorescence from single quantum systems as photon antibunching. In multichromophoric systems, exciton diffusion and subsequent annihilation occurs. These processes also yield photon antibunching but cannot be interpreted reliably. Here we develop picosecond time-resolved antibunching to identify and decode such processes. We use this method to measure the true number of chromophores on well-defined multichromophoric DNA-origami structures, and precisely determine the distance-dependent rates of annihilation between excitons. Further, this allows us to measure exciton diffusion in mesoscopic H- and J-type conjugated-polymer aggregates. We distinguish between one-dimensional intra-chain and three-dimensional inter-chain exciton diffusion at different times after excitation and determine the disorder-dependent diffusion lengths. Our method provides a powerful lens through which excitons can be studied at the single-particle level, enabling the rational design of improved excitonic probes such as ultra-bright fluorescent nanoparticles and materials for optoelectronic devices.

---

[1] School of Chemistry, University of Glasgow, Glasgow, UK. [2] Department Chemie and Center for NanoScience (CeNS), Ludwig-Maximilians-Universität München, München, Germany. [3] Institut für Experimentelle und Angewandte Physik and Regensburg Center for Ultrafast Nanoscopy (RUN), Universität Regensburg, Regensburg, Germany. [4] Kekulé-Institut für Organische Chemie und Biochemie, Universität Bonn, Bonn, Germany. [5] These authors contributed equally: Gordon J. Hedley, Tim Schröder. ✉email: Gordon.Hedley@glasgow.ac.uk; Jan.Vogelsang@physik.uni-regensburg.de

n a wide range of fluorescent nanoparticles such as conjugated polymers, semiconductor quantum dots, perovskite nano-particles, light-harvesting complexes and many other natural or synthetic multichromophoric nanoparticles (mcNP), multiple excitons can exist simultaneously and in close proximity to each other[1–10]. The number of chromophores as well as their inter-actions through exciton diffusion and annihilation processes are key parameters to describe the photophysical characteristics of mcNPs such as brightness[11,12], photoluminescence (PL) lifetime, exciton harvesting efficiency[13] and photostability[12,14], all of which are also important for the performance of materials in optoelectronic devices. Photon antibunching has been used to count chromophores[15–17]; however, this is typically not viable when exciton diffusion and singlet-singlet annihilation (SSA) occur as illustrated in Fig. 1a. Single-photon emission from mcNPs has been interpreted as evidence of long-range inter-chromophore interactions in a number of large multi-chromophoric systems[1,2,8,18–22]. However, in these cases information about the number of physical chromophores in the mcNPs is lost. Here, we demonstrate that picosecond time-resolved antibunching (psTRAB) can be used to disentangle information on the number of physical chromophores and exci-ton diffusion and annihilation processes. psTRAB exploits the fact that exciton diffusion and annihilation are time-dependent processes. Fingerprints of these processes are thus concealed in the PL photon stream of antibunching experiments under pulsed excitation[6,23].

The degree of single photon emission is commonly measured by two photodetectors in a Hanbury Brown and Twiss (HBT) geometric configuration and is therefore sensitive to two-photon events. With this technique, it is either possible to count the number of chromophores, provided that SSA is neglected, or to measure the SSA rate if the exact number of chromophores is known. In practical situations, neither the number of chromo-phores nor the SSA rate are usually known for mcNPs, which severely limits the usefulness of this conventional technique.

With psTRAB, we analyse the photon stream of antibunching experiments with pulsed excitation by grouping photons with respect to their arrival time after the laser pulse and cross-correlating them to determine the probability of consecutive emission of two photons. Immediately after a laser pulse, SSA has not yet occurred and the emitted photons exhibit photon statistics corresponding to the number of physical chromophores present. As exciton diffusion and annihilation begin to dominate, the number of independent emitters decreases. Thus, the time-dependence of the photon statistics synchronised by the laser pulse reports on (i) the number of physical emitters present and (ii) the time evolution of exciton diffusion and annihilation.

To demonstrate the psTRAB technique, we have used DNA origami to construct mcNPs with a known number of chromo-phores and well-defined spacing between them to accurately measure annihilation and benchmark our method. We then measure psTRAB of mesoscopic deterministic aggregates of conjugated polymers—the building blocks of films used in optoelectronic devices[2]. There we find that during the first 250 ps after excitation, diffusion of excitons mainly occurs between one and two dimensions, both along the polymer backbone and between π-stacked chains. The diffusion then becomes three-dimensional at later times, with an order-of-magnitude difference in the rate of annihilation between ordered H-type aggregates and disordered J-type aggregates. We can also extract the exciton diffusion lengths using the unique knowledge psTRAB gives on the number of independent chromophores present.

Our approach exploits the ability of modern time-correlated single-photon counting (TCSPC) hardware to record the absolute arrival time of a photon on each detector, both with respect to the
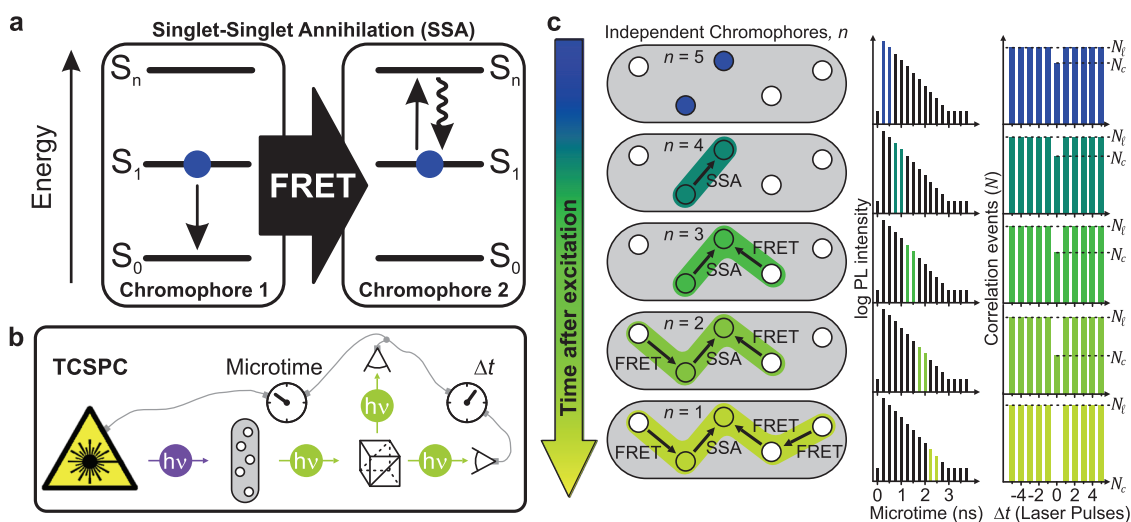
Fig. 1 Picosecond time-resolved antibunching (psTRAB). a Singlet–singlet annihilation (SSA) of a singlet exciton, S_1, on chromophore 1 by Förster resonance energy transfer (FRET) to an exciton on chromophore 2, which excites it into a higher excited state, S_n. Subsequently, chromophore 2 relaxes by internal conversion into its first excited state, S_1. Thus, the exciton (blue dot) on chromophore 1 is annihilated. **b** Principle of time-correlated single-photon counting (TCSPC) combined with a Hanbury Brown and Twiss photon correlator. A pulsed laser (purple) excites a multichromophoric nanoparticle (mcNP) (grey area). The statistics of the PL photon stream (green) are analysed by cross-correlating the signal of two photon detectors. TCSPC yields the time difference between excitation and emission events, i.e. the "microtime", and the time difference between consecutive emitted photons, Δt, as determined by the repetition period of the pulsed laser. **c** On the left, five chromophores (discs) in an mcNP are shown schematically with two singlet excitons (coloured discs), which after excitation can diffuse by site-to-site hopping, i.e. by homo-FRET and annihilate by SSA as a function of the excited-state lifetime. The overall PL decay, constructed from the microtimes, is shown in the centre, with the corresponding binned arrival time windows of photons used to construct the antibunching histograms stated in the right-hand column. The ratio, N_c/N_ℓ, of the number of correlation events in the central peak at $\Delta t = 0$, N_c, versus those in the lateral time-lagged peaks, N_ℓ, allows us to determine the number of independent chromophores, n. As excitons diffuse through homo-FRET and annihilate through SSA, n drops with time.

start of the experiment, but also with respect to the last laser pulse (denoted as the microtime) as shown in Fig. 1b. As an example, consider a nanoparticle with five physical chromophores as depicted by the white discs in Fig. 1c. Absorption of a short pulse of light will create a Frenkel exciton (blue disc). The exciton can hop from one chromophore to another, e.g. by homo-FRET[24,25], in a process referred to as exciton diffusion[26]. Now, if we consider the case where two excitons are created by the same excitation pulse, this hopping allows the excitons to move so that they become adjacent to each other and can annihilate by SSA[19,20]. This process has a strong distance dependence due to the underlying FRET mechanism by which SSA occurs and is often hard to study in a quantitative manner[27]. By inspecting individual mcNPs on a confocal microscope with two single-photon detectors (Fig. 1b) combined with TCSPC we measure the correlation events, N, dependent on the difference in photon arrival times, Δt, between photon events. We are thereby sensitive to the presence of two excitons in the mcNP. A histogram of Δt delay times in integer units of the excitation-pulse period T shows the number of photon detection coincidences from either one excitation pulse or from two separate excitation pulses (Fig. 1c, right column). The ratio of the magnitude of the central peak at $\Delta t = 0$ to that of the lateral peaks, N_c/N_ℓ, provides a measure for the number of independent chromophores, n, provided that the background can be accounted for (see Supplementary Eq. 1 for details on the background correction) according to[16]

$$n = 1 / \left(1 - \frac{N_c}{N_\ell} \right) \qquad (1)$$

By analysing the statistics of the PL photons detected at different time intervals after photoexcitation (panel c, second column), we can construct corresponding picosecond-resolved histograms of the photon statistics and thus measure how many independently emitting chromophores exist on a particular timescale. This is illustrated schematically in Fig. 1c for a 5-chromophore mcNP. The left column depicts the evolution of randomized typical examples of such independent chromophores after a single laser excitation event, whereas the histograms in the middle and right columns are an accumulation of multiple excitation cycles to show the time-averaged result. At early times after excitation (panel c, first row), the two excitons contributing to N_c events (blue discs) have had no time to interact or move via homo-FRET to neighbouring chromophores. From the photon coincidence histogram (right panel) we obtain a value of $n = 5$ with Eq. (1). At a later time (panel c, second row), an exciton on a neighbouring physical chromophore may have, for example, interacted through SSA, and consequently excitation of such chromophores thus does not contribute to N_c anymore, and we obtain $n = 4$ independent chromophores accordingly. These diffusion/SSA processes continue as a function of time, reducing the number of independent chromophores that could support the second exciton. Ultimately, at late times after the excitation pulse, only single photons can be detected because excitons on any other physical chromophore would have had enough time to diffuse and annihilate, yielding $N_c = 0$ and $n = 1$ (panel c, last row). This evolution of the photon statistics and the corresponding number of independent chromophores with time gives us a metric for the effective rate of exciton decay and provides direct microscopic insight into exciton annihilation and diffusion in mcNPs.

Results

Exciton annihilation in DNA origami nanoparticles. To explore the fundamental nature of exciton diffusion and SSA it is desirable to have the best possible control over the number of dye molecules and their spatial position in the mcNP. The dyes need
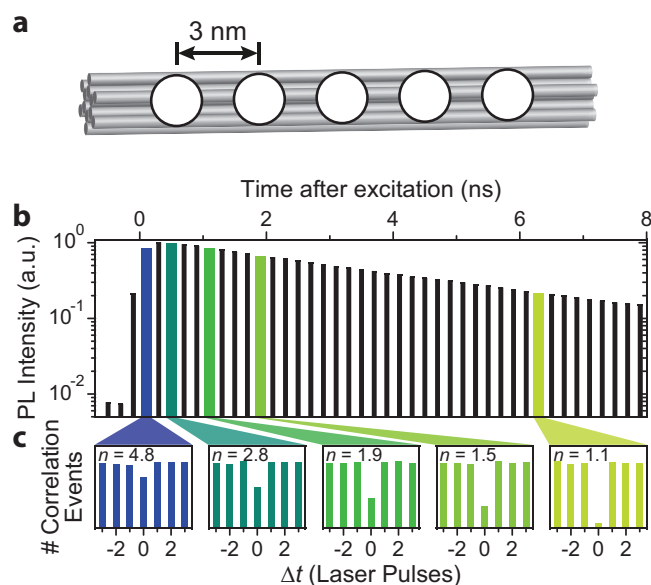
Fig. 2 Tracking exciton diffusion and annihilation in space and time on a well-defined multichromophoric DNA origami structure. a Schematic of a short part of a 225 nm long 12-helix-bundle DNA origami structure with 6 inner and 6 outer helices. Five dyes (white discs) can be positioned at 3 nm spacing from each other. **b** Measured photoluminescence (PL) decay of a single DNA origami structure with five ATTO647N dye molecules. A single-exponential decay is observed with a PL lifetime of ~4.2 ns. Panel **c** shows five corresponding photon statistics histograms for different microtime bins (0–200, 200–400, 800–1000, 1600–1800 and 6400–6600 ps) in terms of the photon correlation events, N, of the two photodetectors. Data were accumulated for 54 single mcNPs. The number of independent chromophores, n, determined from the correlation histogram for each microtime bin is stated above the histograms.

to be within distances to each other corresponding to the range of FRET of ~1–10 nm. We have therefore turned to the method of three-dimensional DNA origami to construct highly defined mcNPs. Similar structures have been used previously to study motor proteins and to characterize super-resolution microscopy techniques[28,29], and are modified here for our needs. The sketch in Fig. 2a shows a short section of a 12-helix bundle with 6 inner and 6 outer helices. The total length of this DNA origami structure is ~225 nm (transmission electron microscopy (TEM) images and structure are shown in Supplementary Figs. 1 and 2). Five labelling positions separated by ~3 nm each are available in the centre of this modular structure.

Based on this 12-helix bundle DNA origami structure, we designed seven different structures with different numbers of dyes and different distances between the dyes (see Supplementary Information for details of DNA origami structures). For the dye we chose ATTO647N, which is highly photostable and bright in the presence of a reducing and oxidizing system (ROXS)[30]. The origami structures were examined on a custom-made confocal fluorescence microscope as described in the "Methods" section (a typical PL transient is shown in Supplementary Fig. 3)[12]. We begin discussing the mcNP with all five dye attachment positions filled with a dye. Figure 2b displays a histogram of photon arrival times, i.e. microtimes, in steps of 200 ps following pulsed excitation with a 636 nm laser. We note that the step size also defines the timing error on the x-axis of the plot. This value of 200 ps was chosen according to the budget of photons available to construct the histograms of photon statistics in Fig. 2c. It is necessary to make a trade-off between the timing resolution of the x-axis and the noise in the photon statistics histograms. This

trade-off depends on the experimental circumstances, i.e. the photon budget which is available. The PL decay is single exponential with a lifetime of 4.2 ns, which is typical for this dye attached to DNA and implies that no strong interchromophoric interactions occur[12].

For this five-dye sample we select 200 ps time windows from the microtime histogram (coloured bars) and calculate the photon statistics for each bin as shown in Fig. 2c. We used the peak of the instrument response function (see Supplementary Fig. 4) to determine zero microtime in the calculations. According to Eq. (1), we estimate the number of independent chromophores, n, in the first 200 ps after excitation to be ~4.8, very close to the expected starting value of 5. Between 200 and 400 ps, n drops to ~2.8 and reaches ~1.1 between 6400 and 6600 ps. The photons emitted by the five-chromophore structure at the latest times show almost complete antibunching. In total, photon events of 54 individual mcNPs were accumulated to obtain enough correlation events for this analysis. Photobleaching and blinking of individual dye molecules during the measurement period will impact the overall photon statistics. For this reason, only the first 5 s of each measurement were evaluated, and only if the overall PL intensity was constant to within 10% over this time. Additionally, while photobleaching and blinking has an influence on the overall strength of photon antibunching, it has no impact on the decay of n with microtime. For example, we indeed obtain the expected starting value of 5 for early microtimes, implying that the measurement is not affected by photobleaching and blinking. The five histograms in Fig. 2c reveal the timescale on which the excitons annihilate with each other to lower the number of independently emitting chromophores from five to one. We note that the fact that the number of chromophores inferred at the earliest times is slightly lower than the expected value of five can be explained by SSA having already occurred during the first 200 ps. One immediate conclusion of this method is that the number of dyes can be measured in an mcNP directly, even if the dyes are not emitting independently. Such knowledge is crucial in quantitative spectroscopic methods[17,31]. A further crucial observation is that, in contrast to ensemble measurements[32], the PL decay retains its monomolecular single-exponential form even though SSA clearly occurs. This is a particularly important observation because the non-exponentiality of ensemble PL decays, i.e., a bimolecular decay, is generally used to extract exciton encounter rates to infer diffusion lengths. In the ensemble, this approach only works at very high excitation fluences which are far from the population densities relevant to devices. However, it is crucial to realize that SSA always occurs, even at the lowest excitation fluences, because exciton diffusion always occurs. Our photon correlation technique is sensitive precisely and only to these rare events of double-chromophore excitation, which can be reached at very low fluences at the cost of extended integration times. The detection of these rare events is ultimately limited by the background photons, e.g. the dark count rate of the photo detectors.

Having established that we can recover the number of dyes in an mcNP with our method, we now apply this approach to different DNA origami structures to examine the dynamics of the SSA mechanism in detail. Figure 3 plots the number of independently emitting chromophores n for each 200 ps time gate versus the corresponding microtime for seven different DNA origami structures. We start with the simplest model system with only one dye (dark grey dots in panel a). Except for the first two data points, these values are constant at $n = 1.02$, which is expected for a single dye. This value is close to unity and only limited by the signal-to-background ratio (SBR) as discussed in Supplementary Fig. 5 and ref. [15]. The fast decay in the first two data points originates from multiple excitations of the dye within

the same laser pulse of ~80 ps width[33]. Now we introduce a second dye at a distance of ~12 nm (panel b, light grey dots), which should be far enough away to prevent SSA between the excitons. Indeed, the data can be described with a constant n of 1.85 ± 0.01, which is slightly below the expected value of two, most likely because of slightly different PL intensities of the two dye molecules at the different binding sites of the DNA origami structure. Crucially, again, no decay of n is observed for this sample, implying a negligible exciton annihilation rate.

Next, we examine the more interesting cases, where we build structures with two dyes sufficiently close to each other such that SSA can occur. The red and orange dots in Fig. 3b display the data measured on structures carrying two dyes at ~3 and ~6 nm spacing. n starts out slightly below the expected value of two for both samples, and a decay during the first 2 ns down to $n = 1.02$ is observed for the 3 nm sample. These datasets are accurately described by a single-exponential model of the number of independently emitting chromophores,

$$n(t) = \{y_0 - [A \cdot \exp(-k_{SSA}\, t)]\}^{-1} \qquad (2)$$

with the offset, y_0, amplitude, A, and the exciton annihilation rate, k_{SSA} (see "Methods" for a derivation of Eq. 2). The overall number of physical dyes present in the structure is then given by $n_{dyes} = (y_0 - A)^{-1}$. In Fig. 3b, we extract $k_{SSA} = 1.72 \pm 0.06$ ns^{-1} for the two dyes separated by 3 nm and $k_{SSA} = 0.06 \pm 0.01$ ns^{-1} for the dyes separated by 6 nm, with $n_{dyes} = 1.8 \pm 0.03$ in both cases. As expected, k_{SSA} drops significantly when doubling the distance between the two dyes, indicating that we are in the important regime where SSA is controlled by FRET and therefore by dye spacing. Subsequently, we placed three dyes separated by ~6 nm each (Fig. 3c, cyan dots). Fitting with Eq. 2 yields $k_{SSA} = 0.06 \pm 0.01$ ns^{-1} and $n_{dyes} = 2.7 \pm 0.1$, which is consistent because we expect no SSA between the left-most and right-most dyes, and the same SSA rate for the neighbouring dyes as in panel b.

Upon moving the three dyes closer to each other, now only separated by 3 nm (Fig. 3c, blue dots), Eq. (2) is no longer sufficient to describe the time evolution of n since next-nearest neighbour interactions arise. We therefore used an analogous biexponential model of SSA, with a fast rate for neighbouring dyes and a slow rate, which combines direct annihilation of next-nearest-neighbouring dyes and exciton hopping with subsequent annihilation of neighbouring dyes, to describe the blue dataset in panel c,

$$n(t) = \{y_0 - [A_1 \exp(-k_{SSA,1} \cdot t) + A_2 \exp(-k_{SSA,2} \cdot t)]\}^{-1} \quad (3)$$

We derive from this dynamics an average amplitude-weighted SSA-rate $\langle k_{SSA} \rangle = (A_1 k_{SSA,1} + A_2 k_{SSA,2})/(A_1 + A_2) = 0.98 \pm 0.09$ ns^{-1} (see Supplementary Information for complete fitting results in Supplementary Table 2) and a number of dyes, $n_{dyes} = (y_0 - (A_1 + A_2))^{-1} = 2.9 \pm 0.1$. Finally, for the DNA origami structure bearing all five dyes (Fig. 3d, violet dots), we extract $\langle k_{SSA} \rangle = 0.72 \pm 0.07$ ns^{-1} and $n_{dyes} = 4.7 \pm 0.2$ by using Eq. (3).

The crucial observation is that at long microtimes, n decays to 1 for all samples with $k_{SSA} > 0$. This is particularly intriguing for the five-dye sample, where we would anticipate the case in which two excitons remain on the left-most and right-most dyes. According to the experiment with two dyes placed 12 nm apart (panel a, light grey dots), no direct SSA should occur in this case. However, the fact that the five-dye sample still decreases down to only one emitting independent chromophore, rather than two, allows us to conclude that exciton hopping, i.e. exciton diffusion, occurs between the five dyes. We note that all measurements of the DNA origami samples were conducted in buffered solution
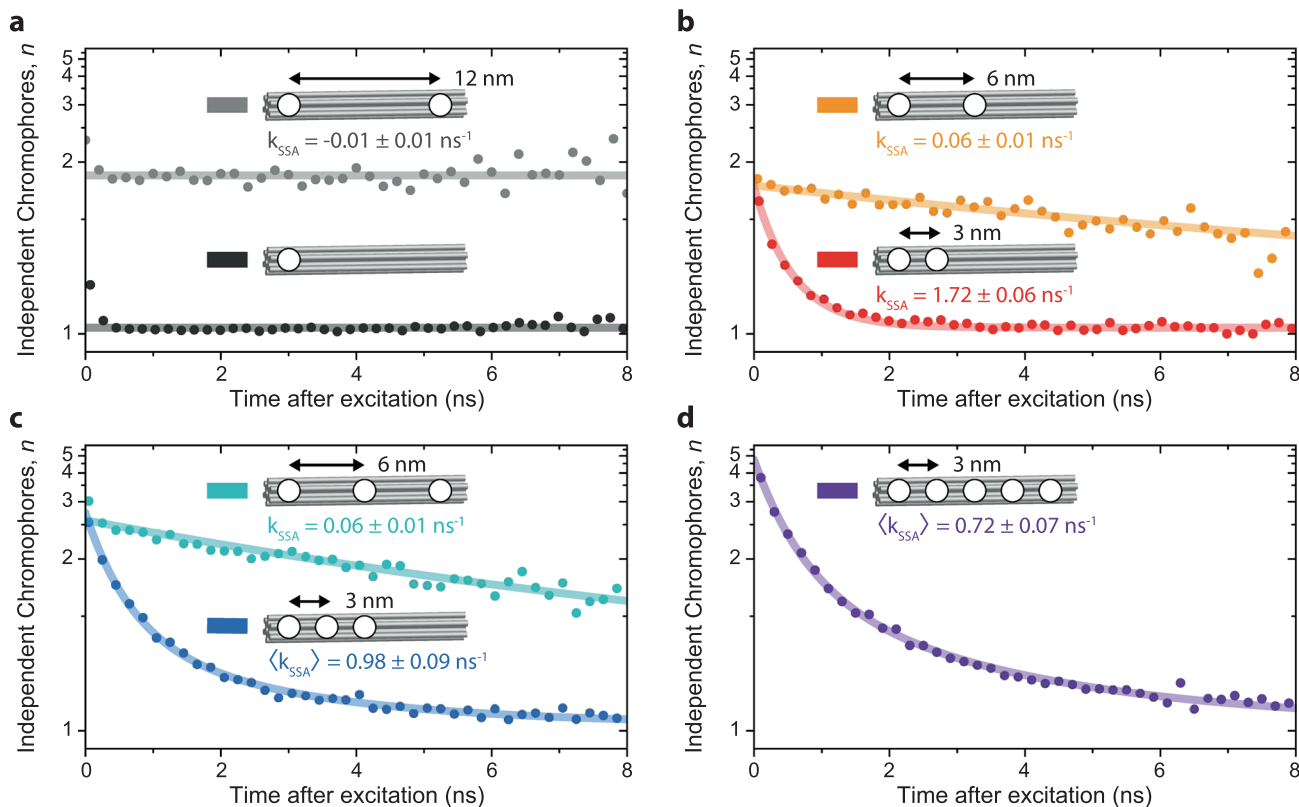
Fig. 3 Exciton annihilation in multiple well-defined mcNPs. Evolution of the number of independently emitting chromophores, n, as a function of the time after excitation for seven different structures. The structures have different numbers of dyes attached with different spacings between them. The y-axes are reciprocal for better comparison between the graphs. **a** One dye (dark grey) and two dyes separated by 12 nm (light grey). **b** Two dyes separated by 3 nm (red) and 6 nm (orange). The curves superimposed are described by a monoexponential model of exciton annihilation (Eq. (2)). **c** Three dyes separated by 6 nm (cyan) and 3 nm (blue). The cyan curve is described by Eq. (2), but the blue points follow a biexponential decay with an average rate k_{SSA} (Eq. (3)). **d** Five dyes separated by 3 nm. The curve is described by the biexponential decay of Eq. (3). Between 54 and 98 single mcNPs were measured individually, and the photon statistics of each measurement accumulated to obtain each curve. All measurements were performed under oxygen removal and with a reducing and oxidizing system (ROXS) present to ensure photostabilization[30]. Each particle was measured for only 5 s so that photobleaching and spectral shifts were negligible.

and consequently, the dyes were free to rotate on the DNA origami. We therefore neglect the possibility of a particular preferred orientation of the transition-dipole moments arising. However, this approximation is no longer valid for mcNPs, which are fixed in space, e.g., set inside a solid matrix. Here, the transition-dipole moment orientation can have a significant impact on the SSA rate, i.e., the morphology plays a crucial role on the dynamics of psTRAB. This conclusion offers a motivation to study morphologically different mcNPs in which significant exciton diffusion arises.

Exciton diffusion in conjugated polymer aggregates. To examine exciton diffusion in conjugated polymers in the meso-scopic size regime, aggregates of chains were grown with distinct electronic and structural properties. These structures are formed by two poly(para-phenylene-ethynylene-butadiynylene) (PPEB)-based conjugated polymers (Fig. 4a). With a small variation of the alkyl side-chains, ordered aggregates with either H-type inter-chromophoric coupling (PPEB-1, lilac) or disordered aggregates with J-type intrachromophoric coupling (PPEB-2, brown) can be grown by solvent vapour annealing[18]. Samples were prepared as described in ref.18, yielding individual small aggregates isolated in poly(methylmethacrylate) (PMMA) and measured on a confocal fluorescence microscope as reviewed briefly in the "Methods" section and described elsewhere[34]. 631 single aggregates of PPEB-

1, each comprising on average approximately 54 chains, and 705 aggregates of PPEB-2 (each ~9 chains, see Supplementary Figs. 6 and 7 and discussion thereof in the Supplementary Information), were grown and measured individually. Only the first 5 s of each PL trace were evaluated (see Supplementary Fig. 8 for examples of PL traces of the H- and J-type aggregates), provided that the PL intensity was constant to within 10%. Following the above procedure, $n(t)$ was determined using psTRAB as shown in Fig. 4b (Supplementary Fig. 10 shows the corresponding photon anti-bunching histograms). We use different widths of time-windows to generate the evolution of $n(t)$, with 3 ps chosen at early times, increasing to 80 ps (in the H-type aggregates) and 160 ps (in the J-type aggregates) at later times. We observe a clear decay of n with time, signifying excited-state interactions primarily due to SSA. We note that this measurement is independent of the excitation intensity in this region of excitation densities as discussed in Supplementary Fig. 9. A substantial difference between the decay dynamics exists for the two aggregates. For the H-type aggregates, n drops rapidly over the first 250 ps and then continues before levelling off at ~2000 ps. The J-type aggregates show a smaller initial fast drop, followed by a slower linear decay before levelling off at a slightly higher value of n at times >2000 ps.

First, we note that, in analogy to the DNA origami model system in Fig. 3d, the decay of n with time constitutes a signature of exciton annihilation mediated by exciton diffusion. Because diffusion is now likely to dominate, however, the dynamics
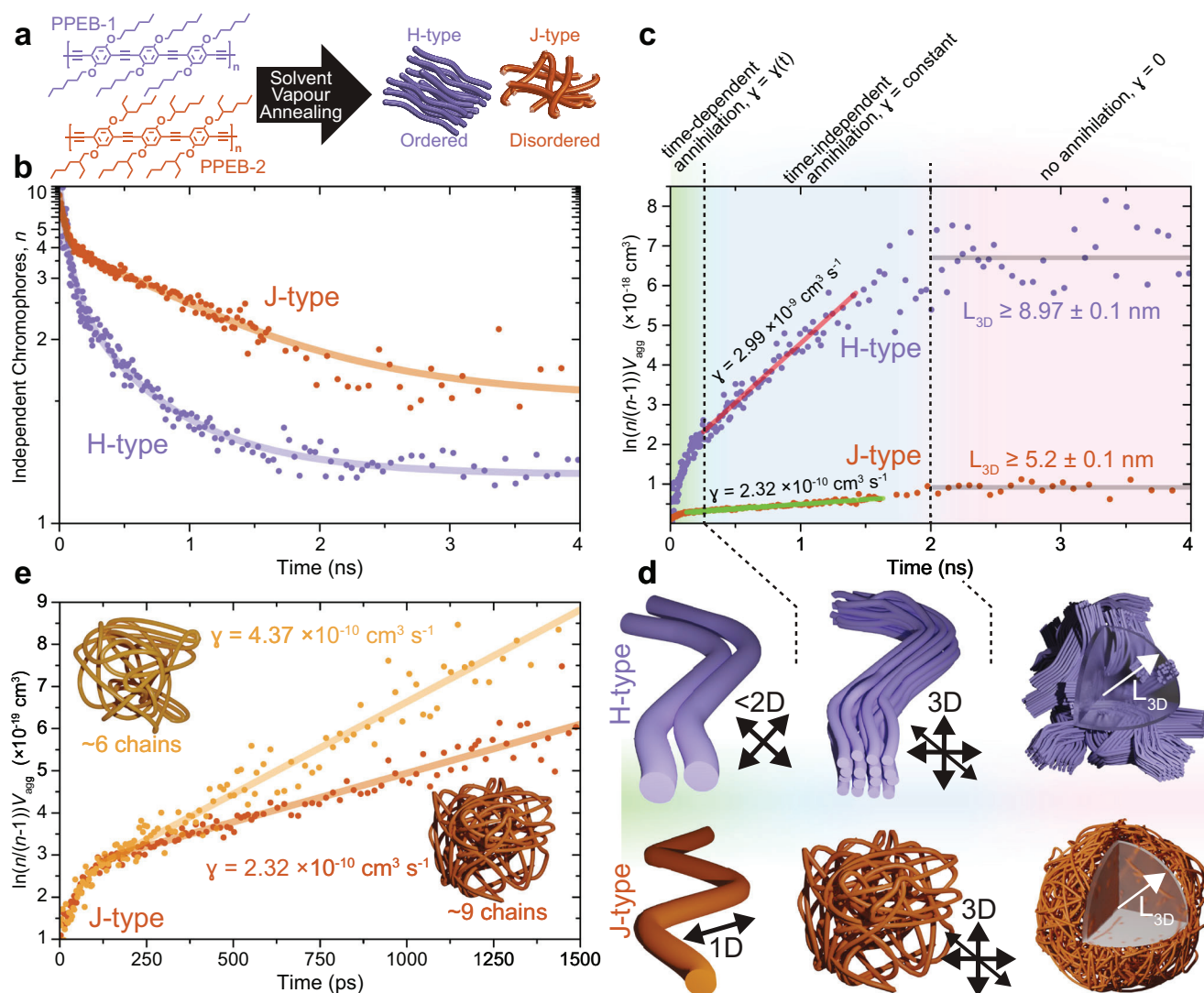
Fig. 4 Following exciton diffusion dynamics in isolated conjugated polymer aggregates. a PPEB polymers that are grown into H-type (PPEB-1, lilac) or J-type (PPEB-2, brown) aggregates by solvent vapour annealing. **b** Temporal evolution of the number of independent chromophores in the aggregate, determined by psTRAB, for the H-type and J-type aggregates. A significant difference in the dynamics is observed, with lines being guides to the eye. **c** Plotting of the time-dependent quantity $\ln\left(\frac{n}{n-1}\right) \cdot V_{agg}$ for the H- and J-type aggregates. The gradients of the curves correspond to the exciton annihilation rate, γ, of diffusion-controlled annihilation. Three regions of the dynamics are identified: at early time (0–250 ps), γ is time-dependent; at intermediate times (250–2,000 ps) γ is constant and tenfold higher in the H- compared to the J-type aggregate; and at late times (> 2000 ps) γ is zero. These regions are interpreted in **d**, indicating that early-time diffusion is one- or less than two-dimensional and intermediate time diffusion is three-dimensional; at late times annihilation ceases because the exciton density is too low. The latter range provides a lower limit of the three-dimensional diffusion length, L_{3D}. In **e** the nine-chain J-type aggregate shown in panel **c** (brown) is compared with a smaller six-chain J-type aggregate (orange). The gradient (γ) is a factor of two smaller in the larger aggregate, indicating that three-dimensional diffusivity is reduced when more chains are present. This reduction is consistent with reduced ordering of the chains as the aggregate size grows, and thus reduced interchain coupling. The six-chain dataset is made up of 260 individually measured single aggregates.

generally cannot be fitted with one fixed k_{SSA} rate. Instead, the annihilation is governed by a rate equation for a second-order reaction[35]. The clear difference between the H- and J-type aggregates indicates that the process of exciton diffusion is not the same in both of them. To examine this difference in a quantifiable manner, we plot the evolution with time of the quantity $\ln\left(\frac{n}{n-1}\right) \cdot V_{agg}$ as shown in Fig. 4c, where V_{agg} is the calculated aggregate volume (see "Methods" for a full description of this equation and Supplementary Information for how the volumes were obtained). This allows us to quantify and compare exciton diffusion, as data plotted in this manner allows the instantaneous rate of bimolecular exciton annihilation, γ, to be determined from the slope and compared against ensemble equivalents. A linear

function signifies a constant, time-independent γ, whereas curvature implies that γ has a time-dependence. Typically, in exciton annihilation measurements, the underlying excited-state decay has to be accounted for[36], complicating analysis in extracting diffusion relevant properties. The advantage of psTRAB is that we directly obtain a measure of the exciton diffusion and are thus uniquely sensitive to weak and slow diffusion. This contrasts with conventional ensemble measurements of the non-exponential decay in PL intensity, which require high exciton densities to see an appreciable effect of annihilation. It is important also to stress that psTRAB offers a unique way to observe the very rare circumstances where two excitons exist in a nanoscale object, and consequently to see how

the probability of them coexisting changes on the picosecond to nanosecond timescale as diffusion-assisted exciton annihilation occurs. The equivalent ensemble measurements of SSA require appreciable, i.e. measurable, fractions of excitons to annihilate with each other to be distinct from exciton luminescence where no annihilation has occurred. Consequently, as noted, psTRAB allows measurements of weaker and slower processes to be made than would otherwise be possible, with the measured photon coincidences in the PPEB H-aggregates typically ~300 parts per million, well below the overall luminescence signal's shot noise limit. With the data plotted as $\ln\left(\frac{n}{n-1}\right) \cdot V_{\text{agg}}$ as in Fig. 4c, for both H- and J-type aggregates three regions are identified. At early times (<250 ps) non-linear behaviour is observed, indicating that γ is time-dependent. Exciton diffusion is therefore one- or less than two-dimensional[37]. At times 250–2000 ps, both aggregate types show linear behaviour, thus γ is time-independent and the diffusion three-dimensional[38,39], with values of γ found to be in the range of 10^{-9} to 10^{-10} cm^3 s^{-1}, in good agreement with typical conjugated polymers[32,39–41]. Finally, at times >2000 ps, $\gamma = 0$, i.e. annihilation has ceased as the exciton density is too low to support continued interactions.

The psTRAB results also allow insight into the nanoscale organization of material in the aggregates, as sketched in Fig. 4d. At early times, the time-dependent γ indicates that exciton motion is one- or less than two-dimensional, most likely in the dispersive regime, and is therefore consistent with ensemble observations of annihilation on the timescale of a few picoseconds[42]. In the context of the H-type aggregate, this motion will be along the chains and across the interchain π-stack. This conclusion is in agreement with a high degree of chain alignment, evidenced by the PL intensity modulation depths determined when rotating the polarization of the exciting laser[18]. The J-type aggregate also shows time-dependent annihilation at early times. Here, however, simple one-dimensional motion will be favoured since strong intrachain coupling is dominant as evidenced by the J-type emission characteristics[18]. At later times, the time-independence of γ indicates that exciton motion is three-dimensional in both aggregate types. γ is an order of magnitude lower in this time region for the J- than for the H-type. This difference relates to the nature of chromophoric coupling and disorder in the aggregates. In H-type aggregates, chains with the smallest degree of disorder will show the strongest interchain electronic coupling, facilitating efficient three-dimensional diffusion. In J-type aggregates, in contrast, which do not show a high polarization anisotropy[18], chains are relatively disordered. Poor chain alignment will lead to weak interchain electronic coupling and a lower value of γ. Exciton diffusion is then limited by the random chain alignment that excitons encounter when diffusing. The impact of chain disorder on exciton diffusion can also be examined by comparing the psTRAB of the 9-chain J-type aggregate with a smaller one that comprises of ~6 chains shown in Fig. 4e. In the region where γ is time-independent and three-dimensional diffusion dominates, γ is almost a factor of two higher in the 6-chain aggregate, indicating increased order in the smaller aggregate which facilitates effective interchain site-to-site hopping. We also note that at early times (0–125 ps), in the J-type aggregates a significantly stronger time-dependent gradient of the psTRAB functionality is observed, consistent with fast one-dimensional exciton motion along the chain. We are cautious with regard to over-interpreting these data, however, since such exciton motion is likely to be much faster than the time resolution of our experiment. Indeed, we would expect the one-dimensional exciton motion along the chain in strongly coupled J-type aggregates to be higher than the two-dimensional diffusion along-chain and across π-stacks in H-aggregates, where intrachain coupling can be weaker[43,44].

Finally, at late times where $\gamma \to 0$, we enter the regime where the exciton density is too low to support continued annihilation. These conditions can be used to obtain a lower limit on the exciton diffusion length, L_{3D}. The rationale for this approach is simple: we know the volume of the aggregate and the number of independent chromophores that the aggregate can support when we can no longer measure annihilation occurring, i.e. when excitons no longer interact with each other. Division yields the volume that a single independent chromophore occupies, equivalent to the volume explored by an exciton. If diffusion is presumed to arise in a spherical volume in three dimensions, a diffusion length, L_{3D}, can be determined. The value will be a lower limit as the length is technically defined as the distance excitons diffuse in their lifetime rather than once the exciton density is too low to support continued interactions, but the difference between these two definitions will be small at these late times. We find lower limits of $L_{3D} \approx 9$ nm for the H-type aggregate and $L_{3D} \approx 5.2$ nm for the J-type aggregate, consistent with typical literature values for conjugated polymers[26,36,39,45]. The unique advantage of our chromophore-counting method is that the calculation of these values contains no presumptions other than the mass density of the aggregate. L_{3D} is derived from simple observables and is only possible because we consider single objects at the discretised level of excitons and the resulting photon correlation.

Discussion

Knowledge of the nanoscale organization of a material, the electronic coupling between chromophores, and energy transfer pathways is important in a wide variety of systems. In this work we have introduced a powerful method to quantify exciton–exciton annihilation and exciton diffusion in multi-chromophoric mesoscopic objects. This is achieved by resolving the fluorescence photon statistics on a picosecond timescale. Using deterministic DNA origami structures, we position dyes at specific distances from each other and obtain direct measurements of the rate of annihilation between two excitons and the true number of dyes. This accuracy is a direct consequence of utilizing two-detector coincidences that are sensitive to two-photon emission events. Our method can measure the annihilation rate γ in well-defined structures and directly yields the number of physical dyes present in each sample. We stress that such chromophore counting is not possible with standard time-integrated photon-correlation measurements. The technique can be expanded to look at nanoparticles grown from multiple single conjugated-polymer chains. In these polymer aggregates, SSA is governed mainly by exciton diffusion instead of fixed distance FRET-based annihilation between chromophores. In addition, the method offers facile differentiation between J- and H-type aggregates, determining valuable material properties such as the exciton diffusion length, the dimensionality of diffusion and the degree of nanoscale disorder in the aggregate. The psTRAB technique therefore offers valuable opportunities to explore the nanoscale organization and excitonic coupling of chromophores in light-emitting materials with unprecedented detail.

Methods

Photon correlation, data analysis, and derivation of Eq. (2). The psTRAB is computed from raw time-stamped TCSPC data using MATLAB. The scripts developed operate similarly to conventional calculations of cross-correlations[46]. The following parameters are stored for each photon event: (i) the "macrotime" at which the photon arrived, i.e. the integer multiple of the corresponding excitation laser repetition period T; (ii) the "microtime", t, which corresponds to the time the photon was detected after the excitation pulse excited the NP; and (iii) the detection channel, i.e. the photon counter A or B. The events are cross-correlated with respect to their macrotimes, after which the microtimes are evaluated as follows: (i) we store the shorter microtime, t, of each correlation event (e.g. the

microtime of channel A) and neglect the longer microtime, $t + \Delta t$. (ii) For selected microtime intervals, histograms of correlation events are constructed as a function of the macrotime delay between the channels. Finally, the scripts sum over multiple measurements of individual aggregates to produce an overall psTRAB result. As detailed in the Supplementary Information, we rationalize the number of correlation events, $N_c(t, t + \Delta t)$, for a given delay time $\Delta t < T - t$ between two photon events arising from the same excitation pulse, as follows:

$$N_c(t, t + \Delta t) = N_{exc} \cdot P(t) \cdot P'(t + \Delta t) \quad (4)$$

Here, N_{exc} is the total number of observed laser excitation pulses, $P(t)$ is the probability of detecting the first photon at microtime t and $P'(t + \Delta t)$ is the probability of detecting the second photon at microtime $t + \Delta t < T$. In case the exciton annihilation is determined by a single exponential decay rate k_{SSA}, these probabilities are calculated as

$$P(t) = n_{dyes} p_0 e^{-(k_r + k_{nr} + k_{ET})t} \quad (5)$$

$$P'(t + \Delta t) = (n_{dyes} - 1) p_0 e^{-(k_r + k_{nr} + k_{ET})t} e^{-(k_r + k_{nr})\Delta t}, \quad (6)$$

where n_{dyes} is the number of chromophores, p_0 summarizes the probability of the chromophore being excited by the laser pulse and the probability of detecting the emitted photon, k_r and k_{nr} are the radiative and non-radiative decay rates and $k_{ET} = k_{SSA}/2$ is the energy-transfer rate between two excited chromophores. Note that in general $P'(t) \neq P(t)$ since the exciton emitting the first photon at time t can reside on any one of the n_{dyes} chromophores, while the exciton emitting the second photon resides on one of the $(n_{dyes} - 1)$ remaining chromophores. At microtime delays $0 < \Delta t < T - t$, the number of excitons does not decay any further through energy transfer, since only a single exciton is left. The number of correlation events $N_\ell(t, t + \Delta t)$, where the second photon is detected at non-zero macrotime delays and thus arises due to a separate laser excitation event, is instead calculated from

$$N_\ell(t, t + \Delta t) = N_{exc} \cdot P''(t) \cdot P''(t + \Delta t), \quad (7)$$

where

$$P'' = n_{dyes} p_0 e^{-(k_r + k_{nr})t} \quad (8)$$

is independent of energy transfer, since only single excitons are present after each laser excitation. The ratio N_c/N_ℓ of central to lateral correlation events is thus directly connected to the number of chromophores in the mcNP and the time dynamics of the annihilation process as

$$\frac{N_c}{N_\ell} = \frac{n_{dyes}(n_{dyes} - 1)}{n_{dyes}^2} e^{-k_{SSA}t} = \frac{n_{dyes} - 1}{n_{dyes}} e^{-k_{SSA}t} \quad (9)$$

The result is independent of k_{nr} implying that additional quenching processes due to singlet–triplet annihilation or the interaction of singlet excitons with dark states such as charge-separated states do not impact the ratio N_c/N_ℓ. Note that the result is independent of Δt and it can also be calculated from the time-integrated number of correlations

$$N_c(t) = \int_0^{T-t} N_c(t, t + \Delta t)d(\Delta t), \; N_\ell(t) = \int_0^{T-t} N_\ell(t, t + \Delta t)d(\Delta t) \quad (10)$$

which significantly reduces the noise associated with experimental event data.

Comparing the derived expression for N_c/N_ℓ with Eq. (1) defining the number of independent chromophores n, we obtain

$$n(t) = \left(1 - \frac{n_{dyes} - 1}{n_{dyes}} \exp(-k_{SSA}t)\right)^{-1}. \quad (11)$$

Equation (11) corresponds to Eq. (2) with $y_0 = 1$ and $A = 1 - n_{dyes}^{-1}$. A quantum-statistical description of photon correlations in an n-chromophore system, using a master equation approach, is given in the Supplementary Information together with Supplementary Figs. 11–13. Note that the assumption of any specific decay law for singlet–singlet annihilation such as an exponential decay according to $e^{-k_{SSA}t}$ is not strictly necessary. To that end, psTRAB N_c/N_ℓ can be used to directly measure the decay law associated with exciton–exciton interactions, which is connected to the mean first passage time of the random walk performed by the excitons. The technique can obviously be extended to higher-order photon correlations, using more than one beam splitter in the Hanbury Brown and Twiss setup, to determine the functional difference between two-exciton interactions and higher-order contributions.

DNA origami microscopy. A custom-made confocal microscope based on an Olympus IX-71 inverted microscope was used. Multichromophoric DNA-origami structures (see Supplementary Information for details on DNA–origami structures and a complete list of all primers used in Supplementary Table 4) were excited by a pulsed laser (636 nm, ~80 ps full-width half-maximum, 80 MHz, LDH-D-C-640; PicoQuant GmbH) operated at 40 MHz repetition rate. Circularly polarized light was obtained by a linear polarizer (LPVISE100-A, Thorlabs GmbH) and a quarter-wave plate (AQWP05M-600, Thorlabs GmbH). The light was focused onto the sample by an oil-immersion objective (UPLSAPO100XO, NA 1.40, Olympus Deutschland GmbH). The sample was moved by a piezo stage (P-517.3CD, Physik

Instrumente (PI) GmbH & Co. KG) controlled by a piezo controller (E-727.3CDA, Physik Instrumente (PI) GmbH & Co. KG). The emission was separated from the excitation beam by a dichroic beam splitter (zt532/640rpc, Chroma) and focused onto a 50-µm pinhole (Thorlabs GmbH). The emission light was separated from scattered excitation light by a 647 nm long-pass filter (RazorEdge LP 647, Semrock) and split into two detection channels by a non-polarizing 50:50 beam splitter (CCM1-BS013/M, Thorlabs GmbH). In each detection channel, afterglow of the avalanche photodiode was blocked by a 750 nm short-pass filter (FES0750, Thorlabs GmbH). Emission was focused onto avalanche photodiodes (SPCM-AQRH-14-TR; Excelitas Technologies GmbH & Co. KG) and signals were registered by a multichannel picosecond event timer (HydraHarp 400, PicoQuant GmbH). The setup was controlled by a commercial software package (SymPhoTime64, Picoquant GmbH).

PPEB aggregate microscopy. Single polymer aggregates were measured on a custom-designed confocal microscope as described elsewhere[34]. For excitation, the frequency-doubled output of a Ti:Sapphire oscillator (~100 fs, 80 MHz, 810 and 880 nm) (Chameleon, Coherent) was used, centred at 405 nm for PPEB-1 and 440 nm for PPEB-2. Femtosecond excitation was required to ensure that double excitation of the aggregates did not occur, because the excited state lifetime for the J-type coupled PPEB-2 aggregates is significantly shorter than for the DNA-origami dyes[18], preventing the use of conventional picosecond laser diodes. The laser was spatially expanded, spectrally cleaned and coupled into the microscope base (IX71, Olympus Deutschland GmbH), where it filled the backplane of a ×60 1.35 NA objective (UPLSAPO60XO, Olympus Deutschland GmbH). The sample was placed on a piezo stage (P-527.3CL, Physik Instrumente GmbH, Germany), which was scanned to generate microscope images and locate individual aggregates. The PL was detected using two single-photon detectors (PD-25-CTE, Micro Photon Devices S.r.l., Italy) connected to a multichannel picosecond event timer (HydraHarp 400, PicoQuant GmbH, Germany) allowing TCSPC and cross-correlations to be performed. The piezo stage and photon counting hardware were controlled using a customized code in LabVIEW (National Instruments).

Exciton diffusion in PPEB aggregates. Bulk exciton–exciton annihilation by SSA is conventionally described by a simple second-order reaction equation, $\frac{d}{dt}\rho_{exc} = -\gamma(t)\rho_{exc}^2$, where ρ_{exc} is the exciton density and $\gamma(t)$ is the diffusion-controlled annihilation rate. In the context of our psTRAB method, differentiation of Eq. (11) ultimately leads to

$$\frac{d}{dt}n = -k_{SSA} \cdot n(n-1). \quad (12)$$

for the number of independent chromophores. This function is the correct form of the second-order reaction equation in cases where the number of reactants is low, since the reaction rate of change is proportional to the number of pairs that can be chosen. The psTRAB measurements thus resolves SSA on the single-nanoparticle level in a form that can be thought of qualitatively as tracking the mutual annihilation of independent chromophores by bimolecular interaction. From Eq. (12), we derive the following linear form governing the exciton annihilation rate $\gamma = k_{SSA} V_{agg}$, where V_{agg} is the aggregate volume:

$$-V_{agg} \cdot \ln\left(\frac{n-1}{n}\right) = \gamma \cdot t - V_{agg} \cdot \ln\left(\frac{n_0 - 1}{n_0}\right). \quad (13)$$

See the Supplementary Information for details on how V_{agg} is obtained by simply invoking knowledge of the mass and mass density of the polymer chain and the number of chains in the aggregate. Thus, plotting $\ln\left(\frac{n}{n-1}\right) \cdot V_{agg}$ as a function of t as in Fig. 4c, e allows γ to be determined from the gradient by straightline fitting.

Data availability
All relevant data are available from the authors.

Code availability
All relevant codes to analyse the data are available from the authors

References
1. Hollars, C. W., Lane, S. M. & Huser, T. Controlled non-classical photon emission from single conjugated polymer molecules. *Chem. Phys. Lett.* **370**, 393–398 (2003).
2. Stangl, T. et al. Mesoscopic quantum emitters from deterministic aggregates of conjugated polymers. *Proc. Natl Acad. Sci. USA* **112**, E5560–E5566 (2015).

3. Utzat, H. et al. Probing linewidths and biexciton quantum yields of single cesium lead halide nanocrystals in solution. *Nano Lett.* **17**, 6838–6846 (2017).

4. Nair, G., Zhao, J. & Bawendi, M. G. Biexciton quantum yield of single semiconductor nanocrystals from photon statistics. *Nano Lett.* **11**, 1136–1140 (2011).

5. Sun, C. et al. Biexciton binding of Dirac fermions confined in colloidal graphene quantum dots. *Nano Lett.* **15**, 5472–5476 (2015).

6. Mangum, B. D., Ghosh, Y., Hollingsworth, J. A. & Htoon, H. Disentangling the effects of clustering and multi-exciton emission in second-order photon correlation experiments. *Opt. Express* **21**, 7419–7426 (2013).

7. Trofymchuk, K. et al. Giant light-harvesting nanoantenna for single-molecule detection in ambient light. *Nat. Photon.* **11**, 657–663 (2017).

8. Wientjes, E., Renger, J., Curto, A. G., Cogdell, R. & van Hulst, N. F. Strong antenna-enhanced fluorescence of a single light-harvesting complex shows photon antibunching. *Nat. Commun.* **5**, 4236 (2014).

9. Tinnefeld, P. et al. Antibunching in the emission of a single tetrachromophoric dendritic system. *J. Am. Chem. Soc.* **124**, 14310–14311 (2002).

10. Fisher, B., Caruge, J. M., Zehnder, D. & Bawendi, M. Room-temperature ordered photon emission from multiexciton states in single CdSe core-shell nanocrystals. *Phys. Rev. Lett.* **94**, 087403 (2005).

11. Steiner, F., Vogelsang, J. & Lupton, J. M. Singlet-triplet annihilation limits exciton yield in poly(3-hexylthiophene). *Phys. Rev. Lett.* **112**, 137402 (2014).

12. Schröder, T., Scheible, M. B., Steiner, F., Vogelsang, J. & Tinnefeld, P. Interchromophoric interactions determine the maximum brightness density in DNA origami structures. *Nano Lett.* **19**, 1275–1281 (2019).

13. Hedley, G. J., Ruseckas, A. & Samuel, I. D. W. Light harvesting for organic photovoltaics. *Chem. Rev.* **117**, 796–837 (2017).

14. Tinnefeld, P. et al. Higher-excited-state photophysical pathways in multichromophoric systems revealed by single-molecule fluorescence spectroscopy. *ChemPhysChem* **5**, 1786–1790 (2004).

15. Weston, K. D. et al. Measuring the number of independent emitters in single-molecule fluorescence images and trajectories using coincident photons. *Anal. Chem.* **74**, 5342–5349 (2002).

16. Ta, H., Wolfrum, J. & Herten, D. P. An extended scheme for counting fluorescent molecules by photon-antibunching. *Laser Phys.* **20**, 119–124 (2010).

17. Grußmayer, K. S. & Herten, D. P. Time-resolved molecule counting by photon statistics across the visible spectrum. *Phys. Chem. Chem. Phys.* **19**, 8962–8969 (2017).

18. Eder, T. et al. Switching between H- and J-type electronic coupling in single conjugated polymer aggregates. *Nat. Commun.* **8**, 1641 (2017).

19. Hofkens, J. et al. Revealing competitive Forster-type resonance energy-transfer pathways in single bichromophoric molecules. *Proc. Natl Acad. Sci. USA* **100**, 13146–13151 (2003).

20. Hübner, C. G. et al. Photon antibunching and collective effects in the fluorescence of single bichromophoric molecules. *Phys. Rev. Lett.* **91**, 093903 (2003).

21. Fuckel, B., Hinze, G., Nolde, F., Müllen, K. & Basché, T. Quantification of the singlet-singlet annihilation times of individual bichromophoric molecules by photon coincidence measurements. *J. Phys. Chem. A* **114**, 7671–7676 (2010).

22. Thiessen, A. et al. Unraveling the chromophoric disorder of poly(3-hexylthiophene). *Proc. Natl Acad. Sci. USA* **110**, E3550–E3556 (2013).

23. Benjamin, E. et al. Temperature dependence of excitonic and biexcitonic decay rates in colloidal nanoplatelets by time-gated photon correlation. *J. Phys. Chem. Lett.* **11**, 6513–6518 (2020).

24. Stangl, T. et al. Temporal switching of homo-FRET pathways in single-chromophore dimer models of pi-conjugated polymers. *J. Am. Chem. Soc.* **135**, 78–81 (2013).

25. Müller, J. G., Lupton, J. M., Feldmann, J., Lemmer, U. & Scherf, U. Ultrafast intramolecular energy transfer in single rigid-rod conjugated polymer chains probed by polarization sensitive single chromophore spectroscopy. *Appl. Phys. Lett.* **84**, 1183 (2004).

26. Lin, J. D. A. et al. Systematic study of exciton diffusion length in organic semiconductors by six experimental methods. *Mater. Horiz.* **1**, 280–285 (2014).

27. Daniel, C. et al. Exciton bimolecular annihilation dynamics in supramolecular nanostructures of conjugated oligomers. *Phys. Rev. B* **68**, 235212 (2003).

28. Derr, N. D. et al. Tug-of-war in motor protein ensembles revealed with a programmable DNA origami scaffold. *Science* **338**, 662–665 (2012).

29. Schmied, J. J. et al. DNA origami-based standards for quantitative fluorescence microscopy. *Nat. Protoc.* **9**, 1367–1391 (2014).

30. Vogelsang, J. et al. A reducing and oxidizing system minimizes photobleaching and blinking of fluorescent dyes. *Angew. Chem. Int. Ed.* **47**, 5465–5469 (2008).

31. Grußmayer, K., Yserentant, K. & Herten, D. P. Photons in–numbers out: perspectives in quantitative fluorescence microscopy for in situ protein counting. *Methods Appl. Fluoresc.* **7**, 012003 (2019).

32. Gulbinas, V. et al. Exciton diffusion and relaxation in methyl-substituted polyparaphenylene polymer films. *J. Chem. Phys.* **127**, 144907 (2007).

33. Schedlbauer, J. et al. Ultrafast single-molecule fluorescence measured by femtosecond double-pulse excitation photon antibunching. *Nano Lett.* **20**, 1074–1079 (2020).

34. Hedley, G. J., Steiner, F., Vogelsang, J. & Lupton, J. M. Fluctuations in the emission polarization and spectrum in single chains of a common conjugated polymer for organic photovoltaics. *Small* **14**, 1804312 (2018).

35. Alemany, P. A., Zanette, D. H. & Wio, H. S. Time-dependent reactivity for diffusion-controlled annihilation and coagulation in 2 dimensions. *Phys. Rev. E* **50**, 3646–3655 (1994).

36. Mikhnenko, O. V., Blom, P. W. M. & Thuc-Quyen, N. Exciton diffusion in organic semiconductors. *Energy Environ. Sci.* **8**, 1867–1888 (2015).

37. Gulbinas, V., Chachisvilis, M., Valkunas, L. & Sundstrom, V. Excited state dynamics of phthalocyanine films. *J. Phys. Chem.* **100**, 2213–2219 (1996).

38. Shaw, P. E., Ruseckas, A., Peet, J., Bazan, G. C. & Samuel, I. D. W. Exciton-exciton annihilation in mixed-phase polyfluorene films. *Adv. Funct. Mater.* **20**, 155–161 (2010).

39. Shaw, P. E., Ruseckas, A. & Samuel, I. D. W. Exciton diffusion measurements in poly(3-hexylthiophene). *Adv. Mater.* **20**, 3516–3520 (2008).

40. King, S. M., Dai, D., Rothe, C. & Monkman, A. P. Exciton annihilation in a polyfluorene: low threshold for singlet-singlet annihilation and the absence of singlet-triplet annihilation. *Phys. Rev. B* **76**, 085204 (2007).

41. Masri, Z. et al. Molecular weight dependence of exciton diffusion in poly(3-hexylthiophene). *Adv. Energy Mater.* **3**, 1445–1453 (2013).

42. Maniloff, E. S., Klimov, V. I. & McBranch, D. W. Intensity-dependent relaxation dynamics and the nature of the excited-state species in solid-state conducting polymers. *Phys. Rev. B* **56**, 1876–1881 (1997).

43. Spano, F. C. & Silva, C. in *Annu. Rev. Phys. Chem.* **65**, 477–500 (2014).

44. Eder, T. et al. Interplay between J- and H-type coupling in aggregates of pi-conjugated polymers: a single-molecule perspective. *Angew. Chem. Int. Ed.* **58**, 18898–18902 (2019).

45. Haugeneder, A. et al. Exciton diffusion and dissociation in conjugated polymer fullerene blends and heterostructures. *Phys. Rev. B* **59**, 15346–15351 (1999).

46. Gamari, B. D. et al. Inexpensive electronics and software for photon statistics and correlation spectroscopy. *Am. J. Phys.* **82**, 712–722 (2014).

Acknowledgements

Author contributions

G.J.H., F.S., F.J.H. and J.V. devised the psTRAB methodology and developed the tech-nique. T.S., J.V. and P.T. designed the DNA origami structures. T.S. prepared, measured and analysed the DNA origami structures and data. D.L., K.R. and S.H. designed and synthesized the conjugated polymers. G.J.H., F.S. and T.E. measured and analysed the PPEB aggregate data. S.B. developed the analytic and quantum-statistical treatment of psTRAB. G.J.H., T.S., F.S., S.B., P.T., J.M.L. and J.V. contributed to manuscript writing.

Funding

Competing interests

The authors declare no competing interests.

Additional information

Supplementary information The online version contains supplementary material available at https://doi.org/10.1038/s41467-021-21474-z.

Correspondence and requests for materials should be addressed to G.J.H. or J.V.

Peer review information *Nature Communications* thanks the anonymous reviewer(s) for their contribution to the peer review of this work. Peer reviewer reports are available.

Reprints and permission information is available at http://www.nature.com/reprints

Publisher's note Springer Nature remains neutral with regard to jurisdictional claims in published maps and institutional affiliations.

Supplementary Information for

Picosecond time-resolved photon antibunching measures nanoscale exciton motion and the true number of chromophores

Gordon J. Hedley[1,†,*], Tim Schröder[2, †], Florian Steiner[2], Theresa Eder[3], Felix Hofmann[3], Sebastian Bange[3], Dirk Laux,[4] Sigurd Höger,[4] Philip Tinnefeld[2], John M. Lupton[3] and Jan Vogelsang[3,*]

[1]School of Chemistry, University of Glasgow, University Avenue, Glasgow, G12 8QQ, United Kingdom

[2]Department Chemie and Center for NanoScience (CeNS), Ludwig-Maximilians-Universität München, Butenandtstraße 5-13 Haus E, 81377 München, Germany

[3]Institut für Experimentelle und Angewandte Physik, Universität Regensburg, Universitätsstraße 31, 93053 Regensburg, Germany

[4]Kekulé-Institut für Organische Chemie und Biochemie, Universität Bonn, Gerhard-Domagk-Strasse 1, 53121 Bonn, Germany

Supplementary Methods

1. Details of DNA origami structures and sample preparation

The DNA origami structure[1] was modified using caDNAno (version 0.2.2, design schematics in Supplementary Figure 1). The scaffold is an 8064 nucleotide long ssDNA extracted from M13mp18 bacteriophages. All staple strands were purchased from Eurofins Genomics GmbH as well as the dye labeled oligonucleotides (see at the end of Supplementary Information). The ATTO 542 modified oligonucleotides for external labeling were purchased from biomers.net. Scaffold and oligonucleotides were mixed according to Supplementary Table1 for origami folding. The folding buffer (FB) is a Tris-EDTA buffer (1x TE, 10 mM Tris-HCl, 1 mM EDTA•Na$_2$) with 20 mM MgCl$_2$ and 5 mM NaCl. In the annealing process, the mixture was heated and slowly cooled down with a nonlinear thermal ramp over 16 hours according to reference.[2] After annealing, the excess staples were removed with polyethylene glycol (PEG) precipitation. The samples were mixed with an equal volume of PEG precipitation buffer (1× TAE, 15 % (w/v) PEG-8000, 500 mM NaCl, 12 mM MgCl$_2$) and centrifuged at 16 krcf (thousand relative centrifugal force, i.e. 1000 g) for 30 min at 4 °C. After removing the supernatant, the pellet was suspended in 1× FB. Afterwards, the DNA origami was externally labeled with ATTO 542 modified oligonucleotides. A threefold excess with respect to the extended staples was used and incubated for 20 min in a wet chamber at room temperature. The DNA origami structures were purified via gel electrophoresis. A 1.5 % agarose gel containing a Tris base, acetic acid and EDTA buffer (0.5× TAE, 20 mM Tris-HCl, 10 mM acetic acid, 0.5 mM EDTA) and 12 mM MgCl$_2$ was used at 60 V for 2 hours in a gel box cooled in an ice-water bath. The gel was not stained to avoid staining reagent-dye interactions. On a blue illuminated table DNA origami structures could be seen due to the numerous ATTO 542 dyes. DNA origami structures were recovered from the target band. The samples were stored at -26 °C until further use.

Folding Table

Final concentrations for DNA origami folding are given in Supplementary Table 1. The meaning of the reagents is described below:

Supplementary Table 1: Folding reagents with final concentrations.

Reagent	Final concentration / nM
scaffold	25
core staples	225
biotin staples	250
extended staples	225
dye and refill staples	225

scaffold: Single-stranded viral 8064 nt ssDNA from M13mp18.

core staples: Contains every unmodified staples of the rectangular DNA origami. The wildtype structure is given in reference[1].

biotin staples: Four biotin modified staples. Modifications are placed at the 3' end.

extended staples: 13 staples extended at the 3' end for external labeling. The extended sequence is: 5' TTTTCCTCTACCACCTACATCAC 3'. Sequence for the ATTO542 oligonucleotides: 5' GTGATGTAGGTGGTAGAGGA-ATTO542 3'

dye and refill staples: Oligonucleotides labeled with ATTO 647N at the 5' end. For structures which do not need all five dyes the respective oligonucleotides were substituted with unmodified oligonucleotides.

Confirming successful DNA origami structure assembly with TEM imaging

Successful assembly of the modified DNA origami structure was confirmed with TEM imaging. The origami structures were imaged on Ar-plasma cleaned TEM grids (Formvar/carbon, 400 mesh, Cu, TedPella, Inc., USA). The DNA origami structures were stained with a 2 % uranyl formate solution. The imaging was performed on a JEM-1100 microscope (JEOL GmbH, Japan) with an acceleration voltage of 80 kV.
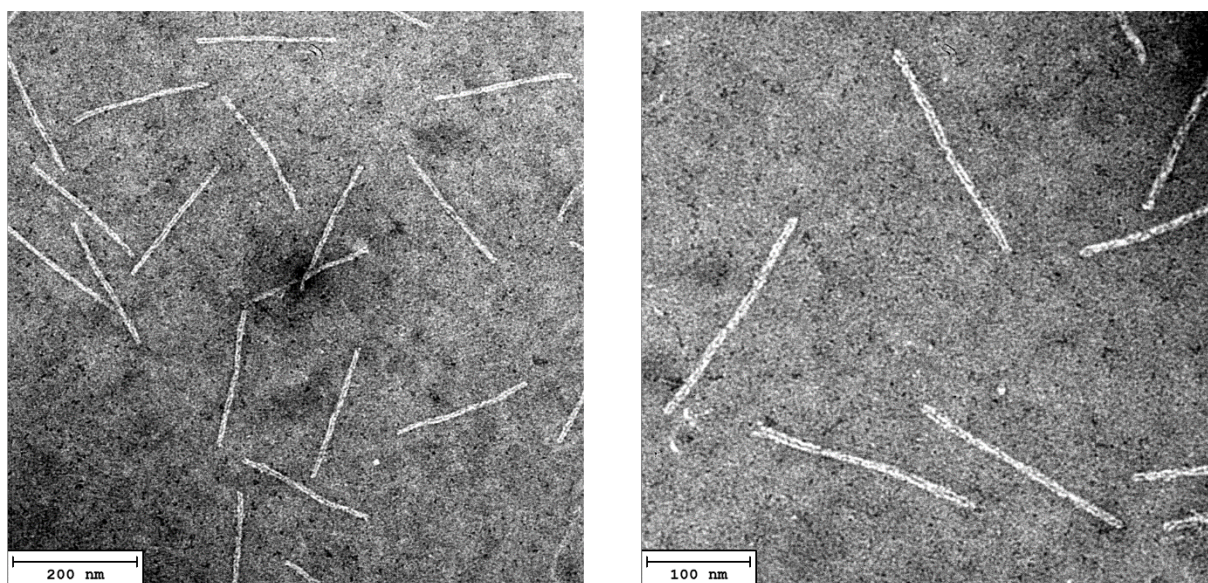
Supplementary Figure 1. Two representative negative stain images of the modified DNA origami structure with different magnifications. The expected length of the DNA origami structure is 225 nm. The TEM images show successful assembly of the DNA origami structures. No nicks were found at the position which was modified for our needs and is located at the center of the structure (orange and blue staples in Supplementary Figure 2).

Surface preparation and immobilization

Samples were measured in LabTek™ chamber slides (Thermo Fisher Scientific Inc.) which were cleaned twice for 20 minutes with 0.1 M hydrofluoric acid (AppliChem GmbH) and washed afterwards three times with ultrapure water. For sample immobilization the glass surface was coated with biotin labeled bovine serum albumin (BSA) (1 mg/mL Sigma-Aldrich Chemie GmbH) and NeutrAvidin (1 mg/mL, Sigma-Aldrich Chemie GmbH). The DNA origami structures (60 pM in 1x FB) were immobilized by the biotin-NeutrAvidin binding.

Sample preparation for single-molecule measurements

Traces were recorded from immobilized DNA origami structures. Photo blinking and photo bleaching was reduced with an oxidizing and reducing buffer system ($1\times$ TAE, 12 mM MgCl$_2$, 2 mM Trolox/Troloxquinone, 1 % (w/v) D-(+)-Glycose) [3] in combination with an oxygen scavenging system [4] (1 mg mL^{-1} glucose oxidase, 0.4 % (v/v) catalase (50 μg mL^{-1}), 30 % glycerol, 12.5 mM KCl in 50 mM TRIS). The oxygen scavenging system was added to the oxidation and reducing buffer at a concentration of 10 % (v/v) in the LabTek^{TM} system. DNA origami structures were excited with a laser power adjusted to 1 μW for all samples, except for the 5-dye sample which was measured with 0.5 μW to reduce spectral shifts and photo bleaching. The laser repetition rate was 40 MHz.

Traces for psTRAB data processing were recorded for 10 seconds. Origami structures with five dyes were recorded for 5 seconds.

DNA origami structure
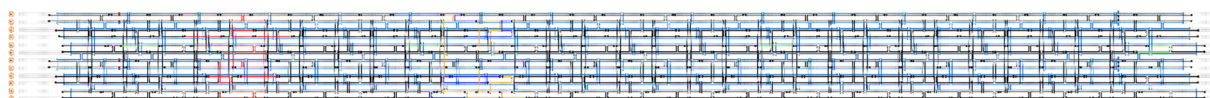
Supplementary Figure 2. *caDNAno sketch of the DNA origami structure used. Modified staples are colored. Green staples are biotin labeled. Red staples are extended at the 3' (5' TTTTCCTCTACCACCTACATCAC) end for external labeling with ATTO 542 modified oligonucleotides. Orange staples are labeled at the 5' end with ATTO 647N. Blue staples are next to the ATTO 647N labeled staples to stabilize the structure.*

psTRAB data processing

Every trace was evaluated and only traces with constant fluorescence signal and without photobleaching were used for further data processing. This is necessary because singlet-singlet-annihilation leads to highly excited states of the organic fluorophores which are prone to bleaching. Additionally, small spectral shifts were observed more frequently. In our analysis, we only used whole traces. A bleaching event changes the exciton-exciton-interaction, which contaminates the photon statistics simply because the number of physical emitters changes over time. Therefore, it is important that we only sum over traces which arise from the same number of physical emitters that give a constant fluorescence signal over the 10 seconds of recording.

2. PL transient of a five-dye sample
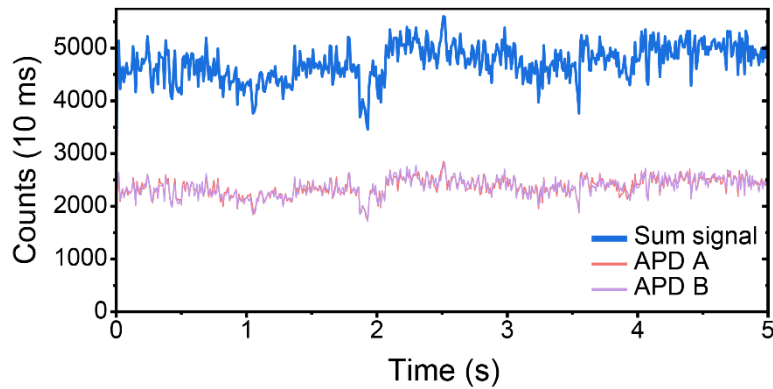
Supplementary Figure 3. *Representative PL trajectory of a five-dye origami sample with 10 ms binning. The blue trajectory is the sum signal of both detection channels which are shown in red and purple. All five dye trajectories were recorded for five seconds to prevent photodamage and spectral shifts.*

3. Instrument response function of the microscope for the DNA origami samples
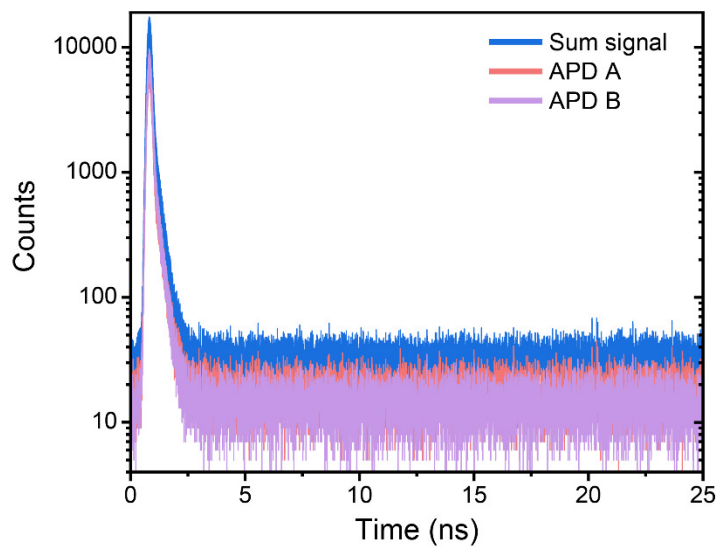
Supplementary Figure 4. *Instrument response function of the DNA origami setup with 4 ps binning. The microtime = 0 in figure 2b and 3 corresponds to the peak of the sum signal (blue).*

Supplementary Discussions

4. Number of independent emitters n as a function of SBR

For calculating the expected n for a single dye on the DNA origami setup the signal-to-background ratio (SBR) was calculated from a single-particle trajectory and a background trace from the same sample. Uncorrelated background adds correlation events equally to N_c and N_l. This raises the N_c/N_l ratio and therefore a high SBR is desirable. Supplementary Figure 5a shows the average of the SBR ratios of both APDs. The microtime $= 0$ corresponds to the peak of the IRF as shown in Supplementary Figure 4. Due to scattering from the excitation laser pulse the SBR rises after the IRF. After reaching its maximum it decays due to the exponential fluorescence decay. The expected N_c/N_l ratio was calculated according to the adapted relation from Weston *et al.* [5]:

$$\frac{N_c}{N_l} = \frac{1+\frac{S}{B}}{\left(1+\frac{S}{2B}\right)^2} \qquad \text{(Supplementary Equation 1)}$$

This relation gives the expected N_c/N_l ratio for a single independent emitter as a function of signal S and background B. For infinite SBR this value becomes zero.

S6
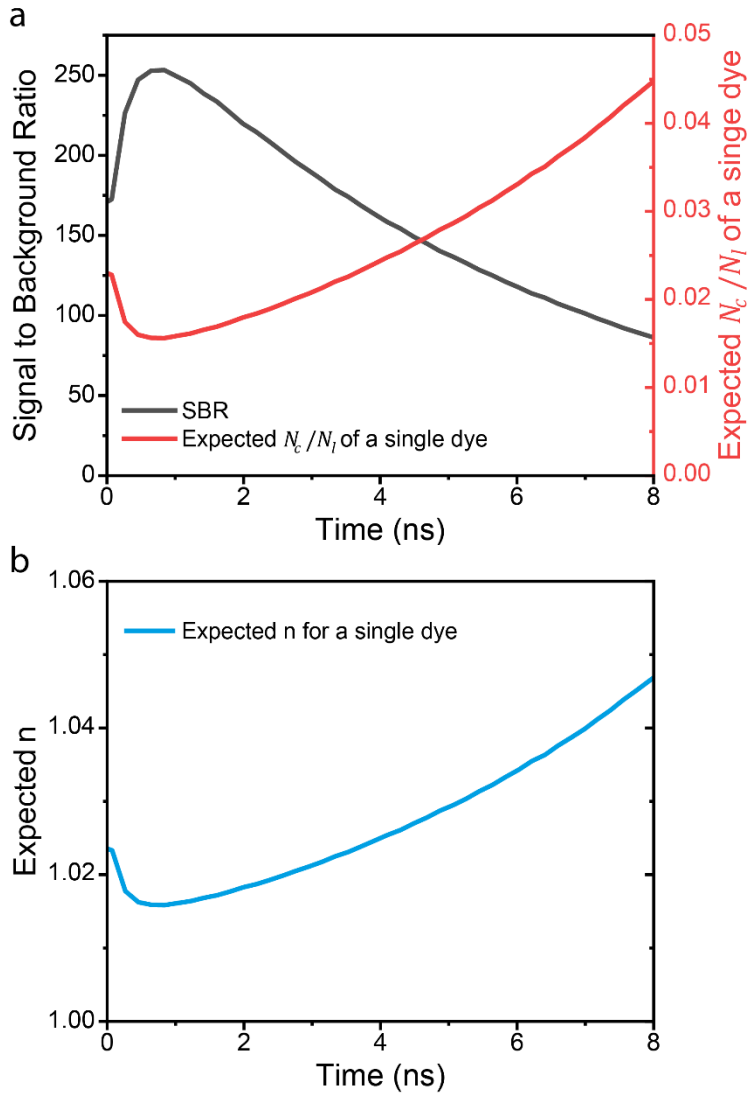
Supplementary Figure 5. *(a) Signal-to-background ratio of a single fluorescent dye in a DNA origami structure shown in black. Time = 0 corresponds to the peak of the IRF as shown in Supplementary Figure 4. The corresponding N_c/N_l ratio is shown in red. (b) Expected n for measured SBR in (a) according to Supplementary Equation 1. For infinite SBR this value becomes one.*

5. Complete fitting results of DNA origami structures

Supplementary Table 2: Complete fitting results with standard error of DNA origami structures according to eq. (3). Values in parentheses were fixed.

y_0 (1)	0.9821 ± 0.0017	0.5390 ± 0.0044	(0.9821)	(0.9821)	(0.9821)	(0.9821)	(0.9821)
A_1 (1)	(0)	0.0001 ± 0.0043	0.4094 ± 0.0057	0.414 ± 0.010	0.5948 ± 0.0064	0.351 ± 0.037	0.350 ± 0.037
k_1 (ns^{-1})	(0)	-0.0078 ± 0.0048	1.718 ± 0.054	0.054 ± 0.0061	0.0628 ± 0.0033	1.44 ± 0.13	1.26 ± 0.12
A_2 (1)	(0)	(0)	(0)	(0)	(0)	0.264 ± 0.038	0.420 ± 0.038
k_2 (ns^{-1})	(0)	(0)	(0)	(0)	(0)	0.356 ± 0.038	0.272 ± 0.021

6. Determination of the size of aggregates

Polymer chain numbers are estimated by counting spots in fluorescence images of samples before and after solvent vapour annealing (SVA). The starting concentration allows single polymer chains to be counted, as shown in Supplementary Figure 6, where we count the spots. This gives us the number of single chains.
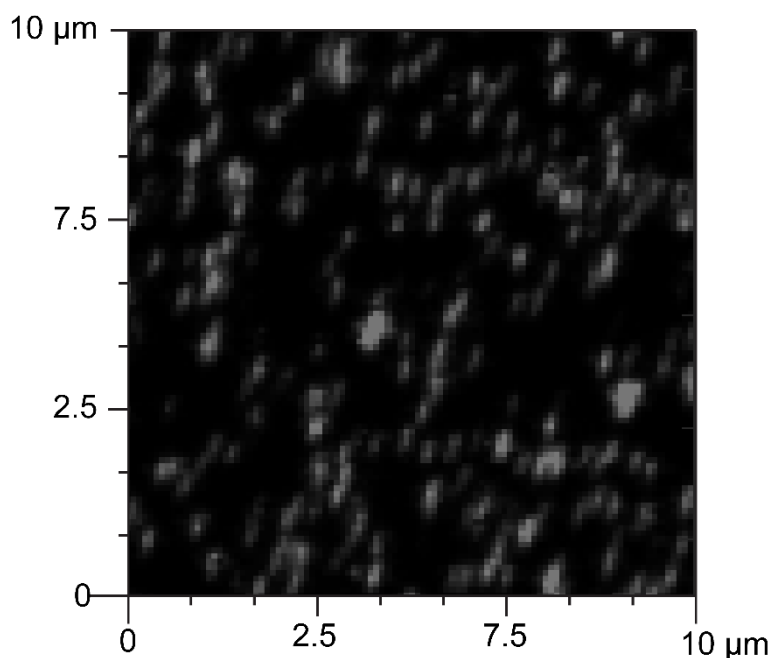
Supplementary Figure 6. *Fluorescence image of PPEB-2 chains, showing single-chain density.*

We then anneal this film under varying conditions, which swells it, allowing the chains to become mobile and aggregate. We then record a fluorescence image again and count the number of spots, which gives us the number of aggregates as shown in Supplementary Figure 7.

10:90
chloroform:acetone

40:60
chloroform:acetone
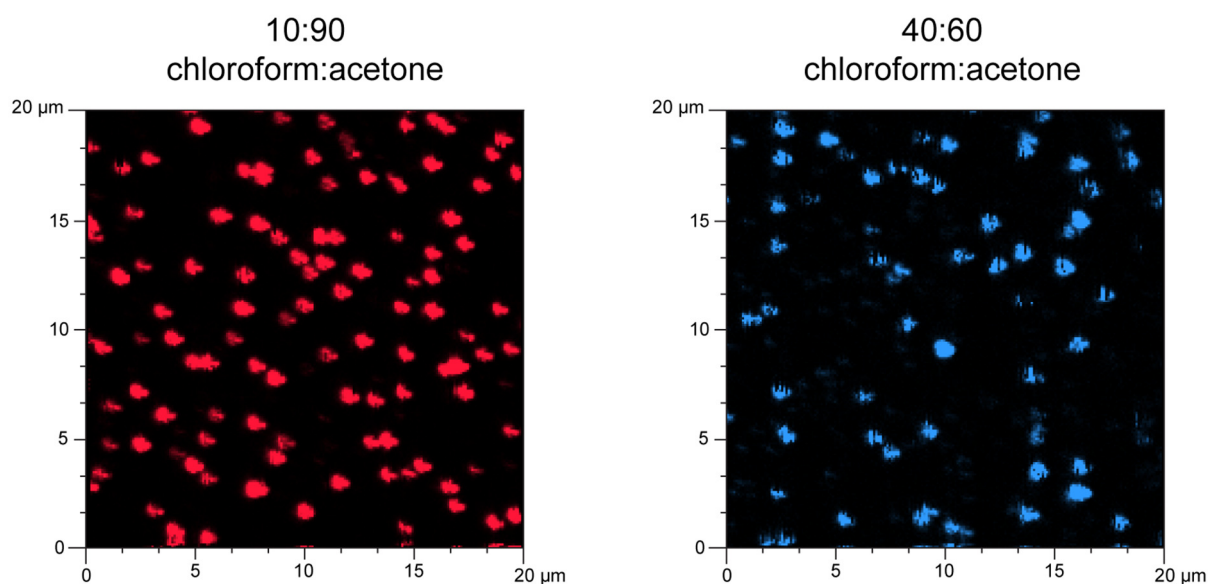
Supplementary Figure 7. *Fluorescence image of PPEB-2 aggregates after solvent vapour annealing, with chloroform:acetone percentages as denoted. Counting of the number of aggregates across multiple images allows the number of chains per aggregate to be deduced.*

Simple division allows us to ascertain than on average each aggregate thus contains a certain number of chains. We repeat this across several images and under the different SVA conditions to allow us to determine the number of chains per aggregate, with results as shown below in Supplementary Table 3.

Supplementary Table 3: Average number of PPEB-2 chains per aggregate for two SVA conditions.

SVA conditions (chloroform:acetone ratio)	Average number of chains per aggregate	Standard deviation
10:90	8.83	0.32
40:60	6.44	0.19

Knowing the average number of polymer chains contained in an aggregate (54 for PPEB-1[6] and the values as denoted above for PPEB-2), the average molecular weight of a chain (40 kDa with PDI of 1.45 for PPEB-1 and 66 kDa with PDI 1.05 for PPEB-2)[7, 8] and assuming[3] a mass density of 1 g cm^{-3} we can then deduce the average volume of an aggregate. In our case, we get 3.59×10^{-18} cm^3 for 54 chains of PPEB-1, 9.67×10^{-19} cm^3 for 9 chains and 7.06×10^{-19} cm^3 for 6 chains of PPEB-2.

7. PPEB aggregate traces

Supplementary Figure 8 plots PL intensity traces for PPEB-1 and PPEB-2, with 10 ms binning. Traces do not show bleaching and the aggregate emission is relatively stable.
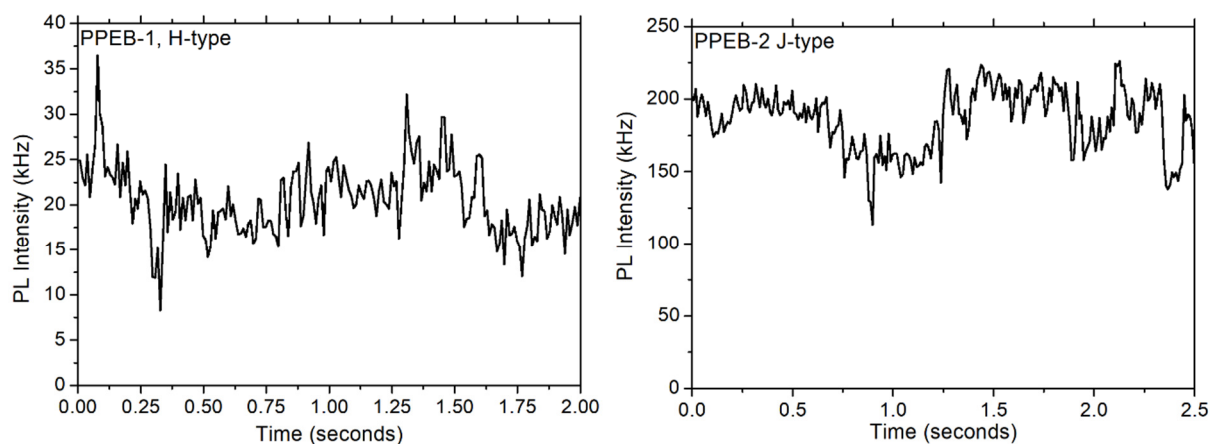
Supplementary Figure 8. *PL intensity traces for PPEB-1 (left) and PPEB-2 (right) aggregates. The data is binned at 10 ms time resolution.*

8. Independence of psTRAB of PPEB aggregates on excitation density

Shown in Supplementary Figure 9 are accumulated psTRAB decays for PPEB-1 H-type aggregates each at two values of excitation fluence: 1.78 µJ cm^{-2} (631 aggregates measured) and 3.56 µJ cm^{-2} (90 aggregates measured). The fluence is determined by measuring the power at the objective, using a visible-range silicon photodiode detector on a Coherent Fieldmaster II power meter, and estimating the diffraction-limited spot size with the 1.35 NA objective as ~366 nm diameter. We find that at these two fluences, the psTRAB results are essentially the identical. Obviously, the range over which such a fluence dependence can be performed is rather limited since the photon correlation spectroscopy requires substantial fluence to begin with, and higher fluences accelerate photodegradation.
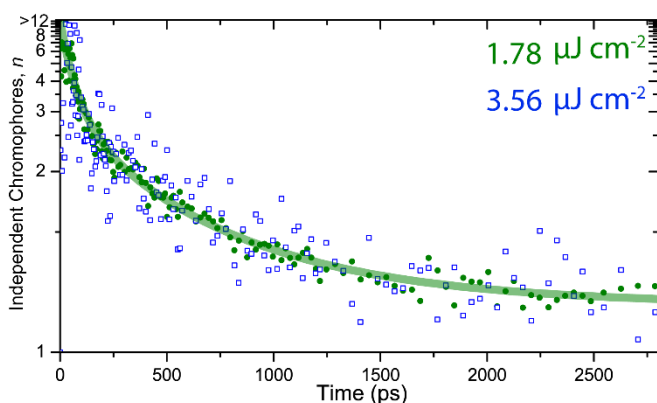
Supplementary Figure 9. *Power dependence of the psTRAB results for 631 and 90 single PPEB-1 H-type aggregates, showing identical data for fluences of 1.78 µJ cm^{-2} (solid green circles) and 3.56 µJ cm^{-2} (open blue squares) along with the guide-for-the-eye (green line).*

9. Evolution with time of photon-antibunching histograms

Shown in Supplementary Figure 10 are the extracted photon-antibunching histograms for the J-type (panel b) and H-type (panel c) PPEB aggregates, along with the psTRAB decays as discussed in the main text (panel a, cf. Figure 4b). These five histograms each in panels b,c are extracted for the five time ranges indicated by green shading (0-67 ps, 117-317 ps, 467-667 ps, 817-1417 ps, 2-2.75 ns).
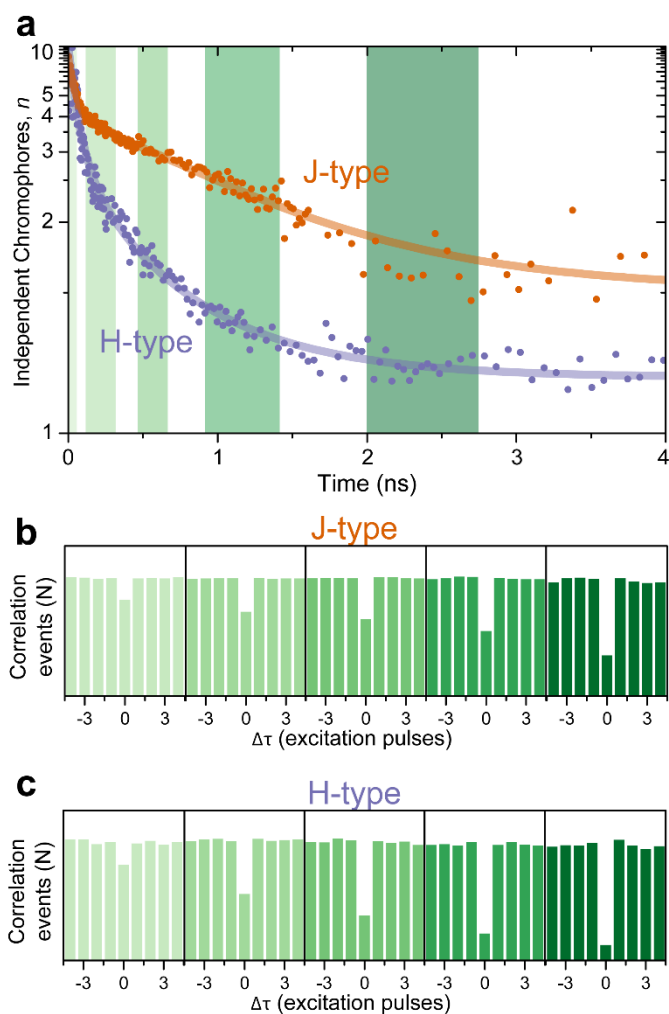
***Supplementary Figure 10.** The psTRAB dynamics of the J- and H-type aggregates, discussed in Figure 4b in the main text (a) along with the extracted photon-antibunching histograms for the J-type (panel b) and H-type (panel c) aggregates. The histograms are extracted from the coloured time windows as indicated, going from left to right of: 0-67 ps, 117-317 ps, 467-667 ps, 817-1417 ps, and 2-2.75 ns.*

10. Quantum-statistical description of psTRAB photon correlations

Definition of the correlation-ratio observable

For n_dyes chromophores emitting into free space without a cavity, the second-order correlation of emitted photons detected at times t and $t + \Delta t$ can be calculated from the second-order correlation of chromophore deexcitation

$$G^{(2)}(t, t + \Delta t) = \sum_{i,j=0}^{n_\text{dyes}} \langle a_i^\dagger(t) a_j^\dagger(t + \Delta t) a_j(t + \Delta t) a_i(t) \rangle,$$

where $a_i(t)$ is the operator on the 2^{n_dyes} dimensional Hilbert space that destroys the excitation of chromophore i, each chromophore being modeled as a two-level system with only ground and excited states. For the case of excitation by laser impulses at regularly spaced times t_0, $t_0 \pm T, t_0 \pm 2T, ...$ we define the *central-bin* and the *lateral-bin delay-integrated second-order correlation* at time $t_0 < t < t_0 + T$ as

$$G_\text{c}^{(2)}(t) = \int_0^{T-t} G^{(2)}(t, t + \Delta t) d(\Delta t) \quad \text{and}$$

$$G_\text{l}^{(2)}(t) = \int_T^{2T-t} G^{(2)}(t, t + \Delta t) d(\Delta t),$$

respectively. Finally, the *central-to-lateral-bin second-order correlation ratio* is defined as $G_\text{c}^{(2)}(t)/G_\text{l}^{(2)}(t) \equiv N_\text{c}(t)/N_\text{l}(t)$.
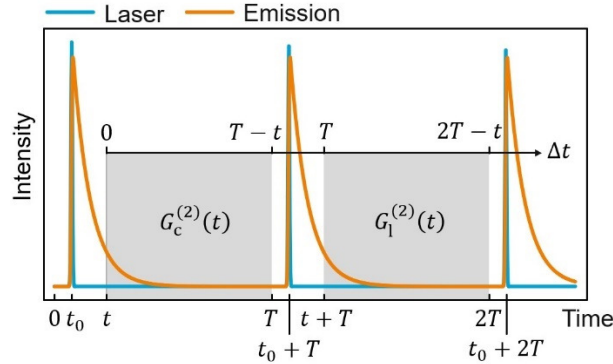
Supplementary Figure 11. *Visualization of the temporal integration ranges used for $G_\text{c}^{(2)}(t)$ and $G_\text{l}^{(2)}(t)$. The first photon is detected at time $t > t_0$, and the second photon is detected at time $t + \Delta t$ chosen from either the same central laser repetition period (left gray domain) or the lateral laser repetition period (right gray domain).*

Quantum-mechanical description of n_dyes coupled chromophores under optical driving

We describe each chromophore by a two-level Hilbert space $\mathcal{H}_2$ with basis states $|0\rangle$ (ground state) and $|1\rangle$ (singlet excited state) and use the usual definitions for the lowering operator $a = |0\rangle\langle 1|$ and the raising operator $a^\dagger = |1\rangle\langle 0|$. The Hamiltonian for a single dye chromophore coupled to a short-impulse laser light field $\mathcal{E}(t) = \mathcal{E}_0 \sin(\omega t) \sum_{j \in \mathbb{Z}} e^{-2\ln(2)\left(\frac{t+j\cdot T}{\Delta t_\text{fwhm}}\right)^2}$ is

$$H = \hbar\omega_0 \, a^\dagger a + \hbar\Omega(t)(a + a^\dagger)\sin(\omega t),$$

where $\hbar\omega_0$ is the excited-state energy, $\Omega(t) = \frac{\mu}{\hbar}\mathcal{E}_0\sum_{j\in\mathbb{Z}}e^{-2\ln(2)\left(\frac{t+jT}{\Delta t_{\text{fwhm}}}\right)^2}$ is the slowly-varying Rabi frequency and μ is the transition dipole strength. Using the Hermitian operator $A = \omega\, a^\dagger a$ and the corresponding unitary transformation

$$U = e^{iAt} = e^{i\omega t}a^\dagger a + a\, a^\dagger,$$

the Hamiltonian can be transformed as

$$\widetilde{H} = UHU^\dagger + i\hbar\frac{dU}{dt}U^\dagger = UHU^\dagger - \hbar A,$$

resulting in the rotating-frame Hamiltonian

$$\widetilde{H} = \hbar(\omega_0 - \omega)a^\dagger a + \frac{\hbar\Omega(t)}{2i}\left(a\left(1 - e^{-2i\omega t}\right) - a^\dagger\left(1 - e^{2i\omega t}\right)\right).$$

In the rotating-frame approximation and for resonant excitation $\omega = \omega_0$, high-frequency components at $\pm 2\omega$ are dropped and the Hamiltonian reduces to

$$\widetilde{H} = \frac{\hbar\Omega(t)}{2i}\left(a - a^\dagger\right).$$

Generalizing for the case of n_{dyes} chromophores, the Hilbert space is constructed as the tensor product $\mathcal{H}_2 \otimes \ldots \otimes \mathcal{H}_2$ and

$$\widetilde{H} = \frac{\hbar\Omega(t)}{2i}\sum_i\left(a_i - a_i^\dagger\right).$$

Since we are not interested in the coherences, calculation of the system dynamics in the rotating frame is sufficient to derive expectation values for the relevant photon correlation. In order to account for spontaneous emission and singlet-singlet annihilation, we describe the system state by a $2^{n_{\text{dyes}}} \times 2^{n_{\text{dyes}}}$ dimensional density matrix $\rho(t)$ and treat its time dynamics on the level of a Lindblad master equation[9]

$$\frac{d}{dt}\rho(t) = \mathcal{L}(t)\rho(t) = -\frac{i}{\hbar}[H(t),\rho(t)] + \sum_{j=1}^{n_{\text{dyes}}}\frac{1}{2}\left(2c_j\rho(t)c_j^\dagger - \rho(t)c_j^\dagger c_j - c_j^\dagger c_j\rho(t)\right) +$$
$$\sum_{j\neq k}\frac{1}{2}\left(2d_{jk}\rho(t)d_{jk}^\dagger - \rho(t)d_{jk}^\dagger d_{jk} - d_{jk}^\dagger d_{jk}\rho(t)\right).$$

The quantum-jump operators for spontaneous emission are $c_j = \sqrt{k_{\text{r}}}a_j$ and those for singlet-singlet annihilation are $d_{jk} = \sqrt{k_{\text{ET}}}a_j a_k^\dagger a_k$. In the context of our constrained two-level description, the latter operator effectively models energy transfer from chromophore j to chromophore k at a rate $k_{\text{ET}} = \frac{1}{2}k_{\text{SSA}}$, assuming that after excursions to higher excited states (not included in our Hilbert space), the receiving chromophore immediately returns to the first excited state. Here, k_{SSA} is the total exponential decay rate at which an individual pair of excitations decays by singlet-singlet annihilation to a single excitation.

Two-time correlations for the excitations (i.e. for the emitted photons) can be calculated in the context of the validity of the Lindblad equation by using the quantum-regression theorem[10]

$$\langle a_i^\dagger(t)a_j^\dagger(t+\tau)a_j(t+\tau)a_i(t)\rangle = \text{Tr}\left(a_j^\dagger a_j\Lambda_i(t,t+\tau)\right),$$

where $\Lambda_i(t,t+\tau)$ describes the system that at time t is reduced by one excitation on chromophore i and then follows the same differential equation as the original density matrix.

$$\Lambda_i(t,t) = a_i\rho(t)a_i^\dagger$$

$$\frac{\partial}{\partial \tau} \Lambda_i(t, t + \tau) = \mathcal{L}(t + \tau) \Lambda_i(t, t + \tau).$$

The two-time correlation can thus be calculated by the product of probabilities of removing one excitation from the system at time t, and removing the other one at time $t + \tau$ from the system that was disturbed at time t by reducing the number of excitations by one.

As an example, the system dynamics is solved by numerical integration for the case of three chromophores on the *Mathematica* computer algebra platform (Wolfram Research, USA). Parameters where chosen to model chromophores with unity quantum efficiency, a radiative rate of $k_r = 0.25 \cdot 10^9 \text{ s}^{-1}$, and a singlet-singlet annihilation rate of $k_{SSA} = 0.25 \cdot 10^9 \text{ s}^{-1}$. Excitation conditions were $\Delta t_{fwhm} = 50$ ps laser impulse width, $T = 50$ ns repetition interval and an instantaneous peak Rabi frequency of $2 \cdot 10^9 \text{ s}^{-1}$. The number of excitations in the coupled set of chromophores can be calculated as $\text{Tr}(\rho(t) \sum_i a_i^\dagger a_i)$.
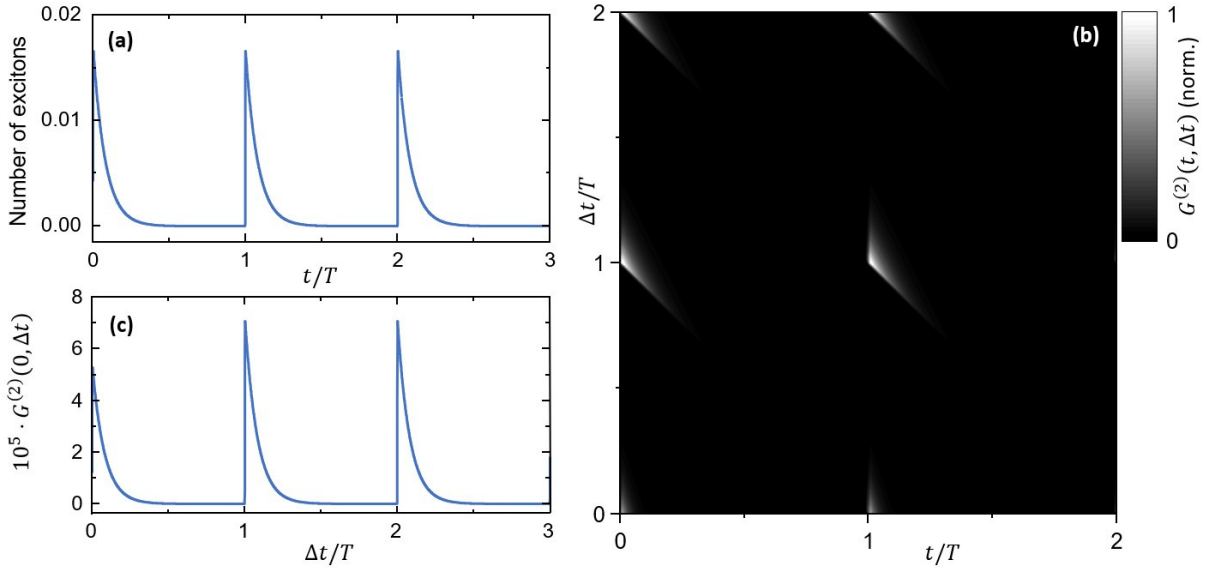
Supplementary Figure 12. *(a) Number of excitons in a three-chromophore system as a function of time t under pulsed laser excitation. Due to the low excitation strength, singlet-singlet annihilation has no measurable impact on the emission intensity. (b) Normalized two-time correlation $G^{(2)}(t, t + \Delta t)$ as a function of t and Δt in units of the pulse repetition period T. (c) For delay times $\tau < t - T$, the correlation is reduced due to the loss of one exciton in the system at time t. The example shows the case of $t = 0$.*
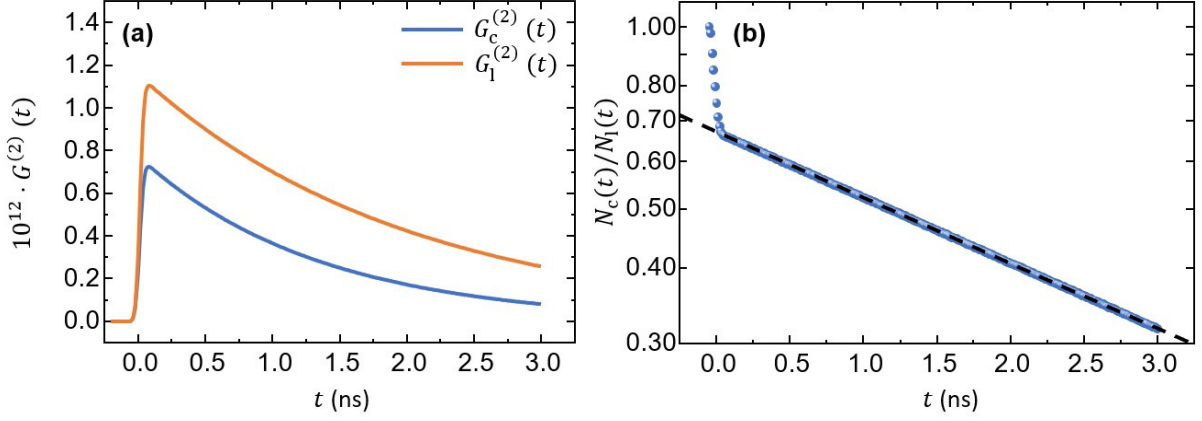
Supplementary Figure 13. (a) Central-bin photon correlation $G_c^{(2)}(t)$ (blue) and lateral-bin photon correlation $G_l^{(2)}(t)$ (orange) as a function of time t after laser excitation. (b) After the end of the excitation pulse, the correlation ratio $N_c(t)/N_l(t) = G_c^{(2)}(t)/G_l^{(2)}(t)$ (blue) follows the exponential decay $\frac{n_{\text{dyes}}-1}{n_{\text{dyes}}} e^{-k_{\text{SSA}}t}$ that directly reflects the annihilation dynamics of exciton pairs (dashed line). The initial decay of the correlation ratio from 1 to $(n_{dyes} - 1)/n_{dyes}$ is due to the high probability of re-excitation if the first photon is detected early during the excitation pulse.

Analytical treatment

The system can be treated analytically for the case of negligibly short excitation impulses, assuming that the dynamics is treated in the limit of vanishing Rabi frequency $\Omega \to 0$. We first discuss the the $n_{\text{dyes}} = 2$ system analytically, assuming that at $t < 0$ the system reaches equilibrium due to optical pumping. In this case, the total number of excitations in the system is $p_0 n_{\text{dyes}}$, where the probability p_0 for a single dye chromophore to be excited depends on the excitation intensity. From the probability of detecting a photon we find the emission intensity $I(t) = k_r \text{Tr}\left((a_1^\dagger a_1 + a_2^\dagger a_2)\rho(t)\right)$ to be

$$I(t) = \frac{k_r}{2} e^{-(2k_r+k_{\text{SSA}})t} p_0 n_{\text{dyes}} \left(\frac{k_{\text{SSA}}p_0 n_{\text{dyes}}}{4(k_r+k_{\text{SSA}})} + \left(1 - \frac{k_{\text{SSA}}p_0 n_{\text{dyes}}}{4(k_r+k_{\text{SSA}})}\right) e^{(k_r+k_{\text{SSA}})t}\right)$$

Experimentally, one works in the low-excitation regime $p_0 n_{\text{dyes}} \ll 1$, and more specifically $k_{\text{SSA}} p_0 n_{\text{dyes}} \ll 4(k_r + k_{\text{SSA}})$. In this limit, the intensity is $I(t) \approx k_r p_0 e^{-k_r t}$. Since in this case the system is only ever singly excited, the photon correlations are calculated as

$$G_c^{(2)}(t, t+\tau) = k_r^2 n_{\text{dyes}}(n_{\text{dyes}} - 1)\text{Tr}\left(a_2^\dagger a_2 \Lambda(t, t+\tau)\right) \cdot \text{Tr}(a_1^\dagger a_1 \rho(t))$$

$$G_l^{(2)}(t, t+\tau) = k_r^2 n_{\text{dyes}}^2 \text{Tr}\left(a_2^\dagger a_2 \rho(t+\tau)\right) \cdot \text{Tr}\left(a_1^\dagger a_1 \rho(t)\right).$$

Since the analytical description lacks the action of the pulsed excitation, the central-bin and lateral-bin correlations must be calculated differently than in the experimental case. For the central-bin correlation, annihilation of one excitation at time t on chromophore 1 defines the new initial state $\Lambda(t, t) = a_1 \rho(t) a_1^\dagger$. There are $n_{\text{dyes}} = 2$ choices for the first emitting chromophore and only $(n_{\text{dyes}} - 1) = 1$ choice for the second, since the first chromophore cannot be reexcited. For the lateral-bin correlation, annihilation of the first exciton on one of the n chromophores does not change the density matrix, since the system fully recovers from one to the next excitation pulse. The number of available chromophores to emit the second photon is thus also $n_{\text{dyes}} = 2$. In the limit of $p_0 n_{\text{dyes}} \ll 1$, one finds

$$G_{\mathrm{c}}^{(2)}(t, t + \tau) = \frac{k_{\mathrm{r}}^2}{4} n_{\mathrm{dyes}} (n_{\mathrm{dyes}} - 1) p_0^2 e^{-(k_{\mathrm{r}}+k_{\mathrm{ET}})t} e^{-(k_{\mathrm{r}}+k_{\mathrm{ET}})t} e^{-k_{\mathrm{r}}\tau}$$

$$G_{\mathrm{l}}^{(2)}(t, t + \tau) = \frac{k_{\mathrm{r}}^2}{4} n_{\mathrm{dyes}}^2 p_0^2 e^{-k_{\mathrm{r}}t} e^{-k_{\mathrm{r}}t} e^{-k_{\mathrm{r}}\tau}$$

Integration over the delay time τ then yields

$$G_{\mathrm{c}}^{(2)}(t) = \int_0^\infty G_{\mathrm{c}}^{(2)}(t, t + \tau) d\tau = \frac{k_{\mathrm{r}}}{4} n_{\mathrm{dyes}} (n_{\mathrm{dyes}} - 1) p_0^2 e^{-(2k_{\mathrm{r}}+k_{\mathrm{SSA}})t}$$

$$G_{\mathrm{l}}^{(2)}(t) = \int_0^\infty G_{\mathrm{l}}^{(2)}(t, t + \tau) d\tau = \frac{k_{\mathrm{r}}}{4} n_{\mathrm{dyes}}^2 p_0^2 e^{-2k_{\mathrm{r}}t}$$

and a correlation ratio of

$$\frac{N_{\mathrm{c}}(t)}{N_{\mathrm{l}}(t)} = \frac{G_{\mathrm{c}}^{(2)}(t)}{G_{\mathrm{l}}^{(2)}(t)} = \frac{n_{\mathrm{dyes}} - 1}{n_{\mathrm{dyes}}} e^{-k_{\mathrm{SSA}}t}.$$

These results for $n_{\mathrm{dyes}} = 2$ can be directly rationalized for higher numbers of chromophores and the case of non-radiative decay at rate k_{nr}. Under conditions of $p_0 n_{\mathrm{dyes}} \ll 1$, the probability to find two excited chromophores after each of two adjacent excitation pulses is negligible, even for systems with $n_{\mathrm{dyes}} > 2$ chromophores. Thus, lateral-bin correlations derive from chromophore ensembles with only *one* excitation present and are devoid of the effect of singlet-singlet annihilation. On the other hand, central-bin correlations can only exist if indeed two or more excitations are present after the laser excitation pulse. Since $p_0 n_{\mathrm{dyes}}$ is small, cases with more than two excitations need not be considered. Obviously, the probability to find two excitations decays proportionally to $e^{-k_{\mathrm{SSA}}t}$, where k_{SSA} is the *exponential decay rate for pairs of singlet excitons*, such that in a macroscopic ensemble with a high number of excitons n_{exc}, one would expect a non-exponential decay according to $\frac{d}{dt} n_{\mathrm{exc}} = -n_{\mathrm{exc}}(n_{\mathrm{exc}} - 1)k_{\mathrm{SSA}}$. Microscopically however, each excited chromophore is exponentially quenched by each other excited chromophore at the *energy transfer rate* $k_{\mathrm{ET}} = k_{\mathrm{SSA}}/2$. Applying the quantum-regression theorem, the probability of finding the second photon emission at time $t + \tau$ for the central-bin second-order correlation is calculated by assuming that the number of excitons is *reduced to one* at time t. There is a total number of n chromophores to choose from as source of the first detected photon, and neglecting the possibility of double-excitations of individual chromophores, a total of $(n_{\mathrm{dyes}} - 1)$ chromophores exist that can potentially carry the second exciton. The central-bin second-order correlation is thus calculated as

$$G_{\mathrm{c}}^{(2)}(t, t + \tau) = n_{\mathrm{dyes}} k_{\mathrm{r}} p_0 \, e^{-(k_{\mathrm{r}}+k_{\mathrm{nr}}+k_{\mathrm{ET}})t} \cdot k_{\mathrm{r}}(n_{\mathrm{dyes}} - 1) p_0 e^{-(k_{\mathrm{r}}+k_{\mathrm{nr}}+k_{\mathrm{ET}})t} e^{-(k_{\mathrm{r}}+k_{\mathrm{nr}})\tau}$$

$$G_{\mathrm{c}}^{(2)}(t) = n_{\mathrm{dyes}} (n_{\mathrm{dyes}} - 1) p_0^2 k_{\mathrm{r}}^2 \tau_{\mathrm{PL}} e^{-2(k_{\mathrm{r}}+k_{\mathrm{nr}})t} e^{-k_{\mathrm{SSA}}t},$$

where $\tau_{\mathrm{PL}} = 1/(k_{\mathrm{r}} + k_{\mathrm{nr}})$ is the single-chromophore photoluminescence lifetime. For the lateral-bin correlation, the only relevant contribution comes from the configuration where there is exactly one exciton in the chromophore system when the first photon is emitted and exactly one photon in the chromophore system when the second photon is emitted after the next (lateral) excitation pulse. Thus, singlet-singlet quenching does not contribute to the lateral-bin second-order correlation. Again, n_{dyes} chromophores can potentially emit the first photon, but in contrast to the calculation of the central-bin correlation, for the lateral-bin correlation the system is re-excited in-between the two photon detection events, and thus the number of chromophores that can emit the second photon is also n_{dyes}:

$$G_l^{(2)}(t, t+\tau) = n_{\text{dyes}} k_r\, p_0\, e^{-(k_r+k_{\text{nr}})t} \cdot k_r n_{\text{dyes}}\, p_0 e^{-(k_r+k_{\text{nr}})t} e^{-(k_r+k_{\text{nr}})\tau}$$

$$G_l^{(2)}(t) = n_{\text{dyes}}^2 p_0^2 k_r^2 \tau_{\text{PL}}\, e^{-2(k_r+k_{\text{nr}})t}.$$

The resulting central-to-lateral-bin second-order correlation ratio for the general case of n_{dyes} chromophores is thus again simply

$$\frac{N_c(t)}{N_l(t)} = \frac{G_c^{(2)}(t)}{G_l^{(2)}(t)} = \frac{n_{\text{dyes}}-1}{n_{\text{dyes}}} e^{-k_{\text{SSA}}t}.$$

An important observation in this treatment is that the choice of the singlet-singlet annihilation mechanism and the associated decay law $e^{-k_{\text{SSA}}t}$ is entirely arbitrary. The immediate conclusion is that the correlation ratio can be used to directly determine the actual decay function for the doubly-excited system.

Supplementary Table 4: Sequences for the modified DNA origami structure.

5' position	Sequence	Comment
0[286]	AAAACGAAAGAGGCTCATTATAC	
11[105]	ACACAACATACGAGGGATGTGGCTATTAATCGGCC	
9[567]	ATCATTTACATAAAAGTATCAAAATTATAAGAAACTTCAATA	
7[567]	CAGCTTTGAATACCAAGTTACAA	
5[455]	CATGCCAGTGAGCGCTAATATCCAATAATAAGAGC	
2[223]	CCGAACTTTAATAAAAGCAAAGCGGATT	
5[497]	TTGAGAATATCTTTCCTTATCACTCATCGAGAACA	
9[315]	CAGATATAGGCTTGAACAGACGTTAGTAAAGCCCAAAAATTT	
5[287]	GCGCAGCGACCAGCGATTATATATCATCGCCTGAT	
8[69]	TCGGTCATACCGGGGGTTTCTGC	
11[219]	GTGCCTGCTTTAAACAGGGAGAGAGTTTCAAAGCGAACCA	
10[457]	AAAAGATAGGGTTGAGTGT	
2[643]	GATAGTGCAACATGATATTTTTGAATGG	
0[347]	AGCGTATCATTCCACAGACCCGCCACAGTTGCAGCAAGCG	
9[483]	ATAATGAATCCTGAGATTACGAGCATGTGACAAAAACTTATT	
8[573]	AAATGCGTTATACAAATTCTTAC	
2[433]	AGGGACAAAATCTTCCAGCGCCAAAGAC	
7[63]	GCCCGCACAGGCGGCCTTTAGTG	
4[377]	CTATTTCGGAACGAGTGAGAATA	
0[698]	TTTTTCGGGAGCTAAACAGGTTGTTAGAATCAGAGTTTTT	
4[587]	CATCGGGAGAAATTCAAATATAT	
7[506]	AAATCAGCCAGTAATAACACTATTTTTGAAGCCTTAAATC	
7[170]	TTTTTATCCAATAAATCTCTACCCCGGTAAAACTAGCATG	
5[161]	GTATACAGGTAATGTGTAGGTAGTCAAATCACCAT	
4[396]	AACAGAGTGCCTGGGGTTTTGCTCACAGAAGGATTAGGAT	
3[350]	GTCACCAGTACAAGGTTGAGGCA	
5[581]	ACATCATTTAAATTGCGTAGAAACAGTACCTTTTA	
5[623]	ATACCCTTCGTGCCACGCTGAACCTTGCTGAACCT	
8[130]	GGGCGTGAAATATTAGCGCCATTCGC	
9[357]	TCTTATACTCAGAAAGGCTTTTGATGATATTGACACGCTATT	

11[345]	GAGAGCCTCAGAACCGCATTTTCTGTAACGATCTAAAGTT	
5[329]	TTCATTTTCTGCTAAACAACTGAACAACTAAAGGA	
8[489]	AAAACGGAATACCCAAAAGAACT	
0[202]	GACCGGAAGCAATTGCGGGAGAA	
3[182]	GCTAAATCGGTTTGACTATTATA	
3[392]	ATATTCACAAACAAATTCATATG	
6[69]	AAAAGTGTCAGCAACAATTGCAGGCGCT	
11[567]	ACCATCACCCAAATAAACAGTTCATTTGATTCGCC	
7[590]	AATCGTTGAGTAACATTGGAATTACCTAATTACATTTAAC	
11[93]	GCTCAAGTTGGGTAACGGGCGGAAAAATTTGTGAGAGATA	
0[305]	ACTACCTTTAAACGGGTAACAGGGAGACGGGCA	
4[270]	TCAACATCAGTTAAATAGCGAGAGTGAGACGACGATAAAA	
6[153]	TAAATCGGTTGGTGCACATCAAAAATAA	
10[163]	TCAGCTAACTCACATTAAT	
7[231]	TGCAACACTATCATAACCCTCGT	
4[438]	ACCAAATTACCAGGTCATAGCCCCGAGTTTTCATCGGCAT	
8[195]	TTAACAAGAGAATCGATGAACGG	
3[625]	AGACAACCTGAACAGTATTCGAC	
8[363]	TGAACAGCTTGATACCGATAGTT	
0[412]	TCACCGTCACCGGCGCAGTCTCT	
4[706]	TTTTTGTCCATCACGCAAATTCCGAGTAAAAGAGTCTTTTT	
11[315]	ACAGCTGATTGCCCGTCGCTGCGCCCACACGTTGA	
8[424]	CGGAAGCACGCAAACTTATTAGCGTT	
0[431]	ATTCAAGGGGAAGGTAAATGTGGCAAATAAATC	
3[602]	TGATTATCAGATATACGTGGCAC	
4[545]	TGACCTAAATTTTTAAACCAAGT	
3[679]	GGTTGCTTTGACGAGCACGTTTTT	
6[573]	TGATTTAGAAAACTCAAGAGTCAATAGT	
11[441]	AAAAGAATAGCCCGATACATACGCAGTAAGCTATC	
8[634]	TACATAAATTCTGGGCACTAACAACT	
3[541]	CATAGTTAATTTGTAAATGTCGC	
11[147]	TGCCTAATGAGTGAGAAAAGCTCATATGTAGCTGA	
9[651]	AATAGCTGTCACACGCAACGGTACGCCAGCGCTTAATGTAGTA	
0[557]	TACCTAATATCAAAATCATTCAATATTACGTGA	
4[60]	TCAGAGGTGTGTCGGCCAGAATGAGTGCACTCTGTGGT	
3[476]	TTTTTTGTTTAATAAAGTAATTC	
8[382]	AAGTAAGAGCCGCCAGTACCAGGCGG	
3[79]	GTGGAACGACGGGCTCTCAACTT	
4[102]	CCAGCCAAACTTCTGATTGCCGTTTTGGGTAAAGTTAAAC	
3[121]	AATCAGTTAAAACGTGGGAGAAA	
3[224]	GCATCAAAAAGAAGTAAATTGGG	
7[212]	TTTCACGAGAATGACCATTTTCATTTGGTCAATAACCTGT	
8[678]	CCTACATACGTAGCGGCCAGCCATTGCAACAGGTTTTT	
5[539]	TTCGCTATTCGCAAGACAAAGTTAATTTCATCTTC	
7[17]	TTTTTATCCAGCGCAGTGTCACTGC	

8[298]	CATAGAATTTGCGGTTTGAAAGAGGA	
10[79]	GTATGTGAAATTGTTATCC	
7[273]	ACTACTTAGCCGGAACGAGGCGC	
11[387]	GGCGACACCACCCTCAGGTTGTACTGTACCGTTCCAGTAA	
6[447]	TTACCTCTTAGCAAATTTCAACCGATTG	
8[508]	GGTTTGCGCATTTTAACGCGAGGCGT	
10[415]	CCTCCGAAATCGGCAAAAT	
4[480]	TAAGCCAGAGAGCCAGAAGGAAACTCGATAGCCGAACAAA	
0[179]	GCCTTATACCCTGTAATACCAATTCTTGCGCTC	
9[147]	CATTCAACCCAAAATGTAGAACCCTCATGAATTAGTACAACC	
7[525]	TATGTGATAAATAAGGCGTTAAA	
0[454]	AGACGGGAGAATTGACGGAAATT	
11[681]	AAAGGGCGCTGGCAAGTATTGGC	
4[228]	GAGCTTAAGAGGTCCCAATTCTGCAATTCCATATAACAGT	
3[331]	TACCGGGATAGCAATGAATATAT	
4[335]	ATTGCGAATAATGTACAACGGAG	
2[265]	TATGCATTACAGAGGATGGTTTAATTTC	
4[564]	TTTAGAACGCGAATTACTAGAAAACTATAAACACCGGAAT	
11[597]	GAGGTAACGTTATTAATTTTAAAACAAATAATGGAAGGGT	
5[25]	TTTTTCCGGTGCAGCACCGATCCCTTACACTTGCC	
1[17]	TTTTTTGGTAATGGGTAACCATCCCACTTTTT	
8[531]	AACGAACCTCCCGACTTGCGGGA	
0[515]	CTGAAAACCTGTTTATCAAACATGTAACGTCAA	
8[592]	AAAATTTTTTAAAATGAGCAAAAGAA	
7[609]	ATTTGGCAAATCAACAGTTGAAA	
11[639]	CCGATAATAAAAGGGACTTAACACCGCGAACCACCAGCAG	
3[583]	GGAATCGGAACATTGCACGTTAA	
2[349]	TGTAGGGGATTTAGTAACACTGAGTTTC	
3[434]	AAAAGGGCGACAATTATTTATCC	
5[371]	ATCAGAGCCTTTAACGGGGTCTTAATGCCCCCTGC	
7[338]	GGAGCAGCCACCACCCTTCGCATAACGACAATGACAACAA	
3[56]	ATCAGCGGGGTCAGCTTTCAGAG	
0[473]	AAAAAAGGCAGCCTTTACAATCTTACCAGTTTG	
6[698]	TTTTTAACAATATTACCGTCGCTGGTAATATCCAGTTTTT	
8[88]	AGCCTCCCCAGGGTCCGGCAAACGCG	
6[405]	CAAGTGCTGAGTAAGAAAATAAATCCTC	
7[632]	GGAATAACAGAGATAGACATACAAACTTGAGGATTTAGAA	
0[76]	GACTTTCTCCGTGGCGCGGTTG	
2[97]	GCGAAAGACGCAAAGCCGCCACGGGAAC	
4[648]	GCATCGAGCCAGATATCTTTAGGACCTGAGGAAGGTTATC	
4[606]	ACAGTTTTTCAGATTTCAATTACCGTCGCAGAGGCGAATT	
7[548]	TAAGATCTGTAAATCGTTGTTAATTGTAAAGCCAACGCTC	
11[555]	CCCACATGTGAGTGAATAACTGATGCTTTTAACCTCCGGC	
9[399]	ATAAGAAGCCACCCAAACTTGAGCCATTATCAATACATCAGT	
11[189]	ACTGCCCGCTTTCCTGAAAAGCTATATTTTAAATA	

3[499]	TGTCCAAGTACCAGAAACCCCAG	
4[209]	AATGCTGTAGCTGAGAAAGGCCG	
7[357]	GTGTATTAAGAGGCTGAGACTCC	
8[237]	GCTTGACCATTAGATACATTTCG	
9[609]	GATGAATAAATCCTGTAGGTGAGGCGGTAGCGTAAGTCCTCA	
0[328]	TTGTCGTCTTTCTACGTAATGCC	
11[513]	CTCCAATTTAGGCAGAGACAATCAATCAAGAAAAATAATA	
3[560]	AAGACGCTGAGACCAGAAGGAGC	
7[42]	GCGCCTGAATGCCAACGGCCCAGCCTCCCGCGTGCCTGTTCTTCTTTTT	
0[370]	GCGTCATACATGCCCTCATAGTT	
11[303]	GTGAGTTAAAGGCCGCTGACACTCATGAAGGCACCAACCT	
3[373]	GGTCACGCCAGCACAGGAGTTAG	
4[51]	GGGTTACCTGCAGCCAGCGGTGTTTTT	
7[254]	TTACCAATAAGGCTTGCAGTGCGGAAGTTTAGACTGGATA	
8[466]	GGCATAAGCGTCTTCGAGGAAACGCA	
3[247]	CTTGAAAACACCCTAACGGCATA	
8[405]	GGTGCCGTCGAGAGGGTTGATAT	
10[331]	TCGTTCACCGCCTGGCCCT	
8[615]	GTTGAAACAAACATCAAGAAAAC	
6[531]	GACCGTCGAACGGGGAAGCTAATGCAGA	
6[363]	TGAAATTGTTTCAGGGAACTACAACGCC	
10[625]	AACACCCTAAAGGGAGCCC	
6[279]	CATGTCAGAGATTTGATGTGAATTACCT	
11[429]	CCCTTCATATAAAAGAACGTAGAGCCTTAAAGGTGAATTA	
11[651]	TTGACGGGGAAAGCTTCACCAGAAATGGCATCACT	
6[615]	GTCAGTCGTTTAACGAGATGGCAATTCA	
7[422]	AGCGCCACCACGGAATACGCCTCAGACCAGAGCCACCACC	
4[312]	ATTTGCCAAGCGGAACTGACCAACGAGTCAATCATAAGGG	
8[550]	CAGTAAGAACCTTGAGCCTGTTTAGT	
4[503]	AGCAAGCCGTTTAAGAATTGAGT	
2[601]	TCAATAATAAAGTGTATCATCATATTCC	
9[21]	TTTTTGCGTCCGTGCCTGCATCAGACGTTTTT	
11[483]	GAACAAGAGTCCACCAATTTTTTAGTTGTCGTAGG	
10[499]	CTATATTAAAGAACGTGGA	
4[186]	GAGACAAAGATTATCAGGTCATTGACGAGAGATCTACAAA	
9[63]	TTCACCTAGCGTGGCGGGTGAAGGGATACCAGTGCATAAAAA	
11[609]	AGCACTAAATCGGATCGTATTTAGACTTATATCTG	
4[293]	AAATTGTGTCGAGAATACCACAT	
3[667]	GGCGCCCCGCCGAATCCTGAGAAGTGAGGCCGATTAAAGG	
3[205]	GTCAGAATCAGGCAGGATTCGCG	
0[622]	AAGATAAAACAGTTGGATTATAC	
6[111]	TCAGGTGAAATTTCTACGGAAACAATCG	
10[205]	AGCAGTCGGGAAACCTGTC	
6[489]	AATCATAATAACCCGGCGTCAAAAATGA	
0[496]	TCCCATCCTAATGAGAATAACAT	

0[221]	CGAGCACAGACTTCAAATACCTCAAAAGCTGCA	
9[231]	TTAGTGTGAATCCCTCTAATAAAACGAAAGAACGATGAATTA	
4[629]	CAAATATCAAACCAGATGAATAT	
0[664]	GATTTTAGACAGGCATTAAAAATA	
10[667]	AGACGGCGAACGTGGCGAG	
0[599]	TTCTGGAATAATCCTGATTTTGCCCGGCCGTAA	
3[23]	TTTGCAACCAGCTTACGGCGGTGGTGAGGTTTCAGTTGAGGATCCTTTTT	
8[340]	GCGCCCGCACCCTCTCGAGGTGAATT	
7[674]	GCCTTACGCTGCGCGTAAAATTATTTTTTGACGCTCAATC	
7[86]	ATGAATCCCAGTCACGATCGAACGTGCCGGCCAGAGCACA	
5[245]	CGCCTGACGGTAGAAAGATTCTAATGCAGATACAT	
8[657]	GTATTAGAGCCGTCAATAGATAA	
3[308]	CTAAAGACTTTTAGGAACCCATG	
2[702]	TTTTTTATAACGTGCTTTCCTCTTTATAACAGTACTAT	
4[671]	TACTTCTTTGATAAAAATCTAAA	
2[391]	ATTAAAATAAGTGCGACGATTGGCCTTG	
9[189]	GAGCAAGGTGGCATTTACTCCAACAGGTTCTTTACGTCAACA	
4[167]	CAATATGATATTGATGGGCGCAT	
7[147]	GCTAATGCCGGAGAGGGTAGCTA	
7[464]	AAGCACAGAGCCTAATTATTGTTAGCGATTAAGACTCCTT	
8[172]	TAATCGTAGCATTACCTGAGAGTCTG	
0[580]	TAGAACCTACCAGTCTGAGAGAC	
4[354]	GAAAGTTCAACAATCAGCTTGCTTAGCTTTAATTGTATCG	
8[46]	CAGCATCAACCGCACGGCGGGCCGTT	
2[181]	TTATGGCCTGAGCACCTCAGAGCATAAA	
3[644]	CTATTAGTCTTTCGCCGCTACAG	
8[111]	CTTTTTTTTCGTCTCGTCGCTGGC	
11[231]	TTAATGAATCGGCCATTCATTCCAATACGCATAGT	
3[518]	AACAACATGTTCATCCTTGAAAA	
5[77]	AACGTTGTAGAAACAGCGGATAGTTGGGCGGTTGT	
10[706]	TTTTTAGGAGCGGGCGCTAGGAAGGGAAGAAAGCGAATTTTT	
9[441]	TGCCATACATAAAGATTAACTGAACACCAACAGCCGGAATAG	
7[189]	GGCTAAAGTACGGTGTCTGGAAG	
6[237]	AAGAGATTCATTTTGTTTAAGAGGAAGC	
5[203]	TGTAAATCATGCTCCTTTTGATAATTGCTGAATAT	
7[315]	AATCCAAAAAAAAGGCTCCAAAA	
10[583]	TGGCAAGTTTTTTGGGGTC	
2[559]	GAATTATCCAATAACGATAGCTTAGATT	
11[364]	GTCCACGCGCCACCTCACCGTTGAAACA	
11[471]	TGTTCCAACGCTAACGAACAAGTCAGCAGGGAAGCGCATT	
4[522]	ACCGCATTCCAACGGTATTCTAAGCGAGATATAGAAGGCT	
7[380]	TCAAGCAGAACCACCACTCACTCAGGTAGCCCGGAATAGG	
8[447]	ATTCTTTTCATAATCAAAATCAC	
6[321]	AAATCCCCGAAACAATTCATGAGGAAGT	
10[541]	CATTCTATCAGGGCGATGG	

10[373]	TACCTGGTTTGCCCCAGCA	
5[413]	AGAGTTTATACCAGTAGCACCTGAAACCATCGATA	
9[105]	GTCCGTCCTGCAAGATCGTCGGATTCTCTTCGCATTGGACGA	
11[63]	ATAGCTGTTTCCTGGAACGTCCATAACGCCGTAAA	
11[177]	TGCGTACTAATAGTAGTTGAAATGCATATTTCAACGCAAG	
8[702]	TTTTTAAAAACGCTCATGGAAATA	
7[441]	TTGAAGCCCTTTTTAAGAAAAGT	
11[525]	AGGGCGAAAAACCGATTTAACGTAGGGCAAATACC	
2[475]	AAATAGGTAATTTACAAATAAGAAACGA	
9[525]	TTTAGCAAACGCCACAATATAACTATATTCCCTTATAAATGG	
7[399]	TATTGCCTTTAGCGTCAGACTGT	
0[389]	GAATTGTAGCCAGAATGGATCAGAGCAAATCCT	
2[307]	TTCCATTGACCCAAAGAGGCTTTGAGGA	
7[651]	TAAGTAGAAGAACTCAAACTATCG	
2[517]	ACGCGTCGGCTGTAAGACGACGACAATA	
7[483]	GTTTACCGCGCCCAATAGCAAGC	
2[55]	TTCGCCATAAACTCTGGAGGTGTCCAGC	
10[48]	GCAGCACTTTGCTCTGAGCCGGGTCACTGTTGCCCTGCGGCTTTTT	
6[657]	TGCCTGAACAGCAAATGAATGCGCGAACT	
3[163]	TAAAGAGGCAAAATATTTTATAA	
0[538]	TTAGGTTGGGTTATAGATAAGTC	
4[419]	GCAGCACCGTAAGTGCCCGTATA	
8[214]	CAAATGGTTCAGAAGAACGAGTAGAT	
3[415]	GTTTATGTCACATGGGAATCCAC	
0[641]	CCGAACCCCCTAAAACATCGACCAGTTTAGAGC	
8[321]	CCGAACGGTGTACAGACCAGGCG	
3[457]	CAATCCAAAATACTGAACAGTAG	
6[195]	TGCAACTCAAAAGGCCGTACCAAAAACA	
0[95]	CCGGAAGACGTACAGCGCCGCGATTACAATTCC	
11[399]	GTTTGATGGTGGTTCAGAACCCCGCCTCACAGAAT	
11[25]	TTTTTCCGGGTACCGAGCTCGAATTCGTAATCTGGTCA	
0[53]	CGGTAGTACTCAATCCGCTGCTGGTCATGGTC	
8[256]	AAAATTCCATTCAGGCTTTTGCAAAAGAAGTCA	
3[266]	AACTTTAATCATGGGTAGCAACGGCTACGACAGCAACTAAAA	
10[247]	AATAACGCGCGGGGAGAGGCGGTT	
0[251]	TGGGAAGAAAAATCTACGTGCGTTTTAATT	
0[263]	CAGTCTTGATTTTAAGAAAC	
8[286]	GACCTTCATTTTGCCAGAGGGGGTAATAGT	
7[296]	AGACGTCGTCACCCTCAGACCTGCTC	
4[461]	AAGAAACAATGACCGGAAACGTC	biotin labeled
4[83]	GTACATCGACATCGTTAACGGCA	biotin labeled
5[665]	ATACCACCATCAGTGAGGCCAAACCGTTGTAGCAA	biotin labeled
4[251]	AACGCCAAAAGGCGGATGGCTTA	biotin labeled
5[119]	CATAATATTCCGTAATGGGATCCGTGCATCTGCCA	external labeling
3[98]	GGATAACCTCACAATTTTTGTTA	external labeling

S22

89

4[125]	GTTTGAGGGGACCTCATTTGCCG	external labeling
4[144]	CGTAAAGGTCACGAAACCAGGCAATAGCACCGCTTCTGGT	external labeling
0[137]	CATCAGCGTCTGGCCTTCCACAGGAACCTGGGG	external labeling
10[121]	GGGCCGGAAGCATAAAGTG	external labeling
11[135]	TAAAGGATTGTATAAGCGCACAAACGACATTAAATGTGAG	external labeling
7[128]	TTCCGAATTGTAAACGTGTCGCCAGCATCGGTGCGGGCCT	external labeling
3[140]	CAATAGGAACGCAAATTAAGCAA	external labeling
7[105]	GAAAGATCGCACTCCAGCCAGCT	external labeling
0[160]	GATAAAAATTTTTAGCCAGCTTT	external labeling
8[153]	TCAGGCTGCGCAACTGTTGGGAA	external labeling
0[118]	CGAGTAACAACCGTTTACCAGTC	external labeling
2[139]	TTCGCGGATTGATTGCTCATTTTTTAAC	external labeling
10[293]	ACCGGATGTTTTTCTTTTCACCA	5' ATTO 647N
10[279]	ACCCAAATGGCAAAAGAATACTCGGAACAGAATCC	5' ATTO 647N
10[286]	ATTCATTAGAGTAATCTTGACGCTGGCT	5' ATTO 647N
10[265]	AACAAAGCTGCTGTAACAACAAGGACGT	5' ATTO 647N
10[272]	TCAACGTTGCGTATTGGGCGCCAGGGTG	5' ATTO 647N

Supplementary References

1. Derr, N. D. *et al.* Tug-of-war in motor protein ensembles revealed with a programmable DNA origami scaffold. *Science* **338,** 662–665 (2012).
2. Nickels, P. C. *et al.* Molecular force spectroscopy with a DNA origami-based nanoscopic force clamp. *Science* **354,** 305–307 (2016).
3. Vogelsang, J. *et al.* A reducing and oxidizing system minimizes photobleaching and blinking of fluorescent dyes. *Angew. Chem. Int. Ed.* **47,** 5465–5469 (2008).
4. Holzmeister, P., Wünsch, B., Gietl, A. & Tinnefeld, P. Single-molecule photophysics of dark quenchers as non-fluorescent FRET acceptors. *Photochem. Photobiol. Sci.* **13,** 853–858 (2014).
5. Weston, K. D. *et al.* Measuring the Number of Independent Emitters in Single-Molecule Fluorescence Images and Trajectories Using Coincident Photons. *Anal. Chem.* **74,** 5342–5349 (2002).
6. Stangl, T. *et al.* Mesoscopic quantum emitters from deterministic aggregates of conjugated polymers. *Proc. Natl. Acad. Sci.* **112**, E5560-E5566 (2015).
7. Eder, T. *et al.* Switching between H- and J-type electronic coupling in single conjugated polymer aggregates. *Nat. Commun.* **8**, 1641 (2017).
8. Morawska, P. O. *et al.* Side-Chain Influence on the Mass Density and Refractive Index of Polyfluorenes and Star-Shaped Oligofluorene Truxenes. *J. Phys. Chem. C* **119**, 22102-22107 (2015).
9. Manzano, D. A short introduction to the Lindblad master equation. *AIP Advances.* **10**, 025106 (2020).
10. Fischer, K. A. *et al.* Dynamical modeling of pulsed two-photon interference. *New J. Phys.* **18**, 113053 (2016).

4.3 How Blinking Affects Photon Correlations in Multichromophoric Nanoparticles

Tim Schröder, Sebastian Bange, Jakob Schedlbauer, Florian Steiner, John M. Lupton, Philip Tinnefeld, and Jan Vogelsang

Single photon emission is the trade mark signature of a quantum system as it can only emit a maximum of one single photon per excitation cycle. The phenomenon shows as an absence in correlation amplitude for zero lag times and is referred to as photon antibunching. It is well understood for an isolated single photon source. If multiple single photon sources are present, in theory their number can be deduced by the degree of photon antibunching. However, most single photon sources like organic dyes are neither independent in close proximity nor do they yield a constant photon stream. Dark state formation can affect the measured degree of photon antibunching. However, the impact of photo blinking on photon antibunching has not yet been discussed in the literature.

The degree of photon antibunching can be determent either by the value at $g^{(2)}(0)$ or by the ratio of central to lateral correlation $\frac{N_C}{N_L}$ events. However, both procedures yield different results for the number of emitters in the presence of additional bunching amplitudes caused e.g. by photoblinking. Our collaboration partners from Regensburg first showed this in simulations with continuous wave excitation. My simulations for pulsed excitation showed the same result and we concluded that independent blinking chromophores must be interpreted with $g^{(2)}(0)$ and collective blinking chromophores due to SDA must be interpreted with $\frac{N_C}{N_L}$.

In experiments, I realized independent blinking of two ATTO 647N dyes on a DNA origami structure with an interdye distance of 12 nm. I induced photo blinking with an enzymatic oxygen scavenger and a buffer with freshly prepared trolox as reducing agent. As in the simulations, the $g^{(2)}(0)$ normalization yielded the expected degree of photon antibunching of ~ 0.5 for two dyes. The normalization with respect to the bunching amplitude $\frac{N_C}{N_L}$ underestimated the number of dyes. The realization of collective blinking was challenging because it originates from SDA. If SDA is observed, SSA will most likely also occur and effect the degree of photon antibunching as well. I minimized SSA by separating the ATTO 647N dyes by 6 nm. Additionally, I placed a FRET switch between the dyes. The 1,4-oxazine dye, ATTO 700, stochastically entered the anionic radical state under ROXS conditions and thereby diminished the quenching of the two ATTO647N dyes due to the blue-shift in the absorption spectrum. I separated the emission of the ATTO 700 dye at 694 nm from the ATTO 647N emission and was able to demonstrate that collective blinking requires $\frac{N_C}{N_L}$ normalization. Consequently, $g^{(2)}(0)$ normalization overestimated the number of chromophores for collective blinking dyes.

For experiments with unknown blinking characteristics, I presented two approaches to identify the blinking mechanism. First, I changed the bunching amplitude by varying the excitation laser power in the experiment. The $g^{(2)}(0)$ value with independent blinking remained unaffected and always provides the expected value for two chromophores. In the case of collective blinking, on the other hand, the $g^{(2)}(0)$ value scaled with the bunching amplitude, which implied an antibunching normalization with respect to the bunching amplitude. I demonstrated this for both types of blinking.

A more elegant way without a second excitation power is the variation of the bunching amplitude by microtime gating. The bunching amplitude is proportional to the fractional intensity difference between two intensity states. In case of collective blinking dyes, a dye is quenched by a dye in the dark state which acts as quenching moiety. As a result, it is subject to an additional non-radiative rate, which manifests itself in a shorter fluorescence lifetime. The non-quenched component can be isolated with microtime gating, which maximizes the bunching amplitude and effects $g^{(2)}(0)$. If $g^{(2)}(0)$ scales linearly with the bunching amplitude, the $\frac{N_C}{N_L}$ normalization must be chosen, which remains constant for each microtime gate. I was also able to show that the microtime gating with independent blinking does not affect the bunching amplitude and that $g^{(2)}(0)$ also remains constant. Additionally, the microtime gating approach provides the equilibrium constants and the SDA rate constant.

All in all, I was able to demonstrate in simulations and experiments that different blink mechanisms require different normalizations of the photon antibunching. In addition, I was able to provide universal guidelines for choosing the correct spectroscopic observable for counting chromophores.

ACS NANO

How Blinking Affects Photon Correlations in Multichromophoric Nanoparticles

Tim Schröder, Sebastian Bange, Jakob Schedlbauer, Florian Steiner, John M. Lupton, Philip Tinnefeld, and Jan Vogelsang*

ACCESS | Metrics & More | Article Recommendations | Supporting Information

ABSTRACT: A single chromophore can only emit a maximum of one single photon per excitation cycle. This limitation results in a phenomenon commonly referred to as photon antibunching (pAB). When multiple chromophores contribute to the fluorescence measured, the degree of pAB has been used as a metric to "count" the number of chromophores. But the fact that chromophores can switch randomly between bright and dark states also impacts pAB and can lead to incorrect chromophore numbers being determined from pAB measurements. By both simulations and experiment, we demonstrate how pAB is affected by independent and collective chromophore blinking, enabling us to formulate universal guidelines for correct interpretation of pAB measurements. We use DNA-origami nanostructures to design multichromophoric model systems that exhibit either independent or collective chromophore blinking. Two approaches are presented that can distinguish experimentally between these two blinking mechanisms. The first one utilizes the different excitation intensity dependence on the blinking mechanisms. The second approach exploits the fact that collective blinking implies energy transfer to a quenching moiety, which is a time-dependent process. In pulsed-excitation experiments, the degree of collective blinking can therefore be altered by time gating the fluorescence photon stream, enabling us to extract the energy-transfer rate to a quencher. The ability to distinguish between different blinking mechanisms is valuable in materials science, such as for multichromophoric nanoparticles like conjugated-polymer chains as well as in biophysics, for example, for quantitative analysis of protein assemblies by counting chromophores.

KEYWORDS: single-molecule spectroscopy, photon statistics, DNA-origami structures, photophysics, quantum optics
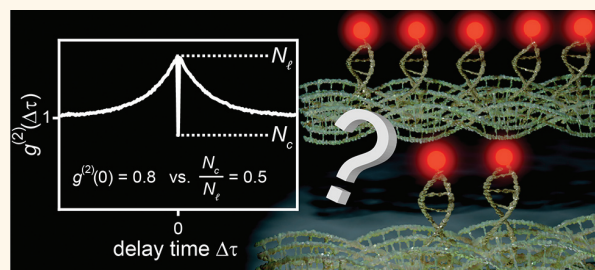
Counting the night sky's visible stars is a formidable task, not least due to omnipresent atmospheric flickering and clouds masking the line of sight. The challenge is fundamentally limited by the ability to resolve emission from close stars, which can only be overcome by ever-larger telescopes. The same limitation exists in the nanocosm when counting fluorescent chromophores. If the chromophores cannot be resolved in space,[1−5] one turns to measuring the autocorrelation statistics of emitted photons with a Hanbury Brown and Twiss (HBT) setup as illustrated in Figure 1a.[6−9] A single chromophore can only emit a single photon per unit of time that it spends in the excited state, a trademark signature of systems as varied as organic dyes,[10−13] nitrogen vacancies in diamonds,[14,15] and single ions.[16−18] This property manifests itself as a lack of autocorrelation amplitude for zero delay time, a phenomenon which is commonly referred to as photon antibunching (pAB). Correlation statistics and pAB are well understood for single chromophores but become very challenging to interpret for multiple chromophores in a nanoparticle. Such systems are studied in

a range of material systems that are typically not associated with single photon emission, such as 2D materials,[19] clusters of quantum dots,[20] and molecular crystals.[9,21] The degree of pAB can serve as a probe for the number of emitting units in the system and may indicate excited-state processes such as defect emission,[22] tri- and biexciton emission,[23] and singlet−singlet annihilation (SSA).[24−26] It is often challenging to disentangle these different contributions to pAB to truly understand the underlying photophysics of a system. Recently, multichromophoric DNA-origami structures and conjugated-polymer aggregates allowed us to demonstrate that the number of chromophores can indeed be counted, even if the dye
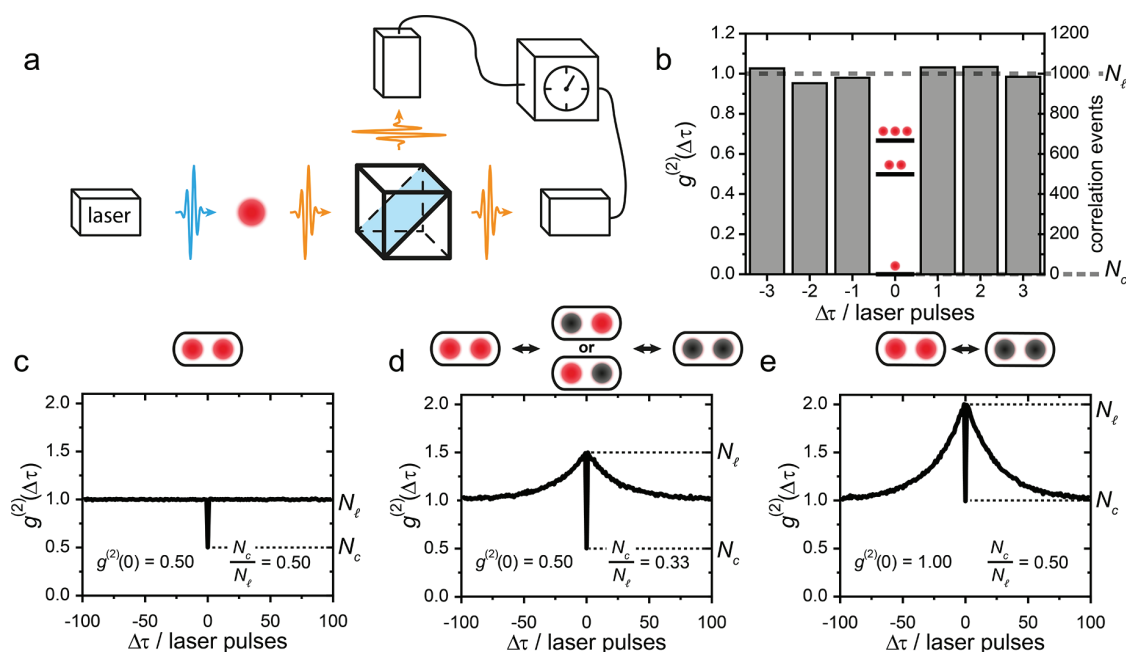
Figure 1. (a) Schematic representation of the experimental setup. A pulsed laser (blue) excites a single chromophore (red circle). The fluorescence (orange) is collected and detected in a HBT photon correlator with a 50/50 beam splitter, two single-photon detectors, and a time correlator. (b) Correlation histogram with the second-order intensity correlation $g^{(2)}(\Delta\tau)$ on the left ordinate and the total correlation events N on the right ordinate, respectively. The height of the central correlation count N_c reflects the number of chromophores on a reciprocal scale, examples of which are indicated by red dots. (c) Correlation histogram for two simulated, ideal chromophores without any dark states. (d) Correlation histogram for two simulated, independently blinking chromophores. The blinking results in photon bunching in the correlation histogram, while $g^{(2)}(0)$ yields the correct number of chromophores. (e) Correlation histogram for two simulated, collectively blinking chromophores. For this blinking behavior, N_c/N_l yields the correct number of chromophores, but not $g^{(2)}(0)$.

molecules interact with each other,[27,28] for example, by SSA.[24−26,29] Such chromophore counting in nanoparticles is not only of significance in the context of materials science[9] but also plays an important role in biophysics. Many protein assemblies could, in principle, be studied quantitatively by labeling them with fluorescent dyes and subsequently counting the chromophores. Dynamic processes such as self-association and oligomerization of proteins are prominent examples and are crucial to the operational mechanism of many such proteins.[30−33] Nanoscale clustering of membrane proteins, for example, has emerged as a common feature, possibly initiating and amplifying signal transduction across the plasma membrane, for example, in the immune response of T cells.[34] Direct experimental access to the number of participating proteins in such a process is therefore a prerequisite for a quantitative technique to study these mechanisms.

Similar to counting twinkling stars, the problem of chromophore counting is compounded by the presence of random switching between states (blinking), typically between a state that shows fluorescence (bright) and a state that is essentially nonfluorescent (dark). Consider two identical but independently blinking chromophores that for a given irradiance each spend 10% and 90% of their time in the fluorescent and nonfluorescent state, respectively. Only for 1% of the measurement time would both chromophores simultaneously reside in their fluorescent state. During 81% of the measurement time, both chromophores would simultaneously be in their dark state and would thus not contribute to the photon statistics. For the remaining 18% of the measurement time, though, only one single dye molecule is

emissive. Although two blinking dyes are present in principle, the measured fluorescence intensity autocorrelation and the pAB are then dominated by the characteristics of one single dye molecule. Obviously, this situation changes dramatically when the blinking process of the two chromophores is correlated. The occurrence of luminescence blinking and the type of blinking, that is, collective or individual, must therefore be taken into consideration for the correct interpretation of the pAB signature. Unfortunately, chromophore blinking is a common process with many different physical origins, for example, the formation of triplet states,[35−37] radical states,[36,38,39] energy transfer to a nearby quencher,[40−42] or nonradiative Auger recombination such as occurs in semiconductor nanocrystals.[43] In some cases, the blinking can be reduced by photostabilizing agents,[38,44−49] but it is almost impossible to completely turn off the blinking, especially for chromophores embedded in solid-state environments.

Here, we demonstrate how the pAB signature is affected by independent and collective chromophore blinking by using both simulations of the rate equations as well as controlled experimental model systems, allowing us to formulate universal guidelines for the correct interpretation of pAB data in any multichromophoric aggregate material system.

We make use of DNA origami to design multichromophoric probes, which exhibit either independent or collective blinking of the chromophores, and present two approaches to distinguish experimentally between these two blinking mechanisms. The first one utilizes different dependencies of the pAB signature on the excitation intensities with respect to the blinking mechanism. The second approach exploits the fact that collective blinking implies energy transfer to a quencher,

which is a time-dependent process. Therefore, the effective degree of collective blinking can be altered by time-gating the photon stream under pulsed excitation, which also enables us to extract the energy-transfer rate to a quencher.

RESULTS AND DISCUSSION

The inherent challenge in counting blinking chromophores by pAB with an HBT setup is illustrated in Figure 1. Under a confocal microscope, a pulsed laser source excites a chromophore (red circle). The excited electronic system releases the stored energy by emitting at most one fluorescence photon per excitation pulse and chromophore. A 50/50 beam splitter distributes the fluorescence photons on two photodetectors, and a time correlated single photon counting (TCSPC) system records the events detected. This allows calculation of the normalized second-order intensity correlation:.[50,51]

$$g^{(2)}(\Delta\tau) = \frac{\langle I_1(t) \cdot I_2(t+\Delta\tau)\rangle}{\langle I_1(t)\rangle\langle I_2(t)\rangle} \tag{1}$$

which correlates the intensity measured on one detector with the intensity measured on the other one as a function of the lag time $\Delta\tau$.

This correlation is shown on the left ordinate in Figure 1b. On the other hand, one can also simply count the number of correlation events, N, that is, the simultaneously detected photon events on both detectors as a function of lag time $\Delta\tau$. This approach is indicated on the right ordinate in Figure 1b, binned in integral multiples of the excitation pulse repetition time. There are essentially two ways that the degree of pAB has been defined in the past, either by the ratio of central correlation events, N_c, to the average of lateral correlation events, N_l, as indicated in Figure 1b or by the value of $g^{(2)}(\Delta\tau)$ for $\Delta\tau = 0$. The N_l value commonly does not include values past ± 3 laser pulse periods or ± 37.5 ns at a repetition rate of 80 MHz. In a system carrying n chromophores, the number of correlation events for $\Delta\tau = 0$, that is, N_c, is given by $n \cdot (n-1)$, because the first photon can be emitted by n chromophores and the second photon only by the remaining $n-1$ chromophores. On the other hand, the number of correlation events for $\Delta\tau \neq 0$, that is, N_l, is given by n^2, because also the second photon can be emitted by n chromophores in the next excitation cycle. Therefore, N_c/N_l equals $n \cdot (n-1)/n^2 = (n-1)/n$. In an ideal system, where chromophores do not undergo dark-state formation or SSA, the number of chromophores, n, can therefore be calculated from $n = (1 - N_c/N_l)^{-1}$, which also agrees to $n = (1 - g^{(2)}(0))^{-1}$ assuming $g^{(2)}(0) = N_c/N_l$,[7] essentially corresponding to using two different normalization methods for the intensity autocorrelation.

For a single chromophore, both N_c/N_l and $g^{(2)}(0)$ are zero. For two and three nonblinking chromophores, these values are 0.50 and 0.67, respectively, as shown in Figure 1b. For ideal nonblinking chromophores, both equations result in the correct number of chromophores n. Figure 1c shows the correlation analysis for two simulated, nonblinking chromophores (see Supporting Information for details). Both normalizations, $g^{(2)}(0)$ and N_c/N_l, yield a value of 0.5, which matches the expectation for two chromophores. In experiments, however, chromophores do not only transition between the electronic ground and first excited state. Through quantum jumps from the singlet to the triplet state, which has an

excited-state lifetime many orders of magnitude longer,[35,36] the otherwise continuous emission of photons, that is, cycling between electronic ground and excited states, is interrupted, which causes blinking. Blinking fluorescence trajectories lead to $g^{(2)}(\Delta\tau)$ values larger than 1 (bunching) if $\Delta\tau$ falls within the range of the lifetimes of bright and dark states. Effectively, the bunching behavior stems from the fact that the photon stream, which originates from the transitions while the dye is in its singlet manifold, is interrupted for the time scale of the lifetime of the dark state. For this reason, the photons appear to be bunched provided that the molecule actually fluoresces.

Figure 1d shows $g^{(2)}(\Delta\tau)$ for the simulated emission of two equal and independent chromophores that blink stochastically. Here, we must consider three cases. First, a case where both chromophores are in the bright state. Second, a case where only one chromophore is in the bright state, and third, a case where both are in the dark state. The photon bunching associated with the emission intermittency causes $g^{(2)}(\Delta\tau)$ values of 1.5 in the range of $\Delta\tau$ values from which N_l is calculated. The calculated degree of pAB is now quite different for the two metrics $g^{(2)}(0)$ and N_c/N_l. The value of 0.5 expected for two chromophores is only retrieved from $g^{(2)}(0)$, whereas N_c/N_l is reduced to 0.33, which would normally be associated with an effective value of $n = 1.5$ chromophores, which, of course, is unphysical. The normalization to N_l effectively averages over the two cases where either only one or both chromophores are in the bright state. On the other hand, only situations where both chromophores are in the bright state contribute to central-bin photon correlation events N_c.

Next, we consider collective blinking of two chromophores in Figure 1e. Correlated blinking is expected to occur in multichromophoric aggregates such as conjugated polymers or light-harvesting complexes,[52−55] in which, for example, a triplet exciton can annihilate multiple singlet excitons.[56−59] In this case, the degree of pAB based on the correlation events in central and lateral bins now yields the correct value of $N_c/N_l = 0.5$ expected for two chromophores, while $g^{(2)}(0) = 1$, which would instead correspond to an infinite number of chromophores. Obviously, $g^{(2)}(0)$ underestimates the degree of pAB for the correlated system since it averages over the emitting and the nonemitting states and thus scales linearly with the bunching amplitude. In extreme cases, even values above 1 are possible, which is usually the characteristic of thermal or chaotic light emission.

Although it is straightforward to simulate both independently and collectively blinking quantum systems, the effect of the different blinking mechanisms has not been demonstrated experimentally so far. As a model system for independently blinking chromophores, we positioned two ATTO 647N dye molecules in a DNA origami structure, which provides us with precise control over the distance between the two dyes as well as their immediate environment.[60−62] A dye separation of 12 nm was chosen to minimize any mutual interaction. Both chromophores were excited with a pulsed laser at a wavelength of 640 nm with a repetition rate of 40 MHz. To minimize photobleaching over time, we used an enzymatic oxygen scavenger system of glucose oxidase and catalase.[49] For fast blinking kinetics, 2 mM of freshly prepared Trolox is added to the buffer.[49] With fresh Trolox, fast blinking is observed due to the formation of radical anions that are reoxidized by trace amounts of Trolox-quinone, yielding off-times in the range of 10−100 ms.[49] A short section of a fluorescence time trace of
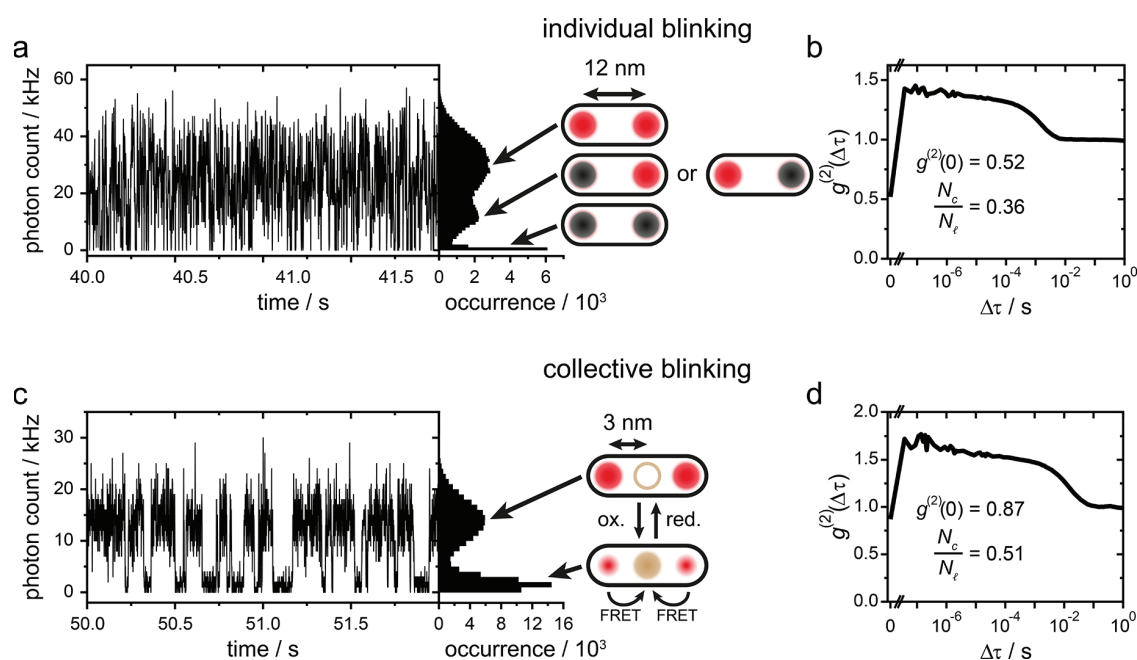
Figure 2. (a) A short section of a representative fluorescence transient of two independently blinking ATTO 647N dyes with 12 nm spacing at 1.1 kW/cm² excitation power and 1 ms time binning. The intensity histogram on the right side is based on the full trajectory covering 38 s of measurement time and shows three characteristic intensity levels at 0, 15, and 30 kHz. (b) Corresponding second-order intensity correlation on a logarithmic delay-time scale. In this case, $g^{(2)}(0)$ yields the correct value for two dyes. (c) A short section of a representative fluorescence transient of two collectively blinking ATTO 647N dyes, controlled by an intermediate ATTO 700 FRET switch, measured at 1.1 kW/cm² excitation power and 1 ms time binning. The separation between the two ATTO 647N dyes is ∼6 nm to minimize SSA, while at the same time allowing for sufficient quenching by the ATTO 700 dye. The intensity histogram on the right is based on the full intensity trajectory covering 110 s of measurement time and shows only two intensity levels. (d) Second-order intensity correlation corresponding to the fluorescence time trace of (c) on a logarithmic delay-time scale. Here, N_c/N_l instead yields the correct value for two dyes.

such a model system at 1.1 kW/cm² excitation power is shown in Figure 2a (for the complete fluorescence trajectory, see Figure S4). In the intensity histogram calculated based on the full data set and shown on the right of Figure 2a, three characteristic intensity levels at 0, 15, and 30 kHz can be identified. These correspond to either none, only one, or both dyes being in the dark state, respectively. The second-order intensity correlation $g^{(2)}(\Delta\tau)$ in Figure 2b is shown on a logarithmic time scale, which allows better appreciation of the intensity dynamics over several orders of magnitude in delay time.[63] As expected for two dye chromophores, $g^{(2)}(0) = 0.52$ for this data set. On the other hand, $N_c/N_l = 0.36$, a value much lower than expected. This value is artificially lowered because the intensity level with only one chromophore being in the bright state contributes only to lateral correlation events N_l, but not to central correlation events N_c.

Experimental realization of collective blinking of two organic dye molecules is much more challenging.[24] The main difficulty is that collectively blinking systems exhibit weak interchromophoric coupling not only through singlet—dark-state annihilation (SDA) but also due to SSA. Such processes all depend on energy—transfer efficiency, which is governed by the spectral and photophysical properties of the dyes involved.[24] This significantly reduces the chance of detecting photon pairs and lowers the apparent number of chromophores.[24—27,64,65] SSA therefore usually tends to counteract the apparent increase of $g^{(2)}(0)$ in systems with collective blinking. In order to study the role of collective blinking, reliable and well-controlled model systems are thus needed, which at the same time show both strong SDA and negligible levels of SSA. To this end, dye

molecules need to be separated by a distance at which the effect of SSA can be neglected. On the other hand, the weak chromophore—chromophore coupling necessary for SDA and collective blinking to occur needs to be retained. We overcome this problem by placing a switchable Förster resonance energy transfer (FRET) absorber between two ATTO 647N dyes that are separated by 6 nm, enough to reliably suppress SSA.[40] The FRET switch is a 1,4-oxazine dye, ATTO 700 with an excited-state lifetime of ∼1.6 ns. In its singlet state, it acts as an energy sink and quenches both ATTO 647N dyes equally. The quencher or acceptor dye ATTO 700 is placed in the center of both donor dyes ATTO 647N, and therefore the FRET rate of the donor dyes to the acceptor is approximately equal. We note that this equality might not be valid if the acceptor dye is already in an excited state due to absorption of the energy of one donor dye. But even in this case, the quencher is capable of absorbing energy by transitioning to higher excited states S_n, that is, SSA occurs. However, the fluorescence lifetime of the acceptor dye is very short with 1.6 ns compared to the donor dyes with 4.3 ns. For this reason, it is unlikely that the acceptor is still in its excited S_1 state once energy transfer occurs from the second donor dye. The acceptor dye will rather relax quickly and can absorb the energy of the remaining donor dye, through ground-state absorption. This is also a very rare process because we are working in an excitation regime in which two excited donor dyes are a very rare event (an estimation of the occurrence frequency is given in the Supporting Information). What we mean here by collective blinking is that, if the acceptor dye ATTO 700 is in its ground state S_0, it will absorb the excitation energy by FRET from

96

both donor dyes and therefore quenches both donor dyes simultaneously. Once the acceptor dye is reduced, it is not capable of absorbing energy any longer so that both donor dyes fluoresce simultaneously. We note that the orientation in space and the differences in excitation efficiency of the chromophores are not an issue in our model system because the dyes are linked by a C_6-linker to the DNA origami structure. Therefore, the dyes are free to rotate and the energy-transfer process averages over all possible orientations of both donor and acceptor chromophores. However, in real systems, such as in conjugated polymer nanoparticles, the orientation of chromophores is fixed in space and plays a significant role regarding the energy-transfer dynamics, as discussed in ref 27. The fluorescence of ATTO 700 can be spectrally separated from the ATTO 647N emission and will thus not contribute to the measured photon statistics. By chemically reducing the ATTO 700 dye, its absorption spectrum shifts to the blue, resulting in less quenching of the ATTO 647N dyes due to the reduced spectral overlap. A subsequent oxidation reaction recovers the ground state and the concomitant quenching action on ATTO 647N. In our experiment, a reducing and oxidizing buffer (ROXS) of Trolox and Troloxquinone switches the ATTO 700 oxidation state stochastically.[40] A section of the resulting ATTO 647N fluorescence intensity time trace at 1.1 kW/cm² excitation power is shown in Figure 2c. Here, only two intensity states are clearly visible, both in the time trace as well as in the corresponding intensity histogram (the complete fluorescence time trace is shown in Figure S5). The intensity correlation in Figure 2d shows the expected photon bunching on a time scale of tens of milliseconds. For this data set, $g^{(2)}(0) = 0.87$ is indeed much larger than the expected value of 0.5. The resulting apparent number of $n \approx 7{-}8$ chromophores obviously overestimates the actual number of chromophores, because it scales with the photon bunching amplitude as discussed above. In contrast, $N_c/N_l = 0.51$ yields the correct degree of pAB.

As we have demonstrated so far, the applicability of the degree of pAB as measured by either N_c/N_l or $g^{(2)}(0)$ for chromophore counting is strongly influenced by the switching dynamics between bright and dark states and the associated contributions to photon bunching. While the average time that a chromophore stays in the dark state is constant in our experiments, the time for switching into the dark state shortens with rising excitation power, as was demonstrated before and is illustrated in the Supporting Information for the fluorescence transient of Figure S4 for the dyes used here.[56,66] Figure 3 shows histograms for the degree of pAB for the two-chromophore model systems at excitation powers of 1.1 kW/cm² and 4.3 kW/cm². We note that the fluorescence signal increases linearly from ~15 kHz up to ~58.5 kHz for excitation powers of 1.1 and 4.3 kW/cm², respectively, which means that we are in a linear excitation regime where SSA and multiphoton processes with photophysical pathways involving higher excited states can be neglected.[67] Figure 3a,b shows results for $g^{(2)}(0)$ and N_c/N_l, respectively, for the system with independently blinking chromophores. A total of 89 dye-labeled DNA-origami structures were measured. Only DNA-origami structures were measured on which all dyes were attached. Even though the dyes are very photostable under ROXS stabilization, photobleaching or spectral shifts will occur eventually during the measurement and impact the photon statistics. Therefore, we analyzed the individual transients until
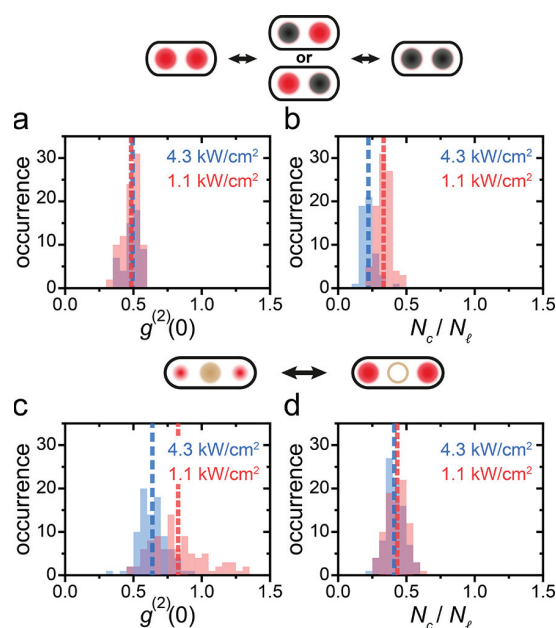
Figure 3. (a) Histogram of $g^{(2)}(0)$ values for 87 single DNA-origami particles with two independently blinking ATTO 647N dyes at excitation powers of 1.1 kW/cm² (red) and 4.3 kW/cm² (blue). The distributions have mean values of 0.483 ± 0.006 and 0.493 ± 0.007. (b) Corresponding histograms of N_c/N_l values of two independently blinking ATTO 647N dyes. The mean values are 0.333 ± 0.006 and 0.221 ± 0.007. (c) Histogram of $g^{(2)}(0)$ values for 87 measured particles of two collectively blinking ATTO 647N dyes. The mean values are 0.82 ± 0.02 and 0.63 ± 0.01. (d) Corresponding N_c/N_l values of two independently blinking ATTO 647N dyes with mean values of 0.432 ± 0.008 and 0.411 ± 0.007.

a bleaching event occurs or a significant spectral shift was observed as demonstrated in Figures S4−S6. For both excitation intensities, similar Gaussian $g^{(2)}(0)$ distributions with mean values of 0.483 ± 0.006 at 1.1 kW/cm² and 0.493 ± 0.007 at 4.3 kW/cm² are found, close to the expected value of 0.5 for two chromophores. On the other hand, the histograms for N_c/N_l in Figure 3b show a systematic shift toward lower values for the higher excitation intensity, as the photon bunching amplitude is suppressed. We obtain average values of 0.333 ± 0.006 for 1.1 kW/cm² and 0.221 ± 0.007 at 4.3 kW/cm². These results can again be rationalized by the sensitivity of the N_l measurement to cases where only one chromophore is in the dark state. These cases do not contribute to the value of N_c.

Figure 3c,d shows histograms for $g^{(2)}(0)$ and N_c/N_l values determined for 87 different measurements of collectively blinking single DNA-origami structures using the same set of excitation powers. The blinking kinetics of ATTO 700 attached to the DNA origami is less uniform compared to the case of independent blinking, so that the histograms appear broader than those in Figure 3a,b. The calculated mean values for $g^{(2)}(0)$ are therefore systematically shifted toward higher numbers. For the $g^{(2)}(0)$ histograms in Figure 3c, the mean values are 0.82 ± 0.02 at 1.1 kW/cm² and 0.63 ± 0.01 at 4.3 kW/cm², corresponding to apparent numbers of chromophores n of 5.5 and 2.7, respectively. In this experiment, the amplitude scales inversely proportionally to the excitation intensity. The acceptor dye switches faster into its reduced
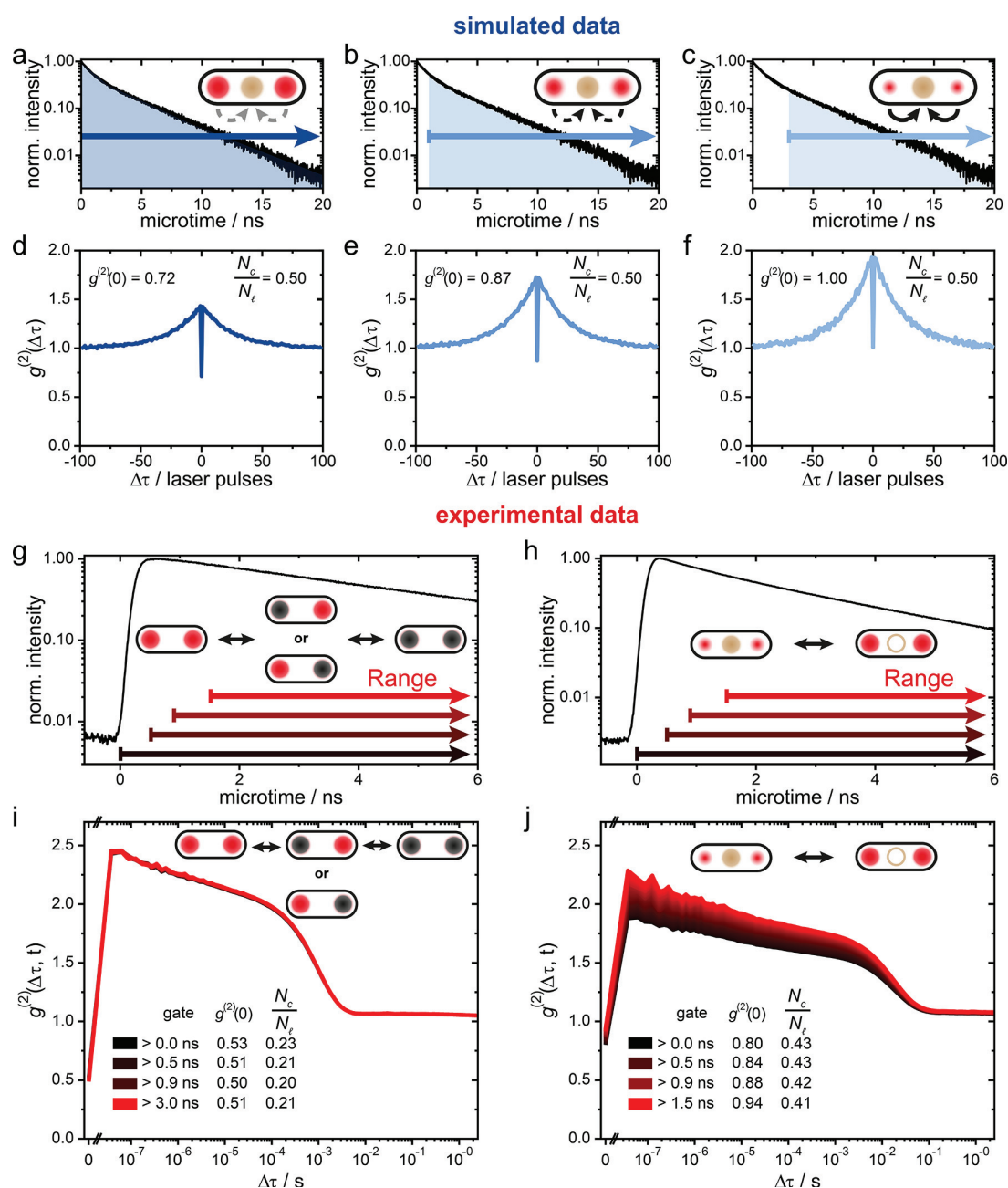
Figure 4. (a−c) Simulated fluorescence decay of two collectively blinking dye molecules showing a biexponential decay. (d−f) Corresponding second-order intensity correlation, $g^{(2)}(\Delta\tau)$, of the long-pass gated intensity time trace. Time gates are indicated by arrows and highlighted in blue (a−c). (g) Experimental fluorescence decay of two independently blinking ATTO 647N dyes. (h) Fluorescence decay of two collectively blinking ATTO 647N dye molecules. (i) Corresponding $g^{(2)}(\Delta\tau)$ of accumulated fluorescence transients at 4.3 kW/cm² excitation intensity of 35 single nanoparticles shown for four different time gates. No change of the correlation amplitude is observed with photon gating. The $g^{(2)}(0)$ and N_c/N_l values stay constant for different time gates, but only $g^{(2)}(0)$ yields the expected value of ∼0.5. (j) Corresponding $g^{(2)}(\Delta\tau)$ of 39 accumulated fluorescence transients at 1.1 kW/cm² excitation intensity for different time gates. The correlation amplitude increases for later gate times due to the increased intensity contrast of the two luminescence intensity states. The $g^{(2)}(0)$ values scale linearly with the correlation amplitude, but only $N_c/N_l \approx 0.5$ reflects the expected number of chromophores considering the weak SSA occurring between the two dyes.

state at higher excitation power, deactivating the quenching effect.[40] The shift back to its neutral ground state though depends on the buffer conditions, which are kept constant in the experiment. The ATTO 647N dyes therefore spend less time in the quenched state at higher excitation intensities, causing lower photon correlation amplitudes. Both N_c and N_l

are equally sensitive to this effect since both chromophores are either in their bright or dark state, and the N_c/N_l values are nominally unaffected by changes in excitation power. The N_c/N_l histograms extracted from the 87 measurements show overlapping Gaussian distributions with a mean of 0.432 ±

0.008 for 1.1 kW/cm^2 and 0.411 ± 0.007 for 4.3 kW/cm^2 excitation intensity, slightly below the value of 0.5 expected for two chromophores. This observation indicates that the two ATTO 647N dyes are not entirely independent of each other after all, but may be subject to weak SSA.

So far, we have only demonstrated the effect of different blinking characteristics on the photon statistics using well-defined model systems, in which energy-transfer processes between the dyes can be largely neglected. In more realistic multichromophoric nanoparticles (mcNPs), however, one must consider the interplay between SSA and SDA (see Figure S6). For this reason, we introduce a second method to distinguish between independently and collectively blinking dyes. In mcNPs with efficient interchromophoric energy transfer, spontaneous triplet exciton formation on one chromophore can lead to efficient singlet−triplet annihilation (STA) for the others,[24,41,56] causing collective blinking. The observed fluorescence lifetime is then shortened, resulting in a lower fluorescence quantum yield and weaker fluorescence intensity. The fluorescence decay in this case is not monoexponential anymore because the emission switches between states with and without the presence of the triplet exciton. In contrast, the fluorescence decay of mcNPs with independently blinking dyes, that is, without STA, shows a monoexponential time dependence, as triplet exciton for-mation on one chromophore does not affect the others. This stark difference in the fluorescence decay behavior can be exploited by microtime gating following pulsed excitation, that is, by selecting subpopulations of fluorescence photons with increasing arrival times after excitation[68−70] and calculating $g^{(2)}(\Delta\tau)$ for each subpopulation.

The correlation amplitude depends on the contrast between the two emission intensity states.[50,51,57,69] For the case of independently blinking chromophores, we neither expect a change of the correlation amplitude nor of the pAB for the different gate times, simply because the intensity contrast between the states does not change as a function of time after excitation. This is different for collectively blinking chromo-phores. The contrast between the two states increases from early to late microtime gates because the fluorescence of the quenched state decays faster than the fluorescence of the unquenched state. The result is a larger intensity contrast for later microtime gates. In the following, we demonstrate this with numerical simulations (see Supporting Information for details). In Figure 4a, we simulated collective blinking for a two-chromophore system with a FRET switch, modeled to mimic the experimental situation. As expected, the fluores-cence decay is biexponential. If we consider all emitted photons (indicated by the blue area), both emission intensity states contribute to $g^{(2)}(\Delta\tau)$, shown in Figure 4d. The correlation data show a limited amount of photon bunching, and only N_c/N_l corresponds to the correct value for a two-chromophore system. Experimentally, one would not be able to decide at this point whether to use N_c/N_l or $g^{(2)}(0)$ for counting the chromophores, because the underlying blinking mechanism is unknown. If photons emitted at later times (>1 ns) are considered, however, as in Figure 4b, it becomes more likely that energy transfer and SDA take place, which reduces the donor fluorescence intensity. The result is an increased intensity contrast between the bright and dark fluorescence states that leads to a higher photon correlation amplitude, shown in Figure 4e. The $g^{(2)}(0)$ indicates an apparent number of 6−7 chromophores, while N_c/N_l stays constant and

corresponds to two chromophores. Finally, we correlate only the latest arriving photons (>3 ns), for which we do not expect to see fluorescence from the quenched state. The correlation amplitude is maximized here and only depends on the ratio of the reducing rate and the oxidizing rate of the FRET switch. The $g^{(2)}(0)$ in Figure 4f evidently scales with the amplitude and even leads to a value that one would expect for an infinite number of chromophores, whereas N_c/N_l still indicates two chromophores with a value of $N_c/N_l = 0.50$.

Finally, we apply this microtime gating analysis to our experimental data. To perform a second-order intensity correlation with acceptable photon statistics even for the smallest time differences $\Delta\tau$, we accumulated 35 individual data sets collected from independently blinking dyes and 39 data sets from collectively blinking dyes. The starting point of the long-pass microtime gate was chosen to increase in steps of 20 ps for each intensity correlation. The fluorescence decay of two independently blinking ATTO 647N dye molecules in Figure 4g is monoexponential, with a fluorescence lifetime of $\tau_{fl} = 4.3 ± 0.1$ ns. The measured intensity correlations are shown in Figure 4i, with gate times indicated by color and a corresponding arrow in Figure 4g. The correlation curve and the extracted values of $g^{(2)}(0)$ and N_c/N_l are independent of the chosen gate time, indicating independently blinking chromophores. Based on this observation, $g^{(2)}(0)$ must be chosen to calculate the number of chromophores. Without any gating of the photons, $g^{(2)}(0) = 0.53$, slightly larger than the value of 0.5 expected for a two-chromophore system. We attribute this discrepancy to multiple excitation cycles of one single dye molecule within the same laser pulse of duration ~80 ps.[71] Long-pass gates starting at 500 ps do not suffer from this artifact.

The fluorescence decay of two collectively blinking ATTO 647N dyes in Figure 4h is biexponential, and we obtain $\tau_{fl,1} = 0.6 ± 0.1$ ns and $\tau_{fl,2} = 2.7 ± 0.1$ ns as fluorescence lifetimes by reconvolution fits (see Figure S10). The intensity correlation for each gate is shown in Figure 4j with a color gradient from early (black) to late (red) gate times. The correlation amplitude rises with gate time because the contrast between the two intensity states becomes larger as a function of time after excitation. This increase is a characteristic signature of collectively blinking chromophores when an additional non-radiative pathway is introduced due to dark-state formation in a multichromophoric system. The observed $g^{(2)}(0)$ values start out at $g^{(2)}(0) = 0.8$ for the case of all photons being detected. This value would already correspond to 5 emitting chromophores, which, of course, is an unphysical result for the given material system. The value rises further for increased gate times, with the correlation amplitude reaching $g^{(2)}(0) = 0.94$ for photons detected after 1.5 ns, which would correspond to almost 17 chromophores emitting. The rise of $g^2(0)$ with increasing gate delay is directly linked to the SDA quenching rate, which can be extracted by plotting the correlation amplitude against the starting time of the photon gate (see Figure S8 for a simulation and Figure S9 for experimental data; an explanation is given in the Supporting Information). From these dynamics, the SDA rate is determined to be $k_{SDA} = 1.3 ± 0.3$ ns^{-1}. In contrast, the metric N_c/N_l yields values ranging from 0.43 for the case of all photons being detected to 0.41 for photons detected after a gate delay of 1.5 ns. These values are somewhat smaller than one would expect for two chromo-phores, which may be anticipated since the dye molecules are

only separated by ~6 nm: In addition to SDA, SSA can still take place and reduce the probability of detecting two photons from one excitation pulse.[27] Weak SSA is also indicated by the decreasing values of N_c/N_l from early to late microtime gates.[27] Microtime gating thus allows us to clearly discern the two types of blinking, independent and collective, and provides a guideline to choosing the correct spectroscopic observable for counting chromophores. For systems with strong SSA, techniques such as psTRAB must be used with the correct normalization of the photon bunching amplitude in order to correctly estimate the number of chromophores and the SSA rate.[27,70]

CONCLUSION

The issue of correct normalization of pAB measurements for blinking multichromophoric systems has mostly been neglected previously but is evidently key to counting blinking chromophores and interpreting the mutual interactions between chromophores. Different types of blinking of a multichromophoric system, that is, independent or collective blinking, require very different normalizations of the pAB data. We have illustrated these challenges by both simulations and experiments. For independently blinking dyes, the normalization to lateral photon correlation events N_c/N_l averages over the photon statistics due to either one or two chromophores being in the fluorescent state and thus underestimates the number of chromophores. For collectively blinking dyes, on the other hand, the number of chromophores is instead overestimated by the normalization to the average intensity as carried out for $g^{(2)}(0)$.

We have introduced two approaches to distinguish between these two blinking mechanisms experimentally. The first approach varies the excitation power to change the blinking rate and the associated correlation amplitude. Both independent and collective blinking show inverse scaling of the correlation amplitude with excitation intensity. The second approach uses photon gating of the photon arrival times after pulsed excitation. Concomitant variation of the correlation amplitudes is characteristic for collective blinking and indicates that a N_c/N_l normalization is required. However, in actual multichromophoric systems such as conjugated-polymer nanoparticles or light-harvesting complexes, both types of blinking mechanisms might occur simultaneously or change dynamically, due to the formation of a quencher. For simply counting the number of chromophores, we suggest that one should construct a second-order correlation curve only from the earliest photons after excitation, for example, using a time window of ~0−400 ps after excitation, if the PL lifetime is in the range of ~4 ns as for the dyes studied here. For these photons, a possible quenching process due to excitation energy transfer to a quencher within the multichromophoric aggregate can be neglected. Such energy transfer is imperative for a collective blinking process. This means that such a second-order correlation curve acquired with early time photons is dominated only by the independent blinking process, for which $g^{(2)}(0)$ must be considered to count the correct number of chromophores. On the other hand, we can also choose a time gate long after excitation, which will show a combination of both independent and collective blinking mechanisms in the second-order correlation curve. Using both correlation curves, that is, for an early time window and a late-time gate, it will, in principle, be possible to also extract the quenching rate by a

quencher and estimate the degree of independent and collective blinking in the multichromophoric system. Although we refrain from discussing an experimental application here, a simulation demonstrating that $g^{(2)}(0)$ for an early time gate yields the correct number of chromophores in a system which exhibits both blinking mechanisms is given in the Figure S12. We note that in a HBT setup up to 8 chromophores can be counted reliably by the photon statistics,[72] but one must always ensure that PL spectra, intensity, and lifetime are very similar for the individual dyes and that bleaching of the dyes is negligible. To count a higher number of chromophores by photon statistics, we refer to the work of Kurz et al., in which the detection scheme was extended to four detectors and a sophisticated analysis, referred to as "counting by photon statistics", is employed.[73] These authors demonstrated that up to 36 chromophores can be counted on a DNA origami structure.[73] Our work provides a more unifying picture for the correct interpretation of pAB data, resolving some possible controversies in the literature and offering a powerful tool for future analysis. After all, blinking of chromophores is the norm rather than the exception in most real physical systems.

MATERIALS AND METHODS

Optical Setup. A home-built confocal microscope based on an Olympus IX-71 inverted microscope was used for all experiments. DNA-origami structures were excited by a pulsed laser (636 nm, ~80 ps full width at half-maximum, LDH-D-C-640; PicoQuant GmbH) operated at 40 MHz repetition rate. The laser power was focused to a diffraction-limited spot, with power adjusted to either 1.1 kW/cm^2 or 4.3 kW/cm^2 by means of a neutral-density filter (ND06A, Thorlabs GmbH). Circularly polarized light was obtained by a linear polarizer (LPVISE100-A, Thorlabs GmbH) and a quarter-wave plate (AQWP05M-600, Thorlabs GmbH). The light was focused onto the sample by an oil-immersion objective (UPLSAPO100XO, NA 1.40, Olympus Deutschland GmbH). The sample was moved by a piezo stage (P-517.3CD, Physik Instrumente (PI) GmbH & Co. KG) controlled by a piezo controller (E-727.3CDA, Physik Instrumente (PI) GmbH & Co. KG). The emission was separated from the excitation beam by a dichroic beam splitter (zt532/640rpc, Chroma Technologies) and focused onto a 50 μm diameter pinhole (Thorlabs GmbH). The emission light was separated from scattered excitation light by a 647 nm long-pass filter (RazorEdge LP 647, Semrock Inc.). For collective blinking experiments, an additional 694 nm (FF02-694/SP-25, Semrock) short-pass filter was added to block the ATTO 700 emission. The filtered emission was split into two detection channels by a nonpolarizing 50:50 beam splitter (CCM1-BS013/M, Thorlabs GmbH). In each detection channel, the afterglow luminescence of the avalanche photodiode was blocked by a 750 nm short-pass filter (FES0750, Thorlabs GmbH). Emission was focused onto avalanche photodiodes (SPCM-AQRH-14-TR, Excelitas Technologies GmbH & Co. KG), and the signals were registered by a multichannel picosecond event timer (HydraHarp 400, PicoQuant GmbH). The setup was controlled by a commercial software package (SymPho-Time64, PicoQuant GmbH).

DNA-Origami Structure Fabrication. All DNA oligonucleotides were purchased at Eurofins Genomics Germany GmbH. The scaffold is an 8064 nucleotide-long ssDNA extracted from M13mp18 bacteriophages. Oligonucleotides modified with ATTO 542 for external labeling were purchased from biomers.net GmbH. For details of the DNA-origami structures, sample preparation, and purification, see the Supporting Information. The DNA-origami structures were immobilized on a LabTekTM chamber slide (Thermo Fisher Scientific Inc.) coated with BSA-biotin/neutravidin (Merck KGaA). See the protocol details in the Supporting Information.

Data Acquisition and Analysis. DNA origami structures were picked from 10 μm × 10 μm scans. The structures were measured with both 1.1 kW/cm^2 and 4.3 kW/cm^2 excitation intensities until

one dye bleached. For experiments showing independently blinking dyes, a reducing buffer system (1 × TAE, 12 mM MgCl$_2$, 2 mM Trolox (freshly prepared), 1% (w/v) D-(+)-glucose) in combination with an oxygen scavenging system (250 U/mL glucose oxidase and 2000 U/mL catalase) was used. For collective blinking, a reducing and oxidizing buffer system (1 × TAE, 12 mM MgCl$_2$, 2 mM Trolox/Troloxquinone, 1% (w/v) D-(+)-glucose) was used. The oxygen scavenging system was the same as in the independent blinking experiments. All chemicals were purchased from Merck KGaA.

Only those single-particle luminescence data sets which showed a minimum of 100 lateral-bin correlation events were analyzed to ensure an acceptable signal-to-noise ratio. The intensity correlation was performed using a self-written Python script employing the correlation algorithm introduced by Laurence et al.[74]

ASSOCIATED CONTENT

Supporting Information

The Supporting Information is available free of charge at https://pubs.acs.org/doi/10.1021/acsnano.1c06649.

> Detailed DNA origami structures, sample preparation, details for the simulations, single-molecule intensity time traces, theory, simulation for the effect of microtime gating on the photon bunching amplitude, and simulations for simultaneous collective and individual blinking (PDF)

AUTHOR INFORMATION

Corresponding Author

Jan Vogelsang − *Institut für Experimentelle und Angewandte Physik and Regensburg Center for Ultrafast Nanoscopy (RUN), Universität Regensburg, 93040 Regensburg, Germany;* orcid.org/0000-0001-7952-9342; Email: jan.vogelsang@ur.de

Authors

Tim Schröder − *Department Chemie and Center for NanoScience (CeNS), Ludwig-Maximilians-Universität München, 81377 München, Germany*

Sebastian Bange − *Institut für Experimentelle und Angewandte Physik and Regensburg Center for Ultrafast Nanoscopy (RUN), Universität Regensburg, 93040 Regensburg, Germany;* orcid.org/0000-0002-5850-264X

Jakob Schedlbauer − *Institut für Experimentelle und Angewandte Physik and Regensburg Center for Ultrafast Nanoscopy (RUN), Universität Regensburg, 93040 Regensburg, Germany*

Florian Steiner − *Department Chemie and Center for NanoScience (CeNS), Ludwig-Maximilians-Universität München, 81377 München, Germany;* orcid.org/0000-0002-9148-5837

John M. Lupton − *Institut für Experimentelle und Angewandte Physik and Regensburg Center for Ultrafast Nanoscopy (RUN), Universität Regensburg, 93040 Regensburg, Germany*

Philip Tinnefeld − *Department Chemie and Center for NanoScience (CeNS), Ludwig-Maximilians-Universität München, 81377 München, Germany;* orcid.org/0000-0003-4290-7770

Complete contact information is available at:
https://pubs.acs.org/10.1021/acsnano.1c06649

Author Contributions

S.B., J.M.L., and J.V. devised the methodology of the correct normalization of photon antibunching. T.S., F.S., P.T., and J.V. designed the experiment and DNA-origami structures. T.S. prepared, measured, and analyzed the DNA-origami structures and data. T.S and J.S. developed the microtime-gated correlation analysis. T.S. and S.B. designed the simulations. T.S., S.B., F.S., J.M.L., P.T., and J.V. contributed to manuscript writing.

Notes

The authors declare no competing financial interest.

REFERENCES

(1) Krüger, C. L.; Zeuner, M.-T.; Cottrell, G. S.; Widera, D.; Heilemann, M. Quantitative Single-Molecule Imaging of TLR4 Reveals Ligand-Specific Receptor Dimerization. *Sci. Signaling* **2017**, *10*, eaan1308.

(2) Nerreter, T.; Letschert, S.; Götz, R.; Doose, S.; Danhof, S.; Einsele, H.; Sauer, M.; Hudecek, M. Super-Resolution Microscopy Reveals Ultra-Low CD19 Expression on Myeloma Cells That Triggers Elimination by CD19 CAR-T. *Nat. Commun.* **2019**, *10*, 3137.

(3) Lukeš, T.; Glatzová, D.; Kvíčalová, Z.; Levet, F.; Benda, A.; Letschert, S.; Sauer, M.; Brdička, T.; Lasser, T.; Cebecauer, M. Quantifying Protein Densities on Cell Membranes Using Super-Resolution Optical Fluctuation Imaging. *Nat. Commun.* **2017**, *8*, 1731.

(4) Pape, J. K.; Stephan, T.; Balzarotti, F.; Büchner, R.; Lange, F.; Riedel, D.; Jakobs, S.; Hell, S. W. Multicolor 3D MINFLUX Nanoscopy of Mitochondrial MICOS Proteins. *Proc. Natl. Acad. Sci. U. S. A.* **2020**, *117*, 20607−20614.

(5) Jungmann, R.; Avendaño, M. S.; Dai, M.; Woehrstein, J. B.; Agasti, S. S.; Feiger, Z.; Rodal, A.; Yin, P. Quantitative Super-Resolution Imaging with qPAINT. *Nat. Methods* **2016**, *13*, 439−442.

(6) Weston, K. D.; Dyck, M.; Tinnefeld, P.; Müller, C.; Herten, D. P.; Sauer, M. Measuring the Number of Independent Emitters in Single-Molecule Fluorescence Images and Trajectories Using Coincident Photons. *Anal. Chem.* **2002**, *74*, 5342−5349.

(7) Ta, H.; Kiel, A.; Wahl, M.; Herten, D.-P. Experimental Approach to Extend the Range for Counting Fluorescent Molecules Based on Photon-Antibunching. *Phys. Chem. Chem. Phys.* **2010**, *12*, 10295−10300.

(8) Grußmayer, K. S.; Herten, D.-P. Time-Resolved Molecule Counting by Photon Statistics across the Visible Spectrum. *Phys. Chem. Chem. Phys.* **2017**, *19*, 8962−8969.

(9) Lupton, J. M.; Vogelsang, J. Photon Correlations Probe the Quantized Nature of Light Emission from Optoelectronic Materials. *Appl. Phys. Rev.* **2021**, *8*, 041302.

(10) Lounis, B.; Moerner, W. E. Single Photons on Demand from a Single Molecule at Room Temperature. *Nature* **2000**, *407*, 491−493.

(11) Fleury; Segura; Zumofen; Hecht; Wild. Nonclassical Photon Statistics in Single-Molecule Fluorescence at Room Temperature. *Phys. Rev. Lett.* **2000**, *84*, 1148−1151.

(12) Ambrose, W. P.; Basché, T.; Moerner, W. E. Detection and Spectroscopy of Single Pentacene Molecules in a p-Terphenyl Crystal by Means of Fluorescence Excitation. *J. Chem. Phys.* **1991**, *95*, 7150−7163.

(13) Basché, T.; Moerner, W. E.; Orrit, M.; Talon, H. Photon Antibunching in the Fluorescence of a Single Dye Molecule Trapped in a Solid. *Phys. Rev. Lett.* **1992**, *69*, 1516−1519.

(14) Kurtsiefer, C.; Mayer, S.; Zarda, P.; Weinfurter, H. Stable Solid-State Source of Single Photons. *Phys. Rev. Lett.* **2000**, *85*, 290−293.

(15) Brouri, R.; Beveratos, A.; Poizat, J. P.; Grangier, P. Photon Antibunching in the Fluorescence of Individual Color Centers in Diamond. *Opt. Lett.* **2000**, *25*, 1294−1296.

(16) Maunz, P.; Moehring, D. L.; Olmschenk, S.; Younge, K. C.; Matsukevich, D. N.; Monroe, C. Quantum Interference of Photon Pairs from Two Remote Trapped Atomic Ions. *Nat. Phys.* **2007**, *3*, 538−541.

(17) Kolesov, R.; Xia, K.; Reuter, R.; Stöhr, R.; Zappe, A.; Meijer, J.; Hemmer, P. R.; Wrachtrup, J. Optical Detection of a Single Rare-Earth Ion in a Crystal. *Nat. Commun.* **2012**, *3*, 1029.

(18) Barros, H. G.; Stute, A.; Northup, T. E.; Russo, C.; Schmidt, P. O.; Blatt, R. Deterministic Single-Photon Source from a Single Ion. *New J. Phys.* **2009**, *11*, 103004.

(19) Toth, M.; Aharonovich, I. Single Photon Sources in Atomically Thin Materials. *Annu. Rev. Phys. Chem.* **2019**, *70*, 123−142.

(20) Lv, B.; Zhang, H.; Wang, L.; Zhang, C.; Wang, X.; Zhang, J.; Xiao, M. Photon Antibunching in a Cluster of Giant CdSe/CdS Nanocrystals. *Nat. Commun.* **2018**, *9*, 1536.

(21) Stangl, T.; Wilhelm, P.; Remmerssen, K.; Höger, S.; Vogelsang, J.; Lupton, J. M. Mesoscopic Quantum Emitters from Deterministic Aggregates of Conjugated Polymers. *Proc. Natl. Acad. Sci. U. S. A.* **2015**, *112*, E5560−6.

(22) Koperski, M.; Nogajewski, K.; Arora, A.; Cherkez, V.; Mallet, P.; Veuillen, J.-Y.; Marcus, J.; Kossacki, P.; Potemski, M. Single Photon Emitters in Exfoliated WSe2 Structures. *Nat. Nanotechnol.* **2015**, *10*, 503−506.

(23) Fisher, B.; Caruge, J. M.; Zehnder, D.; Bawendi, M. Room-Temperature Ordered Photon Emission from Multiexciton States in Single CdSe Core-Shell Nanocrystals. *Phys. Rev. Lett.* **2005**, *94*, 87403.

(24) Hofkens, J.; Cotlet, M.; Vosch, T.; Tinnefeld, P.; Weston, K. D.; Ego, C.; Grimsdale, A.; Mullen, K.; Beljonne, D.; Bredas, J. L.; Jordens, J.; Schweitzer, G.; Sauer, M.; De Schryver, F. Revealing Competitive Forster-Type Resonance Energy-Transfer Pathways in Single Bichromophoric Molecules. *Proc. Natl. Acad. Sci. U. S. A.* **2003**, *100*, 13146−13151.

(25) Hübner, C. G.; Zumofen, G.; Renn, A.; Herrmann, A.; Müllen, K.; Basché, T. Photon Antibunching and Collective Effects in the Fluorescence of Single Bichromophoric Molecules. *Phys. Rev. Lett.* **2003**, *91*, 93903.

(26) Tinnefeld, P.; Weston, K. D.; Vosch, T.; Cotlet, M.; Weil, T.; Hofkens, J.; Mullen, K.; De Schryver, F. C.; Sauer, M. Antibunching in the Emission of a Single Tetrachromophoric Dendritic System. *J. Am. Chem. Soc.* **2002**, *124*, 14310−14311.

(27) Hedley, G. J.; Schröder, T.; Steiner, F.; Eder, T.; Hofmann, F. J.; Bange, S.; Laux, D.; Höger, S.; Tinnefeld, P.; Lupton, J. M.; Vogelsang, J. Picosecond Time-Resolved Photon Antibunching Measures Nanoscale Exciton Motion and the True Number of Chromophores. *Nat. Commun.* **2021**, *12*, 1327.

(28) Schindler, F.; Jacob, J.; Grimsdale, A. C.; Scherf, U.; Müllen, K.; Lupton, J. M.; Feldmann, J. Counting Chromophores in Conjugated Polymers. *Angew. Chem., Int. Ed.* **2005**, *44*, 1520−1525.

(29) Becker, K.; Lagoudakis, P. G.; Gaefke, G.; Höger, S.; Lupton, J. M. Exciton Accumulation in Pi-Conjugated Wires Encapsulated by Light-Harvesting Macrocycles. *Angew. Chem., Int. Ed.* **2007**, *46*, 3450−3455.

(30) Matthews, J. M. *Protein Dimerization and Oligomerization in Biology* 747; Springer: New York, 2012.

(31) Havugimana, P. C.; Hart, G. T.; Nepusz, T.; Yang, H.; Turinsky, A. L.; Li, Z.; Wang, P. I.; Boutz, D. R.; Fong, V.; Phanse, S.; Babu, M.; Craig, S. A.; Hu, P.; Wan, C.; Vlasblom, J.; Dar, V.-u.-N.; Bezginov, A.; Clark, G. W.; Wu, G. C.; Wodak, S. J.; et al. A Census of Human Soluble Protein Complexes. *Cell* **2012**, *150*, 1068−1081.

(32) Ahnert, S. E.; Marsh, J. A.; Hernández, H.; Robinson, C. V.; Teichmann, S. A. Principles of Assembly Reveal a Periodic Table of Protein Complexes. *Science* **2015**, *350*, aaa2245.

(33) Drew, K.; Lee, C.; Huizar, R. L.; Tu, F.; Borgeson, B.; McWhite, C. D.; Ma, Y.; Wallingford, J. B.; Marcotte, E. M. Integration of Over 9,000 Mass Spectrometry Experiments Builds a Global Map of Human Protein Complexes. *Mol. Syst. Biol.* **2017**, *13*, 932.

(34) Goyette, J.; Gaus, K. Mechanisms of Protein Nanoscale Clustering. *Curr. Opin. Cell Biol.* **2017**, *44*, 86−92.

(35) Basché, T.; Kummer, S.; Bräuchle, C. Direct Spectroscopic Observation of Quantum Jumps of a Single Molecule. *Nature* **1995**, *373*, 132−134.

(36) Ha, T.; Tinnefeld, P. Photophysics of Fluorescent Probes for Single-Molecule Biophysics and Super-Resolution Imaging. *Annu. Rev. Phys. Chem.* **2012**, *63*, 595−617.

(37) Widengren, J.; Chmyrov, A.; Eggeling, C.; Löfdahl, P.-A.; Seidel, C. A. M. Strategies to Improve Photostabilities in Ultra-sensitive Fluorescence Spectroscopy. *J. Phys. Chem. A* **2007**, *111*, 429−440.

(38) Vogelsang, J.; Kasper, R.; Steinhauer, C.; Person, B.; Heilemann, M.; Sauer, M.; Tinnefeld, P. A Reducing and Oxidizing System Minimizes Photobleaching and Blinking of Fluorescent Dyes. *Angew. Chem., Int. Ed.* **2008**, *47*, 5465−5469.

(39) Zondervan, R.; Kulzer, F.; Orlinskii, S. B.; Orrit, M. Photoblinking of Rhodamine 6G in Poly(vinyl Alcohol): Radical Dark State Formed through the Triplet. *J. Phys. Chem. A* **2003**, *107*, 6770−6776.

(40) Vogelsang, J.; Cordes, T.; Forthmann, C.; Steinhauer, C.; Tinnefeld, P. Intrinsically Resolution Enhancing Probes for Confocal Microscopy. *Nano Lett.* **2010**, *10*, 672−679.

(41) Tinnefeld, P.; Buschmann, V.; Weston, K. D.; Sauer, M. Direct Observation of Collective Blinking and Energy Transfer in a Bichromophoric System. *J. Phys. Chem. A* **2003**, *107*, 323−327.

(42) Holzmeister, P.; Wünsch, B.; Gietl, A.; Tinnefeld, P. Single-Molecule Photophysics of Dark Quenchers as Non-Fluorescent FRET Acceptors. *Photochem. Photobiol. Sci.* **2014**, *13*, 853−858.

(43) Efros, A. L.; Nesbitt, D. J. Origin and Control of Blinking in Quantum Dots. *Nat. Nanotechnol.* **2016**, *11*, 661−671.

(44) Glembockyte, V.; Lincoln, R.; Cosa, G. Cy3 Photoprotection Mediated by Ni2+ for Extended Single-Molecule Imaging: Old Tricks for New Techniques. *J. Am. Chem. Soc.* **2015**, *137*, 1116−1122.

(45) van der Velde, J. H. M.; Oelerich, J.; Huang, J.; Smit, J. H.; Aminian Jazi, A.; Galiani, S.; Kolmakov, K.; Gouridis, G.; Eggeling, C.; Herrmann, A.; Roelfes, G.; Cordes, T. A Simple and Versatile Design Concept for Fluorophore Derivatives with Intramolecular Photo-stabilization. *Nat. Commun.* **2016**, *7*, 10144.

(46) Pati, A. K.; El Bakouri, O.; Jockusch, S.; Zhou, Z.; Altman, R. B.; Fitzgerald, G. A.; Asher, W. B.; Terry, D. S.; Borgia, A.; Holsey, M. D.; Batchelder, J. E.; Abeywickrama, C.; Huddle, B.; Rufa, D.; Javitch, J. A.; Ottosson, H.; Blanchard, S. C. Tuning the Baird Aromatic Triplet-State Energy of Cyclooctatetraene to Maximize the Self-Healing Mechanism in Organic Fluorophores. *Proc. Natl. Acad. Sci. U. S. A.* **2020**, *117*, 24305−24315.

(47) Holzmeister, P.; Gietl, A.; Tinnefeld, P. Geminate Recombi-nation as a Photoprotection Mechanism for Fluorescent Dyes. *Angew. Chem., Int. Ed.* **2014**, *53*, 5685−5688.

(48) Gidi, Y.; Payne, L.; Glembockyte, V.; Michie, M. S.; Schnermann, M. J.; Cosa, G. Unifying Mechanism for Thiol-Induced Photoswitching and Photostability of Cyanine Dyes. *J. Am. Chem. Soc.* **2020**, *142*, 12681−12689.

(49) Cordes, T.; Vogelsang, J.; Tinnefeld, P. On the Mechanism of Trolox as Antiblinking and Antibleaching Reagent. *J. Am. Chem. Soc.* **2009**, *131*, 5018−5019.

(50) Orrit, M. Photon Statistics in Single Molecule Experiments. *Single Mol.* **2002**, *3*, 255−265.

(51) Zumbusch; Fleury; Brown; Bernard; Orrit. Probing Individual Two-Level Systems in a Polymer by Correlation of Single Molecule Fluorescence. *Phys. Rev. Lett.* **1993**, *70*, 3584−3587.

(52) Wientjes, E.; Renger, J.; Curto, A. G.; Cogdell, R.; van Hulst, N. F. Strong Antenna-Enhanced Fluorescence of a Single Light-Harvesting Complex Shows Photon Antibunching. *Nat. Commun.* **2014**, *5*, 4236.

(53) Bopp, M. A.; Sytnik, A.; Howard, T. D.; Cogdell, R. J.; Hochstrasser, R. M. The Dynamics of Structural Deformations of Immobilized Single Light-Harvesting Complexes. *Proc. Natl. Acad. Sci. U. S. A.* **1999**, *96*, 11271−11276.

102

(54) Krüger, T. P. J.; van Grondelle, R. The Role of Energy Losses in Photosynthetic Light Harvesting. *J. Phys. B: At., Mol. Opt. Phys.* **2017**, *50*, 132001.

(55) Gwizdala, M.; Berera, R.; Kirilovsky, D.; van Grondelle, R.; Krüger, T. P. J. Controlling Light Harvesting with Light. *J. Am. Chem. Soc.* **2016**, *138*, 11616−11622.

(56) Steiner, F.; Vogelsang, J.; Lupton, J. M. Singlet-Triplet Annihilation Limits Exciton Yield in Poly(3-Hexylthiophene). *Phys. Rev. Lett.* **2014**, *112*, 137402.

(57) Yu, J.; Lammi, R.; Gesquiere, A. J.; Barbara, P. F. Singlet-Triplet and Triplet-Triplet Interactions in Conjugated Polymer Single Molecules. *J. Phys. Chem. B* **2005**, *109*, 10025−10034.

(58) Bout, D. A. V.; Yip, W.-T.; Hu, D.; Fu, D.-K.; Swager, T. M.; Barbara, P. F. Discrete Intensity Jumps and Intramolecular Electronic Energy Transfer in the Spectroscopy of Single Conjugated Polymer Molecules. *Science* **1997**, *277*, 1074−1077.

(59) Schedlbauer, J.; Scherf, U.; Vogelsang, J.; Lupton, J. M. Dynamic Quenching of Triplet Excitons in Single Conjugated-Polymer Chains. *J. Phys. Chem. Lett.* **2020**, *11*, 5192−5198.

(60) Schmied, J. J.; Gietl, A.; Holzmeister, P.; Forthmann, C.; Steinhauer, C.; Dammeyer, T.; Tinnefeld, P. Fluorescence and Super-Resolution Standards Based on DNA Origami. *Nat. Methods* **2012**, *9*, 1133−1134.

(61) Gietl, A.; Holzmeister, P.; Grohmann, D.; Tinnefeld, P. DNA Origami as Biocompatible Surface to Match Single-Molecule and Ensemble Experiments. *Nucleic Acids Res.* **2012**, *40*, e110.

(62) Scheckenbach, M.; Bauer, J.; Zähringer, J.; Selbach, F.; Tinnefeld, P. DNA Origami Nanorulers and Emerging Reference Structures. *APL Mater.* **2020**, *8*, 110902.

(63) Widengren, J.; Mets, Ü.; Rigler, R. Photodynamic Properties of Green Fluorescent Proteins Investigated by Fluorescence Correlation Spectroscopy. *Chem. Phys.* **1999**, *250*, 171−186.

(64) Schröder, T.; Scheible, M. B.; Steiner, F.; Vogelsang, J.; Tinnefeld, P. Interchromophoric Interactions Determine the Maximum Brightness Density in DNA Origami Structures. *Nano Lett.* **2019**, *19*, 1275−1281.

(65) Helmerich, D. A.; Beliu, G.; Sauer, M. Multiple-Labeled Antibodies Behave Like Single Emitters in Photoswitching Buffer. *ACS Nano* **2020**, *14*, 12629−12641.

(66) Steinhauer, C.; Forthmann, C.; Vogelsang, J.; Tinnefeld, P. Superresolution Microscopy on the Basis of Engineered Dark States. *J. Am. Chem. Soc.* **2008**, *130*, 16840−16841.

(67) Tinnefeld, P.; Hofkens, J.; Herten, D.-P.; Masuo, S.; Vosch, T.; Cotlet, M.; Habuchi, S.; Mullen, K.; De Schryver, F. C.; Sauer, M. Higher-Excited-State Photophysical Pathways in Multichromophoric Systems Revealed by Single-Molecule Fluorescence Spectroscopy. *ChemPhysChem* **2004**, *5*, 1786−1790.

(68) Keller, R. A.; Ambrose, W. P.; Goodwin, P. M.; Jett, J. H.; Martin, J. C.; Wu, M. Single-Molecule Fluorescence Analysis in Solution. *Appl. Spectrosc.* **1996**, *50*, 12−32.

(69) Lamb, D. C.; Schenk, A.; Röcker, C.; Scalfi-Happ, C.; Nienhaus, G. U. Sensitivity Enhancement in Fluorescence Correlation Spectroscopy of Multiple Species Using Time-Gated Detection. *Biophys. J.* **2000**, *79*, 1129−1138.

(70) Benjamin, E.; Yallapragada, V. J.; Amgar, D.; Yang, G.; Tenne, R.; Oron, D. Temperature Dependence of Excitonic and Biexcitonic Decay Rates in Colloidal Nanoplatelets by Time-Gated Photon Correlation. *J. Phys. Chem. Lett.* **2020**, *11*, 6513−6518.

(71) Schedlbauer, J.; Wilhelm, P.; Grabenhorst, L.; Federl, M. E.; Lalkens, B.; Hinderer, F.; Scherf, U.; Höger, S.; Tinnefeld, P.; Bange, S.; Vogelsang, J.; Lupton, J. M. Ultrafast Single-Molecule Fluorescence Measured by Femtosecond Double-Pulse Excitation Photon Antibunching. *Nano Lett.* **2020**, *20*, 1074−1079.

(72) Masuo, S.; Vosch, T.; Cotlet, M.; Tinnefeld, P.; Habuchi, S.; Bell, T. D. M.; Oesterling, I.; Beljonne, D.; Champagne, B.; Müllen, K.; Sauer, M.; Hofkens, J.; De Schryver, F. C. Multichromophoric Dendrimers as Single-Photon Sources: A Single-Molecule Study. *J. Phys. Chem. B* **2004**, *108*, 16686−16696.

(73) Kurz, A.; Schmied, J. J.; Grußmayer, K. S.; Holzmeister, P.; Tinnefeld, P.; Herten, D.-P. Counting Fluorescent Dye Molecules on DNA Origami by Means of Photon Statistics. *Small* **2013**, *9*, 4061−4068.

(74) Laurence, T. A.; Fore, S.; Huser, T. Fast, Flexible Algorithm for Calculating Photon Correlations. *Opt. Lett.* **2006**, *31*, 829−831.

Supplementary Information for

How Blinking Affects Photon Correlations in Multichromophoric Nanoparticles

Tim Schröder,[1] Sebastian Bange,[2] Jakob Schedlbauer,[2] Florian Steiner,[1] John M. Lupton,[2] Philip Tinnefeld,[1] and Jan Vogelsang[2,]*

[1]Department Chemie and Center for NanoScience (CeNS), Ludwig-Maximilians-Universität

München, Butenandtstr. 5-13, 81377 München, Germany

[2]Institut für Experimentelle und Angewandte Physik, Universität Regensburg,

Universitätsstrasse 31, 93040 Regensburg, Germany

Details of DNA origami structures and sample preparation

The DNA origami structure was modified using caDNAno (version 0.2.2, design schematics in Fig. S1). The scaffold is an 8064-nucleotide-long ssDNA extracted from M13mp18 bacteriophages. All staple strands as well as the dye labeled oligonucleotides were purchased from Eurofins Genomics GmbH (see the end of Supplementary Information). The ATTO 542-modified oligonucleotides for external labeling were purchased from biomers.net. Scaffold and oligonucleotides were mixed according to table S1 for origami folding. The folding buffer (FB) is a Tris-EDTA buffer (1× TE, 10 mM Tris-HCl, 1 mM EDTA•Na$_2$) with 20 mM MgCl$_2$ and 5 mM NaCl. In the annealing process, the mixture was heated and slowly cooled down with a nonlinear thermal ramp over 16 hours according Nickels *et al.*[1] After annealing, the excess staples were removed with polyethylene glycol (PEG) precipitation. The samples were mixed with an equal volume of PEG precipitation buffer (1× TAE, 15 % (w/v) PEG-8000, 500 mM NaCl, 12 mM MgCl$_2$) and centrifuged at 16 krcf (thousand relative centrifugal force, *i.e.* 1000 *g*) for 30 min at 4 °C. After removing the supernatant, the pellet was suspended in 1× FB. Afterwards, the DNA origami was externally labeled with ATTO 542-modified oligonucleotides. A threefold excess with respect to the extended staples was used and the structure was incubated for 20 min in a wet chamber at room temperature. The DNA origami structures were purified *via* gel electrophoresis. A 1.5 % agarose gel containing a Tris base, acetic acid and EDTA buffer (0.5× TAE, 20 mM Tris-HCl, 10 mM acetic acid, 0.5 mM EDTA) and 12 mM MgCl$_2$ was used at 60 V for 2 hours in a gel box cooled in an ice-water bath. The gel was not stained to avoid staining reagent-dye interactions. On a blue-illuminated table DNA origami structures could be seen due to the numerous ATTO 542 dyes. DNA origami structures were recovered from the target band. The samples were stored at -26 °C until further use.

Folding Table

Final concentrations for DNA origami folding are given in Table S1. The meaning of the reagents is described below:

Table S1: Folding reagents with final concentrations.

Reagent	Final concentration / nM
scaffold	25
core staples	225
biotin staples	250
extended staples	225
dye and refill staples	225

scaffold: Single-stranded viral 8064 nt ssDNA from M13mp18.

core staples: Contains every unmodified staples of the rectangular DNA origami. The wildtype structure is given in Ref. [2].

biotin staples: Four biotin modified staples. Modifications are placed at the 3' end.

extended staples: 13 staples extended at the 3' end for external labeling. The extended sequence is: 5' TTTTCCTCTACCACCTACATCAC 3'. Sequence for the ATTO 542 oligonucleotides: 5' GTGATGTAGGTGGTAGAGGA-ATTO 542 3'

**dye and refill staples:** Oligonucleotides labeled with ATTO 647N or ATTO 700 at the 5' end.

DNA origami structures
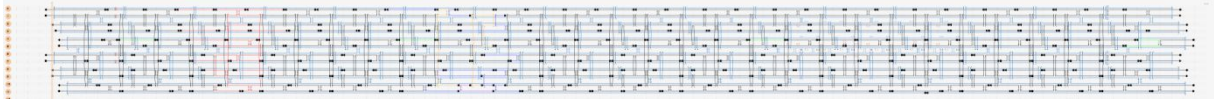
Figure S1. caDNAno sketch of the DNA origami structure used. Modified staples are colored. Green staples are biotin labeled. Red staples are extended at the 3' (5' TTTTCCTCTACCACCTACATCAC) end for external labeling with ATTO 542 modified oligonucleotides. Orange staples are labeled at the 5' end with ATTO 647N violet ones with ATTO 700. Blue staples are next to the ATTO 647N labeled staples to stabilize the structure.
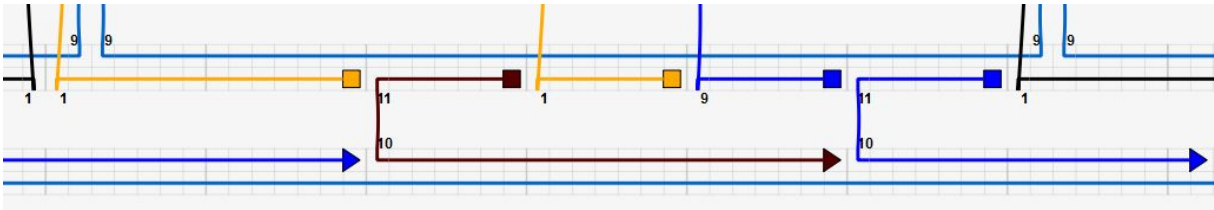
Figure S2. Close up of the DNA origami structure with two ATTO 647N (5' end of the orange staples) dyes separated by 6 nm and an ATTO 700 dye (5' end of the brown staple) for the collective blinking experiment.
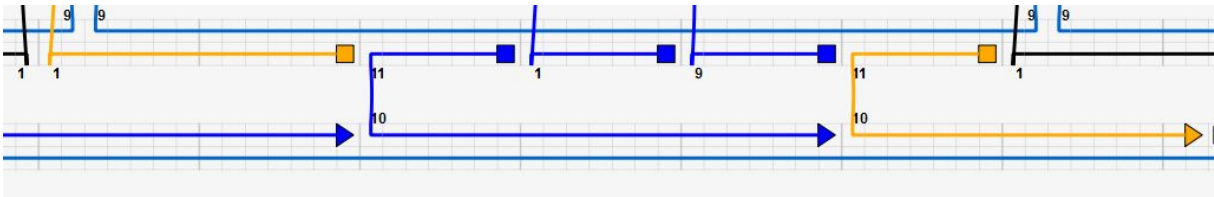
Figure S3. Close up of the DNA origami structure with two ATTO 647N (5' end of the orange staples) dyes separated by 12 nm for the independent blinking experiment.

Simulations for Figures 1 and 4

Simulations were performed with a self-written python script. The probability of detecting a photon was set to be 0.08 for intensity state A and 0.00 for intensity state B. The photons were randomly distributed on two detection channels $Ch0$ and $Ch1$. The laser repetition rate was set to be 50 MHz and 10^7 laser pulses were simulated. The simulations were analyzed based on a correlation algorithm proposed by Laurence *et al.*[3] Positive lag times correspond to the cross correlation of $Ch0 \rightarrow Ch1$ and negative lag times correspond to the correlation of $Ch1 \rightarrow Ch0$.

For blinking dyes the switching rate between state A and B was fixed to $k_A = k_B = 2 \cdot 10^6 \, \text{s}^{-1}$ for each dye.

For Figure 4 the intensity levels were fixed to $I_A = 0.08$ and $I_B = 0.0016$. The fluorescence lifetime of the bright state was set to $\tau_A = 4$ ns and the fluorescence lifetime of the dark state to $\tau_B = 0.8$ ns.

Altering the correlation amplitude by excitation power for independently and collectively blinking dyes

Figure S4a shows an exemplary time trace of two independently blinking ATTO 647N dyes separated by 12 nm. With an oxygen scavenger and 2 mM Trolox as reducing agent the dyes are pushed constantly into the radical anion state. The blue and red parts of the figure correspond to an excitation power of 4.3 kW/cm^2 and 1.1 kW/cm^2, respectively. We started with the high excitation intensity. After 11 seconds, we switched to lower excitation intensity and measured until one dye bleaches at 48 s. We recorded much longer intensity time traces with lower excitation power to ensure an equal signal-to-noise ratio in the correlation calculation. The signal-to-noise ratio scales with the square of the fluorescence intensity.

Figure S4b and S4c show a two-second snapshot of the time trace in panel a, but with 1 ms binning. The intensity histogram in Figure S4b shows that most of the time, both dyes are in the non-fluorescent state for 4.3 kW/cm^2 excitation power. Figure S4c shows that at lower excitation power, the cases for one or two dyes being in their fluorescent state are more prominent.

The cross correlations for the high and low excitation power are shown in S4d with a blue and a red curve, respectively. Higher excitation powers result in higher photon bunching amplitudes for independent dyes because the bunching amplitude scales linearly with the excitation intensity. As expected for two independently blinking dyes, however, $g^{(2)}(0)$ stays constant at ~0.5 for both excitation powers. For independently blinking dyes, the ratio N_c/N_ℓ thus constitutes a pAB normalization that is inappropriate for chromophore counting.
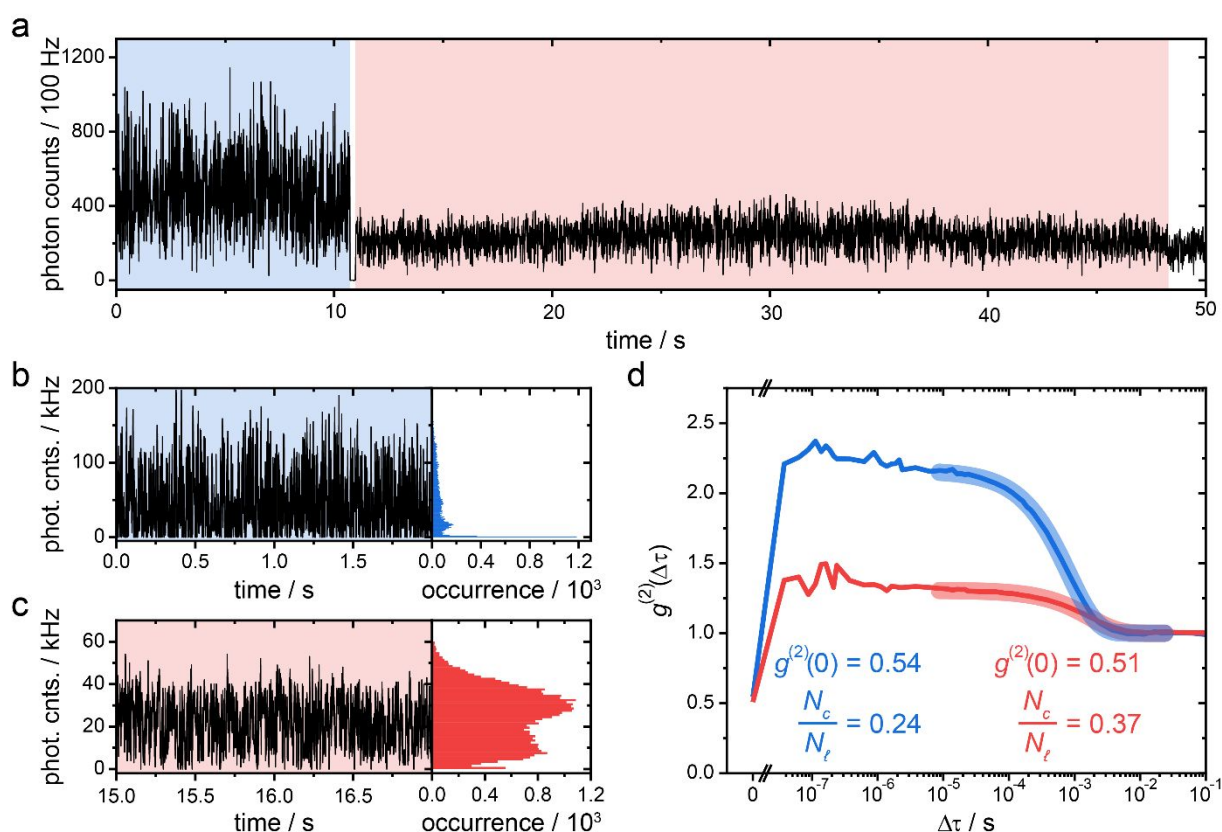
Figure S4. (a) Fluorescence time trace of two independently blinking ATTO 647N dyes separated by 12 nm. The excitation power was altered between 4.1 kW/cm^2 and 1.1 kW/cm^2 as indicated by blue and red background colors, respectively. (b) A two-second snippet of the fluorescence trajectory at 4.1 kW/cm^2 excitation with the corresponding intensity histogram. (c) A two-second snippet of the fluorescence trajectory at 1.1 kW/cm^2 excitation with corresponding intensity histogram. (d) Cross correlation of the fluorescence time trace excited with 4.1 kW/cm^2 and 1.1 kW/cm^2 shown in blue and red, respectively. Corresponding monoexponential fit from equation 9 are depicted in bold lines.

To prove that the transition rate into the singlet manifold k_{on} is power independent, we extract the transition rates from the intensity correlations shown in Figure S4d. For the extraction of the rate constants we have to consider that the observed $g^{(2)}(\Delta\tau)$ correlation is a sum of two intensity correlations each representing one independently blinking dye molecule. Since both dyes experience a similar nano-environment and excitation power, the transition rates into the dark state, k_{off}, and back again, k_{on}, are expected to be the same for both dyes, which is supported by the monoexponential decays seen in Figure S4d. If multiple independent intensity fluctuations are involved, each correlation is weighted with the square of the fractional intensity $\Im$ for each dye.

$$\Im_1 = \frac{I_1}{\Sigma I_{\rm i}}\text{eq. 1}$$

Here, $\Im_1$ denotes the fractional intensity of the first dye with the measured intensity I_1. The total intensity correlation, $g^{(2)}_{\rm total}(\Delta\tau)$, can then be written as:

$$g^{(2)}_{\rm total}(\Delta\tau) = \Sigma\Im_{\rm i}^2 g^{(2)}_{\rm i}(\Delta\tau) + 1 \qquad \text{eq. 2}$$

In our case, the switching kinetics and intensities are the same for two independently blinking ATTO 647N dyes. This results in a fractional intensity of $\Im_1 = \Im_2 = \frac{1}{2}$.

$$g^{(2)}_{\rm total}(\Delta\tau) = \left(\frac{1}{2}\right)^2 g^{(2)}_1(\Delta\tau) + \left(\frac{1}{2}\right)^2 g^{(2)}_2(\Delta\tau) + 1 \qquad \text{eq. 3}$$

Both dyes have the same blinking kinetics and therefore show the same intensity correlation $g^{(2)}_1(\Delta\tau) = g^{(2)}_2(\Delta\tau)$. Stochastic switching between an emitting and a non-emitting state results in a monoexponential decay in the intensity correlation.

$$g^{(2)}_{\rm total}(\Delta\tau) = \Sigma\Im_{\rm i}^2\left[C_{\rm i} \cdot \exp\left(-k_{\rm kineticsi} \cdot \Delta\tau\right)\right] + 1 \qquad \text{eq. 4}$$

For on-off-switching, the bunching amplitude C equals the equilibrium constant

$$C = K = \frac{k_{\rm off}}{k_{\rm on}} \qquad \text{eq. 5}$$

and the correlation relaxation rate $k_{\rm kinetics}$ is the sum of the switching rates

$$k_{\rm kinetics} = k_{\rm on} + k_{\rm off} \qquad \text{eq. 6}$$

The transition rate constants are supposed to be the same for both dyes. Therefore, they will show the same bunching amplitude $C_1 = C_2$ and the same correlation relaxation rate $k_{\rm kinetics1} = k_{\rm kinetics2}$. However, since both amplitudes are weighted by the square of the fractional intensity we have to consider this damping.

$$g^{(2)}_{\rm total}(\Delta\tau) = 1 + \left(\frac{1}{2}\right)^2\left[C_1 \cdot \exp\left(-k_{\rm kinetics1} \cdot \Delta\tau\right)\right] + \left(\frac{1}{2}\right)^2\left[C_2 \cdot \exp\left(-k_{\rm kinetics2} \cdot \Delta\tau\right)\right] \qquad \text{eq. 8}$$

$$= 1 + \frac{1}{2}C \cdot \exp\left(-k_{\rm kinetics} \cdot \Delta\tau\right) \qquad \text{eq. 9}$$

With monoexponential fits using equation 9 we can extract the bunching amplitude C and correlation relaxation rate $k_{\rm kinetics}$, which are listed for the two excitation intensities in Table S2.

Table S2: Monoexponential fit parameters from Figure S4d.

	C	$k_{\rm kinetics}$ / s^{-1}
1.1 kW/cm^2	0.614 ± 0.004	581 ± 16
4.1 kW/cm^2	2.322 ± 0.006	1226 ± 12

With the extracted parameters we calculate the transition rates according to

$$k_{\text{on}} = \frac{k_{\text{kinetics}}}{C + 1} \qquad \text{eq. 10}$$

$$k_{\text{off}} = \frac{k_{\text{kinetics}}}{\frac{1}{c} + 1} \qquad \text{eq. 11}$$

The extracted rates are listed in Table S3.

Table S3: Calculated transition rate constants for two independently blinking dyes.

	k_{on} / s^{-1}	k_{off} / s^{-1}
1.1 kW/ cm^2	359 ± 9	221 ± 5
4.1 kW/ cm^2	369 ± 4	856 ± 8

The rate constant for excursions into the on-state, k_{on}, stays constant within the error for both excitation intensities, as expected. However, the transition rate into the off-state, k_{off}, is power dependent and shows a linear dependency of the excitation power. The power was raised by a factor of $\frac{4.1}{1.1} \sim 3.7$. The rate k_{off} changed by a factor of $\frac{856}{221} \sim 3.8$, which supports our statement of a linear power dependency.

A fluorescence time trace of two collectively blinking ATTO 647N dyes is shown in Figure S5a. We started with the high excitation power of 4.1 kW/cm² and later switched to the lower excitation power of 1.1 kW/cm². At 123 s, one ATTO 647N dye bleached. Figure S5b and S5c show a two-second snapshot of fluorescence trajectories with 1 ms binning. The intensity histogram shows only two intensity states for both excitation powers. The ATTO 700 FRET–switch is constantly switching between a reduced state and the singlet manifold. In the reduced state, the absorption spectrum is blue-shifted and the ATTO 647N fluorescence is not quenched. When the ATTO 700 dye is oxidized again, the ATTO 647N dyes are quenched by efficient FRET. Because we are monitoring the donor fluorescence, the bunching amplitude is inversely proportional to the excitation power. The donor dyes are stabilized by the ROXS buffer. The acceptor dye is mainly excited by FRET from the donor dyes. From its first excited energy state, it has a small chance to enter the long-living triplet state from which it can be reduced by Trolox. The time spent in the reduced state only depends on the Trolox quinone concentration and is independent of the excitation power. This fact is reflected in the intensity histograms of Figure S5b and S5c. For higher excitation power, the ATTO 647N dyes spend more time in the bright emitting state because they shelve the acceptor dye faster in the reduced state. On the other hand, with low excitation power, the donor dyes spend more time in the quenched emitting state because it takes longer to reduce the acceptor dye.
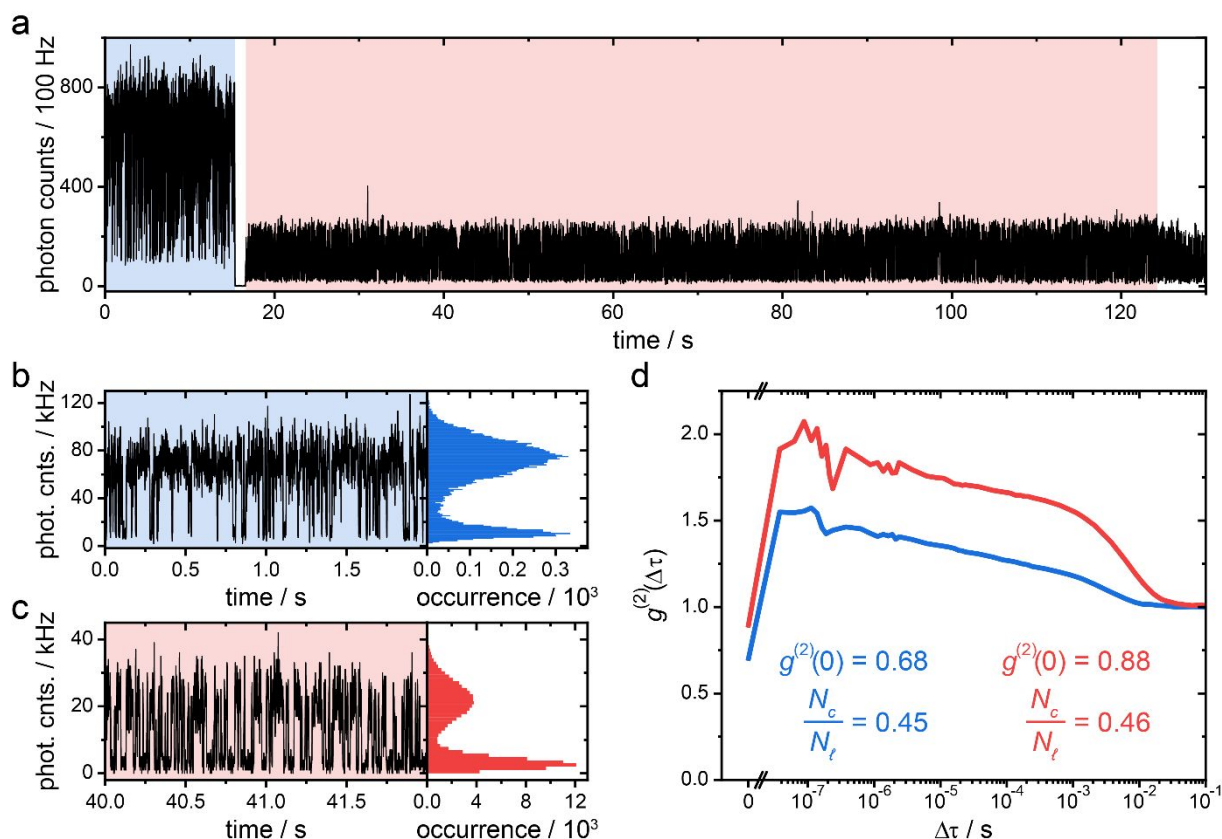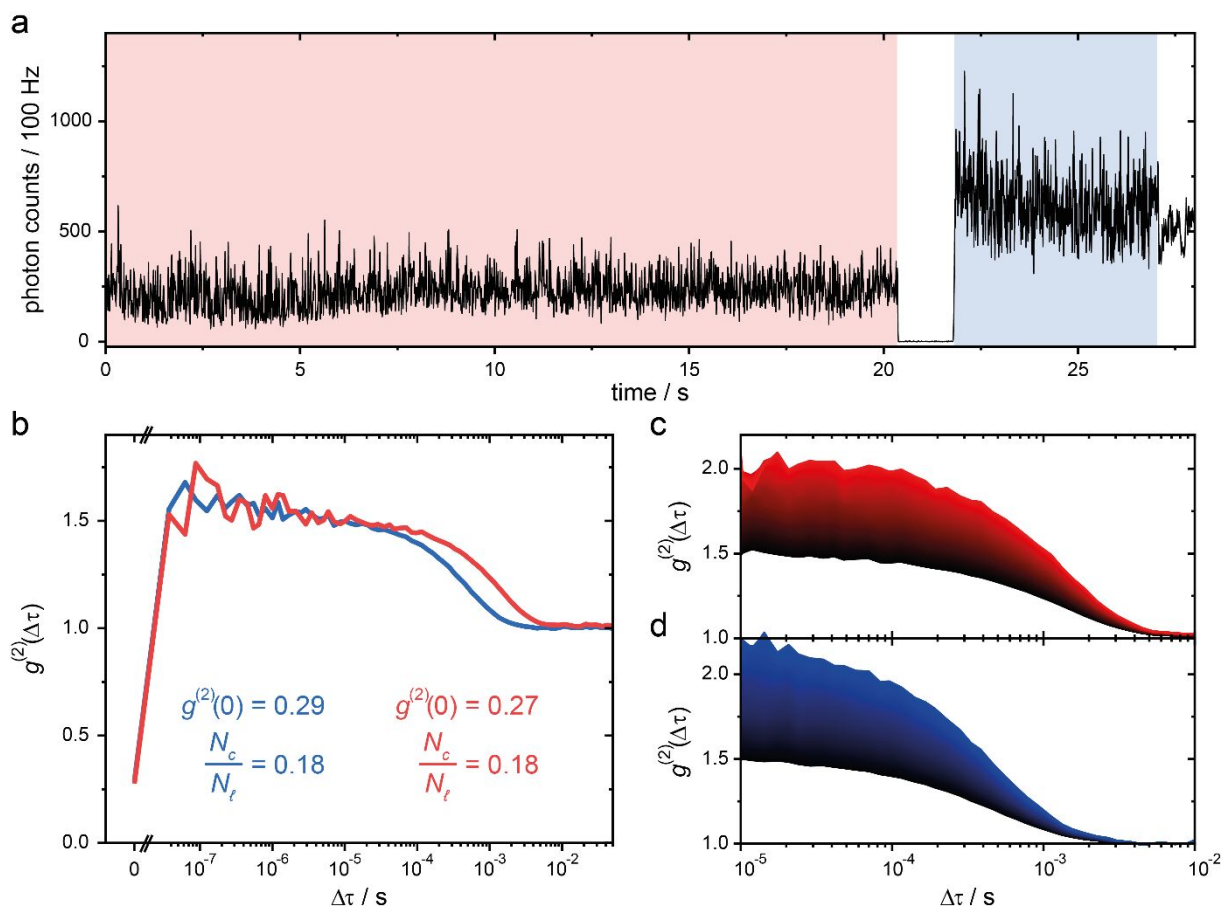
Figure S5. (a) Fluorescence time trace of two collectively blinking ATTO 647N dyes modulated by an ATTO 700 FRET-switch. The excitation power was either 4.1 kW/cm² (blue) or 1.1 kW/cm² (red). (b) Two-second snippet of the fluorescence time trace at 4.1 kW/cm² excitation power and the corresponding intensity histogram. (c) Two-second snippet of the fluorescence trajectory at 1.1 kW/cm² excitation power and the corresponding intensity histogram. (d) Cross correlation of the fluorescence time traces.

Change of excitation power does not correlate with a change in bunching amplitude

As an example of blinking kinetics which does not show a change of the correlation amplitude for different excitation powers, we chose two blinking ATTO 647N which are separated by ~3 nm, *i.e.* by 9 base pairs. The structure was published by Schröder *et al.*[4] The dyes are not independent and interact by singlet-singlet annihilation (SSA) and singlet-dark-state annihilation (SDA). To promote the dye blinking, we removed enzymatic oxygen and excited the dyes at either 1.1 kW/cm² and 4.1 kW/cm². We did not add Trolox to have sufficient singlet-triplet interactions. The fluorescence time trace for both excitation powers is shown in Figure S6a. The correlation amplitude for a single dye usually scales linearly with the excitation power. For two dyes with weak coupling this statement is not true anymore as demonstrated in Figure S6b. The correlation amplitude stays constant, but the correlation relaxation time is shifted to shorter timescales with increasing excitation power. Due to SSA and SDA, the excitation into higher excited states becomes more likely. In higher excited states, the transition rates between the singlet and triplet state are larger and the blinking kinetics becomes faster. In our case, the rates scale with the same factor, although it varies for different dye combinations. For the antibunching measurement, we obtain $g^{(2)}(0) \sim 0.3$ and $N_c/N_\ell \sim 0.2$, which is expected for weakly collectively blinking dyes when they undergo efficient SSA.

When one dye enters the dark state, it quenches the second dye by a FRET mechanism referred to as SDA. This results in a shorter fluorescence lifetime and a quenched fluorescence signal. As described in section S5, changes of the correlation amplitude for different microtime gates shown in Figure S6c, d

110

are a characteristic feature of collectively blinking dyes. Therefore, this correlation amplitude can be assigned to collective blinking kinetics without changing the excitation power, and the normalization of photon antibunching has to be carried out with respect to the bunching amplitude.

Figure S6. (a) Fluorescent trajectory of two collectively blinking ATTO 647N dyes separated by 3 nm. The excitation power was switched from 1.1 kW/cm² (red) to 4.1 kW/cm² (blue). (b) Cross-correlation of the fluorescence time traces for either excitation powers. (c) Cross-correlation for the 1.1 kW/cm² excitation power. The color gradient marks the beginning of the microtime gate used, which was shifted with a 20 ps step size. Black corresponds to early (from 0 ns) gate times and red to late times (up to 6 ns). (d) Cross-correlation for the 4.1 kW/cm² excitation power. The color gradient marks the beginning of the microtime gate, which was shifted in 20 ps step sizes. Black corresponds to early (from 0 ns) gate times and blue to late times (up to 6 ns).

Impact of simultaneous excitation of two chromophores

The corresponding average fluorescence signals of a single chromophore are 15 kHz and 58.5 kHz, respectively, which corresponds to a linear increase for 1.1 kW/cm² and 4.3 kW/cm² excitation irradiance as shown in Figure S4. The excitation irradiance is derived by measuring the power at the back aperture of the objective, which is focused onto a diffraction-limited excitation spot. A short estimation by using the detection rate is given in the following. Two independently blinking chromophores yield, on average, a signal of 30 kHz at 1.1 kW/cm² excitation power, and by estimating a detection efficiency of 20 % this signal corresponds to 75,000 photons emitted per second per molecule. With a fluorescence quantum yield of 65 % we would excite the molecule ~115,000 times per second. The pulsed excitation rate of our laser is set to 40 MHz, which means that we excite the chromophore, on average, with every 348th pulse. If we were to have perfect singlet-singlet annihilation between two chromophores, we would lose one fluorescence photon for every 348 × 348 excitation

pulses. This loss corresponds to 331 excitons per second. Taking into account the detection efficiency of the microscope, this means that ~43 photons per second are lost. The intensity would therefore drop by only 0.3 %. The same calculation yields an intensity drop of ~1.1 % for 4.3 kW/cm² excitation intensity.

Change of photon bunching with microtime gating

Random switching between two intensity states I_A and I_B is depicted in Figure S7a. The corresponding $g^{(2)}(\Delta\tau)$ intensity correlation is depicted in Figure S7b.
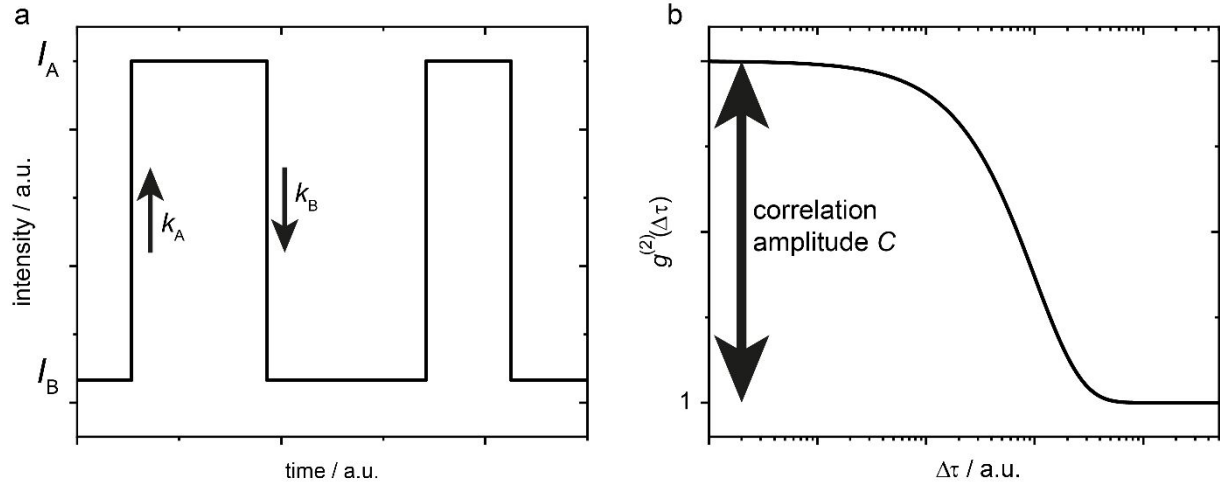
Figure S7. (a) Variation of the fluorescence intensity of a blinking molecule. (b) The corresponding correlation function on a logarithmic time scale. The correlation amplitude C is highlighted.

The correlation amplitude C of a system with two intensity states is given as:[5–8]

$$C = K\left(\frac{I_A - I_B}{I_A + K \cdot I_B}\right)^2 \qquad \text{eq. 12}$$

where I_A is the intensity of the bright fluorescent state A and I_B represents the intensity of the quenched fluorescent state B. K is the equilibrium constant calculated from the rate k_B of A→B state transitions and the rate k_A of B→A state transitions.

$$K = \frac{k_B}{k_A} \qquad \text{eq. 13}$$

The correlation amplitude C relies on the fractional intensity difference between states A and B. The quenched state B has an additional non-radiative decay from the electronic excited state. Therefore, the fluorescence decays faster after excitation in the quenched state which changes C for different microtime gates.

In our approach we vary the beginning of the microtime gate t, *i.e.* we use a long-pass time gate to change $C(t)$. We integrate over the exponential decay of the excited state from t to infinity to calculate the intensity of the quenched and unquenched state, respectively:

$$I_A(t) = \int_t^\infty e^{-(k_r + k_{nr}) \cdot t'} dt' = \frac{e^{-(k_r + k_{nr}) \cdot t}}{k_r + k_{nr}}, \qquad \text{eq. 14}$$

$$I_B(t) = \int_t^\infty e^{-(k_r + k_{nr} + k_{SDA}) \cdot t'} dt' = \frac{e^{-(k_r + k_{nr} + k_{SDA}) \cdot t}}{k_r + k_{nr} + k_{SDA}}. \qquad \text{eq. 15}$$

Here, k_r and k_{nr} are the radiative and non-radiative decay rates of state A, respectively. k_{SDA} is the additional SDA rate present for state B. This leads to:

112

$$C(t) = K\left(\frac{\frac{e^{-(k_\mathrm{r}+k_\mathrm{nr})\cdot t}}{k_\mathrm{r}+k_\mathrm{nr}} - \frac{e^{-(k_\mathrm{r}+k_\mathrm{nr}+k_\mathrm{SDA})\cdot t}}{k_\mathrm{r}+k_\mathrm{nr}+k_\mathrm{SDA}}}{\frac{e^{-(k_\mathrm{r}+k_\mathrm{nr})\cdot t}}{k_\mathrm{r}+k_\mathrm{nr}} + K\cdot\frac{e^{-(k_\mathrm{r}+k_\mathrm{nr}+k_\mathrm{SDA})\cdot t}}{k_\mathrm{r}+k_\mathrm{nr}+k_\mathrm{SDA}}}\right)^2 = K\left(\frac{1 - \frac{k_\mathrm{r}+k_\mathrm{nr}}{k_\mathrm{r}+k_\mathrm{nr}+k_\mathrm{SDA}}e^{-k_\mathrm{SDA}\cdot t}}{1 + K\cdot\frac{k_\mathrm{r}+k_\mathrm{nr}}{k_\mathrm{r}+k_\mathrm{nr}+k_\mathrm{SDA}}e^{-k_\mathrm{SDA}\cdot t}}\right)^2 \qquad \text{eq. 16}$$

The contrast between the integrated intensities rises with the additional depletion rate k_SDA. Equation 16 shows that $C(t)$ depends exponentially on k_SDA. We assume that k_r and k_nr stay constant and we are only interested in the values of K and k_SDA. Therefore, we can rewrite eq. 5 as

$$C(t) = K\left(\frac{1 - e^{-k_\mathrm{SDA}\cdot(t-t_0)}}{1 + K\cdot e^{-k_\mathrm{SDA}\cdot(t-t_0)}}\right)^2, \qquad \text{eq. 17}$$

where t_0 is an artificial shift on the time axis that accounts both for the arrival time of the laser pulse and the fluorescence lifetime ratio $\frac{k_\mathrm{r}+k_\mathrm{nr}}{k_\mathrm{r}+k_\mathrm{nr}+k_\mathrm{SDA}}$.

To demonstrate that this approach allows extraction of k_SDA from measured data, we simulated two simultaneously blinking chromophores similar to the experimental situation. The switching rates were fixed to $k_\mathrm{A} = k_\mathrm{B} = 10^4\,\mathrm{s}^{-1}$ and the fluorescence lifetimes were chosen to be 4 ns for the bright and 1 ns for the quenched state. Therefore, the additional non-radiative rate for quenched state is $k_\mathrm{SDA} = \frac{1}{\tau_\mathrm{B}} - \frac{1}{\tau_\mathrm{A}}$ $= 0.75\,\mathrm{ns}^{-1}$. Figure S8a shows the corresponding $g^{(2)}(\Delta\tau)$ correlation for different starting points t of the microtime gates, which were shifted in steps of 20 ps. Due to the increasing contrast in the intensity levels, the autocorrelation amplitude rises with t. Figure S8b shows $g^{(2)}(\Delta\tau = 10^{-8}\,\mathrm{s})$ in red, which in our case is equivalent to the correlation amplitude $C(t)$ corrected by an offset of 1 for uncorrelated events. We fit the extracted value with

$$g^{(2)}(\Delta\tau = 10^{-8}\,s, t) = 1 + K\left(\frac{1 - e^{-k_\mathrm{SDA}\cdot(t-t_0)}}{1 + K\cdot e^{-k_\mathrm{SDA}\cdot(t-t_0)}}\right)^2 \qquad \text{eq. 18}$$

The value of k_SDA extracted from the fit (bold semitransparent line) is $k_\mathrm{SDA} = 0.748 \pm 0.002\,\mathrm{ns}^{-1}$, close to the expected value of 0.75. Additionally, we plot $g^{(2)}(\Delta\tau = 0,t)$ in black, which shows a saturation towards 1 corresponding to an apparently infinite number of chromophores. The ratio of $g^{(2)}(\Delta\tau = 0,t)$ and $g^{(2)}(\Delta\tau = 3\cdot 10^{-8}\,s, t)$ equals the N_c/N_ℓ ratio and stays constant at a value of 0.5, the expected value for a system with two chromophores.
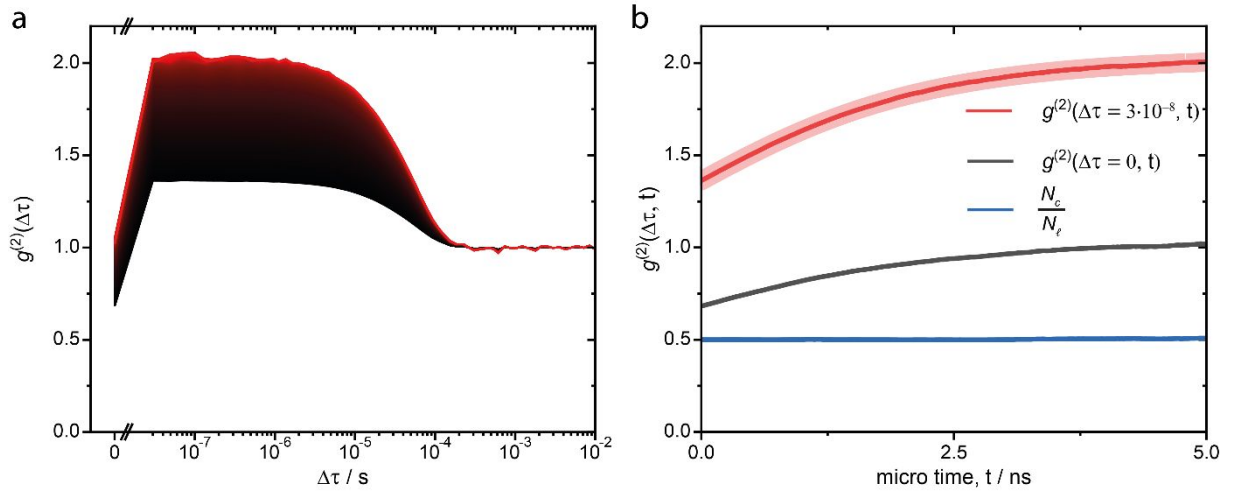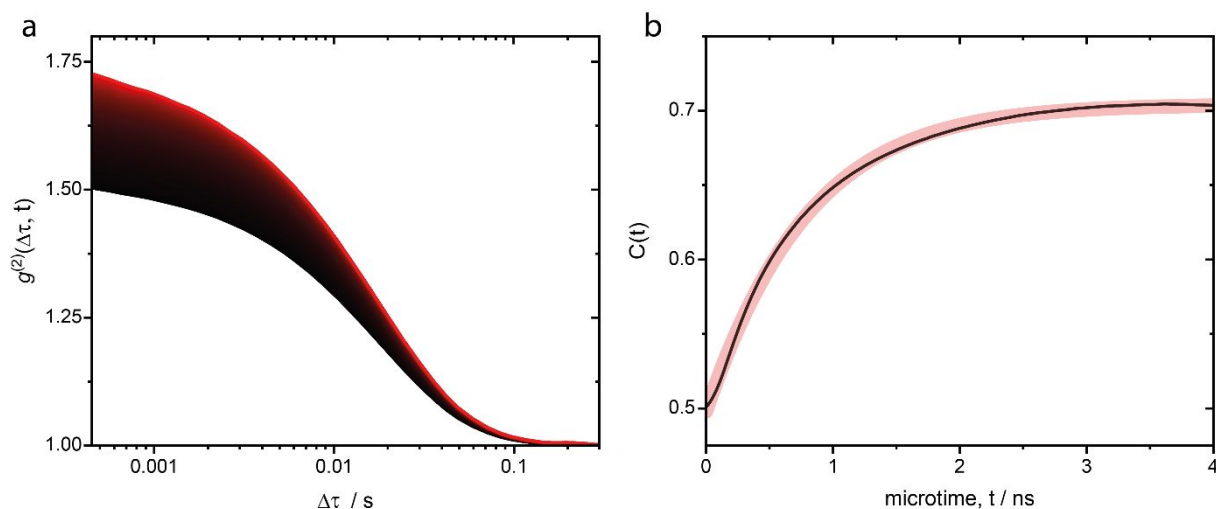

Figure S8. (a) Simulated correlation of two simultaneously blinking dyes. The color gradient marks the beginning of the microtime gate used, which was shifted with a 20 ps step size. Black corresponds to an early (from 0 ns) beginning of the microtime gate and red to a late one (up to 5 ns). (b) Extracted

correlation values for $g^{(2)}(\Delta\tau = 10^{-8}\,s,t)$ (red) and $g^{(2)}(\Delta\tau = 0,t)$ (black). The red data set is fitted with eq. 7 (semitransparent bold red line). The ratio of N_c/N_ℓ is plotted in blue.

To extract the k_{SDA} rate from our experimental data we plotted the blinking amplitude of Figure 4j with a mono-exponential model to extract $C(t)$ for different beginning values of the microtime gate.

$$g^{(2)}(\Delta\tau, t) = 1 + C(t) \cdot \exp\left(-(k_{kinetics}) \cdot \Delta\tau\right) \qquad \text{eq. 19}$$

Here, $k_{kinetics} = k_A + k_B$ is the sum of the kinetic rates that describe the state transitions. The correlation amplitude for different microtime gates is shown in Figure S9a. The extracted correlation amplitudes $C(t)$ are plotted in Figure S9b as a black line and fitted with eq. 6. We extract k_{SDA} from the fit as $k_{SDA} = 1.41 \pm 0.01\ \text{ns}^{-1}$.

Figure S9. (a) Correlation amplitude of two collectively blinking ATTO 647N dyes. The color gradient marks the beginning of the microtime gate used, which was shifted in steps of 20 ps. Black corresponds to an early beginning (from 0 ns) of the microtime gates and red to a late (up to 4 ns) beginning. (b) Fitted correlation amplitude $C(t)$ shown in black, with a fit based on eq. 6 shown as a red semitransparent line.

Fluorescence lifetime fitting and SDA rate extraction

A reconvolution algorithm was used in order to extract the fluorescence lifetimes from the photon arrival time histograms in Figure 4g and 4h. The fluorescence lifetime decay was fitted by a convolution of the instrument response function (I_{IRF}) and the sum of fluorescence lifetime decays with amplitudes A_i, fluorescence lifetime $\tau_{fl,i}$ and the background intensity I_{bg}.

$$I(t) = \left(I_{IRF}(t) * \sum_i A_i \cdot e^{-\frac{t - t_{off}}{\tau_{fl,i}}}\right) + I_{bg} \qquad . \qquad \text{eq. 20}$$

Here, $*$ denotes the convolution operator and t_{off} represents an offset of the decay function that was introduced to compensate an intensity-dependent shift of I_{IRF}. The fit routine iterates over a range of IRF shifts and returns the fit attempt with the best reduced chi-squared test. The reconvolution fits are shown in Figure S10. The monoexponential fit model in Figure S10a works well for the independently blinking chromophore data of Figure 4i. The reduced chi squared is 1.05. A fluorescence lifetime of $4.3 \pm 0.1\ \text{ns}$ was extracted, which is expected for ATTO 647N labeled on dsDNA.[9] The monoexponential model works rather poorly for collectively blinking chrompohores as shown in Figure S10b, with a reduced chi squared of 9.72. A biexponential model is assumed to better model the presence of two intensity states of the dyes. The corresponding reconvolution fit results in reduced chi-squared

values of 1.62 and the obtained lifetimes are $\tau_{fl,1} = 0.6 \pm 0.1$ ns and $\tau_{fl,2} = 2.7 \pm 0.1$ ns. The slow component shows that the ATTO 700 still absorbs slightly in its anionic radical state.
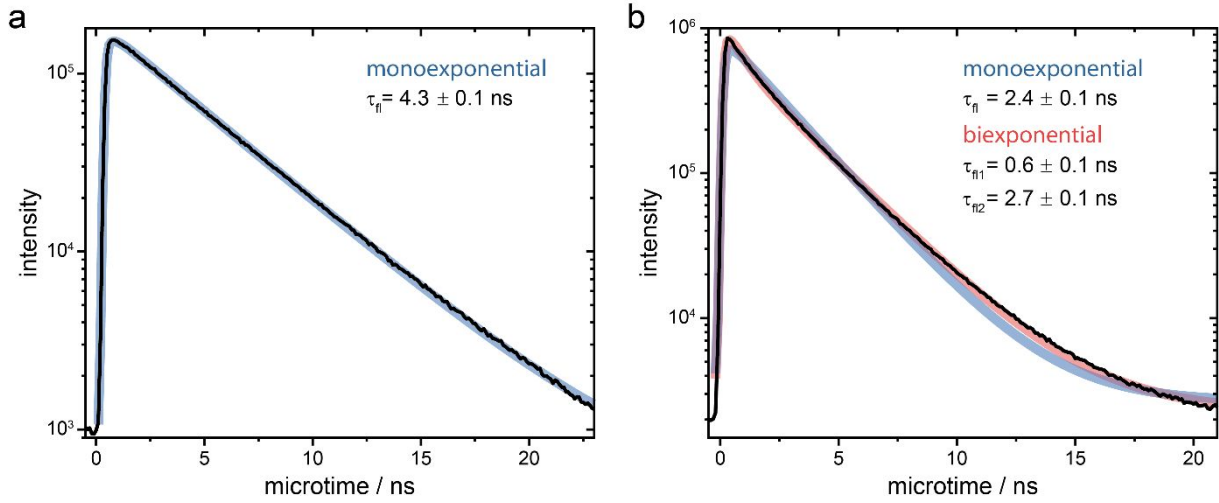
Figure S10. (a) Monoexponential reconvolution fit (blue) of the data from Figure 4g (black) with a microtime binning of 100 ps. (b) Monoexponential (blue) and biexponential (red) reconvolution fits of the data from Figure 4h (black) with a microtime binning of 100 ps.

With the fluorescence lifetimes extracted from the biexponential fit model we are able to calculate the SDA rate and validate our method as discussed in section 5.

$$\frac{1}{\tau_{fl,1}} - \frac{1}{\tau_{fl,2}} = \frac{1}{\frac{1}{k_r + k_{nr} + k_{SDA}}} - \frac{1}{\frac{1}{k_r + k_{nr}}} = k_{SDA} \qquad \text{eq. 21}$$

This approach yields $k_{SDA} = 1.3 \pm 0.3$ ns^{-1}, which is in good agreement with the SDA rate extracted in section 5 of $k_{SDA} = 1.41 \pm 0.01$ ns^{-1}.

Systems with simultaneous collective and independent blinking

Multichromophoric systems could potentially show a combination of collective and independent blinking of chromophores. Both types of blinking require different normalizations of the photon antibunching measurement and therefore neither $g^{(2)}(0)$ nor N_c/N_ℓ yields the correct number of chromophores. Here, we demonstrate by simulations how a suitable subset of fluorescence photons can yield the correct value.

For the simulations we consider a simple two-chromophore system. Two chromophores are collectively quenched by an energy sink. In Figure S11, the collective switching of two chromophores into the quenched and unquenched state is denoted by the transition rate constants k_B and k_A, respectively. The independent blinking of the dyes by switching between a florescent and non-fluorescent state is denoted with k_{off} and the transition rate into the fluorescent state with k_{on}.
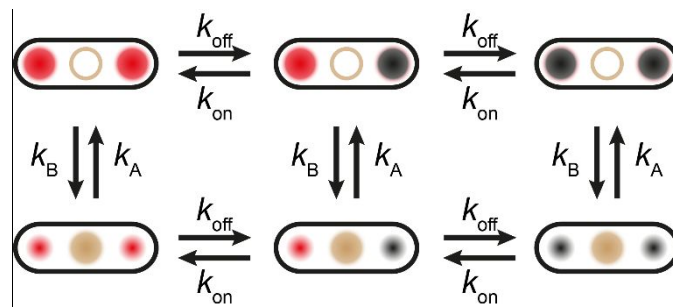
Figure S11. Sketch of all five intensity states of a system with two independently blinking dyes which can also get collectively quenched by an energy sink. We note that both states on the right are considered as one state because both states are completely non-fluorescent.

The simulations were carried out as described in Section 2. The transition rates for Figure S12a,b are set to: $k_A = k_B = 500$ s^{-1} and $k_{on} = k_{off} = 50\ 000$ s^{-1}. The transition rates for Figure S12c,d are set to: $k_A = k_B = 50\ 000$ s^{-1} and $k_{on} = k_{off} = 500$ s^{-1}.
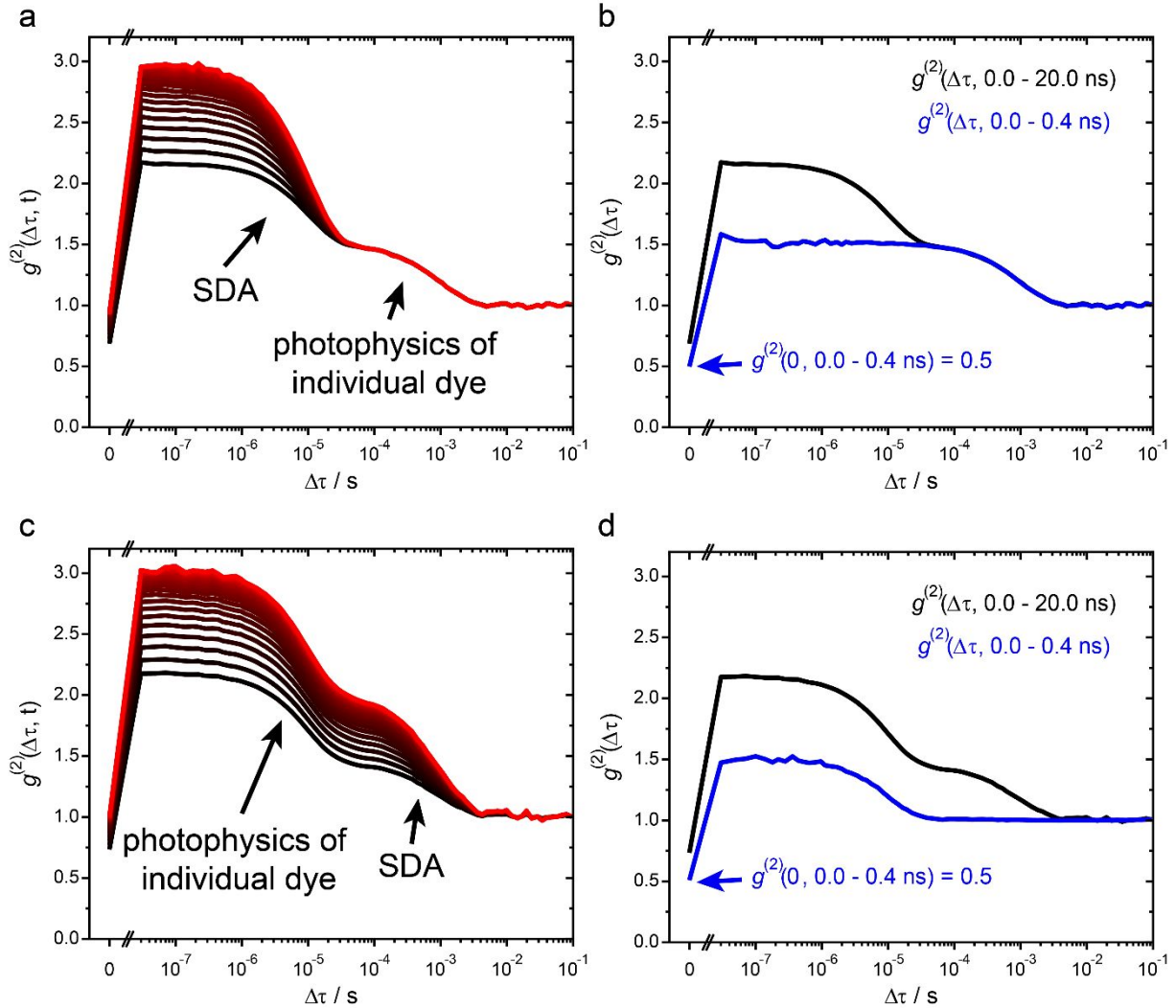
Figure S12. (a, c) Simulated intensity correlation of two collectively blinking dyes, which also show individual blinking. The color gradient marks the beginning of the microtime gate t used, which was shifted in steps of 200 ps. Black corresponds to an early (from 0 ns) beginning of the microtime gate and red to a late one (up to 5 ns). (b, d) Intensity correlation curves considering all photons (black) and only the photons detected within the first 400 ps after pulsed excitation (blue). Note that the bunching amplitude due to collective blinking is missing and that $g^{(2)}(0)$ yields the correct degree of photon antibunching.

The expected antibunching value for two dyes is 0.5. The simulation with faster collective blinking (SDA, Figure S12a) kinetics yields a degree of photon antibunching of $g^{(2)}(0) = 0.69$ and $N_c/N_\ell = 0.32$. The simulation with faster individual blinking (Figure S12c) yields a degree of photon antibunching of $g^{(2)}(0) = 0.73$ and $N_c/N_\ell = 0.34$. $g^{(2)}(0)$ overestimates the number of dyes because collective blinking is present, which raises the $g^{(2)}(0)$ value. N_c/N_ℓ underestimates the number of dyes because the lateral correlation bins are now the sum of the two bunching amplitudes but only the amplitude of the collective blinking is affecting the zero-lag-time correlation $g^{(2)}(0)$.

116

An easy approach to count the number of chromophores is the application of a small microtime gate right after the pulsed excitation. The quenching of the SDA is a time dependent process and becomes more likely as time progresses, which ultimately results in a quenched fluorescence intensity and shortened fluorescence lifetime. If there were only little time for SDA processes, both intensity levels would be equally bright if only photons right after the laser pulse excitation are considered. Within the first few hundred picoseconds no intensity fluctuations due to SDA are observed, resulting in an absence of bunching amplitude in the intensity correlation as depicted by the blue lines in Figure S12b,d. The remaining bunching amplitude results from the independent blinking process and therefore the number of chromophores can be reliably counted by $g^{(2)}(0)$ as demonstrated in Figure S12b,d. Choosing an early time gate is also useful if SSA has to be considered, which is also a time dependent process.[9] With an early microtime gate annihilation processes have most likely not occurred yet and no excitons are lost due to SSA nor SDA.

Table S4: Sequences for the modified DNA origami structure.

5' position	Sequence	Comment
0[286]	AAAACGAAAGAGGCTCATTATAC	
11[105]	ACACAACATACGAGGGATGTGGCTATTAATCGGCC	
9[567]	ATCATTTACATAAAAGTATCAAAATTATAAGAAACTTCAATA	
7[567]	CAGCTTTGAATACCAAGTTACAA	
5[455]	CATGCCAGTGAGCGCTAATATCCAATAATAAGAGC	
2[223]	CCGAACTTTAATAAAAGCAAAGCGGATT	
5[497]	TTGAGAATATCTTTCCTTATCACTCATCGAGAACA	
9[315]	CAGATATAGGCTTGAACAGACGTTAGTAAAGCCCAAAAATTT	
5[287]	GCGCAGCGACCAGCGATTATATATCATCGCCTGAT	
8[69]	TCGGTCATACCGGGGGTTTCTGC	
11[219]	GTGCCTGCTTTAAACAGGGAGAGAGTTTCAAAGCGAACCA	
10[457]	AAAAGATAGGGTTGAGTGT	
2[643]	GATAGTGCAACATGATATTTTTGAATGG	
0[347]	AGCGTATCATTCCACAGACCCGCCACAGTTGCAGCAAGCG	
9[483]	ATAATGAATCCTGAGATTACGAGCATGTGACAAAAACTTATT	
8[573]	AAATGCGTTATACAAATTCTTAC	
2[433]	AGGGACAAAATCTTCCAGCGCCAAAGAC	
7[63]	GCCCGCACAGGCGGCCTTTAGTG	
4[377]	CTATTTCGGAACGAGTGAGAATA	
0[698]	TTTTTCGGGAGCTAAACAGGTTGTTAGAATCAGAGTTTTT	
4[587]	CATCGGGAGAAATTCAAATATAT	
7[506]	AAATCAGCCAGTAATAACACTATTTTTGAAGCCTTAAATC	
7[170]	TTTTTATCCAATAAATCTCTACCCCGGTAAAACTAGCATG	
5[161]	GTATACAGGTAATGTGTAGGTAGTCAAATCACCAT	
4[396]	AACAGAGTGCCTGGGGTTTTGCTCACAGAAGGATTAGGAT	
3[350]	GTCACCAGTACAAGGTTGAGGCA	
5[581]	ACATCATTTAAATTGCGTAGAAACAGTACCTTTTA	
5[623]	ATACCCTTCGTGCCACGCTGAACCTTGCTGAACCT	
8[130]	GGGCGTGAAATATTAGCGCCATTCGC	
9[357]	TCTTATACTCAGAAAGGCTTTTGATGATATTGACACGCTATT	
11[345]	GAGAGCCTCAGAACCGCATTTTCTGTAACGATCTAAAGTT	

5[329]	TTCATTTTCTGCTAAACAACTGAACAACTAAAGGA	
8[489]	AAAACGGAATACCCAAAAGAACT	
0[202]	GACCGGAAGCAATTGCGGGAGAA	
3[182]	GCTAAATCGGTTTGACTATTATA	
3[392]	ATATTCACAAACAAATTCATATG	
6[69]	AAAAGTGTCAGCAACAATTGCAGGCGCT	
11[567]	ACCATCACCCAAATAAACAGTTCATTTGATTCGCC	
7[590]	AATCGTTGAGTAACATTGGAATTACCTAATTACATTTAAC	
11[93]	GCTCAAGTTGGGTAACGGGCGGAAAAATTTGTGAGAGATA	
0[305]	ACTACCTTTAAACGGGTAACAGGGAGACGGGCA	
4[270]	TCAACATCAGTTAAATAGCGAGAGTGAGACGACGATAAAA	
6[153]	TAAATCGGTTGGTGCACATCAAAAATAA	
10[163]	TCAGCTAACTCACATTAAT	
7[231]	TGCAACACTATCATAACCCTCGT	
4[438]	ACCAAATTACCAGGTCATAGCCCCGAGTTTTCATCGGCAT	
8[195]	TTAACAAGAGAATCGATGAACGG	
3[625]	AGACAACCTGAACAGTATTCGAC	
8[363]	TGAACAGCTTGATACCGATAGTT	
0[412]	TCACCGTCACCGGCGCAGTCTCT	
4[706]	TTTTTGTCCATCACGCAAATTCCGAGTAAAAGAGTCTTTTTT	
11[315]	ACAGCTGATTGCCCGTCGCTGCGCCCACACGTTGA	
8[424]	CGGAAGCACGCAAACTTATTAGCGTT	
0[431]	ATTCAAGGGGAAGGTAAATGTGGCAAATAAATC	
3[602]	TGATTATCAGATATACGTGGCAC	
4[545]	TGACCTAAATTTTTAAACCAAGT	
3[679]	GGTTGCTTTGACGAGCACGTTTTT	
6[573]	TGATTTAGAAAACTCAAGAGTCAATAGT	
11[441]	AAAAGAATAGCCCGATACATACGCAGTAAGCTATC	
8[634]	TACATAAATTCTGGGCACTAACAACT	
3[541]	CATAGTTAATTTGTAAATGTCGC	
11[147]	TGCCTAATGAGTGAGAAAAGCTCATATGTAGCTGA	
9[651]	AATAGCTGTCACACGCAACGGTACGCCAGCGCTTAATGTAGTA	
0[557]	TACCTAATATCAAAATCATTCAATATTACGTGA	
4[60]	TCAGAGGTGTGTCGGCCAGAATGAGTGCACTCTGTGGT	
3[476]	TTTTTTGTTTAATAAAGTAATTC	
8[382]	AAGTAAGAGCCGCCAGTACCAGGCGG	
3[79]	GTGGAACGACGGGCTCTCAACTT	
4[102]	CCAGCCAAACTTCTGATTGCCGTTTTGGGTAAAGTTAAAC	
3[121]	AATCAGTTAAAACGTGGGAGAAA	
3[224]	GCATCAAAAAGAAGTAAATTGGG	
7[212]	TTTCACGAGAATGACCATTTTCATTTGGTCAATAACCTGT	
8[678]	CCTACATACGTAGCGGCCAGCCATTGCAACAGGTTTTT	
5[539]	TTCGCTATTCGCAAGACAAAGTTAATTTCATCTTC	
7[17]	TTTTTATCCAGCGCAGTGTCACTGC	
8[298]	CATAGAATTTGCGGTTTGAAAGAGGA	
10[79]	GTATGTGAAATTGTTATCC	

7[273]	ACTACTTAGCCGGAACGAGGCGC	
11[387]	GGCGACACCACCCTCAGGTTGTACTGTACCGTTCCAGTAA	
6[447]	TTACCTCTTAGCAAATTTCAACCGATTG	
8[508]	GGTTTGCGCATTTTAACGCGAGGCGT	
10[415]	CCTCCGAAATCGGCAAAAT	
4[480]	TAAGCCAGAGAGCCAGAAGGAAACTCGATAGCCGAACAAA	
0[179]	GCCTTATACCCTGTAATACCAATTCTTGCGCTC	
9[147]	CATTCAACCCAAAATGTAGAACCCTCATGAATTAGTACAACC	
7[525]	TATGTGATAAATAAGGCGTTAAA	
0[454]	AGACGGGAGAATTGACGGAAATT	
11[681]	AAAGGGCGCTGGCAAGTATTGGC	
4[228]	GAGCTTAAGAGGTCCCAATTCTGCAATTCCATATAACAGT	
3[331]	TACCGGGATAGCAATGAATATAT	
4[335]	ATTGCGAATAATGTACAACGGAG	
2[265]	TATGCATTACAGAGGATGGTTTAATTTC	
4[564]	TTTAGAACGCGAATTACTAGAAAACTATAAACACCGGAAT	
11[597]	GAGGTAACGTTATTAATTTTAAAACAAATAATGGAAGGGT	
5[25]	TTTTTCCGGTGCAGCACCGATCCCTTACACTTGCC	
1[17]	TTTTTTGGTAATGGGTAACCATCCCACTTTTT	
8[531]	AACGAACCTCCCGACTTGCGGGA	
0[515]	CTGAAAACCTGTTTATCAAACATGTAACGTCAA	
8[592]	AAAATTTTTTAAAATGAGCAAAAGAA	
7[609]	ATTTGGCAAATCAACAGTTGAAA	
11[639]	CCGATAATAAAAGGGACTTAACACCGCGAACCACCAGCAG	
3[583]	GGAATCGGAACATTGCACGTTAA	
2[349]	TGTAGGGGATTTAGTAACACTGAGTTTC	
3[434]	AAAAGGGCGACAATTATTTATCC	
5[371]	ATCAGAGCCTTTAACGGGGTCTTAATGCCCCCTGC	
7[338]	GGAGCAGCCACCACCCTTCGCATAACGACAATGACAACAA	
3[56]	ATCAGCGGGGTCAGCTTTCAGAG	
0[473]	AAAAAAGGCAGCCTTTACAATCTTACCAGTTTG	
6[698]	TTTTTAACAATATTACCGTCGCTGGTAATATCCAGTTTTT	
8[88]	AGCCTCCCCAGGGTCCGGCAAACGCG	
6[405]	CAAGTGCTGAGTAAGAAAATAAATCCTC	
7[632]	GGAATAACAGAGATAGACATACAAACTTGAGGATTTAGAA	
0[76]	GACTTTCTCCGTGGCGCGGTTG	
2[97]	GCGAAAGACGCAAAGCCGCCACGGGAAC	
4[648]	GCATCGAGCCAGATATCTTTAGGACCTGAGGAAGGTTATC	
4[606]	ACAGTTTTTCAGATTTCAATTACCGTCGCAGAGGCGAATT	
7[548]	TAAGATCTGTAAATCGTTGTTAATTGTAAAGCCAACGCTC	
11[555]	CCCACATGTGAGTGAATAACTGATGCTTTTAACCTCCGGC	
9[399]	ATAAGAAGCCACCCAAACTTGAGCCATTATCAATACATCAGT	
11[189]	ACTGCCCGCTTTCCTGAAAAGCTATATTTTAAATA	
3[499]	TGTCCAAGTACCAGAAACCCCAG	
4[209]	AATGCTGTAGCTGAGAAAGGCCG	
7[357]	GTGTATTAAGAGGCTGAGACTCC	

8[237]	GCTTGACCATTAGATACATTTCG	
9[609]	GATGAATAAATCCTGTAGGTGAGGCGGTAGCGTAAGTCCTCA	
0[328]	TTGTCGTCTTTCTACGTAATGCC	
11[513]	CTCCAATTTAGGCAGAGACAATCAATCAAGAAAAATAATA	
3[560]	AAGACGCTGAGACCAGAAGGAGC	
7[42]	GCGCCTGAATGCCAACGGCCCAGCCTCCCGCGTGCCTGTTCTTCTTTTT	
0[370]	GCGTCATACATGCCCTCATAGTT	
11[303]	GTGAGTTAAAGGCCGCTGACACTCATGAAGGCACCAACCT	
3[373]	GGTCACGCCAGCACAGGAGTTAG	
4[51]	GGGTTACCTGCAGCCAGCGGTGTTTTT	
7[254]	TTACCAATAAGGCTTGCAGTGCGGAAGTTTAGACTGGATA	
8[466]	GGCATAAGCGTCTTCGAGGAAACGCA	
3[247]	CTTGAAAACACCCTAACGGCATA	
8[405]	GGTGCCGTCGAGAGGGTTGATAT	
10[331]	TCGTTCACCGCCTGGCCCT	
8[615]	GTTGAAACAAACATCAAGAAAAC	
6[531]	GACCGTCGAACGGGGAAGCTAATGCAGA	
6[363]	TGAAATTGTTTCAGGGAACTACAACGCC	
10[625]	AACACCCTAAAGGGAGCCC	
6[279]	CATGTCAGAGATTTGATGTGAATTACCT	
11[429]	CCCTTCATATAAAAGAACGTAGAGCCTTAAAGGTGAATTA	
11[651]	TTGACGGGGAAAGCTTCACCAGAAATGGCATCACT	
6[615]	GTCAGTCGTTTAACGAGATGGCAATTCA	
7[422]	AGCGCCACCACGGAATACGCCTCAGACCAGAGCCACCACC	
4[312]	ATTTGCCAAGCGGAACTGACCAACGAGTCAATCATAAGGG	
8[550]	CAGTAAGAACCTTGAGCCTGTTTAGT	
4[503]	AGCAAGCCGTTTAAGAATTGAGT	
2[601]	TCAATAATAAAGTGTATCATCATATTCC	
9[21]	TTTTTGCGTCCGTGCCTGCATCAGACGTTTTT	
11[483]	GAACAAGAGTCCACCAATTTTTTAGTTGTCGTAGG	
10[499]	CTATATTAAAGAACGTGGA	
4[186]	GAGACAAAGATTATCAGGTCATTGACGAGAGATCTACAAA	
9[63]	TTCACCTAGCGTGGCGGGTGAAGGGATACCAGTGCATAAAAA	
11[609]	AGCACTAAATCGGATCGTATTTAGACTTATATCTG	
4[293]	AAATTGTGTCGAGAATACCACAT	
3[667]	GGCGCCCCGCCGAATCCTGAGAAGTGAGGCCGATTAAAGG	
3[205]	GTCAGAATCAGGCAGGATTCGCG	
0[622]	AAGATAAAACAGTTGGATTATAC	
6[111]	TCAGGTGAAATTTCTACGGAAACAATCG	
10[205]	AGCAGTCGGGAAACCTGTC	
6[489]	AATCATAATAACCCGGCGTCAAAAATGA	
0[496]	TCCCATCCTAATGAGAATAACAT	
0[221]	CGAGCACAGACTTCAAATACCTCAAAAGCTGCA	
9[231]	TTAGTGTGAATCCCTCTAATAAAACGAAAGAACGATGAATTA	
4[629]	CAAATATCAAACCAGATGAATAT	
0[664]	GATTTTAGACAGGCATTAAAAATA	

10[667]	AGACGGCGAACGTGGCGAG	
0[599]	TTCTGGAATAATCCTGATTTTGCCCGGCCGTAA	
3[23]	TTTGCAACCAGCTTACGGCGGTGGTGAGGTTTCAGTTGAGGATCCTTTTT	
8[340]	GCGCCCGCACCCTCTCGAGGTGAATT	
7[674]	GCCTTACGCTGCGCGTAAAATTATTTTTTGACGCTCAATC	
7[86]	ATGAATCCCAGTCACGATCGAACGTGCCGGCCAGAGCACA	
5[245]	CGCCTGACGGTAGAAAGATTCTAATGCAGATACAT	
8[657]	GTATTAGAGCCGTCAATAGATAA	
3[308]	CTAAAGACTTTTAGGAACCCATG	
2[702]	TTTTTTATAACGTGCTTTCCTCTTTATAACAGTACTAT	
4[671]	TACTTCTTTGATAAAAATCTAAA	
2[391]	ATTAAAATAAGTGCGACGATTGGCCTTG	
9[189]	GAGCAAGGTGGCATTTACTCCAACAGGTTCTTTACGTCAACA	
4[167]	CAATATGATATTGATGGGCGCAT	
7[147]	GCTAATGCCGGAGAGGGTAGCTA	
7[464]	AAGCACAGAGCCTAATTATTGTTAGCGATTAAGACTCCTT	
8[172]	TAATCGTAGCATTACCTGAGAGTCTG	
0[580]	TAGAACCTACCAGTCTGAGAGAC	
4[354]	GAAAGTTCAACAATCAGCTTGCTTAGCTTTAATTGTATCG	
8[46]	CAGCATCAACCGCACGGCGGGCCGTT	
2[181]	TTATGGCCTGAGCACCTCAGAGCATAAA	
3[644]	CTATTAGTCTTTCGCCGCTACAG	
8[111]	CTTTTTTTCGTCTCGTCGCTGGC	
11[231]	TTAATGAATCGGCCATTCATTCCAATACGCATAGT	
3[518]	AACAACATGTTCATCCTTGAAAA	
5[77]	AACGTTGTAGAAACAGCGGATAGTTGGGCGGTTGT	
10[706]	TTTTTAGGAGCGGGCGCTAGGAAGGGAAGAAAGCGAATTTTT	
9[441]	TGCCATACATAAAGATTAACTGAACACCAACAGCCGGAATAG	
7[189]	GGCTAAAGTACGGTGTCTGGAAG	
6[237]	AAGAGATTCATTTTGTTTAAGAGGAAGC	
5[203]	TGTAAATCATGCTCCTTTTGATAATTGCTGAATAT	
7[315]	AATCCAAAAAAAAGGCTCCAAAA	
10[583]	TGGCAAGTTTTTTGGGGTC	
2[559]	GAATTATCCAATAACGATAGCTTAGATT	
11[364]	GTCCACGCGCCACCTCACCGTTGAAACA	
11[471]	TGTTCCAACGCTAACGAACAAGTCAGCAGGGAAGCGCATT	
4[522]	ACCGCATTCCAACGGTATTCTAAGCGAGATATAGAAGGCT	
7[380]	TCAAGCAGAACCACCACTCACTCAGGTAGCCCGGAATAGG	
8[447]	ATTCTTTTCATAATCAAAATCAC	
6[321]	AAATCCCCGAAACAATTCATGAGGAAGT	
10[541]	CATTCTATCAGGGCGATGG	
10[373]	TACCTGGTTTGCCCCAGCA	
5[413]	AGAGTTTATACCAGTAGCACCTGAAACCATCGATA	
9[105]	GTCCGTCCTGCAAGATCGTCGGATTCTCTTCGCATTGGACGA	
11[63]	ATAGCTGTTTCCTGGAACGTCCATAACGCCGTAAA	
11[177]	TGCGTACTAATAGTAGTTGAAATGCATATTTCAACGCAAG	

8[702]	TTTTTAAAAACGCTCATGGAAATA	
7[441]	TTGAAGCCCTTTTTAAGAAAAGT	
11[525]	AGGGCGAAAAACCGATTTAACGTAGGGCAAATACC	
2[475]	AAATAGGTAATTTACAAATAAGAAACGA	
9[525]	TTTAGCAAACGCCACAATATAACTATATTCCCTTATAAATGG	
7[399]	TATTGCCTTTAGCGTCAGACTGT	
0[389]	GAATTGTAGCCAGAATGGATCAGAGCAAATCCT	
2[307]	TTCCATTGACCCAAAGAGGCTTTGAGGA	
7[651]	TAAGTAGAAGAACTCAAACTATCG	
2[517]	ACGCGTCGGCTGTAAGACGACGACAATA	
7[483]	GTTTACCGCGCCCAATAGCAAGC	
2[55]	TTCGCCATAAACTCTGGAGGTGTCCAGC	
10[48]	GCAGCACTTTGCTCTGAGCCGGGTCACTGTTGCCCTGCGGCTTTTT	
6[657]	TGCCTGAACAGCAAATGAATGCGCGAACT	
3[163]	TAAAGAGGCAAAATATTTTATAA	
0[538]	TTAGGTTGGGTTATAGATAAGTC	
4[419]	GCAGCACCGTAAGTGCCCGTATA	
8[214]	CAAATGGTTCAGAAGAACGAGTAGAT	
3[415]	GTTTATGTCACATGGGAATCCAC	
0[641]	CCGAACCCCCTAAAACATCGACCAGTTTAGAGC	
8[321]	CCGAACGGTGTACAGACCAGGCG	
3[457]	CAATCCAAAATACTGAACAGTAG	
6[195]	TGCAACTCAAAAGGCCGTACCAAAAACA	
0[95]	CCGGAAGACGTACAGCGCCGCGATTACAATTCC	
11[399]	GTTTGATGGTGGTTCAGAACCCCGCCTCACAGAAT	
11[25]	TTTTTCCGGGTACCGAGCTCGAATTCGTAATCTGGTCA	
0[53]	CGGTAGTACTCAATCCGCTGCTGGTCATGGTC	
8[256]	AAAATTCCATTCAGGCTTTTGCAAAAGAAGTCA	
3[266]	AACTTTAATCATGGGTAGCAACGGCTACGACAGCAACTAAAA	
10[247]	AATAACGCGCGGGGAGAGGCGGTT	
0[251]	TGGGAAGAAAAATCTACGTGCGTTTTAATT	
0[263]	CAGTCTTGATTTTAAGAAC	
8[286]	GACCTTCATTTTGCCAGAGGGGGTAATAGT	
7[296]	AGACGTCGTCACCCTCAGACCTGCTC	
10[293]	ACCGGATGTTTTTCTTTTCACCA	ATTO 647N, only used for independent blinking
10[286]	ATTCATTAGAGTAATCTTGACGCTGGCT	
4[461]	AAGAAACAATGACCGGAAACGTC	biotin labeled
4[83]	GTACATCGACATCGTTAACGGCA	biotin labeled
5[665]	ATACCACCATCAGTGAGGCCAAACCGTTGTAGCAA	biotin labeled
4[251]	AACGCCAAAAGGCGGATGGCTTA	biotin labeled
5[119]	CATAATATTCCGTAATGGGATCCGTGCATCTGCCA	external labeling
3[98]	GGATAACCTCACAATTTTTGTTA	external labeling
4[125]	GTTTGAGGGGACCTCATTTGCCG	external labeling
4[144]	CGTAAAGGTCACGAAACCAGGCAATAGCACCGCTTCTGGT	external labeling

0[137]	CATCAGCGTCTGGCCTTCCACAGGAACCTGGGG	external labeling
10[121]	GGGCCGGAAGCATAAAGTG	external labeling
11[135]	TAAAGGATTGTATAAGCGCACAAACGACATTAAATGTGAG	external labeling
7[128]	TTCCGAATTGTAAACGTGTCGCCAGCATCGGTGCGGGCCT	external labeling
3[140]	CAATAGGAACGCAAATTAAGCAA	external labeling
7[105]	GAAAGATCGCACTCCAGCCAGCT	external labeling
0[160]	GATAAAAATTTTTAGCCAGCTTT	external labeling
8[153]	TCAGGCTGCGCAACTGTTGGGAA	external labeling
0[118]	CGAGTAACAACCGTTTACCAGTC	external labeling
2[139]	TTCGCGGATTGATTGCTCATTTTTTAAC	external labeling
10[279]	ACCCAAATGGCAAAAGAATACTCGGAACAGAATCC	5' ATTO 647N, only used for collective blinking
10[265]	AACAAAGCTGCTGTAACAACAAGGACGT	5' ATTO 647N
10[272]	TCAACGTTGCGTATTGGGCGCCAGGGTG	5' ATTO 700, only used for collective blinking

REFERENCES

1.   Nickels, P. C.; Wünsch, B.; Holzmeister, P.; Bae, W.; Kneer, L. M.; Grohmann, D.; Tinnefeld, P.; Liedl, T. Molecular Force Spectroscopy with a DNA Origami-Based Nanoscopic Force Clamp. *Science* **2016**, *354*, 305–307.

2.   Derr, N. D.; Goodman, B. S.; Jungmann, R.; Leschziner, A. E.; Shih, W. M.; Reck-Peterson, S. L. Tug-of-War in Motor Protein Ensembles Revealed with a Programmable DNA Origami Scaffold. *Science* **2012**, *338*, 662–665.

3.   Laurence, T. A.; Fore, S.; Huser, T. Fast, Flexible Algorithm for Calculating Photon Correlations. *Opt. Lett.* **2006**, *31*, 829–831.

4.   Schröder, T.; Scheible, M. B.; Steiner, F.; Vogelsang, J.; Tinnefeld, P. Interchromophoric Interactions Determine the Maximum Brightness Density in DNA Origami Structures. *Nano Lett.* **2019**, *19*, 1275–1281.

5.   Zumbusch; Fleury; Brown; Bernard; Orrit. Probing Individual Two-Level Systems in a Polymer by Correlation of Single Molecule Fluorescence. *Phys. Rev. Lett.* **1993**, *70*, 3584–3587.

6.   Orrit, M. Photon Statistics in Single Molecule Experiments. *Single Mol.* **2002**, *3*, 255–265.

7.   Lamb, D. C.; Schenk, A.; Röcker, C.; Nienhaus, G. U. Determining Chemical Rate Coefficients Using Time-Gated Fluorescence Correlation Spectroscopy. *J. Phys. Org. Chem.* **2000**, *13*, 654–658.

8.   Yu, J.; Lammi, R.; Gesquiere, A. J.; Barbara, P. F. Singlet-Triplet and Triplet-Triplet Interactions in Conjugated Polymer Single Molecules. *J. Phys. Chem. B* **2005**, *109*, 10025–10034.

9.   Hedley, G. J.; Schröder, T.; Steiner, F.; Eder, T.; Hofmann, F. J.; Bange, S.; Laux, D.; Höger, S.; Tinnefeld, P.; Lupton, J. M.; Vogelsang, J. Picosecond Time-Resolved Photon Antibunching Measures Nanoscale Exciton Motion and the True Number of Chromophores. *Nat. Commun.* **2021**, *12*, 1327.

4.4 Shrinking-Gate Fluorescence Correlation Spectroscopy Yields Equilibrium Constants and Distinguishes Photophysics from Structural Dynamics

Tim Schröder, Johann Bohlen, Sarah Ochmann, Patrick Schüler, Stefan Krause, Don C. Lamb, Philip Tinnefeld

Fluorescence correlation spectroscopy (FCS) is often used to study diffusion characteristics or molecular interactions in solution. In a FRET-experiment, fast structural dynamics between two FRET-states and thus fluctuation of the donor intensity appears as bunching amplitude in the intensity correlation. But extraction of the equilibrium constant is not possible because the amplitude is "convoluted" with the squared fractional intensity difference of the two intensity states, hampering a quantitative analysis of the dynamics. Despite many attempts to overcome this issue by FCS variations such as FLCS or FRET-FCS, prior knowledge of the corresponding fluorescence lifetimes or equilibrium constant is always required.

In this publication, I suggested a shrinking gate FCS (sg-FCS) approach to recover the equilibrium constant without prior knowledge from a two-intensity state system that shows correlated intensity and fluorescence lifetime changes. I provided a model of the microtime dependent bunching amplitude which additionally yields the rate difference of the excited state depopulation rates. Bunching amplitudes originating from photophysics do not alter the fluorescence lifetime and thus the bunching amplitude remains unchanged. With a DNA origami model system, I was able to demonstrate that kinetic values obtained by sg-FCS agree with those from a hidden Markov model which was used as a control analysis. The donor signal stochastically changes between two FRET states in the model structure, as a Cy3B labeled pointer stochastically switches between two complementary binding sites. The FRET acceptor was placed next to one binding site which made it the high-FRET position. I changed the switching speed and equilibrium through the length of the complementary sequence and was able to obtain the equilibrium constant over two and a half orders of magnitude without prior knowledge. I could tune the switching kinetics from the seconds range to the $100 \, \mu s$ range. sg-FCS is not only applicable to surface experiments. I was also able to determine the kinetics of fast dynamics in solution measurements.

In different applications, the versatility of sg-FCS was demonstrated. E.g. we were able to assign the Brownian molecular movement of a tether on graphene with a dye at its tip. The corresponding amplitude changed with sg-FCS while the photophysics amplitudes remained constant.

Next, FRET-based membrane charge sensors showed different FRET efficiencies with different surface charges. We were able to unravel the working mechanism of an organic dye-based membrane charge sensor with sg-FCS. We demonstrated that the donor stochastically switched back and forth between a membrane-bound and unbound state. Furthermore, the surface charges change the energy barrier and the energy difference between the two states altering the switching dynamics.

When TCSPC-data is available, sg-FCS is an easy-to-implement analysis to unravel structural dynamics in a FRET experiment by microtime gated intensity correlation. For sg-FCS no prior

knowledge is required and it enables a fast assignment of the origin of bunching amplitudes to either photophysical or dynamic origin which alter the fluorescence intensity and fluorescence lifetime. In addition, the equilibrium constant can be extracted for a two-state system in order to quantify these dynamics.

Shrinking gate fluorescence correlation spectroscopy yields equilibrium constants and distinguishes photophysics from structural dynamics

Tim Schröder[1], Johann Bohlen[1], Sarah E. Ochmann[1], Patrick Schüler[1], Stefan Krause[1,2], Don C. Lamb[1], Philip Tinnefeld[1]*

[1]Department Chemie and Center for NanoScience (CeNS), Ludwig-Maximilians-Universität München, Butenandtstraße 5-13, 81377 München, Germany

[2] present address: Fraunhofer Institut für Integrierte Schaltungen IIS, Dresden, Münchener Straße 16, 01187 Dresden, Germany

* philip.tinnefeld@cup.uni-muenchen.de

Abstract

Fluorescence correlation spectroscopy is a versatile tool for studying fast conformational changes of biomolecules especially when combined with Förster Resonance Energy Transfer (FRET) experiments. Despite the many methods available for identifying structural dynamics in FRET experiments, determination of the forward and backward transition rate constants and thereby also the equilibrium constant is difficult when two intensity levels are involved. Here, we combine intensity correlation analysis with fluorescence lifetime information by including only a subset of photons in the autocorrelation analysis based on their arrival time with respect to the excitation pulse (microtime). By fitting the correlation amplitude as a function of microtime gate, the transition rate constants from two florescence-intensity level systems and the corresponding equilibrium constants are obtained. This shrinking-gate fluorescence correlation spectroscopy (sg-FCS) approach is demonstrated using simulations and with a DNA origami-based model system in experiments on immobilized and freely diffusing molecules. We further show that sg-FCS can distinguish photophysics from dynamic intensity changes even if a dark quencher, in this case graphene, is involved. Finally, we unravel the mechanism of a FRET-based membrane charge sensor indicating the broad potential of the method. With sg-FCS, we present an algorithm that does not require prior knowledge and is therefore easily implemented when an autocorrelation analysis is carried out on time-correlated single-photon data.

Introduction

Fluorescence Correlation Spectroscopy (FCS) is a widely used tool to determine physical parameters such as concentration[1–3] and kinetic properties such as diffusion constants,[4–7] biomolecular dynamics,[8–10] reaction kinetics[11–13] and photophysical processes.[14,15] Time correlation of the fluorescent signal of freely diffusing molecules through a focused laser beam reveals the time scales of the underlying characteristic signal fluctuations. With the aid of physical models, these time scales can be assigned to the different kinetic processes, the most common process being the diffusion of molecules in and out of the laser focus.

Many variants of FCS such as Förster resonance energy transfer-FCS (FRET-FCS),[16,17] fluorescence lifetime correlation spectroscopy (FLCS),[18,19] time-gated FCS[20] and single-molecule burst-selective FCS[21,22] have evolved improving the specificity for underlying processes as well as the deduced information content.[23,24] Beyond diffusion constants and bimolecular binding constants, the fluorescence intensity correlation function $g^{(2)}(\Delta\tau)$ is also a widely employed algorithm to extract kinetic processes within diffusing molecules as well as from immobilized single quantum emitters.[25–29] For immobilized molecules, the autocorrelation analysis has been used, for example, to quantify physical and biomolecular processes ranging from antibunching[30,31] to intersystem crossing[32,33] and photo-induced electron transfer [34–36] to slower molecular dynamic of DNA hybridization switching.[9,37,38]

Although FCS can theoretically extract kinetic rate constants from the autocorrelation function, it is rarely used to do so in literature. In our lab, we were confronted with the problem that we suspected a correlation component induced by the fluctuating distance of a tethered dye to the quenching surface by graphene energy transfer (GET)[39] in a similar time regime where also photophysical processes (on-off, e.g. triplet transitions) occurred.[38] The problem to separate both contributions arose and we realized that this problem was not sufficiently addressed by other approaches including FLCS and FRET-FCS. FLCS, for example, extracts separate correlation functions when mixtures of species are involved but requires prior knowledge of the fluorescence lifetimes of the species involved.[18,19] FRET-FCS separates photophysical dynamics from on-off processes but is underdetermined for extracting equilibrium constants. Furthermore, it requires fluorescent acceptors.[16]

On-off switching by photophysical processes and distance dependent quenching by, for example, GET or by a FRET acceptor both induce intensity fluctuations that appear as a correlation in the intensity correlation function $g^{(2)}(\Delta\tau)$. The two processes differ in that only the dynamic quenching processes induce a change of the fluorescence lifetime. Thus, we reasoned that it required an algorithm to correlate the fluorescence lifetime information with the amplitude of the correlation function without prior assumptions. These considerations motivated us to revisit the influence of time-gating on the bunching amplitudes in fluorescence correlation spectroscopy and for the correlation analysis in general.

In this paper, we present a simple and versatile method to connect the fluorescence lifetime with the autocorrelation information, termed shrinking-gate FCS (sg-FCS), which enables the separation of dynamic quenching processes from on-off processes. We calculate the fluorescence intensity correlation function using different subsets of photons depending on their time-lag with respect to the laser pulse (i.e. with increasing microtime). Plotting the correlation

2

amplitude as a function of the microtime threshold shows how the correlation amplitude is increasingly dominated by the long-lifetime component. We present a model for this dependence based on a two-state system that yields further important parameters such as transition times and the equilibrium constant that are not directly obtainable from ordinary autocorrelation functions. The analysis can be carried out without prior knowledge of fluorescence lifetimes and it directly reveals whether the correlation amplitudes are of photophysical (on-off) in origin or whether states of different fluorescence lifetimes are involved. Using simulations and DNA origami-pointer model systems, we show that the algorithm works even when the dwell times in the individual states are unbalanced (K << 1 or K >>1). We exemplify the strength of this approach using graphene quenching as well as in single-molecule FRET experiments of a novel membrane surface potential sensor. The method is robust within the defined limits and easy to implement suggesting that it should be considered whenever FCS and related autocorrelation analyses are combined with time-correlated single-photon counting information.

Results

Intensity fluctuations on different time scales, e.g. caused by diffusion, photophysics or distance changes of a FRET pair, are commonly analysed with the normalized second order intensity correlation given by:

$$g^{(2)}(\Delta\tau) = \frac{\langle I(t) \cdot I(t + \Delta\tau)\rangle}{\langle I(t)\rangle^2} \tag{1}$$

which correlates the measured intensity $I(t)$ with the measured intensity as a function of the lag time, $\Delta\tau$.

A process that undergoes stochastic switching between a fluorescent state A and a non-fluorescent state B results in a monoexponential decay component of the $g^{(2)}(\Delta\tau)$ function.[15]

$$A \underset{k_A}{\overset{k_B}{\rightleftharpoons}} B \tag{2}$$

Here, k_A and k_B represent the transition rate constant into state A or state B respectively. For diffusing molecules, the relaxation kinetics is superimposed with the diffusion correlation function according to the following equation of $g^{(2)}(\Delta\tau)$.

$$g^{(2)}(\Delta\tau) = \frac{\gamma_{FCS}}{N} \cdot \frac{1}{1 + \frac{\Delta\tau}{\tau_{diff}}} \frac{1}{\sqrt{1 + \frac{\Delta\tau}{w^2\tau_{diff}}}} \cdot \left(1 + A_{dyn} \cdot e^{-\frac{\Delta\tau}{\tau_{CRT}}}\right) + 1 \tag{3}$$

Here, γ_{FCS} accounts for the approximated Gaussion illumination profile and corresponds to $2^{-\frac{3}{2}}$, N denotes the average number of molecules in the detection volume, τ_{diff} the diffusion dwell time and w accounts for the different axial dimension of the three dimensional confocal volume ($w = \frac{w_z}{w_{xy}}$). The dynamic bunching amplitude A_{dyn} accounts for the photon bunching

3

due to fast fluorescence intensity fluctuations on short time scales and is equal to the equilibrium constant in the case of on-off switching with the correlation relaxation time τ_{CRT}.

To simplify the discussion, we will first consider immobilized molecules undergoing fluctuations between different intensity states. However, we note that sg-FCS is applicable whenever there are two components with different fluorescence lifetimes that exchange due to various quenching mechanisms. With the fitted correlation relaxation time (CRT) and bunching amplitude, the dwell times for each state can be calculated according to $\tau_{CRT} = \frac{1}{k_A + k_B}$ and $A_{dyn} = \frac{k_B}{k_A}$ also yielding the equilibrium constant K. When dynamic quenching with non-zero intensity states are involved such as in FRET experiments, the calculation of the donor bunching amplitude A_{dyn} is "convoluted" with the intensity contrast of the two FRET states.[17,20,40,41]

$$A_{dyn} = K \left(\frac{I_A - I_B}{I_A + K \cdot I_B} \right)^2 \tag{4}$$

where I_A and I_B represent the fluorescence intensity of state A (high intensity, long fluorescence lifetime state) and state B (low intensity short fluorescence lifetime state). K denotes the equilibrium constant as the ratio of the switching rate constants between the high and low intensity states $K = \frac{k_B}{k_A}$. As equation (4) shows, the donor bunching amplitude A_{dyn} for a two intensity-state model relies on the fractional intensity difference. Due to the quadratic intensity difference dependence of the intensity correlation function, no unique solution for K is obtained even when both intensity levels are known (which is commonly not the case or there is some uncertainty involved). We demonstrate this by simulating two intensity trajectories of immobilized molecules, which are shown in Figure 1a (see SI section 1 for detailed information on the simulations). Both intensity trajectories have the same intensities for the high and low intensity states, respectively. It is obvious from the trajectories that the switching kinetics are different and that the red trajectory shows a longer dwell time in the fluorescence-quenched state.
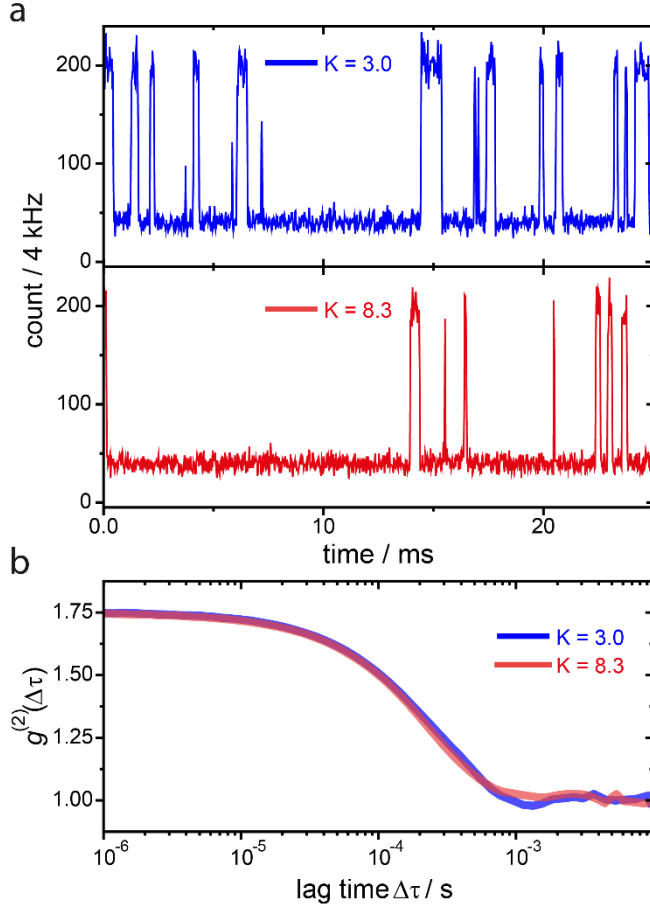
Figure 1: The ambiguity of the intensity autocorrelation function. a) A short section of the simulated intensity trajectories where the respective intensity levels for the bright and quenched states are the same but with different equilibrium constants, K. The rate constants for switching in the blue and red trajectories are given in Table 1. b) The autocorrelation of the full simulated trajectories, portions of which are shown in a).

Despite the different equilibrium constants, K, of the trajectories in Figure 1a, the autocorrelations in Figure 1b are virtually identical. They have the same bunching amplitude $A_{dyn}(t_g)$ and CRT τ_{CRT}. With a single $g^{(2)}(\Delta\tau)$ correlation, it is impossible to extract the switching rate constants and describe the kinetics quantitatively. This important information is, however, accessible by connecting the autocorrelation with the fluorescence lifetime information. We do this using sg-FCS, where subsets of photons are correlated depending on the arrival time of the photon with respect to the laser pulse (the microtime). By varying the threshold for the microtime, the relative intensity of the two states are changed and thereby their influence on the amplitude of the intensity correlation function. Hence, the intensity correlation function becomes a function of delay, $\Delta\tau$, and microtime gate, t_g: $g^{(2)}(\Delta\tau, t_g)$. The effect of the microtime thresholding on the fluorescence intensity trajectory and on the autocorrelation function is depicted in Figure 2a-c using the simulated data from Figure 1. Figure 2a shows the biexponential fluorescence lifetime histogram of the simulated data with $\tau_A = 4.0\ ns$ and $\tau_B = 0.8\ ns$. The shaded area indicates the subset of photons selected for different microtime gates.

5

Figure 2b shows the corresponding intensity time traces and Figure 2c shows the corresponding $g^{(2)}(\Delta\tau, t_g)$ correlation.
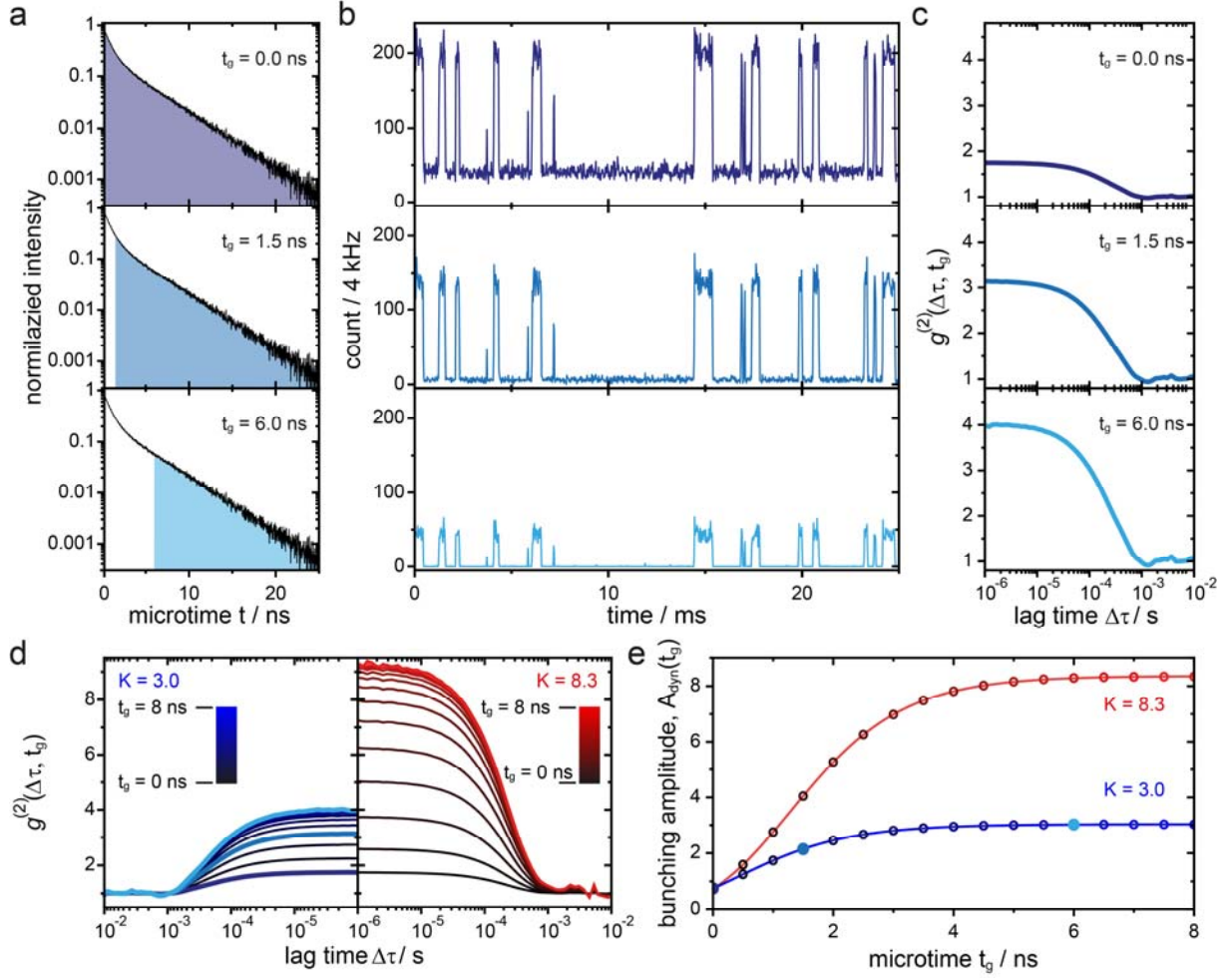
Figure 2: Applying sg-FCS to the simulated data from Figure 1. a) Histograms of simulated photon arrival times in a pulsed-laser excitation experiment. The shaded area indicates the applied mircrotime gate for sg-FCS. b) Extracted intensity trajectories according to the selected photons from the fluorescence lifetime data. c) The corresponding $g^{(2)}(\Delta\tau, t_g)$ of the respective intensity trajectories. d) The autocorrelation function is plotted as a function of the shrinking-gate in sg-FCSs for the simulated intensity trajectories of Figure 1a. The sg-FCS correlation functions are indicated with a color gradient from black $g^{(2)}(\Delta\tau, t_g = 0\,ns)$ to blue (left, $K = 3$) or red (right, $K = 8.3$) $g^{(2)}(\Delta\tau, t_g = 8\,ns)$ with a $0.5\,ns$ step size. Correlations shown in c) are highlighted in the corresponding bold blue color. The $g^{(2)}(\Delta\tau, t_g)$ correlation functions are fitted with a monoexponential model and the obtained correlation amplitudes $A_{dyn}(t_g)$ are plotted in e). The data points are fitted with the model of equation (9) to extract the equilibrium constant K and $k_{\Delta ET}$. The full circles represent the amplitude of the correlation functions in colors corresponding to panels c and d.

When considering all photons in this simulation, i.e. when the microtime threshold is set to $t_g = 0\,ns$, the fluorescence intensity trajectory and autocorrelation function are the same as the

6

ones shown in Figure 1a (blue trajectory). When only photons after $t_g = 1.5 \; ns$ are considered, the intensity of the fluorescence intensity trajectory is reduced. The intensities of the two fluorescent states, however, are not affected equally. The microtime gate preferentially excludes photons from the quenched intensity state I_B because it has the shorter fluorescence lifetime. The result is a higher intensity contrast between the two states, which results in a higher bunching amplitude $A_{dyn}(t_g)$ of the autocorrelation in accordance with equation (4). For a higher microtime threshold of $t_g = 6 \; ns$ after laser excitation, almost no photons from the quenched state remain and the trajectory is dominated by bursts of photons from the bright fluorescent state. With the microtime gating, the situation has changed from a "high intensity" – "low intensity" fluorescent trajectory to an "on" – "off" trajectory similar to photophysical blinking. Therefore, the bunching amplitude $A_{dyn}(t_g)$ is maximized and represents the equilibrium constant K.

Applying shrinking-gate FCS with a stepwise increase of the gating threshold to the trajectories of Figure 1a now yields distinguishable correlation functions (Figure 2d). When considering all photons, the bunching amplitude $A_{dyn}(t_g = 0 \; ns)$ is the smallest and is identical for the two trajectories. By applying sg-FCS from $t_g = 0.0 \; ns$ to $t_g = 8.0 \; ns$ with a step size of $0.5 \; ns$, the amplitudes increase differently and saturate at the respective equilibrium constants that were fed into the simulation.

Each sg-FCS curve is fitted by a monoexponential model yielding the bunching amplitude $A_{dyn}(t_g)$.

$$g^{(2)}(\Delta\tau, t_g) = 1 + A_{dyn}(t_g)e^{-\left(\frac{\Delta\tau}{\tau_{CRT}}\right)} \tag{5}$$

The extracted bunching amplitudes, $A_{dyn}(t_g)$, are plotted as a function of the microtime threshold t_g in Figure 2e. To fit the data, we first consider how the intensity of each state is changing depending on the microtime gate t_g. We assume that both intensity states decay with their characteristic fluorescence lifetime, which is inversely proportional to the excited state decay rate constant.

$$I_A(t_g) = I_0 \int_{t_g}^{\infty} e^{-(k_r+k_{nr})\cdot t'}dt' = \frac{e^{-(k_r+k_{nr})\cdot t_g}}{(k_r + k_{nr})} \tag{6}$$

$$I_B(t_g) = I_0 \int_{t_g}^{\infty} e^{-(k_r+k_{nr}+k_{\Delta ET})\cdot t'}dt' = \frac{e^{-(k_r+k_{nr}+k_{\Delta ET})\cdot t_g}}{(k_r + k_{nr} + k_{\Delta ET})} \tag{7}$$

Here, k_r denotes the radiative rate constant and k_{nr} all non-radiative decay rate constants of the low FRET state, I_A, which includes possible energy transfer to an acceptor dye. $k_{\Delta ET} = k_{ET,high \; FRET} - k_{ET,low \; FRET}$ denotes the additional energy transfer rate constant of the high FRET state, I_B. I_0 is a scaling factor. Considering the different fluorescent decays for both intensities in equation (4), we obtain the microtime threshold dependent bunching amplitude $A_{dyn}(t_g)$:

7

$$A_{dyn}(t_g) = K \left(\frac{1 - \frac{k_r + k_{nr}}{k_r + k_{nr} + k_{ET}} e^{-k_{\Delta ET} \cdot t_g}}{1 + K \cdot \frac{k_r + k_{nr}}{k_r + k_{nr} + k_{ET}} e^{-k_{\Delta ET} \cdot t_g}} \right)^2 \qquad (8)$$

Equation (8) enables us to extract two parameters from sg-FCS. First of all, the exponential term describes the rising intensity contrast between the intensity states with respect to the beginning of the microtime gate, which allows the recovery of $k_{\Delta ET}$. Secondly, at high intensity contrast, the bunching amplitude $A_{dyn}(t_g)$ saturates at the value of the equilibrium constant K. Equation (8) is determined assuming a the excitation pulse is a delta function at $t_g = 0\ ns$. In a real experiment, the arrival of the laser pulse is not exactly synchronized to the start of the TAC bins. Hence, we also have to include an offset of the electronics with respect to the arrival of the laser pulse, t_{shift}.

$$A_{dyn}(t_g) = K \left(\frac{1 - e^{-k_{\Delta ET} \cdot (t_g - t_{shift})}}{1 + K \cdot e^{-k_{\Delta ET} \cdot (t_g - t_{shift})}} \right)^2 \qquad (9)$$

t_{shift} aggravates fitting and extraction of the parameters of interest (see SI section 2 and 3 for a detailed discussion of the fitting model). With equation (9), we can fit the bunching amplitudes $A(t_g)$ in Figure 2e and extract the equilibrium constants, K, and the additional energy transfer rate constant of the high FRET state, $k_{\Delta ET}$ (see Table 1). Both functions in Figure 2e start with an initial intensity contrast of $\frac{I_A}{I_B} = \frac{\tau_A}{\tau_B} = 5$ with fluorescence lifetimes of $\tau_A = 4\ ns$ and $\tau_B = 0.8\ ns$, respectively. The function saturates around a microtime threshold of $t_g = 6\ ns$. At this point, the long component contributes by a factor of $\frac{I_A(t_g = 6\ ns)}{I_B(t_g = 6\ ns)} = e^{k_{\Delta ET} \cdot t_g} \sim 400$ more (for $k_{\Delta ET} = 1\ ns^{-1}$) to the autocorrelation function than the short component. The two graphs saturate at the two different amplitudes representing the different equilibrium constants.

Table 1: The sg-FCS recovered rate constants from a least square fit to the data in Figure 2e along with the corresponding errors given in the fit parameters.

	Simulation	Fit	Simulation	Fit
K / 1	3	3.031 ± 0.001	8.33	8.352 ± 0.003
k_A / s^{-1}	1000	960 ± 10	428.5	432 ± 5
k_B / s^{-1}	3000	2900 ± 30	3571.4	3570 ± 40
$k_{\Delta ET}$ / ns^{-1}	1	1.001 ± 0.001	1	1.002 ± 0.001

When changing from simulations to real data analysis, we have to consider uncorrelated background e.g. from detector dark counts and/or luminescence from the immersion oil. Uncorrelated background leads to a decrease in the correlation amplitude.[42,43] As the fluorescence signal decays after pulsed laser excitation, the signal-to-background ratio decreases for long microtime gates t_g resulting in a decaying bunching amplitude $A_{dyn}(t_g)$. To extract the correct equilibrium constant K, each bunching amplitude has to be background-

8

corrected, which we describe in detail in the supporting information SI section 4 when dealing with experimental data.

To test sg-FCS with real data, we used a two-state molecular model system with well-controllable transition rate constants. A Cy3B-labeled pointer DNA strand is tethered to an L-shaped DNA origami[38,44,45] structure and transiently binds to two protruding strands as depicted in Figure 3a. Next to the lower binding site, an acceptor dye, ATTO647N, is placed so that a high FRET signal is observed when the pointer strand binds to the complementary staple strand placed near the acceptor dye. Hence, switching between a low-FRET state and a high-FRET state is observed and the kinetics can be tuned by the number of bases and the sequence of the complementary strand (for sequence information, see SI section 5). For example, 7 nt complementary bases corresponds to binding times on the millisecond to second timescale.[38,45] The DNA origami structures were immobilized on a BSA-biotin NeutrAvidin passivated glass slide and fluorescence intensity trajectories from single structures were acquired with a confocal microscope. A representative fluorescence intensity trajectory of the donor dye (blue) and the corresponding sensitized acceptor signal (orange) is shown in Figure 3b. The donor and acceptor signal exhibit anticorrelated behavior due to the switching of the protruding pointer strand between the two binding positions.
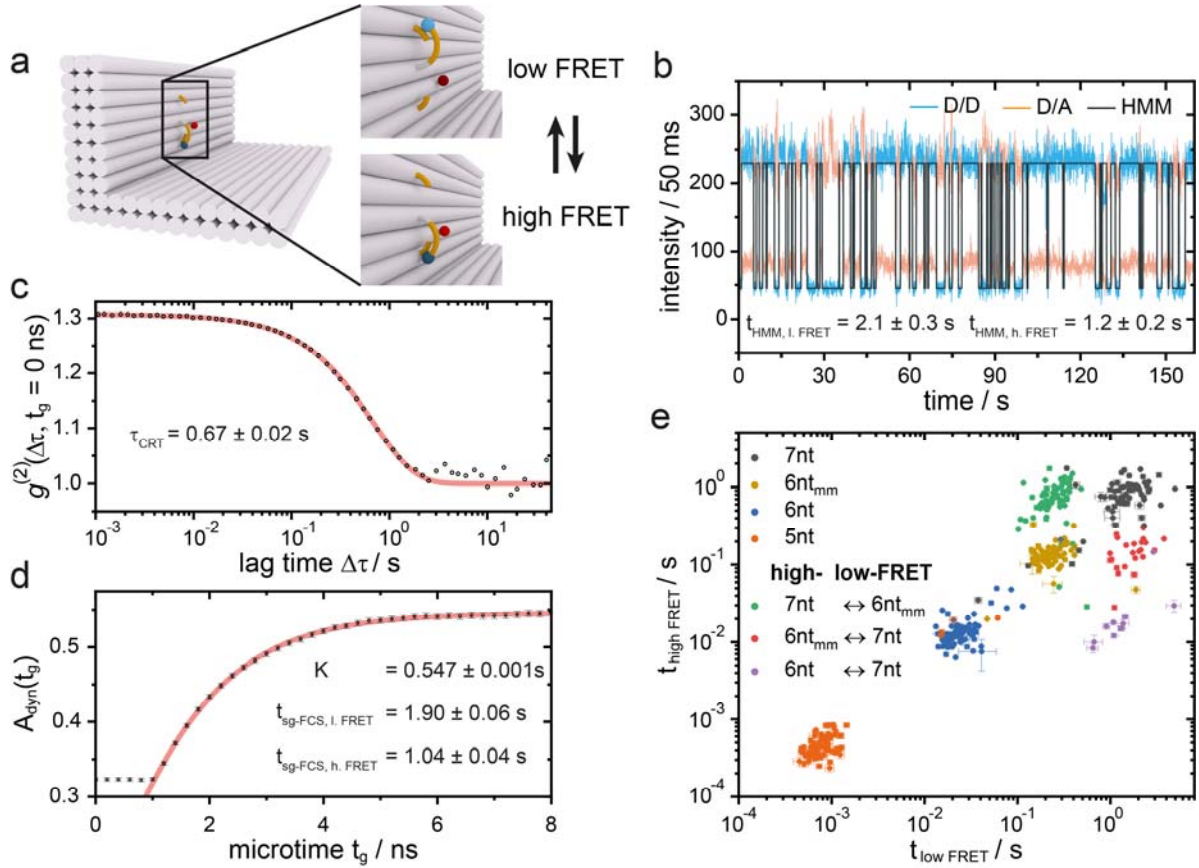
Figure 3: Sg-FCS applied to analyzed the dynamics of a DNA origami. a) Sketch of the L-shaped DNA origami structure. The zoom-ins show the low-FRET (top) and high-FRET (bottom) binding conformations of the blue donor dye (Cy3B). The red acceptor dye (ATTO 647N) position is fixed on the DNA origami structure. b) A typical single particle fluorescence intensity trajectory with 7 nt complementary bases shows the donor intensity (D/D) in blue and the acceptor intensity after donor excitation (D/A) in orange. The black line indicates the most likely FRET trajectory generated by a Hidden Markov Model analysis. c) The $g^{(2)}\left(\Delta\tau, t_g = 0\ ns\right)$ correlation function of the donor fluorescence intensity trajectory (D/D) (black dots) with a monoexponential fit (equation 4, red transparent line). d) Background corrected amplitudes $A_{dyn}\left(t_g\right)$ from the sg-FCS analysis (black dots) fitted using equation (9) (red transparent line). e) A scatterplot of the average binding times in the low- and high-FRET positions acquired from the sg-FCS analysis for a multitude of constructs given in the panel legend. The binding kinetics was tuned by the number of complementary bases. Only trajectories with at least ten transitions between different fluorescence intensity states were analyzed. The complementary bases for the high FRET and low FRET conformations were the same unless indicated otherwise. mm: mismatch.

For the sg-FCS analysis, we first calculate the $g^{(2)}(\Delta\tau)$ autocorrelation function including all photons ($g^{(2)}\left(\Delta\tau, t_g = 0\ ns\right)$) (Figure 3c) to extract the CRT, τ_{CRT}. In this case, $\tau_{CRT} = 0.67 \pm 0.02\ s$. Next, sg-FCS is applied with a step size of $0.2\ ns$ and the background corrected

bunching amplitudes $A_{dyn}(t_g)$ (see SI section 4 for details) are extracted from a monoexponential fit (equation 4) to the autocorrelation function. The bunching amplitudes $A_{dyn}(t_g)$ are plotted in Figure 3d where the error bars correspond to the fit error of the bunching amplitude term $A_{dyn}(t_g)$. The first data points do not show a change in the bunching amplitude $A_{dyn}(t_g)$ because the laser pulse arrives at ~$1\ ns$. Therefore, only data points arriving after $1.2\ ns$ are considered for the fitting, yielding $k_{\Delta ET} = 0.811 \pm 0.008\ ns^{-1}$ and an equilibrium constant of $K = 0.547 \pm 0.01$. The extracted additional energy transfer rate constant of the sg-FCS approach matches the value extracted from the lifetime trace of $k_{\Delta ET_{lifetime}} = 0.8 \pm 0.2\ ns^{-1}$ (see SI Figure S6 section 6). With τ_{CRT} and K, we calculate the dwell times as $t_{sg-FCS,\ low\ FRET} = 1.90 \pm 0.06\ s$ and $t_{sg-FCS,\ high\ FRET} = 1.04 \pm 0.04\ s$. We compared our sg-FCS results with a Hidden Markov Model (HMM) analysis, which is used to analyze real-time trajectories of slow transitions such as those observed for Holliday Junction-kinetics.[46,47] A HMM trajectory of an example trace is plotted as black line on top of the donor signal in Figure 3b and the extracted dwell times are $t_{HMM,\ low\ FRET} = 2.1 \pm 0.3\ s$ and $t_{HMM,\ high\ FRET} = 1.2 \pm 0.2\ s$. This is in good agreement with the sg-FCS results. The dwell times of the high- and low-FRET state for several molecules are registered in a scatter plot in Figure 3e for the 7 nt sample (black dots). Interestingly, the median from 67 trajectories yields a K of $= 0.55$, i.e. < 1 although both FRET positions have equal complementary sequences. This is a real difference in the kinetic rates, which we attribute to details of the origami itself (see SI section 6).

To explore the dynamic range of kinetics that can be assessed by sg-FCS, we vary the protruding binding sites of the DNA origami structure and measure different combinations of complementary sequences (see SI section 5 for sequence information). By removing one G-C stacking interaction, for example, the switching kinetics become ~50-fold faster and a loss of A-T stacking by introducing an A-C mismatch accelerates the kinetics ~5 fold (see Figure 3e). With 5 nt complementary bases, the binding times are shifted into the hundred µs regime and cannot be extracted using an HMM analysis.

When the difference between the transition rates becomes too drastic, the signature of the short-lived state gets lost in the statistical correlation analysis. Nevertheless, sg-FSC is still able to extract a $K \sim 0.01$ for the 6- $\leftrightarrow$ 7-nt binding construct (see the purple data points in Figure 3e). This indicates a hundred times longer dwell time in the low FRET state compared to the high FRET state. Although the correlation amplitudes $A_{dyn}(t_g)$ are small, they are precise due to the high count-rate in our experiment leading to a sufficient signal-to-noise ratio (see SI section 7). The upper limit for our system is an equilibrium constant of $K \sim 8$ (see green data points in Figure 3e), which corresponds to longer dwell times in the high-FRET state leading to less signal in the donor detection channel. Hence, the statistics suffer from low intensities at long thresholds. For shorter gates, the low signal-to-background ratio also limits the analysis (see SI section 7). Interestingly, HMM is able to extract the designed switching kinetics exemplifying its potential to analyze rare events in the regime of slow kinetics (see Figure S5).

We have demonstrated the effectiveness of the sg-FCS analysis on an immobilized model system. However, it can also be applied to diffusing molecules provided that the kinetics are

faster than the diffusion time. Here, we compare the slow-kinetic 7 nt sample with the 5 nt sample. The average diffusion time through the confocal volume is $\tau_{diff} \sim 1.2\ ms$ for the DNA origami structure (see SI section 8 for details). In the surface experiments, the CRT τ_{CRT} of the 7 nt sample is on the $600 - 700\ ms$ time scale, i.e. much slower than the diffusion time, whereas it is faster than the diffusion time ($\tau_{CRT} = 0.3\ ms$) for the 5-nt sample. Carrying out a single-molecule burst analysis at diluted concentration yields two FRET-populations for the 7-nt sample and one population for the 5-nt sample as the fast kinetics of the 5-nt sample yield an averaged FRET-value during the focal transit (see SI section 8 for solution-based pulsed-interleaved excitation FRET experiments and analysis).

Figure 4a shows sg-FCS of the 7 nt sample normalized with respect to the diffusion amplitude $G(0)$. A small bunching amplitude $A_{pp,7nt}(t_g)$ at $\tau_{pp} = 46\ \mu s$ is visible but does not change when the gate is varied indicating an on-off process, i.e. photophysics (pp). The 5-nt sample, on the other hand, shows an additional bunching amplitude $A_{dyn,5nt}(t_g)$ at $\tau_{dyn} = 220\ \mu s$, which varies with the shrinking gate indicative of the expected dynamics (see Figure 4b and SI section 8 Table S2 for fit results). The variation of the bunching amplitude $A_{dyn,5nt}(t_g)$ is illustrated by a color gradient from short (black) to late (blue and red, respectively) microtime thresholds in Figure 4a,b. The extracted kinetics (see SI section 8 for sg-FCS fit) of $t_{l.FRET} = 330 \pm 30\ \mu s$ and $t_{h.FRET} = 700 \pm 70\ \mu s$ agree well with the mean measured kinetics on the surface $t_{l.FRET} = 410 \pm 10\ \mu s$ and $t_{h.FRET} = 770 \pm 20\ \mu s$ with a slight shift towards faster switching kinetics (see Figure 4c), which may be due to the challenges of extracting both the relaxation time and diffusion time from the fit to the autocorrelation function.
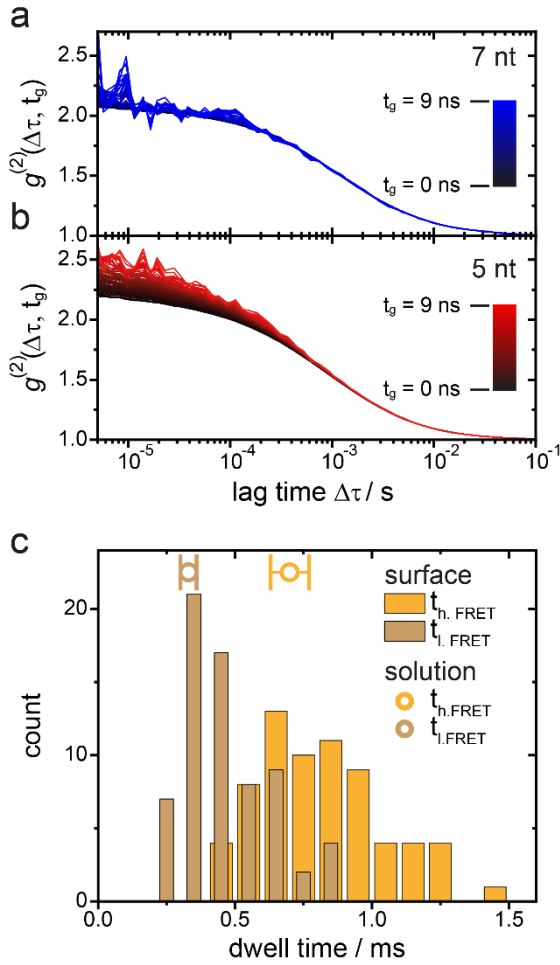
Figure 4: Solution-based sg-FCS. a) Diffusion normalized sg-FCS curves of the 7-nt DNA origami structure, which exhibits slower switching kinetics than the diffusion time in the focal volume. No change in bunching amplitude $A_{pp,7nt}(t_g)$ is observed. sg-FCS correlations are indicated with a color gradient from black $g^{(2)}(\Delta\tau, t_g = 0\,ns)$ to blue $g^{(2)}(\Delta\tau, t_g = 9\,ns)$ with a $0.2\,ns$ step size. b) Diffusion normalized sg-FCS curves of the 5-nt DNA origami structure, which has switching kinetics that is faster than the diffusion time in the focal volume leading to a change of the dynamic bunching amplitude $A_{dyn,5nt}(t_g)$ indicated by the color gradient from black $g^{(2)}(\Delta\tau, t_g = 0\,ns)$ to red $g^{(2)}(\Delta\tau, t_g = 9\,ns)$ with a $0.2\,ns$ step size. c) Histogram of the sg-FCS kinetics of the 5-nt DNA origami structure from surface experiments. The high-FRET dwell times (orange) and low-FRET dwell times (light brown) match the sg-FCS values from solution experiments, which are indicated above the histogram as circles with error bars representing the standard errors.

The application of sg-FCS is not limited to FCS experiments involving FRET, but proves to be very helpful in experiments where photophysics and dynamics appear simultaneously. FRET-FCS gives an anticorrelation for dynamic processes but this approach is only applicable when a fluorescent acceptor dye is present in the experiment. In addition, negative bunching amplitudes of FRET-FCS are reduced by the influence of direct excitation of the acceptor and bleed-through from the donor into the acceptor channel.[16] When a dark quencher is involved,

13

we cannot simply assign the bunching amplitude to dynamics or photophysics using an ordinary $g^{(2)}(\Delta\tau)$ correlation function.
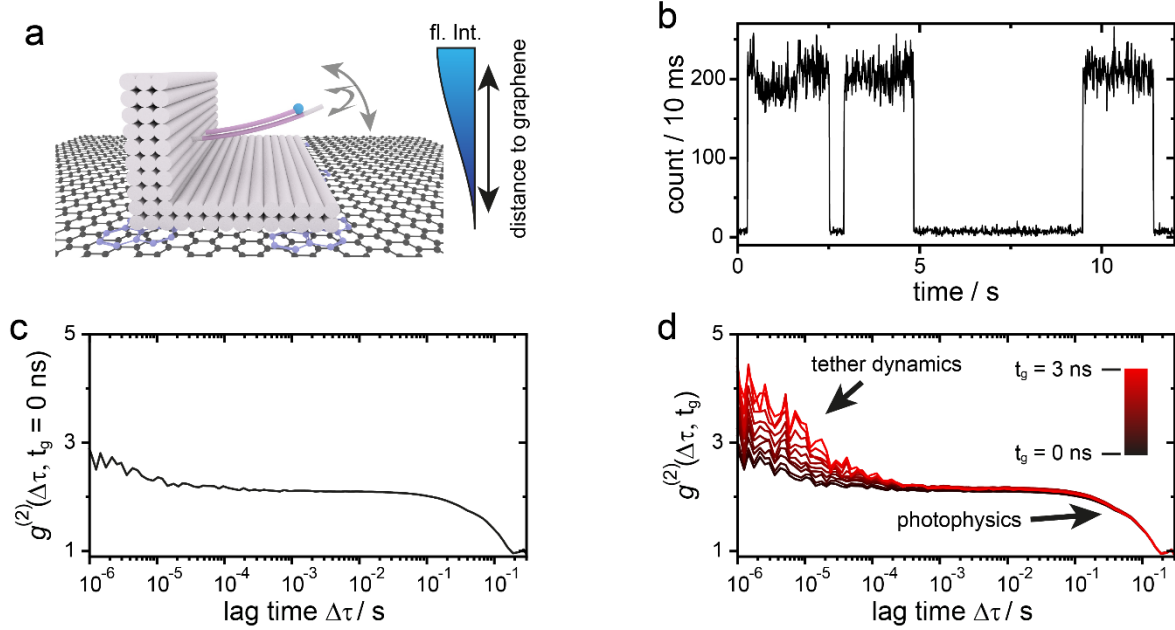
Figure 5: Sg-FCS applied to a dynamically quenching system. a) Sketch of the L-shaped DNA origami structure on a single layer of graphene which acts as 2D FRET quencher. At the tip of the tether, a Cy3B dye (blue dot) is attached, which changes its fluorescence intensity and fluorescence lifetime on the μs timescale due to Brownian fluctuations in the distance between the dye and graphene. Pyrene molecules (in purple) have been attached to the DNA origami to better align the origami on the graphene.[39] b) A single-molecule fluorescence trajectory from a DNA origami on graphene showing variations in fluorescence intensity due to distance fluctuations as well as off states (most likely due to radical ion states[35]) on the second timescale. c) An FCS intensity correlation analysis of the fluorescence trajectory in b). What gives rise to the fast bunching amplitude is not clear from a single autocorrelation function. d) Sg-FCS analysis of the fluorescence trajectory in b). The beginning of the microtime gate is indicated by the color gradient from black $g^{(2)}(\Delta\tau, t_g = 0\ ns)$ to red $g^{(2)}(\Delta\tau, t_g = 3\ ns)$ with a $0.2\ ns$ step size. From the gate dependence of the correlation amplitude, we can attribute the fast bunching term to diffusion of the tether with respect to the graphene surface.

Sg-FCS enables this assignment directly and without a change in the experiment's parameters, when the photophysics results in total quenching and not in a second, low intensity fluorescence state. In this case, the intensity of the off-state does not change with the microtime gate. We demonstrate this using the same L-shaped DNA origami structure placed on top of a monolayer of graphene (Figure 5a). A Cy3B labeled DNA tether of 44 nt long double-stranded DNA (dsDNA) is attached to the DNA origami structure by a 6 nt long single-stranded DNA (ssDNA) such that it can undergo confined Brownian motion. In this experiment, graphene acts as a 2-dimensional energy transfer acceptor resulting in an energy transfer distance dependency of r^{-4} with a broadband quenching efficiency of 50% at a distance of ~18 nm.[39] The closer the dye gets to the graphene, the lower its quantum yield and the shorter its fluorescence lifetime.

14

The DNA origami structure has two layers of dsDNA between graphene and the tether to avoid sticking of the dye to graphene.

The exemplary fluorescence intensity trajectory in Figure 5b shows dark states on the seconds time scale that most likely originate from radical ion states.[34] The autocorrelation function (Figure 5c) reveals an additional component at 10 µs that is not easily assigned to photophysics or to the molecular dynamics of the tether movement in the graphene quenching field. However, as the amplitude of this component clearly increases with the sg-FCS threshold (Figure 5d), it is unequivocally ascribed to a process that is associated with a change in fluorescence lifetime, i.e. the Brownian motion of the tether and the subsequent GET quenching. The photophysics component at 1 s, on the other hand, is clearly not affected by the applied microtime gate. In the example shown in Figure 5b, the time scales of the bunching components are well separated. However, photophysical and dynamic processes can still be distinguished even if they occur on similar time scales by using the appropriate subsets of photons for the fluorescence intensity correlation analyses (see SI section 9 for details).

15
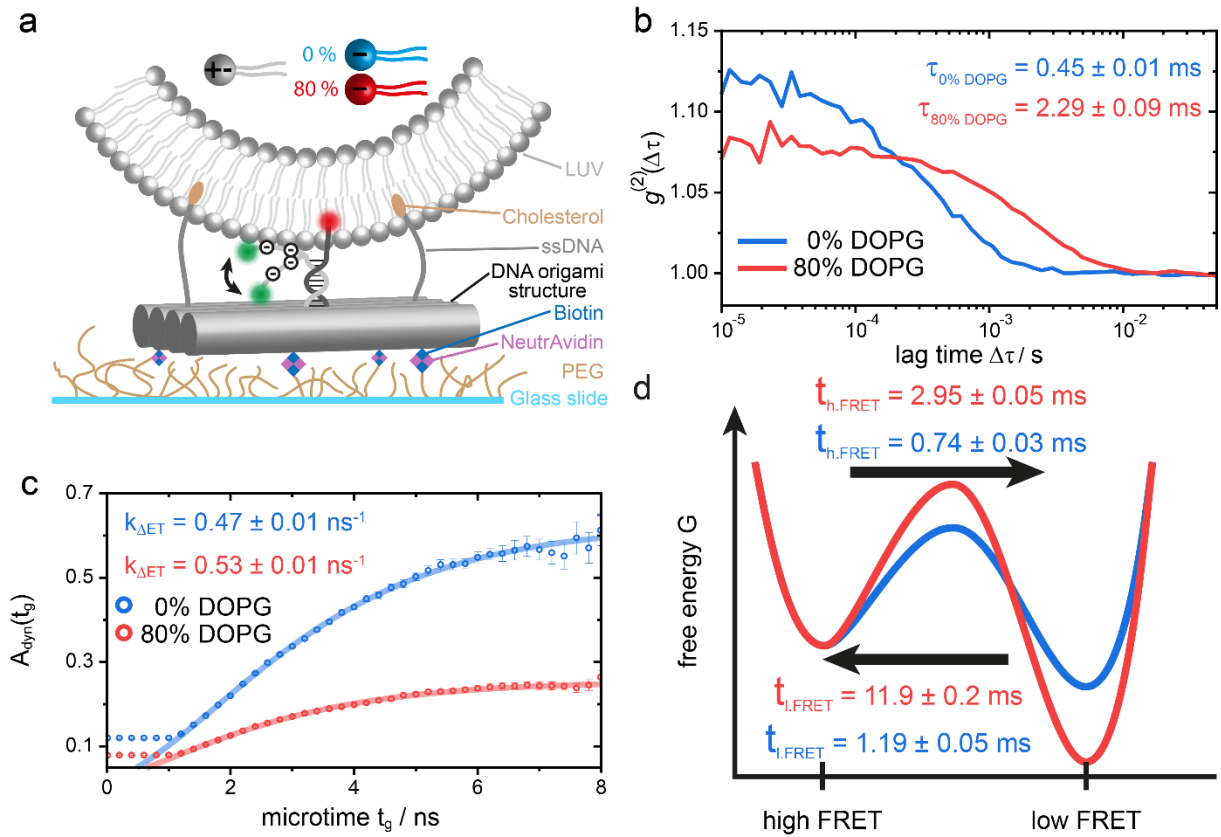
Figure 6: Application of sg-FCS to a FRET-based membrane-voltage nanosensor. a) Sketch of an immobilized charge-sensing DNA origami structure with a protruding donor acceptor dye pair attached to a LUV. b) The $g^{(2)}(\Delta\tau, t_g = 0\,ns)$ autocorrelation function of two representative donor trajectories for vesicles containing 0% DOPG/100% DOPC (blue) and 80% DOPG/20% DOPC (red). c) The sg-FCS extracted bunching amplitudes $A_{dyn,0\%\,DOPG}(t_g)$ (blue circles) and $A_{dyn,80\%\,DOPG}(t_g)$ (red circles) as a function of gate width and fit to a two-state model (bold transparent line) to extract the equilibrium constant K and the quenching rate constant $k_{\Delta ET}$. d) A free energy landscape describing the two states for the sensor with 0% (blue) and 80% DOPG LUVs (red).

The graphene example demonstrates the ability of sg-FCS to distinguish photophysical on-off switching from energy transfer changes in combination with a dark acceptor. In the next example, we use sg-FCS simultaneously determine the equilibrium coefficients and changing FRET efficiencies in a novel FRET sensor[48] designed for measuring membrane surface charges. The membrane surface charges of cells and changes thereof are involved in various cell signaling pathways.[49,50] Our sensor design (Figure 6a) is based on a rectangular DNA origami structure equipped with cholesterol moieties for binding to lipid membranes and with biotin for surface immobilization.[48] A FRET-based sensing unit is placed on the DNA origami structure consisting of the anionic donor dye ATTO542 on a flexible ssDNA leash and the acceptor dye ATTO647N, which localizes in the hydrophobic core of the membrane. The anionic sensing unit is expected to adapt its conformation depending on the charge of the membrane surface.

16

This conformational adaptation is monitored by changes in the FRET signal. We studied the mechanism of the charge sensor on Large Unilamellar Vesicles (LUVs) with different compositions of the zwitterionic lipid DOPC (1,2-dioleoyl-sn-glycero-3-phosphocholine) and the anionic lipid DOPG (1,2-dioleoyl-sn-glycero-3-phospho-(1'-rac-glycerol)) yielding a series of LUVs with different surface charges.

Using millisecond alternating laser excitation (ALEX)[51] on a wide-field setup with an integration time of 100 ms, different uncorrected FRET-efficiencies ($E_{0DOPG} \sim 0.52$ and $E_{80DOPG} \sim 0.42$) were measured for the sensor exposed to LUVs containing 0% and 80% of the anionic lipid DOPG.[48] Intuitively, the decreased FRET signal suggests further separation of the two dyes when the DOPG content is higher. The question arises whether the Coulomb repulsion simply induces a higher average distance of the flexible signaling unit or the system is more complex. Thus, we investigated our DNA origami surface charge sensor on a time-correlated single-photon counting (TCSPC) confocal microscope with higher time resolution. The $g^{(2)}(\Delta\tau)$ intensity correlation function of an exemplary donor intensity trajectory reveals a mono-exponential photon bunching behavior for both lipid compositions (Figure 6b). The 0% DOPG sample (blue) shows a faster CRT of $\tau_{0\% DOPG} = 0.45 \pm 0.01 \, ms$. With the higher DOPG (red correlation) content, the intensity fluctuations are slowed down indicated by an increase in the CRT $\tau_{80\% DOPG} = 2.29 \pm 0.09 \, ms$. The change in the bunching amplitudes $A_{dyn,0\% DOPG}(t_g)$ and $A_{dyn,80\% DOPG}(t_g)$ observed in the sg-FCS analysis (Figure 6c) shows that the origin of the intensity fluctuations is not photophysics related but rather a dynamic process where the system switches between two FRET states on the 100 µs time scale (the acceptor signal upon direct acceptor excitation does not show any intensity fluctuations on this timescale, see SI section 10). From these data, a two-FRET state model evolves in which, for both lipid compositions, the donor dye switches between a membrane bound and a membrane unbound state. Further analysis shows that the FRET efficiency of the membrane bound state is the same for both LUV compositions and that the low-FRET efficiency is slightly decreased further for the negatively charged LUVs.[48] This is, however, not the only cause of the decreased average FRET value but sg-FCS also reveals a shift in the equilibrium constant for 80% DOPG content ($K_{0\% DOPG} = 0.630 \pm 0.006$ and $K_{80\% DOPG} = 0.246 \pm 0.002$), which indicates a longer dwell time in the low-FRET state compared to the high-FRET state. The resulting free energy diagram with the calculated dwell times is depicted in Figure 6d. Overall, a model arises where the sensor works by both a decreased FRET efficiency of the low FRET state and a shift of the equilibrium towards the low FRET state when the LUVs are negatively charged.[48]

Conclusion

Building on an extensive body of previous FCS and fluorescence lifetime work, we present here shrinking-gate FCS, an algorithm that combines correlation spectroscopy with fluorescence lifetime information to extract microscopy reaction rates and equilibrium constants. Without making any assumptions, the algorithm can easily be implemented when TCSPC data is available. Sg-FCS directly reveals terms in the correlation function that are related to fluorescence lifetime changes and distinguishes them from photophysical processes. For two-state systems, analysis of the amplitudes as a function of the shrinking the microtime threshold

in sg-FCS makes it possible to extract the previously hidden equilibrium constants of the switching kinetics. Combining simulations and a robust model system based on a DNA origami pointer system, we prove the versatility by extracting equilibrium constants over a range of 2.5 orders of magnitude. Here, sg-FCS is applied to both immobilized structures and structures freely diffusing in solution.

In our experiments we determine equilibrium constants from ~0.01-10. The asymmetry with respect to $K = 1$ is related to the reduced signal-to-noise ratio when the equilibrium is on the side of the high FRET states. In the future, a model that also incorporates a global fit to the acceptor correlation function could help to overcome this asymmetry and increase the dynamic range of the equilibrium constants. Interestingly, the distinction of photophysical on-off processes or diffusion, and biomolecular dynamics can even be achieved when both processes happen on similar time scales by using different subsets of photons for the correlation.

The fact that sg-FCS could directly reveal new insights for two projects of the lab, including a fluctuating tether on graphene and a new lipid-surface membrane-potential sensor, indicates the broad applicability of the method and suggests implementation of the method whenever TCSPC-data are available in combination with the autocorrelation analysis.

Competing financial interests

The authors declare no competing financial interests.

Acknowledgments

18

References

1.   Eigen, M.; Rigler, R. Sorting single molecules: Application to diagnostics and evolutionary biotechnology. *Proc. Natl. Acad. Sci. U.S.A.* **1994**, *91*, 5740–5747.

2.   Schwille, P.; Meyer-Almes, F. J.; Rigler, R. Dual-color fluorescence cross-correlation spectroscopy for multicomponent diffusional analysis in solution. *Biophys. J.* **1997**, *72*, 1878–1886.

3.   Erokhova, L.; Horner, A.; Kügler, P.; Pohl, P. Monitoring single-channel water permeability in polarized cells. *J. Biol. Chem.* **2011**, *286*, 39926–39932.

4.   Magde, D.; Elson, E.; Webb, W. W. Thermodynamic Fluctuations in a Reacting System—Measurement by Fluorescence Correlation Spectroscopy. *Phys. Rev. Lett.* **1972**, *29*, 705–708.

5.   Rigler, R.; Mets; Widengren, J.; Kask, P. Fluorescence correlation spectroscopy with high count rate and low background: Analysis of translational diffusion. *Eur Biophys J* **1993**, *22*, 169–175.

6.   Müller, C. B.; Loman, A.; Pacheco, V.; Koberling, F.; Willbold, D.; Richtering, W.; Enderlein, J. Precise measurement of diffusion by multi-color dual-focus fluorescence correlation spectroscopy. *Europhys. Lett.* **2008**, *83*, 46001.

7.   Eggeling, C.; Ringemann, C.; Medda, R.; Schwarzmann, G.; Sandhoff, K.; Polyakova, S.; Belov, V. N.; Hein, B.; Middendorff, C. von; Schönle, A.; Hell, S. W. Direct observation of the nanoscale dynamics of membrane lipids in a living cell. *Nature* **2009**, *457*, 1159–1162.

8.   Jensen, M. H.; Sukumaran, M.; Johnson, C. M.; Greger, I. H.; Neuweiler, H. Intrinsic Motions in the N-Terminal Domain of an Ionotropic Glutamate Receptor Detected by Fluorescence Correlation Spectroscopy. *J. Mol. Biol.* **2011**, *414*, 96–105.

9.   Kim, J.; Doose, S.; Neuweiler, H.; Sauer, M. The initial step of DNA hairpin folding: a kinetic analysis using fluorescence correlation spectroscopy. *Nucleic acids research* **2006**, *34*, 2516–2527.

10.   Nettels, D.; Hoffmann, A.; Schuler, B. Unfolded protein and peptide dynamics investigated with single-molecule FRET and correlation spectroscopy from picoseconds to seconds. *J. Phys. Chem. B* **2008**, *112*, 6137–6146.

11.   Magde, D.; Elson, E. L.; Webb, W. W. Fluorescence correlation spectroscopy. II. An experimental realization. *Biopolymers* **1974**, *13*, 29–61.

12.   Saffarian, S.; Collier, I. E.; Marmer, B. L.; Elson, E. L.; Goldberg, G. Interstitial collagenase is a Brownian ratchet driven by proteolysis of collagen. *Science* **2004**, *306*, 108–111.

13.   Chattopadhyay, K.; Saffarian, S.; Elson, E. L.; Frieden, C. Measuring unfolding of proteins in the presence of denaturant using fluorescence correlation spectroscopy. *Biophys. J.* **2005**, *88*, 1413–1422.

14.   Widengren, J.; Mets, U.; Rigler, R. Fluorescence correlation spectroscopy of triplet states in solution: A theoretical and experimental study. *J. Phys. Chem.* **1995**, *99*, 13368–13379.

15.   Widengren, J.; Rigler, R.; Mets, U. Triplet-state monitoring by fluorescence correlation spectroscopy. *J. Fluoresc.* **1994**, *4*, 255–258.

16.   Sahoo, H.; Schwille, P. FRET and FCS-friends or foes? *ChemPhysChem* **2011**, *12*, 532–541.

17.   Torres, T.; Levitus, M. Measuring Conformational Dynamics: A New FCS-FRET Approach. *J. Phys. Chem. B* **2007**, *111*, 7392–7400.

18.   Enderlein, J.; Gregor, I. Using fluorescence lifetime for discriminating detector afterpulsing in fluorescence-correlation spectroscopy. *Rev. Sci. Instrum.* **2005**, *76*, 33102.

19.   Ghosh, A.; Isbaner, S.; Veiga-Gutiérrez, M.; Gregor, I.; Enderlein, J.; Karedla, N. Quantifying Microsecond Transition Times Using Fluorescence Lifetime Correlation Spectroscopy. *The journal of physical chemistry letters* **2017**, *8*, 6022–6028.

20.   Lamb, D. C.; Schenk, A.; Röcker, C.; Scalfi-Happ, C.; Nienhaus, G. U. Sensitivity Enhancement in Fluorescence Correlation Spectroscopy of Multiple Species Using Time-Gated Detection. *Biophys. J.* **2000**, *79*, 1129–1138.

21.   Laurence, T. A.; Kwon, Y.; Yin, E.; Hollars, C. W.; Camarero, J. A.; Barsky, D. Correlation spectroscopy of minor fluorescent species: Signal purification and distribution analysis. *Biophys. J.* **2007**, *92*, 2184–2198.

22.   Eggeling, C.; Fries, J. R.; Brand, L.; Günther, R.; Seidel, C. A. Monitoring conformational dynamics of a single molecule by selective fluorescence spectroscopy. *Proc. Natl. Acad. Sci. U.S.A.* **1998**, *95*, 1556–1561.

23.   Barth, A.; Hendrix, J.; Fried, D.; Barak, Y.; Bayer, E. A.; Lamb, D. C. Dynamic interactions of type I cohesin modules fine-tune the structure of the cellulosome of Clostridium thermocellum. *Proc. Natl. Acad. Sci. U.S.A.* **2018**, *115*, E11274-E11283.

24.   Sanabria, H.; Rodnin, D.; Hemmen, K.; Peulen, T.-O.; Felekyan, S.; Fleissner, M. R.; Dimura, M.; Koberling, F.; Kühnemuth, R.; Hubbell, W.; Gohlke, H.; Seidel, C. A. M. Resolving dynamics and function of transient states in single enzyme molecules. *Nature communications* **2020**, *11*, 1231.

25.   Gurunathan, K.; Levitus, M. FRET fluctuation spectroscopy of diffusing biopolymers: Contributions of conformational dynamics and translational diffusion. *J. Phys. Chem. B* **2010**, *114*, 980–986.

26.   Lamb, D. C.; Schenk, A.; Röcker, C.; Nienhaus, G. U. Determining Chemical Rate Coefficients Using Time-Gated Fluorescence Correlation Spectroscopy. *J. Phys. Org. Chem.* **2000**, *13*, 654–658.

27.   Bonnet, G.; Krichevsky, O.; Libchaber, A. Kinetics of conformational fluctuations in DNA hairpin-loops. *Proc. Natl. Acad. Sci. U.S.A.* **1998**, *95*, 8602–8606.

28.   Doose, S.; Neuweiler, H.; Sauer, M. Fluorescence quenching by photoinduced electron transfer: a reporter for conformational dynamics of macromolecules. *Chemphyschem : a European journal of chemical physics and physical chemistry* **2009**, *10*, 1389–1398.

29.   Doose, S.; Neuweiler, H.; Sauer, M. A close look at fluorescence quenching of organic dyes by tryptophan. *ChemPhysChem* **2005**, *6*, 2277–2285.

30.   Lounis, B.; Moerner, W. E. Single Photons on Demand from a Single Molecule at Room Temperature. *Nature* **2000**, *407*, 491–493.

31.   Tinnefeld, P.; Weston, K. D.; Vosch, T.; Cotlet, M.; Weil, T.; Hofkens, J.; Müllen, K.; Schryver, F. C. de; Sauer, M. Antibunching in the Emission of a Single Tetrachromophoric Dendritic System. *J. Am. Chem. Soc.* **2002**, *124*, 14310–14311.

32.   Orrit, M.; Bernard, J.; Brown, R.; Fleury, L.; Wrachtrup, J.; Borczyskowski, C. von. Single molecule fluorescence: From excitation spectra to time correlation. *J. Lumin.* **1994**, *60-61*, 991–996.

33.   Tinnefeld, P.; Herten, D.-P.; Sauer, M. Photophysical Dynamics of Single Molecules Studied by Spectrally-Resolved Fluorescence Lifetime Imaging Microscopy (SFLIM). *J. Phys. Chem. A* **2001**, *105*, 7989–8003.

34.   Vogelsang, J.; Kasper, R.; Steinhauer, C.; Person, B.; Heilemann, M.; Sauer, M.; Tinnefeld, P. A Reducing and Oxidizing System Minimizes Photobleaching and Blinking of Fluorescent Dyes. *Angew. Chem.* **2008**, *47*, 5465–5469.

35.   Vogelsang, J.; Cordes, T.; Forthmann, C.; Steinhauer, C.; Tinnefeld, P. Controlling the fluorescence of ordinary oxazine dyes for single-molecule switching and superresolution microscopy. *Proc. Natl. Acad. Sci. U.S.A.* **2009**, *106*, 8107–8112.

36.   Cordes, T.; Vogelsang, J.; Tinnefeld, P. On the Mechanism of Trolox as Antiblinking and Antibleaching Reagent. *J. Am. Chem. Soc.* **2009**, *131*, 5018–5019.

37.   Stein, J.; Stehr, F.; Schueler, P.; Blumhardt, P.; Schueder, F.; Mücksch, J.; Jungmann, R.; Schwille, P. Toward Absolute Molecular Numbers in DNA-PAINT. *Nano Lett.* **2019**, *19*, 8182–8190.

38.   Kamińska, I.; Bohlen, J.; Yaadav, R.; Schüler, P.; Raab, M.; Schröder, T.; Zähringer, J.; Zielonka, K.; Krause, S.; Tinnefeld, P. Graphene Energy Transfer for Single‐Molecule Biophysics, Biosensing, and Super‐Resolution Microscopy. *Adv. Mater.* **2021**, 2101099.

39.   Kaminska, I.; Bohlen, J.; Rocchetti, S.; Selbach, F.; Acuna, G. P.; Tinnefeld, P. Distance Dependence of Single-Molecule Energy Transfer to Graphene Measured with DNA Origami Nanopositioners. *Nano Lett.* **2019**, *19*, 4257–4262.

40.   Zumbusch; Fleury; Brown; Bernard; Orrit. Probing Individual Two-Level Systems in a Polymer by Correlation of Single Molecule Fluorescence. *Phys. Rev. Lett.* **1993**, *70*, 3584–3587.

41.   Yu, J.; Lammi, R.; Gesquiere, A. J.; Barbara, P. F. Singlet-Triplet and Triplet-Triplet Interactions in Conjugated Polymer Single Molecules. *J. Phys. Chem. B* **2005**, *109*, 10025–10034.

42.   Hess, S. T.; Webb, W. W. Focal Volume Optics and Experimental Artifacts in Confocal Fluorescence Correlation Spectroscopy. *Biophys. J.* **2002**, *83*, 2300–2317.

43.   Koppel, D. E. Statistical accuracy in fluorescence correlation spectroscopy. *Phys. Rev. A* **1974**, *10*, 1938–1945.

44.   Krause, S.; Ploetz, E.; Bohlen, J.; Schüler, P.; Yaadav, R.; Selbach, F.; Steiner, F.; Kamińska, I.; Tinnefeld, P. Graphene-on-Glass Preparation and Cleaning Methods Characterized by Single-Molecule DNA Origami Fluorescent Probes and Raman Spectroscopy. *ACS nano* **2021**, *15*, 6430–6438.

45.   Masullo, L. A.; Steiner, F.; Zähringer, J.; Lopez, L. F.; Bohlen, J.; Richter, L.; Cole, F.; Tinnefeld, P.; Stefani, F. D. Pulsed Interleaved MINFLUX. *Nano Lett.* **2021**, *21*, 840–846.

46.   McKinney, S. A.; Joo, C.; Ha, T. Analysis of single-molecule FRET trajectories using hidden Markov modeling. *Biophys. J.* **2006**, *91*, 1941–1951.

47.   Nickels, P. C.; Wünsch, B.; Holzmeister, P.; Bae, W.; Kneer, L. M.; Grohmann, D.; Tinnefeld, P.; Liedl, T. Molecular Force Spectroscopy with a DNA Origami-Based Nanoscopic Force Clamp. *Science* **2016**, *354*, 305–307.

48.   Ochmann, S. E.; Schröder, T.; Schulz, C. M.; Tinnefeld, P. Quantitative Single-Molecule Measurements of Membrane Charges with DNA Origami Sensors. *Anal. Chem.* **2022**, *94*, 2633–2640.

49.   Elliott, J. I.; Surprenant, A.; Marelli-Berg, F. M.; Cooper, J. C.; Cassady-Cain, R. L.; Wooding, C.; Linton, K.; Alexander, D. R.; Higgins, C. F. Membrane phosphatidylserine distribution as a non-apoptotic signalling mechanism in lymphocytes. *Nat. Cell Biol.* **2005**, *7*, 808–816.

50.   Rysavy, N. M.; Shimoda, L. M. N.; Dixon, A. M.; Speck, M.; Stokes, A. J.; Turner, H.; Umemoto, E. Y. Beyond apoptosis: The mechanism and function of phosphatidylserine asymmetry in the membrane of activating mast cells. *Bioarchitecture* **2014**, *4*, 127–137.

51.   Margeat, E.; Kapanidis, A. N.; Tinnefeld, P.; Wang, Y.; Mukhopadhyay, J.; Ebright, R. H.; Weiss, S. Direct observation of abortive initiation and promoter escape within single immobilized transcription complexes. *Biophys. J.* **2006**, *90*, 1419–1431.

Supplementary Information for

Shrinking gate fluorescence correlation spectroscopy yields equilibrium constants and distinguishes photophysics from structural dynamics

Tim Schröder[1], Johann Bohlen[1], Sarah E. Ochmann[1], Patrick Schüler[1], Stefan Krause[1,2], Don C. Lamb[1], Philip Tinnefeld[1]*

[1]Department Chemie and Center for NanoScience (CeNS), Ludwig-Maximilians-Universität München, Butenandtstraße 5-13, 81377 München, Germany

[2] present address: Fraunhofer Institut für Integrierte Schaltungen IIS, Dresden, Münchener Straße 16, 01187 Dresden, Germany

* philip.tinnefeld@cup.uni-muenchen.de

Table of contents

1. Simulations

We used Monte Carlo simulations to simulate the fluorescence emission of a dynamic two-fluorescence-intensity-state system with the fluorescence state A and the quenched fluorescence state B. The system switches stochastically between the two states $A \underset{k_A}{\overset{k_B}{\rightleftharpoons}} B$. The rate constant, k_A, denotes the transition from state B to state A and k_B denotes the transition from state A to state B. Simulations were performed with a self-written python script. The system was simulated with pulsed laser excitation. Before each excitation cycle, the system could stochastically undergo a transition into the other intensity state. The laser excitation is set to unity and the probability of detecting a photon is set to be 0.1 for the high fluorescence intensity state I_A and 0.02 for the low fluorescence intensity state I_B. When a photon is detected, a corresponding excited state fluorescence lifetime for this cycle is generated following an exponential distribution with the decay time of the active intensity state. The fluorescence lifetime of the bright state was set to $\tau_A = 4\ ns$ and the fluorescence lifetime of the dark state to $\tau_B = 0.8\ ns$. The laser repetition rate was set to 40 MHz and $3 \cdot 10^7$ laser pulses were simulated (0.75 s). The switching rates between the two fluorescence intensity states were $k_A = 1,000\ s^{-1}$ and $k_B = 3,000\ s^{-1}$ for the $K = 3$ simulation and $k_A = 4,28.5\ s^{-1}$ and $k_B = 3,571.4\ s^{-1}$ for the $K = 8.3$ simulation. The simulated fluorescence intensity trajectories are correlated based on an algorithm proposed by Laurence et al.[1,2]

149

2. The microtime-gate-dependent amplitude $A_{dyn}(t_g)$

The bunching amplitude A_{dyn} of a system cycling between two fluorescence intensity states depends on the square of the fractional fluorescence intensity difference:

$$A_{dyn} = K \left(\frac{I_A - I_B}{I_A + K \cdot I_B} \right)^2 \qquad \text{eq. S1}$$

Here, I_A denotes the intensity of the bright fluorescence state, and I_B denotes the fluorescence intensity of the quenched fluorescence state. K equals the equilibrium constant, which is the ratio of the transition rate constants between the two fluorescence intensity states.

$$K = \frac{k_B}{k_A} \qquad \text{eq. S2}$$

Here, k_A denotes the transition rate constant into the bright state and k_B denotes the transition rate constant into the quenched state. Due to the quadratic fluorescence intensity difference dependence of the fluorescence intensity correlation function, no unique solution for K is obtained even if both fluorescence intensity levels are known. To obtain a unique solution for K, we make use of the microtime information we get using time-correlated single-photon counting (TCSPC) detection. The microtime is the arrival time of the photon with respect to the excitation pulse (t_g). By considering only a subset of the photons, we can vary the fractional fluorescence intensity difference between the two intensity states. With shrinking gate fluorescence correlation spectroscopy (sg-FCS), we introduce a microtime threshold for the microtime gate by considering only photons that are detected at microtimes later than the threshold. To model the change of the bunching amplitude with sg-FCS, we first consider the intensity decay of the two intensity states. After pulsed excitation, both intensity states decay with their characteristic fluorescence decay time.

$$I_A(t_g) = I_0 \int_{t_g}^{\infty} e^{-(k_r + k_{nr}) \cdot t'} dt' = \frac{e^{-(k_r + k_{nr}) \cdot t_g}}{(k_r + k_{nr})} \qquad \text{eq. S3}$$

$$I_B(t_g) = I_0 \int_{t_g}^{\infty} e^{-(k_r + k_{nr} + k_{\Delta ET}) \cdot t'} dt' = \frac{e^{-(k_r + k_{nr} + k_{\Delta ET}) \cdot t_g}}{(k_r + k_{nr} + k_{\Delta ET})} \qquad \text{eq. S4}$$

Here, k_r denotes the radiative rate constant and k_{nr} all non-radiative decay rate constants of the low FRET state, I_A, which includes possible energy transfer to an acceptor dye. $k_{\Delta ET} = k_{ET, high\ FRET} - k_{ET, low\ FRET}$ denotes the additional energy transfer rate of the high FRET state, I_B. I_0 is a scale factor. Considering the different fluorescence decays for both intensities in equation S1, we obtain the microtime threshold dependent bunching amplitude $A_{dyn}(t_g)$:

$$A_{dyn}(t_g) = K \left(\frac{1 - \dfrac{k_r + k_{nr}}{k_r + k_{nr} + k_{\Delta ET}} e^{-k_{\Delta ET} \cdot t_g}}{1 + K \cdot \dfrac{k_r + k_{nr}}{k_r + k_{nr} + k_{\Delta ET}} e^{-k_{\Delta ET} \cdot t_g}} \right)^2 \qquad \text{eq. S5}$$

Figure S1a shows how $A_{dyn}(t_g)$ scales with different K values depicted by the color gradient from small (black) to large (blue). First of all, one sees that $A_{dyn}(t_g)$ scales linearly with K. Secondly, the saturation value of $A_{dyn}(t_g)$ equals K, when t_g, which denotes the beginning of the microtime gate, approaches infinity.

4

$$\lim_{t_g \to \infty} A_{dyn}(t_g) = K \qquad\qquad \text{eq. S6}$$

How quickly the amplitude saturates depends on the additional energy transfer rate constant $k_{\Delta ET}$ of the high-FRET state I_B. In equation S5, $k_{\Delta ET}$ is in the exponent in both the numerator and the denominator. First, we will focus on this exponential influence as it reflects the exponential rising intensity contrast between I_A and I_B. Figure S1b shows the impact of $k_{\Delta ET}$ on $A_{dyn}(t_g)$. Small rate constants are depicted in green and larger rates are depicted in blue. A higher $k_{\Delta ET}$ rate constant leads to faster saturation due to a faster rise in the intensity contrast. For example, the intensity contrast for $t_g = 5\,ns$ compared to the initial intensity contrast assuming a $k_{\Delta ET} = 1\,ns^{-1}$ equals $\frac{I_A(t_g=5\,ns)}{I_B(t_g=5\,ns,\ k_{\Delta ET}=1\,ns^{-1})} \sim 148$ whereas, for $k_{\Delta ET} = 0.15\,ns^{-1}$, it only equals $\frac{I_A(t_g=5\,ns)}{I_B(t_g=5\,ns,\ k_{\Delta ET}=0.15\,ns^{-1})} \sim 2$. The slow increase in intensity contrast with $k_{\Delta ET} = 0.15\,ns^{-1}$ shows as slower saturation. When focusing on the ratio of the fluorescence lifetimes $\frac{k_r+k_{nr}}{k_r+k_{nr}+k_{\Delta ET}} = \frac{\tau_B}{\tau_A}$, the ratio is independent of the microtime gate. However, the lifetime ratio still affects $A_{dyn}(t_g)$ because it reflects the initial intensity contrast between I_A and I_B when all photons are taken into account. A higher intensity contrast results in a higher initial bunching amplitude $A_{dyn}(t_g = 0\,ns)$ (Figure S1b) giving the function a kind of "head start" compared to functions with smaller $k_{\Delta ET}$ values. Overall, larger $k_{\Delta ET}$ leads to a faster saturation due to the larger initial bunching amplitude $A_{dyn}(t_g = 0\,ns)$ and the faster rise in the intensity contrast for later microtime thresholds.
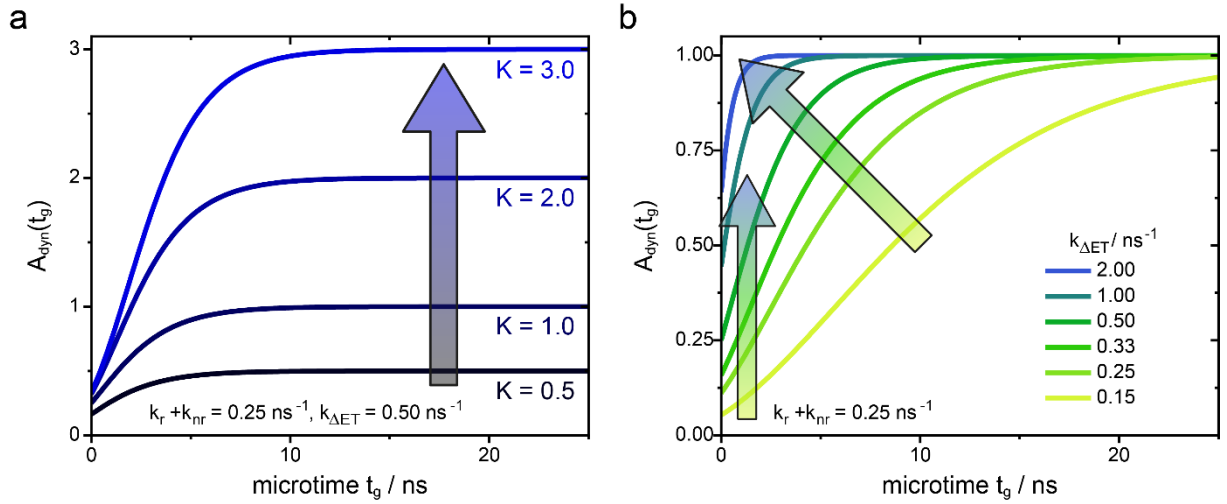
Figure S1: How the bunching amplitude changes with the shrinking microtime gate. a) The dependence of $A_{dyn}(t_g)$ on K. The saturation value of $A_{dyn}(t_g)$ scales linearly with K as depicted by the arrow. b) The dependence of $A_{dyn}(t_g)$ on $k_{\Delta ET}$. Larger $k_{\Delta ET}$ rates lead to faster saturation due to a faster rise of the intensity contrast and a larger initial bunching amplitude $A_{dyn}(t_g = 0\,ns)$ indicated by the two arrows.

5

3. Fitting procedure

Extraction of the fit parameters from the sg-FCS function with experimental data is challenging. Theoretically, from equation S5, it should be possible to extract the fluorescence lifetime of the low FRET state $\tau_A = \frac{1}{k_r + k_{nr}}$. However, in a real experiment, other factors also play a role. For example, the arrival time of the laser pulse is not at microtime $t_g = 0$ resulting in a constant amplitude $A_{dyn}(t_g)$ for the first microtime gates. To account for this, an offset t_0 is needed.

$$A_{dyn}(t_g) = K \left(\frac{1 - \dfrac{k_r + k_{nr}}{k_r + k_{nr} + k_{\Delta ET}} e^{-k_{\Delta ET} \cdot (t_g - t_0)}}{1 + K \cdot \dfrac{k_r + k_{nr}}{k_r + k_{nr} + k_{\Delta ET}} e^{-k_{\Delta ET} \cdot (t_g - t_0)}} \right)^2 \qquad \text{eq. S7}$$

With this modification, we cannot fit our data because a change in $k_{\Delta ET}$ also shifts the ratio in front of the exponent and thereby the curve for $A_{dyn}(t_g)$. Hence, both $k_{\Delta ET}$ and the offset t_0 slide the function on the abscissa.

We propose two ways to overcome this issue. In the first approach, we substitute the lifetime ratio in front of the exponent. The fluorescence lifetime ratio equals the ratio of intensities.

$$\frac{k_r + k_{nr}}{k_r + k_{nr} + k_{\Delta ET}} = \frac{\tau_B}{\tau_A} = \frac{I_B}{I_A} \qquad \text{eq. S8}$$

The correlation amplitude, when all photons are taken into account $A_{dyn}(t_g = 0)$, only depends on the overall intensity ratio $\frac{I_B}{I_A}$.

$$A_{dyn}(t_g = 0) = K \left(\frac{1 - \dfrac{I_B}{I_A}}{1 + K \cdot \dfrac{I_B}{I_A}} \right)^2 \qquad \text{eq. S9}$$

Rearranging equation S9, for the physical reasonable solution yields ($0 \le I_B < I_A$):

$$\frac{I_B}{I_A} = \frac{1 - \sqrt{\dfrac{A_{dyn}(t_g = 0)}{K}}}{\sqrt{A_{dyn}(t_g = 0) \cdot K} - 1} \qquad \text{eq. S10}$$

and we can rewrite equation S3 as:

$$A_{dyn}(t_g) = K \left(\frac{1 - \dfrac{1 - \sqrt{\dfrac{A_{dyn}(t_g = 0)}{K}}}{\sqrt{A_{dyn}(t_g = 0) \cdot K} - 1} e^{-k_{\Delta ET} \cdot (t_g - t_0)}}{1 + K \cdot \dfrac{1 - \sqrt{\dfrac{A_{dyn}(t_g = 0)}{K}}}{\sqrt{A_{dyn}(t_g = 0) \cdot K} - 1} e^{-k_{\Delta ET} \cdot (t_g - t_0)}} \right)^2 \qquad \text{eq. S11}$$

This approach is elegant because it maintains the physical meaning of the laser pulse arrival time, t_0. The ratio in front of the exponential function is fitted using the equilibrium constant, which is the parameter of interest and $A_{dyn}(t_g = 0)$, which we have extracted before. By

6

extracting t_0, we can verify whether the fitted t_0 value is consistent with the known arrival time of the laser pulse. When this is not the case, it may suggest the presence of additional bunching terms (e.g. due to photophysics). With equation S10 and the extracted rate constant $k_{\Delta ET}$, we can calculate the fluorescence lifetime τ_A and τ_B.

$$\frac{1}{\tau_A} = k_r + k_{nr} = \frac{k_{\Delta ET} \cdot \dfrac{1 - \sqrt{\dfrac{A_{dyn}(t_g = 0)}{K}}}{\sqrt{A_{dyn}(t_g = 0) \cdot K - 1}}}{1 - \dfrac{1 - \sqrt{\dfrac{A_{dyn}(t_g = 0)}{K}}}{\sqrt{A_{dyn}(t_g = 0) \cdot K - 1}}} \qquad \text{eq. S12}$$

$$\tau_B = \frac{1}{k_r + k_{nr} + k_{\Delta ET}} = \frac{1}{\dfrac{1}{\tau_A} + k_{\Delta ET}} \qquad \text{eq. S13}$$

It is worth mentioning a second model function that yields K and $k_{\Delta ET}$. As the offset t_0 and the fluorescence lifetime ratio $\frac{k_r + k_{nr}}{k_r + k_{nr} + k_{\Delta ET}}$ shift the function on the abscissa, we can simply use:

$$A(t_g) = K \left(\frac{1 - e^{-k_{\Delta ET} \cdot (t_g - t_{shift})}}{1 + K \cdot e^{-k_{\Delta ET} \cdot (t_g - t_{shift})}} \right)^2 \qquad \text{eq. S14}$$

Here t_{shift} combines the shift due to the laser pulse arrival time and the lifetime ratio but is not interpretable. The second approach is the one we use in the main text.

The analysis routine for a fluorescence intensity trajectory of an experiment with immobilized molecules (no diffusion component) starts by performing sg-FCS, which we fit with a monoexponential model.

$$g^{(2)}(\Delta\tau, t_g) = 1 + A_{dyn}(t_g) e^{-\frac{\Delta\tau}{\tau_{CRT}}} \qquad \text{eq. 15}$$

Here, τ_{CRT} denotes the correlation relaxation time (CRT) and is inversely proportional to the sum of the switching rate constants.

$$\tau_{CRS} = \frac{1}{k_A + k_B} \qquad \text{eq. S16}$$

For the first correlation where $t_g = 0 \ ns$, we extract CRT and fix it for all following fits because the correlation with all photons yields the most precise CRT value. Subsequently, we extract K from fitting all background corrected (see next section) amplitudes $A_{dyn}(t_g)$ with equation S11. The equilibrium constant is defined as:

$$K = \frac{k_B}{k_A} \qquad \text{eq. S17}$$

Using equations S16 and S17, we calculate the switching rates k_A and k_B as well as the dwell times t_A and t_B using:

$$k_A = \frac{1}{t_B} = \frac{1}{\tau_{CRS} \cdot (K+1)} \qquad\qquad \text{eq. S18}$$

$$k_B = \frac{1}{t_A} = \frac{1}{\tau_{CRS} \cdot \left(\frac{1}{K}+1\right)} \qquad\qquad \text{eq. S19}$$

4. Background correction

The uncorrelated background in our experiments originates from SPAD dark counts and phosphorescence of the immersion oil. The background is uncorrelated and decreases our bunching amplitude $A_{dyn}(t_g)$. This becomes especially crucial for longer microtimes, because the fluorescence signal decays exponentially whereas the background counts are constant and thus scale linearly with the microtime gate size. The effect is demonstrated using the data shown in Figure 3c. The result is an exponential decaying signal-to-background ratio (SBR) (see Figure S2a) leading to systematically smaller correlation amplitudes for the later microtime gates as shown in Figure S2b. The extracted bunching amplitudes $A_{dyn,BG}(t_g)$ in Figure S2c show a non-monotonic behavior (blue dots). We can fit the background poisoned bunching amplitudes $A_{dyn,BG}(t_g)$ with a model which takes the decaying SBR into account by considering the fluorescence lifetime decay of the low FRET state τ_A and the linear decay of the integrated background intensity I_{BG}, where I_{BG} is the background intensity within the maximum microtime gate length ($= 1$ / laser repetition rate $=$ maximum usable range of the time-to-amplitude converter (TAC)) t_{TAC}. In our experiments, a 50 MHz laser repetition rate was used and hence, this value was fixed to $t_{TAC} = 20\ ns$. The background can either be measured or fitted. The background contribution in figure S2c was fitted for demonstration purposes.

$$A_{dyn,BG}(t_g) = K \left(\frac{1 - e^{-k_{\Delta ET} \cdot (t_g - t_{shift})}}{1 + K \cdot e^{-k_{\Delta ET} \cdot (t_g - t_{shift})}} \right)^2 \left(\frac{\tau_A \cdot e^{-\left(\frac{t_g}{\tau_A}\right)} + 0.5 \cdot I_{BG} \cdot (t_{TAC} - t_g)}{\tau_A \cdot e^{-\left(\frac{t_g}{\tau_A}\right)}} \right)^{-2} \qquad \text{eq. S20}$$

It is possible to extract the background from a fit to the sg-FCS data as well as the equilibrium constant K and $k_{\Delta ET}$ but the fitting approach was not very robust in our hands.
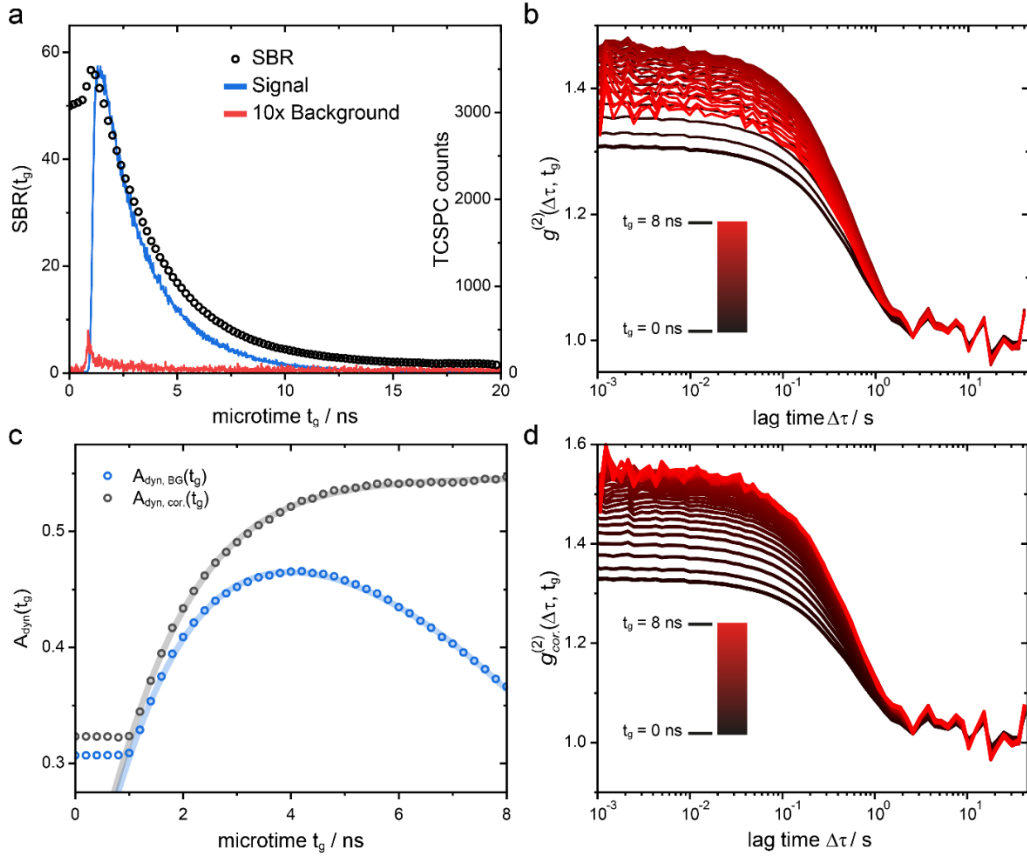
Figure S2: Effect of background on the sg-FCS analysis. a) An example of how the $SBR(t_g)$ changes when microtime gating is applied for the experimental data of the donor trajectory from Figure 3b in the main text. The fluorescence signal is depicted in blue and the background signal in red, which is multiplied by a factor of 10. The shrinking gate step size = 200 ps. b) Impact of the decaying $SBR(t_g)$ on $g^{(2)}(\Delta\tau, t_g)$. Even though the amplitude is supposed to saturate, it starts decreasing for later microtime gates. The color gradient denoting the microtime gate goes from black to red. c) The fitted bunching amplitudes $A_{dyn,BG}(t_g)$ as a function of microtime gate for the uncorrected amplitudes (Eq. S20, blue circles) and from the background corrected bunching amplitudes, $A_{dyn,cor.}(t_g)$ (Eq. S21, black circles). For amplitude correction a background trajectory was measured at the surface of the sample with a mean count rate of 90.7 Hz. The corresponding fits are depicted as bold transparent lines. d) The background corrected $g^{(2)}_{cor.}(\Delta\tau, t_g)$ correlation functions, which shows the expected saturation behavior as a function of gate size.

Alternatively, we can measure a background trajectory and use it to correct the extracted correlation amplitudes $A_{dyn}(t_g)$ for each microtime gate with the measured intensity $I(t_g)$, which includes the fluorescence and the background intensity $I_{BG}(t_g)$. The bunching amplitude $A_{dyn}(t_g)$ is then corrected according to:

$$A_{dyn,cor}(t_g) = A_{dyn}(t_g) \cdot \left(\frac{I(t_g)}{I(t_g) - I_{BG}(t_g)}\right)^2 \qquad \text{eq. S21}$$

10

The corrected bunching amplitudes $A_{dyn,cor.}(t_g)$ are depicted in Figure S2c as black dots and show the expected saturation behavior. K and $k_{\Delta ET}$ are easily extracted this way. This approach is more robust and yields the same values as the model of equation S20. The fitting parameters are listed for both approaches in table S1.

Not only can we correct the fitted correlation amplitudes but also the sg-FCS curves,

$$g_{cor.}^{(2)}(\Delta\tau, t_g) = \left(g^{(2)}(\Delta\tau, t_g) - 1\right) \cdot \left(\frac{I(t_g)}{I(t_g) - I_{BG}(t_g)}\right)^2 + 1 \qquad \text{eq. S22}$$

The corrected autocorrelation functions are shown in Figure S2d.

Table S1: Comparison of extracted fit parameters with the corresponding errors in the parameter determination extracted directly from the fit using the covariance matrix.

	$A(t_g)$ and model eq. S14	$A_{cor.}(t_g)$ and model eq. S8
K / 1	0.538 ± 0.009	0.5461 ± 0.0004
$k_{\Delta ET}$ / ns^{-1}	0.82 ± 0.03	0.805 ± 0.008
t_{shift} / ns	-1.18 ± 0.07	-1.22 ± 0.03
τ_A / ns	2.4 ± 0.1	$-$
I_{BG} / 1	0.0006 ± 0.0002	$-$

5. Kinetic tuning by varying the complementary sequences

We tuned the binding time of the tether to the binding positions on the DNA origami platform by varying the length of the complementary sequences. The pointer sequence stays the same for all experiments but the binding site sequences are altered. The sequences are given in Figure S3. The pointer sequence has the Cy3B modification at the 3' end. When 7 complementary nucleotides (nt) are present, an average binding time of $\langle t_{binding} \rangle \sim 1\,s$ is observed. To lower the binding time and thereby increase the kinetic rates, we remove one nucleotide from the binding site either at the 3' or at the 5' end. The outcome is different, because the duplex stability is base-pair dependent. The G-C base-pair contributes more to duplex stability than the T-A base pair. By removing the A-T stacking with the introduction of a mismatch (mm), which is indicated in orange and called 6nt$_{mm}$ (Figure S3), we reduce the binding time by a factor of ~ 5. Removal of a G-C base-pair, which we term 6 nt, reduces the binding time by a factor of ~ 50. To shift the binding time below the millisecond regime, we remove an additional C-A base-pair (5 nt), which gives an average binding time of $\langle t_{binding} \rangle \sim 600\,\mu s$.
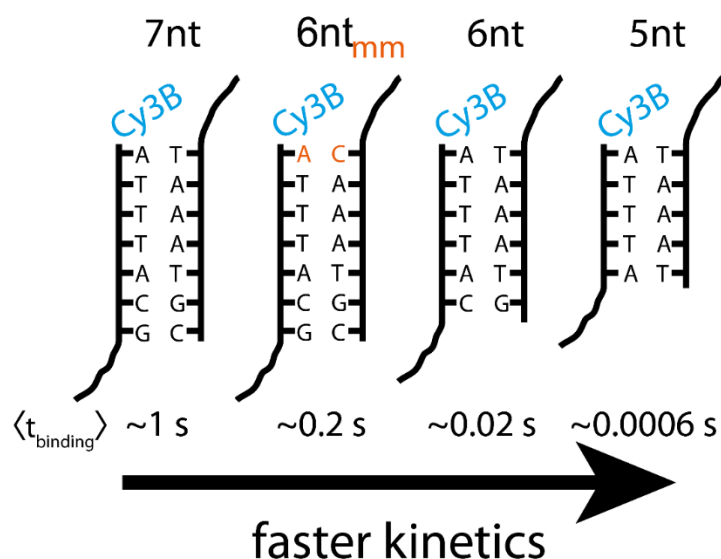
Figure S3: A portion of the DNA sequence used in the DNA pointer experiment. The pointer oligonucleotide is labelled at the 3' end with a Cy3B dye. Various overlaps from 5 nt to 7 nt were used. The mismatched base pair for the 6nt$_{mm}$ sample is indicated in orange.

6. Comparison of the sg-FCS and HMM analyses

To test the limits of sg-FCS, we measure different combinations of binding times for the low- and high-FRET states in surface experiments and compared them to an HMM analysis.[3] Each data point in Figures S4 represents the average binding time of a single structure with the corresponding standard error. Equal sequences for the high and low FRET position exhibit a systematic almost twofold shift towards longer binding times for the low-FRET position. This holds true for all sequence lengths (7 nt -5 nt) and is consistently observed by both the HMM and sg-FCS analyses. This suggests that the difference in dwell times for the high-FRET and low-FRET sites is real. This could be explained by a preferred directionality of the unbound tether and/or an interaction between the fluorophore and/or tether with the surface of the origami in the low-FRET configuration.

In addition to DNA origamis containing symmetric binding sites, we measure different combinations of sequences like e.g. 7 nt overlap for the high-FRET position and a 6 nt_{mm} for the low-FRET position (see Figure S4 green data points). This allowed us to probe how unbalanced the rate constants can be and still be correctly analyzed using sg-FCS. For the vast majority of constructs measured, the acquired binding times from the HMM (Figure S4a) and sg-FCS (Figure S4b) analyses agreed well. Even the outliers from the various samples were consistently detected by both analysis methods demonstrating an excellent consistency between the two approaches in the regimes where they both work well. However, sg-FCS has difficulties when the kinetics rate constants are too unbalanced (see SI Section 7) and the HMM analysis is not suitable for diffusing molecules or for the detection of fast kinetics, which we cannot resolve into a binned fluorescence intensity trajectory.
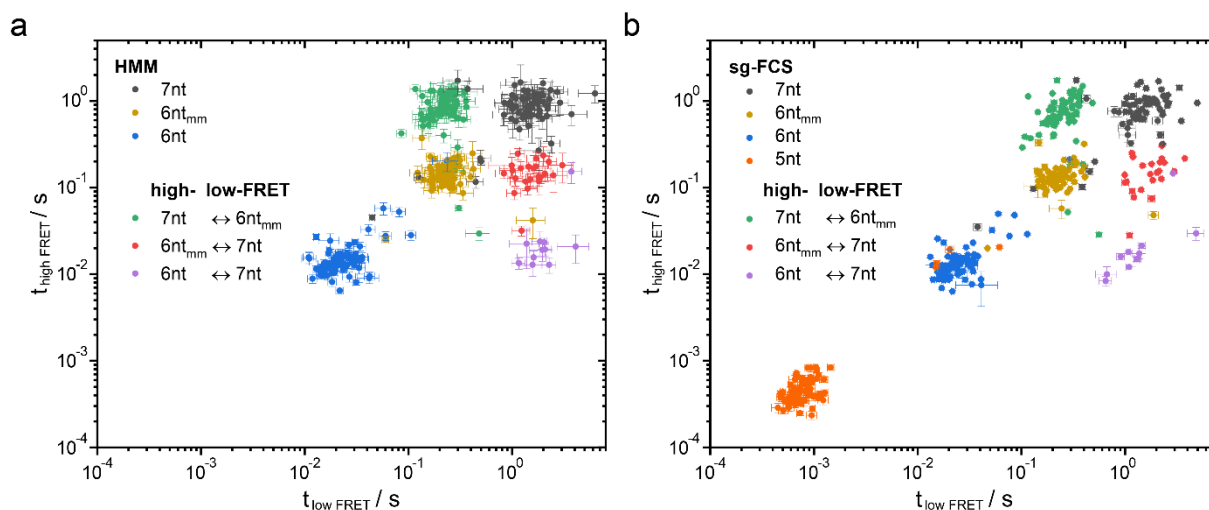
Figure S4: A comparison of an HMM analysis and sg-FCS. a) A scatterplot of the average binding times in the low- and high-FRET position determined by an HMM analysis. b) A scatterplot of the average binding times in the low- and high-FRET position determined by the sg-FCS analysis.
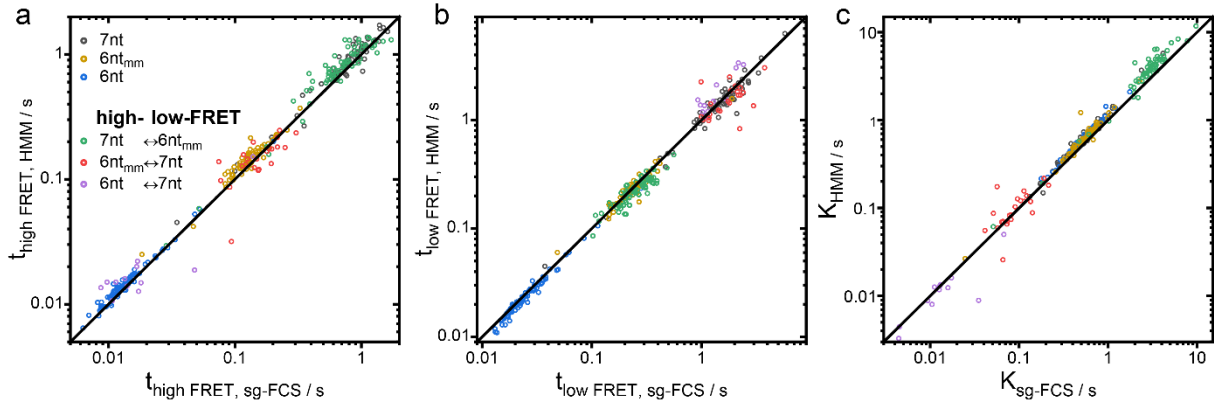
Figure S5: Correlation plots for binding times and equilibrium constants between HMM and sf-FCS. All plots have a black line with a slope 1 and an intercept of 0 to guide the eye. a) A correlation plot of the binding time of the high-FRET state determined from HMM vs. sg-FCS. b) A correlation plot of the binding time of the low-FRET state determined HMM vs. sg FCS. c) A correlation plot of the equilibrium constant determined from HMM vs. sg FCS.

Table S2: Comparison of the mean binding times with standard deviations for the data presented in Figure S4. For non-symmetric samples, the first number corresponds to the number of complementary nucleotides for the binding strand in the high-FRET position, the second one for the low-FRET position.

sample	$t_{\text{sg-FCS l. FRET}}$ / s	$t_{\text{HMM l. FRET}}$ / s	$t_{\text{sg-FCS h. FRET}}$ / s	$t_{\text{HMM h. FRET}}$ / s
7nt $n = 67$	1.59 ± 0.85	1.53 ± 0.87	0.80 ± 0.32	0.88 ± 0.36
6nt $n = 85$	0.029 ± 0.031	0.027 ± 0.026	0.016 ± 0.021	0.017 ± 0.021
5nt $n = 72$	0.0023 ± 0.0077	-	0.0013 ± 0.0037	-
6nt$_{mm}$ $n = 70$	0.26 ± 0.21	0.24 ± 0.17	0.134 ± 0.045	0.148 ± 0.048
6nt-7nt $n = 12$	1.43 ± 0.51	1.88 ± 0.85	0.027 ± 0.036	0.27 ± 0.039
7nt–6nt$_{mm}$ $n = 66$	0.258 ± 0.086	0.229 ± 0.068	0.75 ± 0.33	0.84 ± 0.32
6nt$_{mm}$-7nt $n = 22$	1.82 ± 0.69	1.58 ± 0.55	0.160 ± 0.059	0.151 ± 0.049

In addition, the correlation plots in Figure S5 show a slight deviation for $K < 2$ propably due to imperfect background correction in the sg-FCS data of the HMM and sg-FCS data.

To demonstrate that sg-FCS yields the correct change in the rate of energy transfer due to the differences in FRET efficiencies between the low and high FRET states, we compared the value

14

extracted from sg-FCS (Figure 3d) with the value we obtain from fluorescence lifetime fitting. By extracting the average fluorescence lifetimes of each intensity state, we can calculate $k_{\Delta ET}$:

$$k_{\Delta ET} = \frac{1}{\tau_{high\,FRET}} - \frac{1}{\tau_{low\,FRET}} = \frac{1}{\frac{1}{k_r + k_{nr} + k_{\Delta ET}}} - \frac{1}{\frac{1}{k_r + k_{nr}}} \qquad \text{eq. S23}$$

We obtain $\tau_{high\,FRET} = 0.8 \pm 0.1\,ns$ and $\tau_{low\,FRET} = 2.3 \pm 0.1\,ns$ as the average fluorescence lifetime from Figure S6b. This yields a $k_{\Delta ET_{lifetime}} = 0.8 \pm 0.2\,ns^{-1}$, which is in good agreement with the sg-FCS result of $k_{\Delta ET_{sg-FCS}} = 0.811 \pm 0.008\,ns^{-1}$.
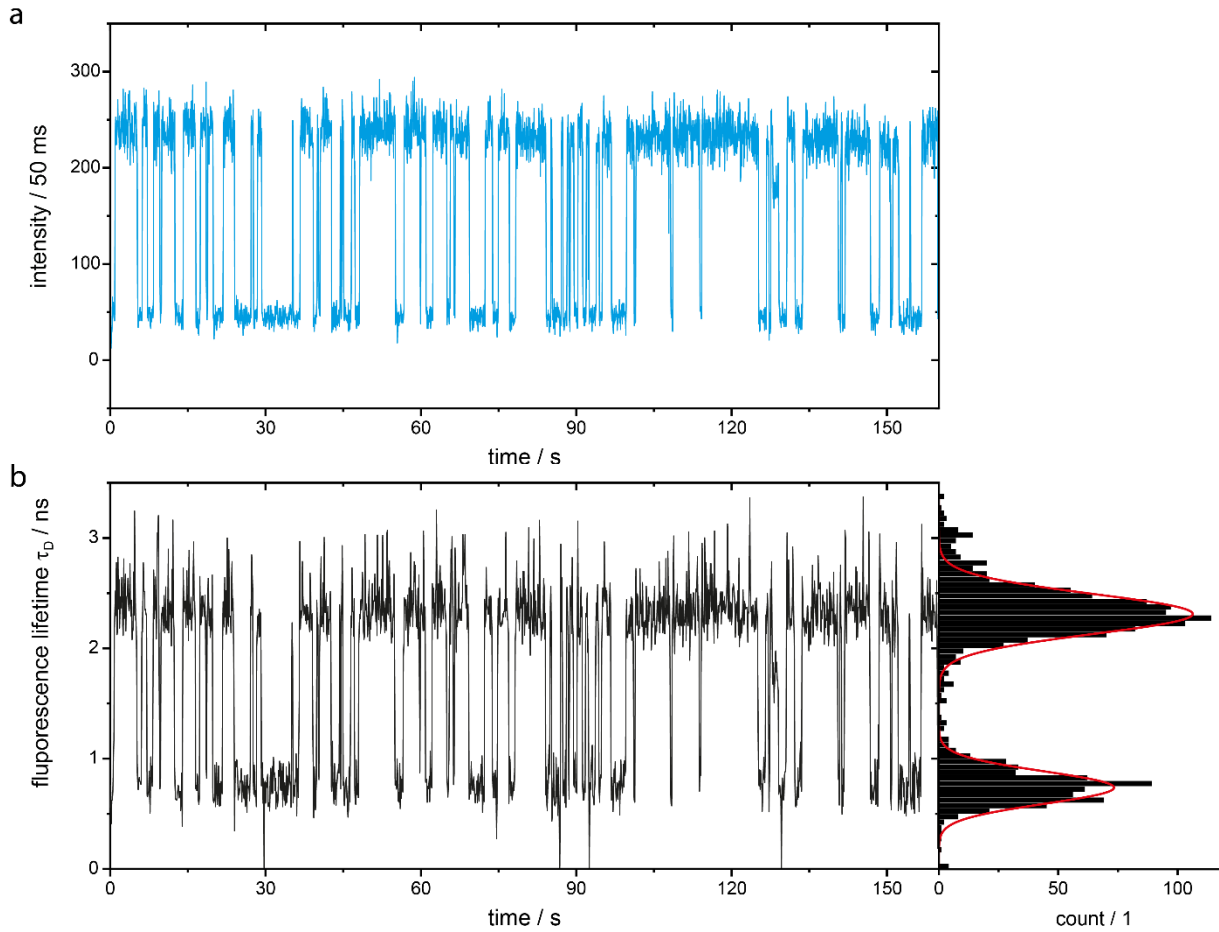
Figure S6: Extraction of the additional energy transfer rate constant from the fluorescence lifetime trajectory. a) Fluorescence intensity trajectory of the donor from Figure 3b. b) The corresponding fluorescence lifetime trajectory with a binning of 100 ms. The mean fluorescence lifetimes were extracted from the histogram on the right with two Gaussian fits (red).

7. Limitations of the sg-FCS analysis

In Figure S4, we plotted the data that we were able to successfully analyze using sg-FCS. We are able to cover a range of equilibrium constants K from $K\sim0.01$ (6 nt high FRET, 7 nt low FRET, purple data points) to $K\sim8$ (7 nt high FRET, 6 nt$_{mm}$ low FRET, green data points) . When K is unbalanced towards the short fluorescence lifetime state, they can no longer be analyzed with sg-FCS. For our measurements here, this occurred when the equilibrium constants reached $K\sim50$. Figure S7a exemplifies this limitation using a sample with 7 nt for the high FRET state and 6 nt for the low FRET state. As the system spends the majority of time in the low FRET state, the fluorescence intensity is low and background becomes a significant issue for the late microtime gates where the saturation of the amplitude is expected. Figure S7b shows the gated correlation functions without background correction. The late gates (red) suffer from the low SBR and the low average count rate, which are reflected by the strong noise. The correlation amplitudes are shown in Figure S7c and can no longer be fully corrected due to the low count rate and the poor SBR. As a result, the model no longer describes the data and the extracted equilibrium constant of sg-FCS is smaller by a factor of 3 compared to the HMM analysis.

Analyzing equilibrium constants for $K \ll 1$ with sg-FCS works over a larger range as more time is spent in the low-FRET state where the donor intensity is high. The higher SBR improves the quality of the analysis and allows a larger imbalance to be quantitatively analyzed. Figure S8a shows data with our DNA origami structure with 7 nt for the low FRET state and 6 nt for the high FRET state. This results in a low bunching amplitude in the $g^{(2)}(\Delta\tau)$ correlation function. However, due to the high average fluorescence intensity, the monoexponential bunching amplitude $A_{dyn}(t_g)$ can still be easily extracted, as shown in Figure S8b. In Figure S8c, the equilibrium constant K can be reliably determined and the calculated dwell times in the high and low FRET states match closely to those determined from the HMM analysis. However, the precision of the determined parameters are noticeably worse than in samples where $K\sim1$.
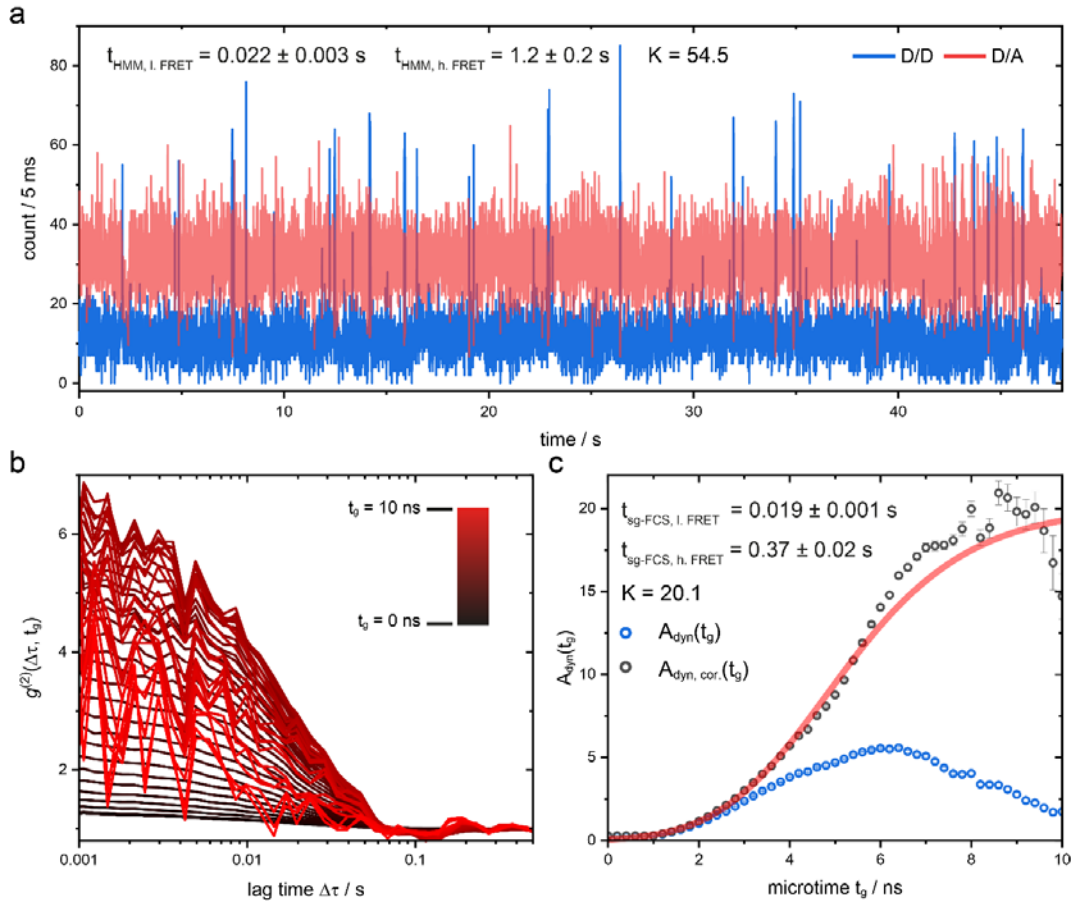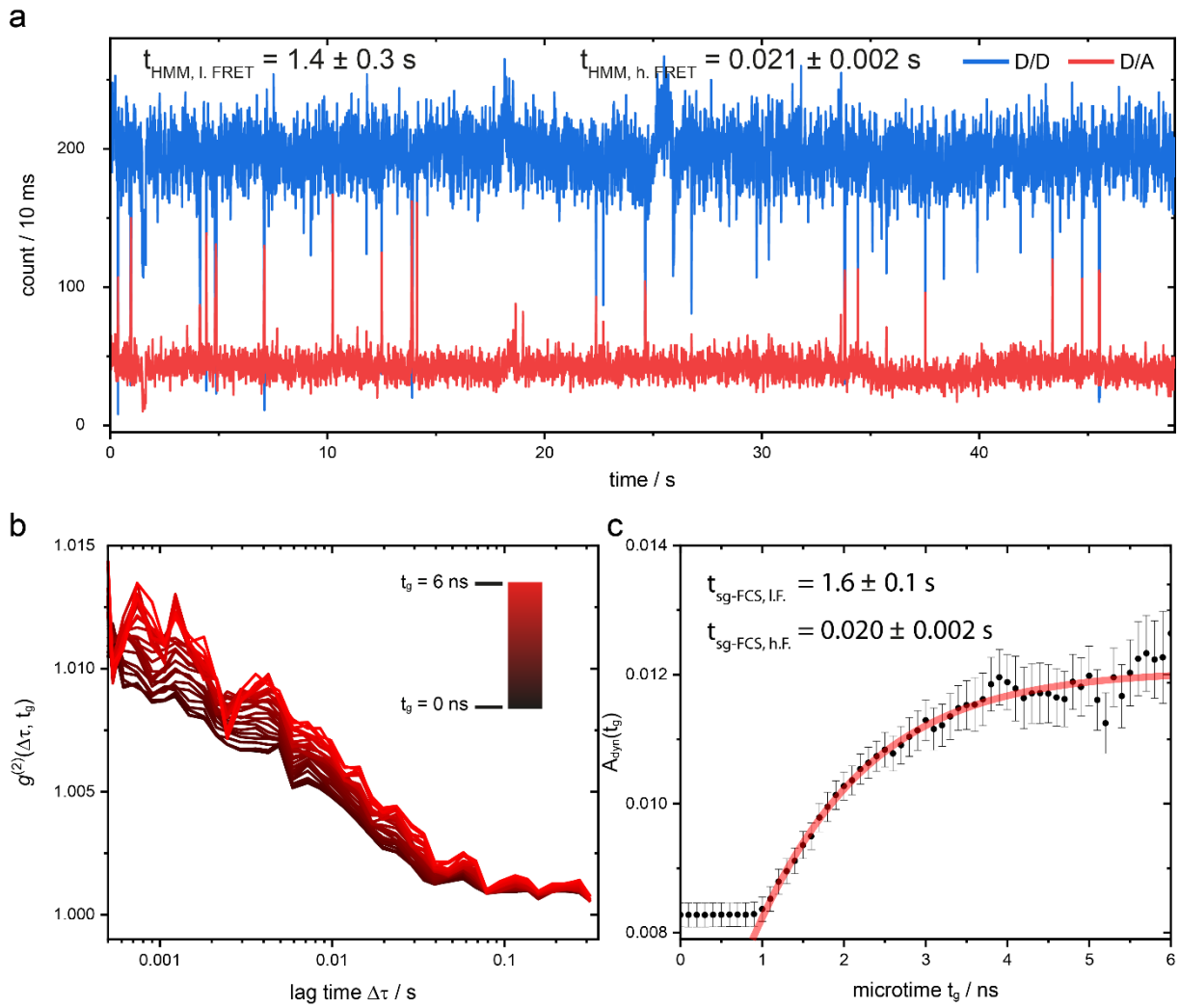
Figure S7: Sg-FCS for a system with a high equilibrium coefficient towards the low intensity, short fluorescence lifetime state. a) A typical single particle fluorescence intensity trajectory for our DNA origami system with a 7 nt binding strand for the high-FRET state and 6 nt binding strand for the low-FRET state. The donor intensity (D/D) is shown in blue and the FRET intensity (D/A) in transparent red. The signals are anticorrelated. The extracted dwell times and equilibrium constant for the HMM analysis are given in the figure. b) Sg-FCS of the donor trajectory. The $g_{cor.}^{(2)}(\Delta\tau,\ t_g)$ is plotted as a function of microtime gate with the color gradient going from black (full gate) to red (late microtime gate). c) The extracted bunching amplitudes $A_{dyn}(t_g)$. The raw amplitudes (blue) and background corrected amplitudes (black) are plotted as a function of microtime gate. The low average fluorescence intensity for late microtime thresholds in combination with the poor SBR prevents extraction of the correct equilibrium constant from the fit (bold red line).

Figure S8: Sg-FCS for a system with a low equilibrium coefficient towards the high intensity, long lifetime state. a) A typical single particle fluorescent trajectory for our DNA origami system with a 7 nt binding strand for the low-FRET state and 6 nt binding strand for the high-FRET state. Donor intensity (D/D) is shown in blue and the FRET intensity (D/A) in transparent red. The signals are anticorrelated. The extracted dwell times from the HMM analysis are given above the plot. b) A sg-FCS analysis of the donor trajectory. The $g_{cor.}^{(2)}(\Delta\tau, t_g)$ is plotted as a function of microtime gate with the color gradient going from black (full gate) to red (late microtime gate). c) The extracted and background corrected bunching amplitudes $A_{dyn}(t_g)$ (black) and corresponding fit (red line).

8. Solution experiments: PIE-FRET and FCS

To demonstrate the suitability of the sg-FCS analysis for experiments with diffusing molecules, we measured the DNA origami platforms in solution. First, we performed PIE-FRET[4] experiments to validate that the switching kinetics between low- and high-FRET states of the 5 nt sample is faster than the diffusion dwell time in the focal volume of ~1 ms. We compared the 5 nt sample to the 7 nt sample, which shows a switching kinetic on the seconds timescale in experiments on immobilized molecules. Hence, the 7 nt sample should appear as two, static species in the PIE-FRET experiment. As depicted in Figure S9a, the 7 nt (blue) sample shows two well-separated FRET distributions with FRET efficiencies of $E_{low} = 0.14 \pm 0.10$ (SD) and $E_{high} = 0.83 \pm 0.07$ (SD). The 5 nt sample (orange), on the other hand, shows a single broad FRET distribution centered between the 7 nt-populations with an efficiency of $E = 0.38 \pm 0.17$ (SD) indicating switching between the two FRET states while diffusing through the focal volume, which is supported by the E vs τ_D plot in Figure S9b where the 5 nt sample is located away from the static FRET line. We also note that we have a very minor donor only population, which does not harm our FCS experiment.

As the donor-only population was very small, we performed sg-FCS experiments with 532 nm excitation only to maximize the photons coming from each molecule. The 7 nt sample shows a small photo physics component at $\tau_{pp} \sim 54\,\mu s$. To fit the dynamic component in the 5 nt sample, a second relaxation time, τ_{dyn}, is needed. To perform the sg-FCS analysis with a diffusing sample, we included a diffusion term in the correlation functions and two relaxation functions for the photophysics and dynamic components:

$$g^{(2)}(\Delta\tau, t_g) = \frac{\gamma_{FCS}}{N} \cdot M(\Delta\tau) \cdot \left(1 + A_{pp,7nt}(t_g) \cdot e^{-\frac{\Delta\tau}{\tau_{pp}}} + A_{dyn,5nt}(t_g) \cdot e^{-\frac{\Delta\tau}{\tau_{dyn}}}\right) \qquad \text{eq. S24}$$

where N denotes the average number of molecules in the focal volume and γ_{FCS} accounts for the approximated Gaussion illumination profile and is given by $2^{-\frac{3}{2}}$. $M(\Delta\tau)$ is the diffusion term:

$$M(\Delta\tau) = \frac{1}{1 + \dfrac{\Delta\tau}{\tau_{diff}}} \frac{1}{\sqrt{1 + \dfrac{\Delta\tau}{w^2 \tau_{diff}}}} \qquad \text{eq. S25}$$

where τ_{diff} denotes the diffusion dwell time and w accounts for the different axial dimension of the three dimensional confocal volume ($w = \dfrac{w_z}{w_{xy}}$).
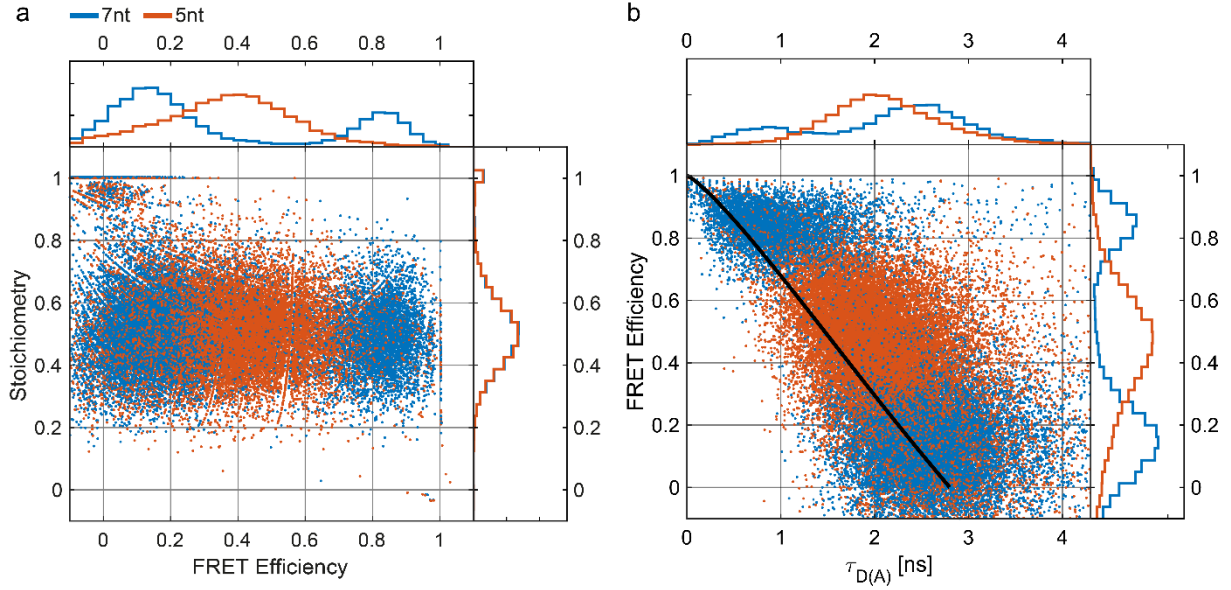
19

Figure S9: Solution burst analysis of the DNA origami platform under PIE excitation. a) An *ES*-scatter plot of the 7 nt sample (blue) and 5 nt sample (orange). The FRET efficiencies are corrected according to Hellenkamp et al.[5] b) An E vs τ_D scatter plot. The black solid line gives the static FRET line for a measured fluorescence lifetime of the donor only population of 2.8 ns. The parameters used for the burst search are: Minimum photons per burst: 30, time window: 500 μs, minimum photons per time window: 10. No additional filters were applied.

For the 7 nt sample, we first extracted the diffusion dwell time τ_{diff} and the CRT of the photophysics term τ_{pp} from the $g^{(2)}(\Delta\tau, t_g = 0\ ns)$ correlation function. The amplitude for the dynamic term, $A_{dyn,\ 5nt}(t_g)$, was set to a constant value of zero. We did not observe a change in $A_{pp,7nt}(t_g)$ with the microtime gate for the 7 nt sample. For the 5 nt sample analysis, we fixed the photophysical terms τ_{pp} and $A_{pp,7nt}(t_g)$ that we determined from the 7 nt sample. By fitting $A_{dyn,5nt}(t_g)$ as a function of microtime (Figure S10), we extracted K and $k_{\Delta ET}$ (see Tables S3 and S4) and calculated the high- and low-FRET dwell times. The results are compared to the surface-based analysis in Table S4.

Table S3: Fit results for the sg-FCS analysis of solution experiments for the 7 nt and 5 nt samples.

	7 nt	5 nt
$\dfrac{\gamma_{FCS}}{N}$	1.672 ± 0.004	1.07 ± 0.01
$\tau_{diff}\ /\ ms$	1.28 ± 0.01	1.12 ± 0.02
$A_{pp,7nt}(t_g = 0\ ns)$	0.079 ± 0.03	$0.079\ (constant)$
$\tau_{pp}\ /\ \mu s$	46 ± 5	$46\ (constant)$
$A_{dyn,5nt}(t_g = 0\ ns)$	$-$	0.11 ± 0.01
$\tau_{dyn}\ /\ \mu s$	$-$	220 ± 20

20

Table S4: Comparison of extracted dwell times from surface and solution experiments.

	Mean surface $n = 74$	solution
$K \ / \ 1$	0.53 ± 0.02	0.46 ± 0.01
$t_{h. \ FRET} \ / \ \mu s$	770 ± 20	700 ± 70
$t_{l. \ FRET} \ / \ \mu s$	410 ± 10	330 ± 30
$k_{\Delta ET} \ / \ ns^{-1}$	0.37 ± 0.02	0.223 ± 0.008
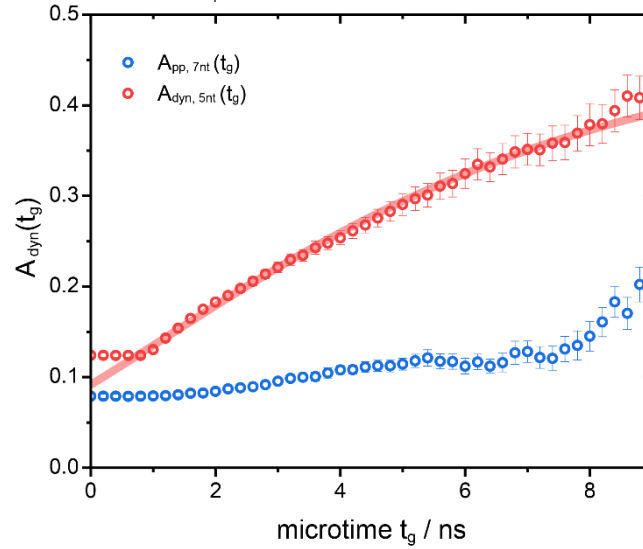
Figure S10: Sg-FCS analysis of solution-based data. The amplitude of the dynamic term, $A_{dyn,5nt}(t_g)$ (red circles), along with the fit to equation S14 (transparent red line) is shown. In addition, the photophysics amplitude $A_{pp,7nt}(t_g)$ of the 7 nt sample is plotted in blue. It stays constant in the beginning. The rise at the end originates from the noise in the correlation function at short timescales.

21

9. Separating dynamic kinetics from photophysics kinetics in the intensity correlation function

The example of Figure 5d of the main text shows well separated photophysics and tether movement kinetics. However, dynamic processes and photophysics can occur on similar time scales. In this case, the bunching amplitude will change with the applied sg-FCS but the extracted equilibrium constant will be overestimated due to the underlying photophysics amplitude.

By using a subset of photons, the photophysics component of the correlation function can be removed in the sg-FCS analysis. Here, we again make use of the time dependency of the dynamic process. When only photons are considered from a very small microtime gate after pulsed excitation, no intensity fluctuations will be observed and hence both intensity states are equally bright. This results in the absence of the dynamic bunching amplitude as depicted in
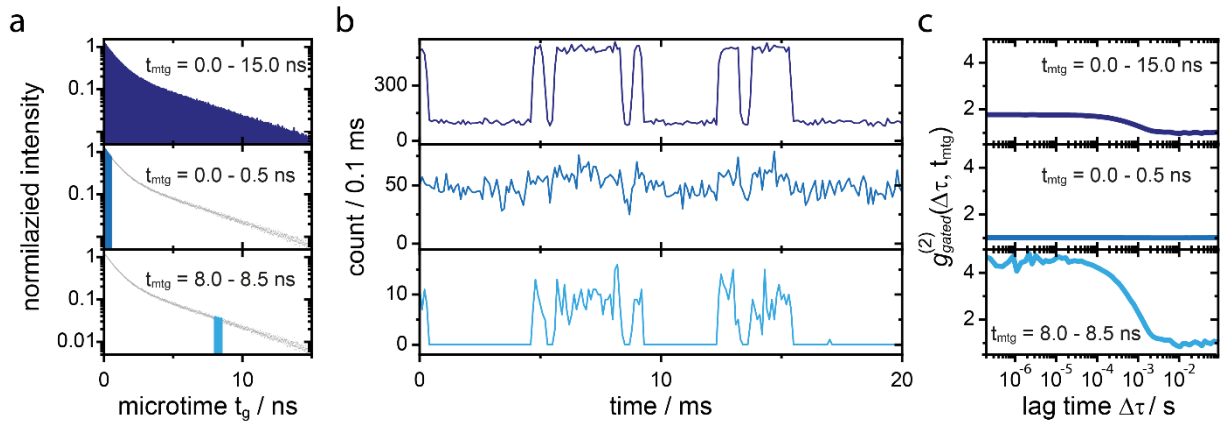
Figure S11: The application of gated-FCS to a simulated data set. a) Histograms are shown for simulated photon arrival times in a pulsed-laser excitation experiment where two fluorescence lifetimes are present. The colored area indicates the applied mircotime gate for gated-FCS. b) The extracted intensity trajectories according to the selected photons from the lifetime data. c) The corresponding $g^{(2)}_{gated}(\Delta\tau, t_{mtg})$ of the respective intensity trajectories. For the simulation, the transition rate constant into the quenched states is $k_B = 3,000\ s^{-1}$ and into the bright state $k_A = 1,000\ s^{-1}$.

Figure S11c. We will refer in further discussions to this type of gating as gated-FCS. Only as the time shifts to longer microtimes do the intensities of the two states start to differ. However, if only photons from a small microtime gate after pulsed laser excitation are considered, the photophysics component stays untouched. Therefore, a bunching amplitude for a small microtime gate after pulsed excitation originates from on-off switching.

To obtain a model for the bunching amplitude of dynamic processes, we start again from the bunching amplitude of two intensity levels.

$$A_{dyn} = K \left(\frac{I_A - I_B}{I_A + K \cdot I_B} \right)^2 \qquad \text{eq. S26}$$

I_A denotes the high-intensity level and I_B denotes the low-intensity level. K denotes the equilibrium constant. Next, we consider the microtime dependent intensity levels. After pulsed laser excitation, the intensities decays with their characteristic fluorescence decay rate.

22

$$I_{A_{gated}}(t_{mtg}) = I_0 \, e^{-(k_r + k_{nr}) \cdot t_{mtg}} \qquad\qquad \text{eq. S27}$$

$$I_{B_{gated}}(t_{mtg}) = I_0 \, e^{-(k_r + k_{nr} + k_{\Delta ET}) \cdot t_{mtg}} \qquad\qquad \text{eq. S28}$$

Here, k_r denotes the radiative rate constant, k_{nr} the sum of all non-radiative decay rate constants for the low-FRET state, I_A, which includes possible energy transfer to an acceptor dye. $k_{\Delta ET} = k_{ET,high\ FRET} - k_{ET,low\ FRET}$ denotes the additional energy transfer rate constant of the high FRET state. t_{mtg} denotes the microtime I_0 and is a scaling factor. Considering the different fluorescent decays for both intensities in equation S1, we obtain the microtime gate dependent bunching amplitude $A_{dyn,gated}(t_g)$.

$$A_{dyn,gated}(t_g) = K \left(\frac{1 - e^{-k_{\Delta ET} \cdot t_{mtg}}}{1 + K \cdot e^{-k_{\Delta ET} \cdot t_{mtg}}} \right)^2 \qquad\qquad \text{eq. S29}$$

This equation enables again the extraction of the equilibrium constant K and the additional energy transfer rate $k_{\Delta ET}$. However, the shrinking gate approach is more reliable, because the approach in this section suffers from poor signal-to-noise ratios for later microtime gates as we will show later. Additionally, $A_{dyn,gated}(t_{mtg})$ takes longer to saturate, which limits the applicability of this approach to later microtime gates due to the exponential fluorescence intensity decay. However, it has the advantage that it can be used to isolate the photophysics component with an early microtime gate. We also want to stress that t_{mtg} in $A_{dyn,gated}(t_{mtg})$ denotes the microtime gate and, in equation S5, t_g denotes the threshold of the microtime long pass gate. As depicted in Figure S12a, $A_{dyn,gated}(t_{mtg})$ starts at zero for $t_{mtg} = 0\ ns$ and rises slowly. Due to the flat beginning of the function, a microtime gate with $200 - 400\ ps$ width can be chosen to isolate the photophysics component with a sufficient signal-to-noise ratio.
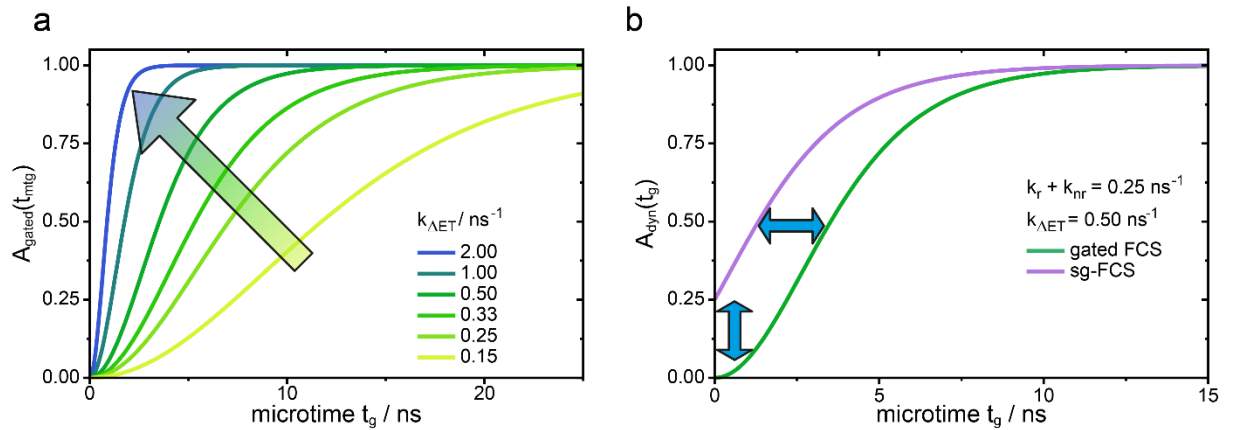

Figure S12: How the bunching amplitude changes with microtime in gated-FCS. a) The dependence of $A_{dyn,gated}(t_{mtg})$ as a function of the microtime for different $k_{\Delta ET}$ values with an infinitesimal micro time gate size. Larger $k_{\Delta ET}$ rate constants lead to faster saturation due to a faster rise of the intensity contrast between two intensity levels. The initial bunching amplitude, $A_{dyn,gated}(t_{mtg} = 0\ ns)$, always starts at zero. b) Comparison of sg-FCS (purple) and gated-FCS (green) for equal rate constants. The sg-FCS amplitude $A_{dyn}(t_g)$ begins with a head start because it considers all photons within the TAC range. The gated-FCS amplitude $A_{dyn,gated}(t_{mtg})$ begins at zero. The sg-FCS function is the gated-FCS function but shifted on the t_g-axis. Therefore, the sg-FCS function has a head start and saturates earlier.

To demonstrate the isolation of the photophysics component from the dynamic component, we simulated a dynamic system that undergoes on-off switching independently of the dynamics as depicted in figure S13. We denote the bright fluorescence state as A and the quenched state as B. The rate constant, k_A, denotes the transition from state B to state A and k_B denotes the transition from state A to state B. The non-fluorescence or dark-state is denoted as D. The rate constant k_{off} denotes the transition into the dark-state and the rate k_{on} denotes the transition into the a fluorescence state.
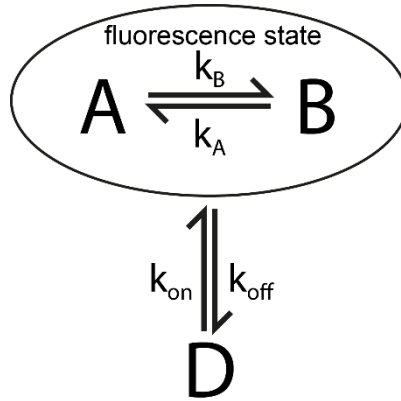
Figure S13: A sketch of the applied model to isolate dynamics between states with a different fluorescence lifetime from an on-off switching. For simplicity, we simulate a system that switches independently of the on- or off-state (D) between a bright (A) and quenched (B) fluorescence state. However, as long as the on- off times are significantly longer than the fluorescence lifetime of the fluorophores, this will impact the ability of sg-FCS to separate photophysical and dynamic processes.

First, we demonstrate the isolation of the dynamic component using a system that shows slow on-off kinetics and fast dynamic kinetics. For the simulation, we use the same intensity and lifetime parameters as described in Section 1. The photophysics transition rate constants are $k_{on} = k_{off} = 400\ s^{-1}$ and the dynamic transition rate constants of $k_A = 40{,}000\ s^{-1}$ and $k_A = 80{,}000\ s^{-1}$. A short portion of a simulated fluorescence intensity trajectory is shown in Figure S14a. The intensity correlation $g^{(2)}(\Delta\tau)$, considering all photons independent of the detection time after pulsed laser excitations, shows a biexponential decay of the correlation amplitude (see Figure S14b). To isolate the photophysics component, which causes the on-off blinking, we use a small microtime gate by only considering photons detected at maximum $400\ ps$ after the pulsed laser excitation, because both fluorescence intensity states A and B are still equally bright in this microtime regime. As expected, the blue intensity correlation in Figure S14c shows only a single bunching amplitude due to the on-off switching, and the dynamic component at shorter time scales is missing. The bunching amplitude also shows the expected amplitude of $A_{dyn,gated}(t_{mtg} = 0.0 - 0.4\ ns) = K_{pp} = 1$. To extract the equilibrium constant from sg-FCS without the photophysics component, we calculate the ratio of the sg-FCS correlation and the gated correlation in Figure S14c. The result is shown in Figure S14d. The photophysics bunching amplitude cancels out and we isolate the fast dynamic component to extract the equilibrium constant $A_{dyn,sg-FCS}(t_g = 8\ ns) = K_{dyn} = 2$.
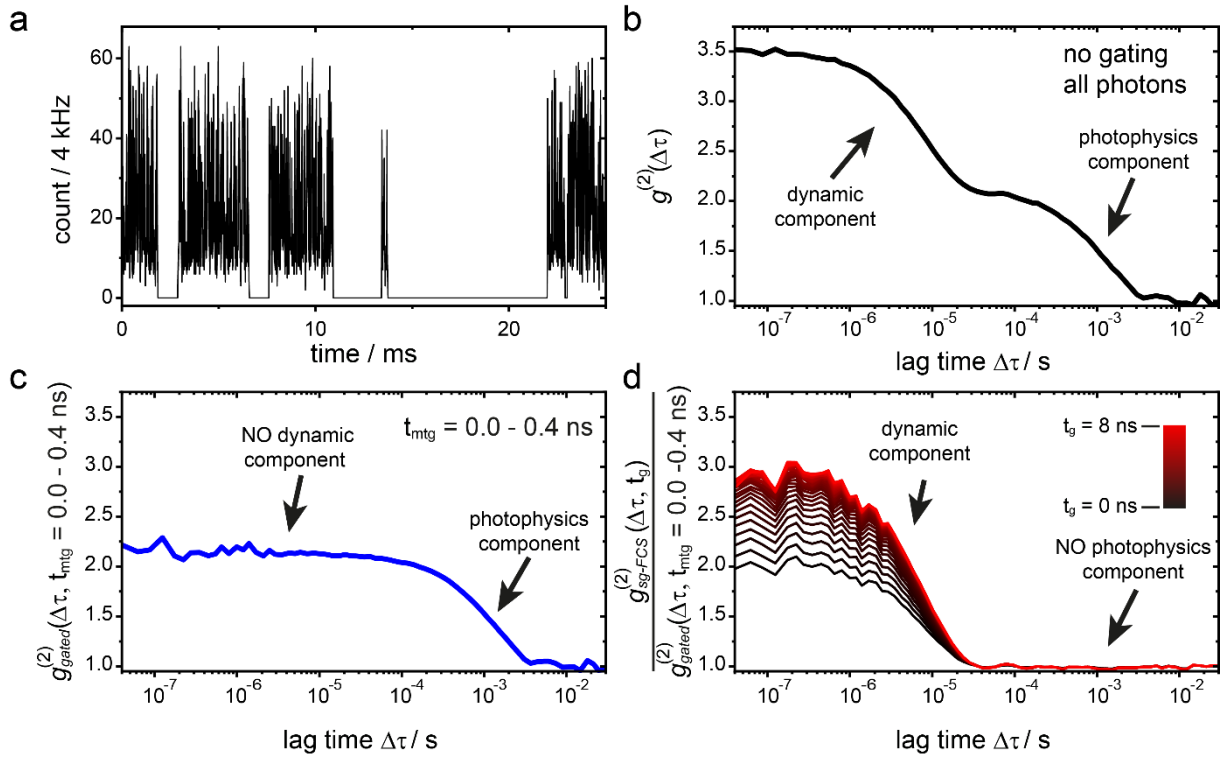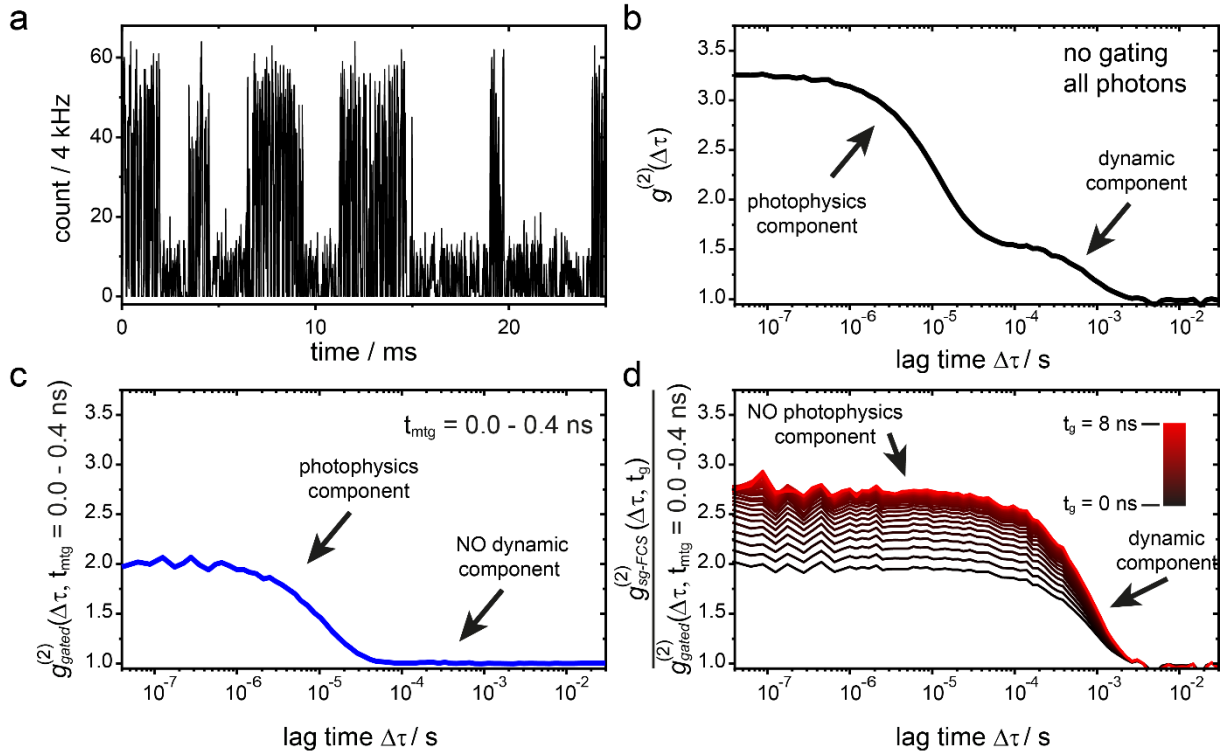
Figure S14: Isolating dynamic and photophysics components by microtime gating. a) A short section of a simulated fluorescence trajectory with fast dynamics and slow photophysics. b) The intensity correlation considering all photons shows two kinetic components. c) The gated correlation, considering only the first $400\,ps$ after pulsed laser excitation, isolates the photophysics component. d) The ratio of sg-FCS and gated-FCS isolates the dynamic component.

To demonstrate that this approach also works when the kinetics rates are reversed, we simulate a fluorescence intensity trajectory which shows fast photophysics (on-off switching) and slow dynamics. For the photophysics rate constants, we use $k_{on} = k_{off} = 40,000\ s^{-1}$ and for the dynamic transition rate constants; $k_A = 400\ s^{-1}$ and $k_A = 800\ s^{-1}$. A short section of the intensity trajectory is given in Figure S15a. The intensity correlation considering all photons, given in Figure S15b, shows again a biexponential decay. Again, the gated-FCS correlation

Figure S15: Isolating dynamic and photophysics components by microtime gating. II. a) A short section of a simulated fluorescence intensity trajectory with fast photophysics and slow dynamics. b) The intensity correlation function considering all photons shows two kinetic components. c) The gated correlation function, considering only the first $400\ ps$ after pulsed laser excitation, isolates the photophysics component. d) The ratio of sg-FCS and gated-FCS isolates the dynamic component.

function considering only the first $400\ ps$ of detected photons after pulsed excitation isolates the photophysics component (see Figure S15c). The bunching amplitude shows the expected amplitude of $A_{dyn,gated}(t_{mtg} = 0.0 - 0.4\ ns) = K_{pp} = 1$. Finally, we isolate the dynamic component by calculation the ratio of sg-FCS and gated-FCS in Figure S15d. The bunching amplitude saturates at the expected value of the bunching amplitude $A_{dyn,sg-FCS}(t_g = 8\ ns) = K_{dyn} = 2$.

At last we demonstrate the case with similar dynamics and photophysics kinetics. As transition rate constants, we use $k_{on} = k_{off} = k_A = 4,000\ s^{-1}$ and $k_B = 8,000 s^{-1}$. A short section of the simulated fluorescence trajectory is given in Figure S16a. The intensity correlation yields a monoexponential decay with underlying dynamic and photophysics components (see Figure S16b). By only applying the sg-FCS approach, the extracted equilibrium constant will be poisoned by the undetected photophysics component. We found two ways to detect underlying photophysics components. The first approach is demonstrated in this section by applying the gated-FCS approach, which simply isolates the photophysics component reliably as shown in Figure S16c and yields the expected bunching amplitude from the simulations, $A_{dyn,gated}(t_{mtg} = 0.0 - 0.4\ ns) = K_{pp} = 1$. The second approach uses equation S11 as fitting function. It considers the laser pulse arrival time, t_0, which should be known from the experimental setup. If the expected t_0 shifts significantly from what is expected, this suggests

26

172

that underlying photophysics is present. Although the second approach gives you a hint for the presence of underlying photophysicsal processes, gated-FCS still needs to be applied for isolation of the dynamic component as shown in Figure S16d. The ratio of sg-FCS and gated-FCS also yields the expected equilibrium constant of the dynamic process $A_{dyn,sg-FCS}(t_g = 8\,ns) = K_{dyn} = 2$.
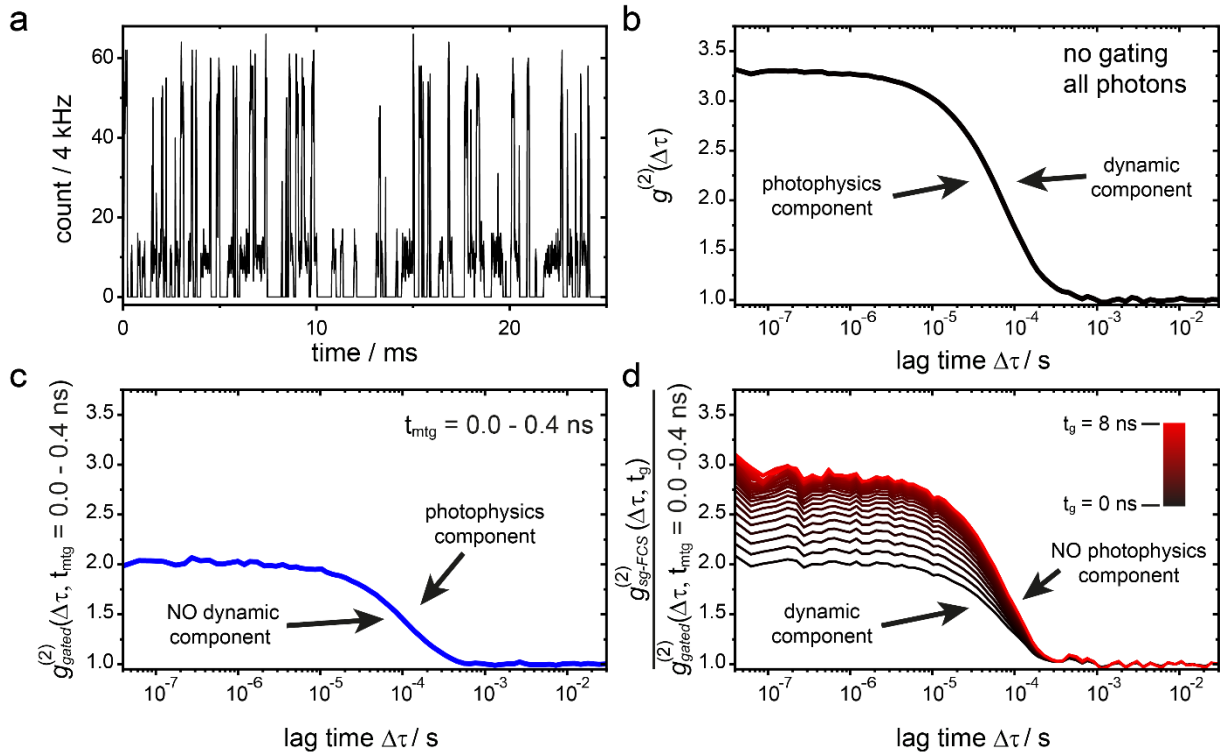

Figure S16: Isolating dynamic and photophysics components by microtime gating. III. a) A short section of a simulated fluorescence trajectory with similar photophysics and dynamics kinetics. b) The intensity correlation function considering all photons shows a single kinetic component. c) The gated correlation function, considering only the first $400\,ps$ after pulsed laser excitation, isolates the photophysics component. d) The ratio of sg-FCS and gated-FCS isolates the dynamic component.

In the main manuscript we only address the sg-FCS approach because it is more photon efficient. The signal-to-noise ratio in a fluorescence intensity correlation function scales linear with the fluorescence intensity. A sg-FCS microtime gate from e.g. $1\,ns$ to $20\,ns$ provides therefore more photons than a gated-FCS microtime gate from $1\,ns$ to $1.5\,ns$. This limits the range of equilibrium constants that can be reliably extracted using gated-FCS. As an example, we analyze the donor trajectory shown in Figure 3b (and Figure S6). The sg-FCS analysis is plotted in Figure S17a,b. We used a $0.5\,ns$ microtime gate. The gated fluorescence intensity correlation functions in Figure S17c show a high noise level. The extracted amplitudes in Figure S17d yield an equilibrium constant of $K_{gated} = 0.011 \pm 0.001$, which is close to the value of the sg-FCS $K_{sg-FCS} = 0.012 \pm 0.0001$. However, due to the poor signal-to-noise level, it is hard to assign the bunching to the dynamic component because the intensity correlation amplitude has a lower limit (0) but no upper limit. Additionally, the gated-FCS fit saturates

before the sg-FCS fit, which is unreasonable according to Figure S12b and suggests a huge noise contribution in the rise. Sg-FCS provides the better signal-to-noise ratio by a more efficient use of the photon arrival time information.
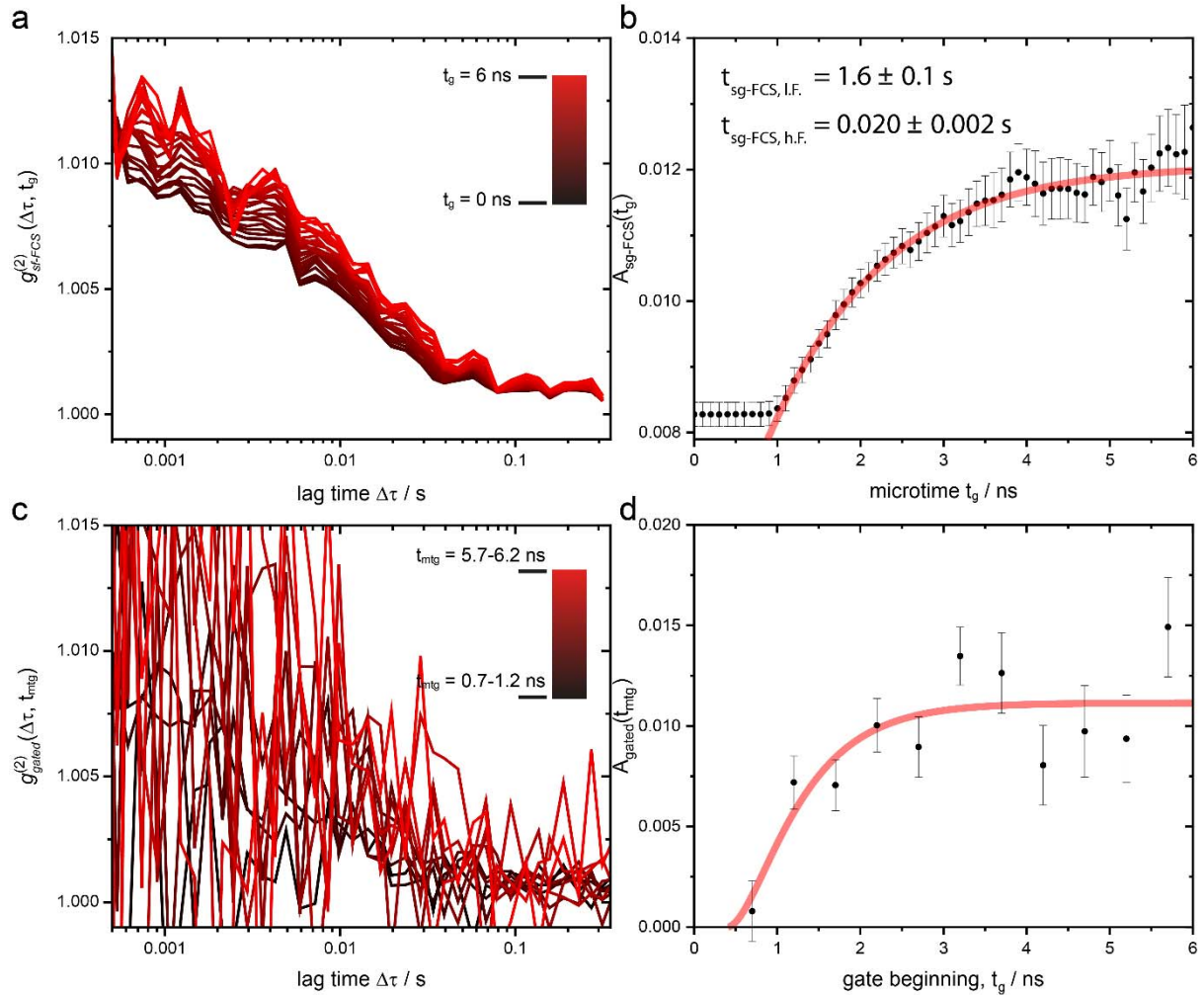

Figure S17: Comparison of sg-FCS and gated-FCS for small equilibrium constants. a) Sg-FCS of the donor trajectory from the DNA origami system shown in Figure 3. The $g_{cor.}^{(2)}(\Delta\tau, t_g)$ is plotted as a function of microtime gate with the color gradient going from black (full gate) to red (late microtime gate). b) The extracted and background corrected bunching amplitudes $A_{dyn,sg-FCS}(t_g)$ (black) and corresponding fit (red line). c) Gated-FCS of the same donor trajectory. The $g_{cor.}^{(2)}(\Delta\tau, t_g)$ is plotted as a function of microtime gate with the color gradient going from black $(0.7 - 1.2\ ns)$ to red $(5.7 - 6.2\ ns)$. d) The extracted and background corrected bunching amplitudes $A_{dyn,gated}(t_g)$ (black) and corresponding fit (red line).

10. PIE excitation for a membrane-surface charge sensor

To make sure that the observed FRET-dynamics for the voltage sensor do not have their origin in photoblinking or a spectral shift of the acceptor dye, we studied the construct also under PIE excitation.[4] The data presented in the main manuscript were acquired using $532\ nm$ excitation only to reduce photo-damage. The presented intensity trajectory in Figure S18a was excited with a $25\ MHz$ repetition rate and the $532\ nm$ and $640\ nm$ excitation pulses were delayed by $20\ ns$ with respect to each other. The ATTO647N dye shows a spectral shift with a low emission in the red detection channel at ~27 s before it photobleaches. The D/ D trajectory (the first D denotes the excitation pulse; the second D denotes the detection channel) is no longer subject to energy transfer. The region of the time trace used for the intensity correlation analysis in Figure S18b is shaded in grey. Only the correlation of the D/D signal (blue) shows a bunching amplitude. Neither the A/A correlation function (red) nor the cross-correlation of D/D to A/A signal shows any photon bunching on the same time scale. Therefore, we account all intensity fluctuations in the D/D channel to a change in distance between the donor and acceptor dyes. In Figure S18c, the sg-FCS reveals that the bunching amplitude is not of photophysical nature but rather a dynamic process with correlated fluorescence intensity and lifetime changes. However, the late microtime gate thresholds result in a noisy correlation, which comes from the low D/D signal. Hence, we did not analyze the sg-FCS results quantitatively. The data in the main text were recorded with $532\ nm$ excitation only, which enables higher laser excitation powers due to less phototoxicity that originates from triplet or radical states excitation in PIE experiments.
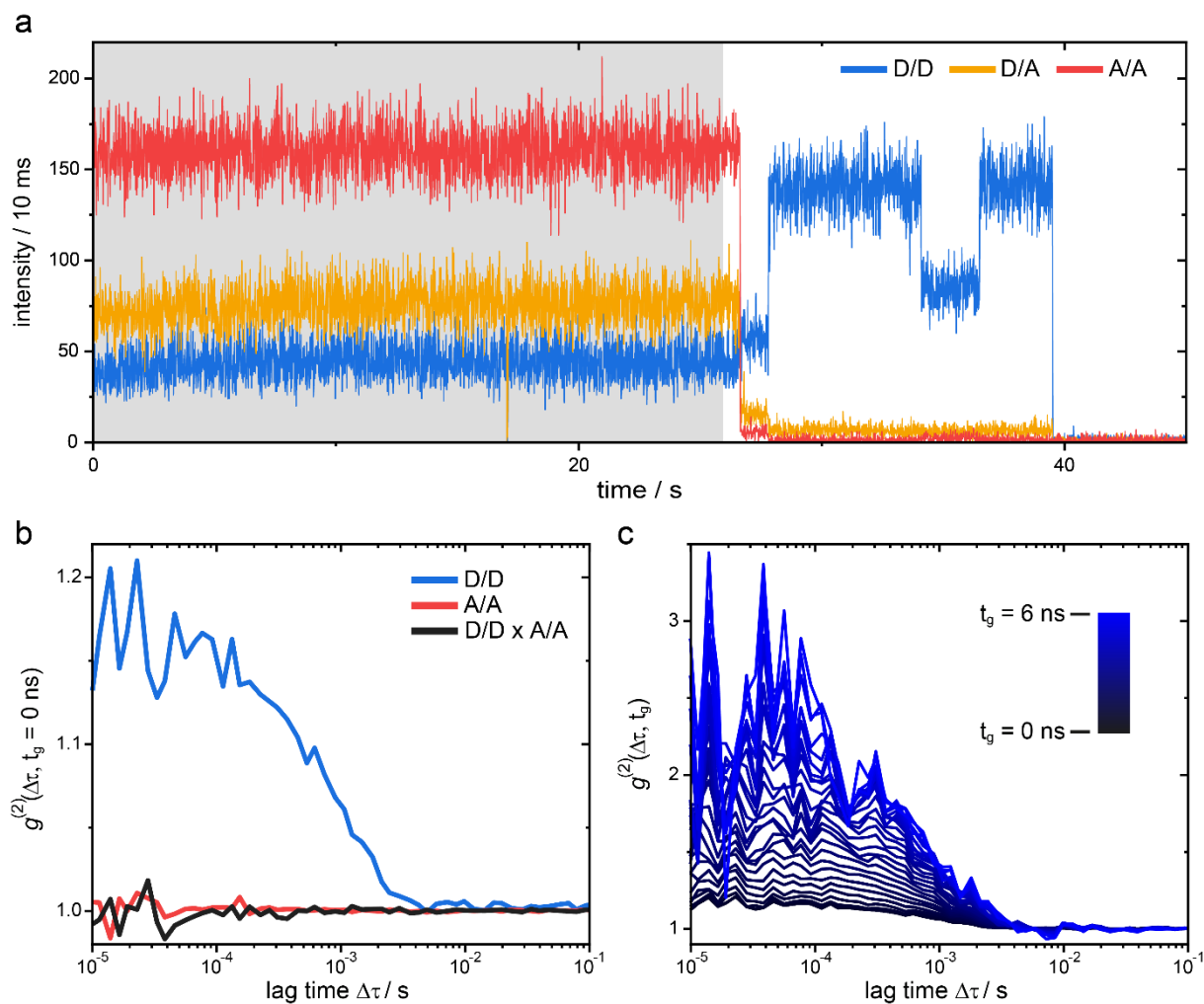
Figures S18: Fluorescence intensity trajectory of a 0% DOPG/100% DOPC sample under PIE excitation. a) A fluorescence intensity trajectory of the donor under donor excitation (D/D, blue), the FRET-signal of the acceptor emission under donor excitation (D/A, orange) and the acceptor signal under acceptor excitation (A/A, red). The signal used for the intensity correlation is shaded in gray. b) An intensity auto-correlation function of the D/D (blue) and A/A (red) signal. The cross-correlation function of the two signals (D/D x A/A) is depicted in black. c) A sg-FCS analysis of the donor signal from b).

11. Supplementary Materials and Methods
Confocal setup

All experiments are performed on a home-built confocal microscope based on an Olympus IX-71 inverted microscope. DNA-origami structures are excited by pulsed lasers (636 nm, LDH-D-C-640; 532 nm, LDH-P- FA-530B; both PicoQuant GmbH). The lasers are coupled into a single mode fiber (P3-488PM-FC, Thorlabs GmbH) to obtain a Gaussian beam profile and to perfectly overlay the two excitation beams. Circular polarized light is obtained by a linear polarizer (LPVISE100-A, Thorlabs GmbH) and a quarter-wave plate (AQWP05M- 600, Thorlabs GmbH). The light is focused onto the sample using an oil-immersion objective (UPLSAPO100XO, NA 1.40, Olympus Deutschland GmbH). The position of the sample is adjusted using a piezo stage (P-517.3CD, Physik Instrumente (PI) GmbH & Co. KG) and controller (E-727.3CDA, Physik Instrumente (PI) GmbH & Co. KG). The emission light is separated from the excitation beam by a dichroic beamsplitter (zt532/640rpc, Chroma) and focused onto a 50 μm diameter pinhole (Thorlabs GmbH). After the pinhole, the donor and acceptor signals are separated by a dichroic beamsplitter (640 LPXR, Chroma) into a green (Brightline HC582/75, AHF; RazorEdge LP 532, Semrock) and red (SP 750, AHF; RazorEdge LP 647, Semrock) detection channel. Emission is focused onto avalanche photodiodes (SPCM-AQRH-14-TR, Excelitas) and the signals are registered by a time-correlated single photon counting (TCSPC) unit (HydraHarp400, PicoQuant). The setup is controlled by a commercial software package (SymPhoTime64, Picoquant GmbH).

Surface experiments were performed using pulsed 532 nm excitation at a repetition rate of 50 MHz. The excitation power on a diffraction limited spot is chosen to be 0.5 kW/cm^2 for all samples that contained a 7 nt binding site. Otherwise, the excitation power was 1.5 kW/cm^2.

For PIE-FRET experiments, both lasers were operated at a 20 MHz repetition rate. The laser pulses are altered on the nanosecond timescale by a multichannel picosecond diode laser driver (PDL 828 "Sepia II", PicoQuant GmbH) with an oscillator module (SOM 828, PicoQuant GmbH). The excitation powers in the diffraction limited spots were chosen to be 6.3 kW/cm^2 for both lasers. Solution-based burst analysis experiments were analyzed using the PAM software package.[6]

DNA origami structure synthesis

For DNA origami structure preparation, we follow the protocol described in Kaminska, Bohlen, at al.[7] and S. Ochmann et al..[8] The L-shaped DNA origami structures were immobilized on a LabTek^{TM} chamber slide (Thermo Fisher Scientific Inc.) coated with BSA-biotin/NeutrAvidin (Merck KGaA).

Data acquisition and analysis: 10 μm × 10 μm scans were used to pick the DNA origami structures. To minimize photoblinking and photobleaching, a reducing and oxidizing buffer system (ROXS) (1×TAE, 12.5 mM MgCl2, 2 mM Trolox (UV radiated until ~13 % of the Trolox was oxidized to Troloxquinone, 1 % (w/v) D-(+)-glucose) was used in combination with an enzymatic oxygen scavenger system (250 U/mL glucose oxidase and 2000 U/mL catalase).

All chemicals were purchased from Merck KGaA. Solution experiments were carried out under the same buffer conditions.

Rectangular DNA origami structures for the lipid surface-charge experiments were immobilized on a PEG-Biotin coated surface by NeutrAvidin. A detailed explanation of the protocol and LUV synthesis can be found in S. Ochmann et al..[8]

12. References

 1.   Laurence, T. A.; Fore, S.; Huser, T. Fast, Flexible Algorithm for Calculating Photon Correlations. *Opt. Lett.* **2006**, *31*, 829–831.
 2.   Ingargiola, A. Pycorrelate 0.3. https://github.com/tritemio/pycorrelate (accessed November 16, 2017).
 3.   Weiss, R.; Du, S.; Grobler, J.; Lebedev, S. hmmlearn. https://github.com/hmmlearn (accessed 03 Febuary 2021).
 4.   Müller, B. K.; Zaychikov, E.; Bräuchle, C.; Lamb, D. C. Pulsed interleaved excitation. *Biophys. J.* **2005**, *89*, 3508–3522.
 5.   Hellenkamp, B.; Schmid, S.; Doroshenko, O.; Opanasyuk, O.; Kühnemuth, R.; Rezaei Adariani, S.; Ambrose, B.; Aznauryan, M.; Barth, A.; Birkedal, V.; Bowen, M. E.; Chen, H.; Cordes, T.; Eilert, T.; Fijen, C.; Gebhardt, C.; Götz, M.; Gouridis, G.; Gratton, E.; Ha, T. *et al.* Precision and accuracy of single-molecule FRET measurements-a multi-laboratory benchmark study. *Nat. Methods* **2018**, *15*, 669–676.
 6.   Schrimpf, W.; Barth, A.; Hendrix, J.; Lamb, D. C. PAM: A Framework for Integrated Analysis of Imaging, Single-Molecule, and Ensemble Fluorescence Data. *Biophysical journal* **2018**, *114*, 1518–1528.
 7.   Kamińska, I.; Bohlen, J.; Yaadav, R.; Schüler, P.; Raab, M.; Schröder, T.; Zähringer, J.; Zielonka, K.; Krause, S.; Tinnefeld, P. Graphene Energy Transfer for Single-Molecule Biophysics, Biosensing, and Super-Resolution Microscopy. *Adv. Mater.* **2021**, *33*, e2101099.
 8.   Ochmann, S. E.; Schröder, T.; Schulz, C. M.; Tinnefeld, P. Quantitative Single-Molecule Measurements of Membrane Charges with DNA Origami Sensors. *Anal. Chem.* **2022**, *94*, 2633–2640.

5 Conclusion and Outlook

The key theme in this thesis is the model free connection of the intensity correlation and the fluorescence lifetime. Intensity correlation is a powerful tool to monitor intensity fluctuations on various timescales. In solution experiments FCS is frequently used in the life-science community with fluorescent probes to extract information on concentrations, diffusion and molecular interactions. However, in case of intensity fluctuations that originate from switches between two fluorescent intensity states, the intensity information is not sufficient to extract quantitative transition rate constants without prior knowledge of the equilibrium constant. Beside the change in quantum efficiency of the system, which results in a quenched intensity signal, a correlated change in excited state lifetime can be measured by TCSPC data acquisition. The fluorescence lifetime information was utilized in FLCS analysis to weight the photons according to their arrival time after pulsed laser excitation with predefined species-filters. However, a major drawback of FLCS is the required prior knowledge of the excited state lifetime of each intensity species. In addition, these filters are mostly imperfect and hence provide distorted equilibrium constants.[45] Additionally, FLCS cannot isolate the dynamic component in the intensity correlation, when it is superimposed with a photophysical component, which does not alter the fluorescence lifetime.

Therefore, a model free approach to connect the fluorescence intensity and fluorescence lifetime data is demonstrated in this thesis. An algorithm was developed to study the microtime dependent intensity correlation which was referred to as sg-FCS. Thereby, the high intensity and long fluorescence lifetime state was isolated and the extraction of the equilibrium constant of a two intensity level system was demonstrated in simulation and experiment without prior knowledge. The model structure for experimental demonstration was based on DNA origami which enables stoichiometric and positional control of dye modifications. It provided fluorescence trajectories with stochastic switches between a high and low FRET state by a protruding ssDNA strand which was labeled with a Cy3B-dye as the donor. Adjacent to one of two binding sites, an acceptor dye was placed and the binding time of the donor oligonucleotide was adjustable by the number of complementary nucleotides. The extracted binding times of the sg-FCS analysis were confirmed by a Hidden Markov Model analysis and the equilibrium constant of fluctuating intensity trajectories was recovered over a range of two and a half orders of magnitude by sg-FCS. It was demonstrated, that sg-FCS is suitable for surface immobilized model-structures and diffusing model-structures. Additionally, sg-FCS was applied to intensity trajectories with continuously distributed intensity and fluorescence lifetime states of a dye labeled tether on graphene. The fluorescence trajectory was also subject to photophysics but the Brownian dynamic component was identified by sg-FCS. Finally, sg-FCS was able to unravel the working mechanism of a FRET-based membrane charge sensor.

Beyond analyzing the photon bunching on long timescales, the degree of photon antibunching on short timescales is a metric to count the number of emitting units in a mcNP. As yet, the significance of the degree of photon antibunching was compromised by SSA and SDA. Especially the effect of photon bunching on the degree of photon antibunching was not discussed in the literature so far. Hence, it was demonstrated in simulation and experiment, that collective blinking chromophores require a normalization with respect to the bunching amplitude, and in case of photon bunching due to independent blinking chromophores, the degree of photon antibunching is given by zero lag time in the intensity correlation ($g^{(2)}(0)$).

Additionally, universal guidelines were provided, to choose the correct normalization in case of an unknown origin of the photon bunching by either vary the bunching amplitude by excitation power, or by microtime gating by using the sg-FCS algorithm. A linear scaling of $g^{(2)}(0)$ with the bunching amplitude points at collective blinking chromophores. Further, the application of sg-FCS did not only recover the blink kinetics but also the SDA rate constant.

In a next step, the fingerprint of SSA was unraveled by microtime gating in an algorithm introduces as psTRAB. As SDA and FRET, SSA changes an exciton's lifetime. By raising the question if a second exciton was present at the time, when the first photon was emitted, psTRAB does not only recover the number of chromophores by correlating early microtime gates, but also monitors the SSA speed in a mcNP at later microtime gates, since SSA is a time dependent process. This was demonstrated by simulation and experiment on DNA origami-based model structures with up to five organic dyes and two different ordered conjugated polymer aggregates. Thereby, psTRAB recovered the number of organic dyes in the DNA origami model structures and the average speed of SSA which was also subject to exciton hopping on systems with more than two dyes. By applying psTRAB to well-ordered H-aggregates trajectories, the SSA was much faster compared to the unordered J-aggregates. Due to the delocalization of the exciton between the single polymer chains in the H-aggregate, SSA was more efficient. The excitons on the unordered J-aggregates were mainly delocalized along one chain, which resulted in slower and therefore less efficient SSA.

At last, the dye-dye interaction in a rigid DNA origami model structure was studied to path the way to small point light sources with unprecedented brightness density. The spacial and stoichiometric control of dye modifications on a DNA origami structure make them a promising alternative to dye loaded polymer beads which are used as labels in the life-sciences. However, the polymer beads suffer from inhomogeneous brightness distributions and a lack of control over the dye-aggregation. In order to systematically study the distance dependent dye-dye interactions in a DNA origami structure, the interdye- distance was altered on the single base-pair level and three regimes of interactions were identified. In close distances the dyes were subject to dynamic and static quenching whereas at larger distances the quenching was intermitted by temporal formation of a separating dsDNA duplex which was not thermally stable up to a separation distance of six nucleotides. At seven base pairs distance, the dyes were physically separated but not independent and SSA and SDA was observed. The SDA resulted in collective blinking of the dyes but lead to a faster recovery from dark states due to higher states transitions. However, the physical separation of the dyes was key to maintain their fluorescence properties. Therefore, a DNA origami structure could be loaded with up to 1000 organic dyes to serve as super bright point light source.
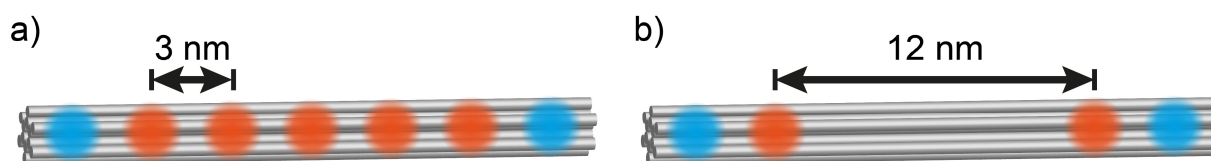

Figure 5.1: a) Model system to exciton diffusion in DNA origami structures. The donor chromophore (blue) transfers the excitons only to the left-most and right-most acceptor dye (orange). Consequently, only exciton diffusion can lead to SSA. b) The negative control structure with no chromophores in the center will inhibit SSA.

Over all the microtime dependent intensity correlation was studied in this thesis to extract quantitative information, like number of chromophores, annihilation speed and switching rate constants, from fluorescence systems which could not be obtained before by conventional intensity correlation. For future works, the SSA speed in mcNP holds information about the exciton diffusion which enables long range exciton annihilations. In order to understand exciton diffusion dependent annihilation processes in mcNP, future DNA origami model structures can be used to model exciton diffusion in mcNP in greater detail. In this work the creation point of the excitons were not defined in multichromophoric DNA origami structure but rather random. Exciton diffusion dependent SSA can be best investigated in more defined systems, by using always the same starting point of the exciton at a designed position. This can be achieved with a donor chromophore which inject the exciton to a designed acceptor position in the chromophore array using FRET. The idea is depicted in figure 5.1a where the central chromophores are no longer directly excited but the excitons will always start at the far left or far right position due to the donor chromophore position. In order to undergo SSA the excitons need to diffuse along the one-dimensional (1D) array of chromophores. The negative control is depicted in figure 5.1b. In contrast to the direct excitation of the chromophore array, SSA is expected to start with a delay as exciton diffusion first needs to occur multiple times underline the long range interaction of SSA.
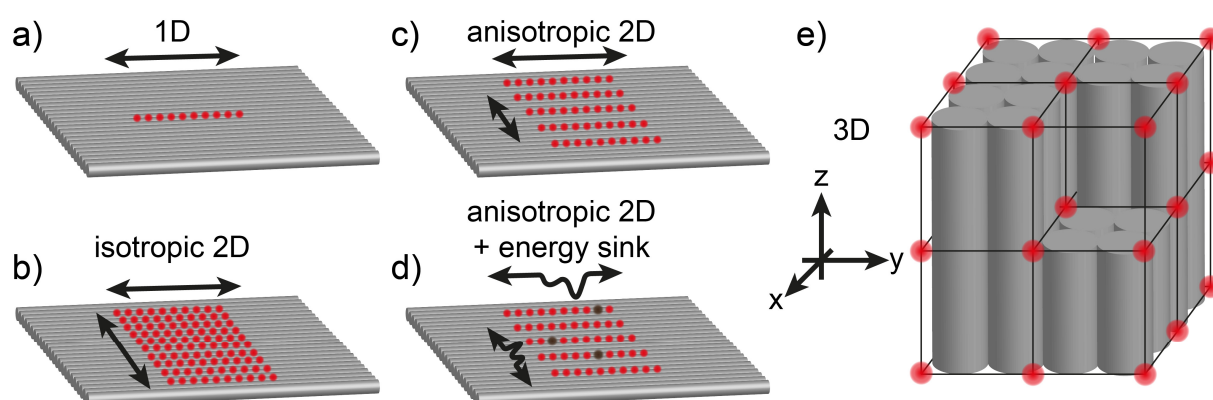

Figure 5.2: Sketches of a) 1D, b) 2D and e) 3D chromophore arrays in DNA origami structures to study the effect of diffusion dimensionality on SSA. c) Sketch of a structure to model anisotropic 2D exciton diffusion. d) Sketch of a structure to model the anisotropic exciton diffusion with energy sinks (black circles).

So far only 1D chromophore arrays with up to five chromophores on DNA origami structures have been studied but multi-dimensional exciton diffusion is expected in mcNPs. The dimensionality of exciton diffusion is expected to affect the SSA rate and can be robustly modeled as well with DNA origami structures. The simplest arrangement to demonstrate the impact of dimensionality on SSA is the comparison of a sample with three dyes in a row to a sample with three dyes in a triangular arrangement. The one dimensional (1D) arrangement yielded two SSA rate constants[139] whereas the triangle arrangement is expected to show only a single annihilation rate constant, because the excitons' distance will always stay. In this arrangement the SSA rate constant will be independent of the exciton diffusion.

More advanced DNA origami model structure to study the effect of dimensionality on SSA are depicted in figure 5.2. Similar to the system used in chapter 4.2, the excitons could be placed as well at defined positions with a FRET donor chromophore as depicted in figure 5.1. Two-dimensional (2D) exciton diffusion of well-ordered conjugated polymer aggregates can be

modeled by uniform chromophore distance for lines and columns (see figure 5.2b) resulting in isotropic exciton diffusion. Furthermore, disordered conjugated polymer aggregates could also be modeled with DNA origami structures using different chromophore distances for lines and columns (see figure 5.2c). This arrangement favors 1D exciton diffusion along one line over 2D diffusion between two lines, resulting in anisotropic exciton diffusion. Thus, SSA will be slowed down between neighboring chromophore lines while SSA within the line remains efficient. Additionally, the chromophore in CP are not expected to be as identical as organic dyes on DNA. Therefore, energy sinks can trap excitons. These energy sinks are expected to be a major reason for the high degree of photon antibunching in P3HT chains.[61] The number of energy sinks varies from aggregate to aggregate which broadens the distribution of the degree of single photon emission. This broadening due to the chromophore heterogeneity can also be modeled with DNA origami structures by introducing slightly red shifted chromophores like Cy5B into a ATTO 647N model structure as depicted in figure 5.2d. The statistic heterogeneity can be created by a competition for incorporation into the DNA origami structure between both dyes for a single labeling position. In the folding buffer, the ratio of both dye-labeled oligonucleotides can be varied to change the labeling probability of the position with a specific dye. The result will be a mixture of structures with different numbers of quenching moieties which should reflect the chromophore heterogeneity in CP. By comparing the distributions, the number of energy sinks in CP can be estimated. At last also three-dimensional (3D) exciton diffusion can be modeled as shown in figure 5.2e.

Building on the enormous fundament of previous work about intensity correlation, the study of microtime dependent correlation amplitudes yields previously inaccessible vital information in single molecule as well as in single particle or aggregate experiments without prior knowledge. As TCSPC data become more available, ideas from this work can spread into many laboratories and can be applied without additional effort. Data analysis with sg-FCS will make intensity correlation more reliable, as it directly shows whether a bunching amplitude is related to photophysical on-off switches, like triplet blinking, or whether the intensity fluctuations correlate with changes in the fluorescence lifetime e.g. due to molecular dynamics in a FRET experiment with an acceptor dye or a quenching surface like graphene. Additionally, excited state processes in mcNP, like SSA and SDA, can now be easily monitored with psTRAB and sg-FCS. Hence, fluorescent materials such as organic semiconductors, transition-metal dichalcogenides or quantum dots can be studied in more detail enabling more efficient materials for light harvesting and light generation for a bright future.

6 References

1.   Hope-Simpson, R. E. Sunspots and flu: A correlation. *Nature* **1978**, *275*, 86.

2.   Hoyle, F.; Wickramasinghe, N. C. Sunspots and influenza. *Nature* **1990**, *343*, 304.

3.   Towers, S. Sunspot activity and influenza pandemics: A statistical assessment of the purported association. *Epidemiol. Infect.* **2017**, *145*, 2640–2655.

4.   Riedel, C.; Gabizon, R.; Wilson, C. A. M.; Hamadani, K.; Tsekouras, K.; Marqusee, S.; Pressé, S.; Bustamante, C. The heat released during catalytic turnover enhances the diffusion of an enzyme. *Nature* **2015**, *517*, 227–230.

5.   Magde, D.; Elson, E.; Webb, W. W. Thermodynamic Fluctuations in a Reacting System—Measurement by Fluorescence Correlation Spectroscopy. *Phys. Rev. Lett.* **1972**, *29*, 705–708.

6.   Magde, D.; Elson, E. L.; Webb, W. W. Fluorescence correlation spectroscopy. II. An experimental realization. *Biopolymers* **1974**, *13*, 29–61.

7.   Koppel, D. E.; Axelrod, D.; Schlessinger, J.; Elson, E. L.; Webb, W. W. Dynamics of fluorescence marker concentration as a probe of mobility. *Biophys. J.* **1976**, *16*, 1315–1329.

8.   Rigler, R.; Mets; Widengren, J.; Kask, P. Fluorescence correlation spectroscopy with high count rate and low background: Analysis of translational diffusion. *Eur Biophys J* **1993**, *22*, 169–175.

9.   Müller, C. B.; Loman, A.; Pacheco, V.; Koberling, F.; Willbold, D.; Richtering, W.; Enderlein, J. Precise measurement of diffusion by multi-color dual-focus fluorescence correlation spectroscopy. *Europhys. Lett.* **2008**, *83*, 46001.

10.   Chen, Z.; Shaw, A.; Wilson, H.; Woringer, M.; Darzacq, X.; Marqusee, S.; Wang, Q.; Bustamante, C. Single-molecule diffusometry reveals no catalysis-induced diffusion enhancement of alkaline phosphatase as proposed by FCS experiments. *Proc. Natl. Acad. Sci. U.S.A.* **2020**, *117*, 21328–21335.

11.   Gebhardt, C.; Lehmann, M.; Reif, M. M.; Zacharias, M.; Gemmecker, G.; Cordes, T. Molecular and Spectroscopic Characterization of Green and Red Cyanine Fluorophores from the Alexa Fluor and AF Series. *ChemPhysChem* **2021**, *22*, 1566–1583.

12.   Kapusta, P.; Erdmann, R.; Ortmann, U.; Wahl, M. Time-Resolved Fluorescence Anisotropy Measurements Made Simple. *J. Fluoresc.* **2003**, *13*, 179–183.

13.   Jahnke, K.; Grubmüller, H.; Igaev, M.; Göpfrich, K. Choice of fluorophore affects dynamic DNA nanostructures. *Nucleic Acids Res.* **2021**, *49*, 4186–4195.

14.   Widengren, J.; Mets, U.; Rigler, R. Fluorescence correlation spectroscopy of triplet states in solution: A theoretical and experimental study. *J. Phys. Chem.* **1995**, *99*, 13368–13379.

15.   Widengren, J.; Chmyrov, A.; Eggeling, C.; Löfdahl, P.-A.; Seidel, C. A. M. Strategies to Improve Photostabilities in Ultrasensitive Fluorescence Spectroscopy. *J. Phys. Chem. A* **2007**, *111*, 429–440.

16.   Schwille, P.; Kummer, S.; Heikal, A. A.; Moerner, W. E.; Webb, W. W. Fluorescence correlation spectroscopy reveals fast optical excitation-driven intramolecular dynamics of yellow fluorescent proteins. *Proc. Natl. Acad. Sci. U.S.A.* **2000**, *97*, 151–156.

17.   Haupts, U.; Maiti, S.; Schwille, P.; Webb, W. W. Dynamics of fluorescence fluctuations in green fluorescent protein observed by fluorescence correlation spectroscopy. *Proc Natl Acad Sci USA* **1998**, *95*, 13573–13578.

18.   Widengren, J.; Schwille, P. Characterization of Photoinduced Isomerization and Back-Isomerization of the Cyanine Dye Cy5 by Fluorescence Correlation Spectroscopy. *J. Phys. Chem. A* **2000**, *104*, 6416–6428.

19.   Einstein, A. Über die von der molekularkinetischen Theorie der Wärme geforderte Bewegung von in ruhenden Flüssigkeiten suspendierten Teilchen. *Ann. Phys.* **1905**, *322*, 549–560.

20.   Aragón, S. R.; Pecora, R. Fluorescence correlation spectroscopy and Brownian rotational diffusion. *Biopolymers* **1975**, *14*, 119–137.

21.   Loman, A.; Gregor, I.; Stutz, C.; Mund, M.; Enderlein, J. Measuring rotational diffusion of macromolecules by fluorescence correlation spectroscopy. *Photochem. Photobiol. Sci.* **2010**, *9*, 627–636.

22.   Kinjo, M.; Rigler, R. Ultrasensitive hybridization analysis using fluorescence correlation spectroscopy. *Nucleic Acids Res* **1995**, *23*, 1795–1799.

23.   Schwille, P.; Oehlenschläger, F.; Walter, N. G. Quantitative hybridization kinetics of DNA probes to RNA in solution followed by diffusional fluorescence correlation analysis. *Biochemistry* **1996**, *35*, 10182–10193.

24.   Schüler, J.; Frank, J.; Trier, U.; Schäfer-Korting, M.; Saenger, W. Interaction kinetics of tetramethylrhodamine transferrin with human transferrin receptor studied by fluorescence correlation spectroscopy. *Biochemistry* **1999**, *38*, 8402–8408.

25.   Schwille, P.; Korlach, J.; Webb, W. W. Fluorescence correlation spectroscopy with single-molecule sensitivity on cell and model membranes. *Cytometry* **1999**, *36*, 176–182.

26.   Wachsmuth, M.; Waldeck, W.; Langowski, J. Anomalous diffusion of fluorescent probes inside living cell nuclei investigated by spatially-resolved fluorescence correlation spectroscopy. *J. Mol. Biol.* **2000**, *298*, 677–689.

27.   Widengren, J.; Rigler, R.; Mets, U. Triplet-state monitoring by fluorescence correlation spectroscopy. *J. Fluoresc.* **1994**, *4*, 255–258.

28.   Orrit, M.; Bernard, J. Single pentacene molecules detected by fluorescence excitation in a p-terphenyl crystal. *Phys. Rev. Lett.* **1990**, *65*, 2716–2719.

29.   Michie, M. S.; Götz, R.; Franke, C.; Bowler, M.; Kumari, N.; Magidson, V.; Levitus, M.; Loncarek, J.; Sauer, M.; Schnermann, M. J. Cyanine Conformational Restraint in the Far-Red Range. *J. Am. Chem. Soc.* **2017**, *139*, 12406–12409.

30.   Matikonda, S. S.; Helmerich, D. A.; Meub, M.; Beliu, G.; Kollmannsberger, P.; Greer, A.; Sauer, M.; Schnermann, M. J. Defining the Basis of Cyanine Phototruncation Enables a New Approach to Single-Molecule Localization Microscopy. *ACS Cent. Sci.* **2021,** 7, 1144–1155.

31.   Vogelsang, J.; Kasper, R.; Steinhauer, C.; Person, B.; Heilemann, M.; Sauer, M.; Tinnefeld, P. A Reducing and Oxidizing System Minimizes Photobleaching and Blinking of Fluorescent Dyes. *Angew. Chem.* **2008**, *47*, 5465–5469.

32.   Cordes, T.; Vogelsang, J.; Tinnefeld, P. On the Mechanism of Trolox as Antiblinking and Antibleaching Reagent. *J. Am. Chem. Soc.* **2009**, *131*, 5018–5019.

33.   Vogelsang, J.; Steinhauer, C.; Forthmann, C.; Stein, I. H.; Person-Skegro, B.; Cordes, T.; Tinnefeld, P. Make them blink: probes for super-resolution microscopy. *ChemPhysChem* **2010**, *11*, 2475–2490.

34.   Steinhauer, C.; Forthmann, C.; Vogelsang, J.; Tinnefeld, P. Superresolution Microscopy on the Basis of Engineered Dark States. *J. Am. Chem. Soc.* **2008**, *130*, 16840–16841.

35.   Tsunoyama, T. A.; Watanabe, Y.; Goto, J.; Naito, K.; Kasai, R. S.; Suzuki, K. G. N.; Fujiwara, T. K.; Kusumi, A. Super-long single-molecule tracking reveals dynamic-anchorage-induced integrin function. *Nat. Chem. Biol.* **2018**, *14*, 497–506.

36.   Zumbusch; Fleury; Brown; Bernard; Orrit. Probing Individual Two-Level Systems in a Polymer by Correlation of Single Molecule Fluorescence. *Phys. Rev. Lett.* **1993**, *70*, 3584–3587.

37.   Sahoo, H.; Schwille, P. FRET and FCS-friends or foes? *ChemPhysChem* **2011**, *12*, 532–541.

38.   Torres, T.; Levitus, M. Measuring Conformational Dynamics: A New FCS-FRET Approach. *J. Phys. Chem. B* **2007**, *111*, 7392–7400.

39.   Förster, T. Zwischenmolekulare Energiewanderung und Fluoreszenz. *Ann. Phys.* **1948**, *437*, 55–75.

40.   Barth, A.; Hendrix, J.; Fried, D.; Barak, Y.; Bayer, E. A.; Lamb, D. C. Dynamic interactions of type I cohesin modules fine-tune the structure of the cellulosome of Clostridium thermocellum. *Proc. Natl. Acad. Sci. U.S.A.* **2018**, *115*, E11274-E11283.

41.   Jensen, M. H.; Sukumaran, M.; Johnson, C. M.; Greger, I. H.; Neuweiler, H. Intrinsic Motions in the N-Terminal Domain of an Ionotropic Glutamate Receptor Detected by Fluorescence Correlation Spectroscopy. *J. Mol. Biol.* **2011**, *414*, 96–105.

42.   Lamb, D. C.; Schenk, A.; Röcker, C.; Scalfi-Happ, C.; Nienhaus, G. U. Sensitivity Enhancement in Fluorescence Correlation Spectroscopy of Multiple Species Using Time-Gated Detection. *Biophys. J.* **2000**, *79*, 1129–1138.

43.   Yu, J.; Lammi, R.; Gesquiere, A. J.; Barbara, P. F. Singlet-Triplet and Triplet-Triplet Interactions in Conjugated Polymer Single Molecules. *J. Phys. Chem. B* **2005**, *109*, 10025–10034.

44.   Böhmer, M.; Wahl, M.; Rahn, H.-J.; Erdmann, R.; Enderlein, J. Time-resolved fluorescence correlation spectroscopy. *Chemical Physics Letters* **2002**, *353*, 439–445.

45.   Barth, A. Single-Molecule Fluorescence Spectroscopy: From Two to Three Colors and Beyond. Dissertation, LMU, München, 2018.

46.   Wientjes, E.; Renger, J.; Curto, A. G.; Cogdell, R.; van Hulst, N. F. Strong Antenna-Enhanced Fluorescence of a Single Light-Harvesting Complex Shows Photon Antibunching. *Nat. Commun.* **2014**, *5*, 4236.

47.   Bopp, M. A.; Sytnik, A.; Howard, T. D.; Cogdell, R. J.; Hochstrasser, R. M. The Dynamics of Structural Deformations of Immobilized Single Light-Harvesting Complexes. *Proc. Natl. Acad. Sci. U.S.A.* **1999**, *96*, 11271–11276.

48.   Gwizdala, M.; Berera, R.; Kirilovsky, D.; van Grondelle, R.; Krüger, T. P. J. Controlling Light Harvesting with Light. *J. Am. Chem. Soc.* **2016**, *138*, 11616–11622.

49.   Reisch, A.; Didier, P.; Richert, L.; Oncul, S.; Arntz, Y.; Mély, Y.; Klymchenko, A. S. Collective fluorescence switching of counterion-assembled dyes in polymer nanoparticles. *Nat. Commun.* **2014**, *5*, 4089.

50.   Lin, H.; Camacho, R.; Tian, Y.; Kaiser, T. E.; Würthner, F.; Scheblykin, I. G. Collective fluorescence blinking in linear J-aggregates assisted by long-distance exciton migration. *Nano Lett.* **2010**, *10*, 620–626.

51.   Stangl, T.; Wilhelm, P.; Remmerssen, K.; Höger, S.; Vogelsang, J.; Lupton, J. M. Mesoscopic Quantum Emitters from Deterministic Aggregates of Conjugated Polymers. *Proc. Natl. Acad. Sci. U.S.A.* **2015**, *112*, 6.

52.   Helmerich, D. A.; Beliu, G.; Sauer, M. Multiple-Labeled Antibodies Behave Like Single Emitters in Photoswitching Buffer. *ACS nano* **2020**, *14*, 12629–12641.

53.   Vogelsang, J.; Adachi, T.; Brazard, J.; Vanden Bout, D. A.; Barbara, P. F. Self-assembly of highly ordered conjugated polymer aggregates with long-range energy transfer. *Nat. Mater.* **2011**, *10*, 942–946.

54.   Eder, T.; Vogelsang, J.; Bange, S.; Remmerssen, K.; Schmitz, D.; Jester, S.-S.; Keller, T. J.; Höger, S.; Lupton, J. M. Interplay between J- and H-type coupling in aggregates of π-conjugated polymers: a single-molecule perspective. *Angew. Chem. Int. Ed.* **2019,** 58, 18898–18902.

55.   Eder, T.; Stangl, T.; Gmelch, M.; Remmerssen, K.; Laux, D.; Höger, S.; Lupton, J. M.; Vogelsang, J. Switching between H- and J-type electronic coupling in single conjugated polymer aggregates. *Nat. Commun.* **2017**, *8*, 1641.

56.   Kasha, M.; Rawls, H. R.; Ashraf El-Bayoumi, M. The exciton model in molecular spectroscopy. *Pure Appl. Chem.* **1965**, *11,* 371–392.

57.   Lippitz, M.; Hübner, C. G.; Christ, T.; Eichner, H.; Bordat, P.; Herrmann, A.; Müllen, K.; Basché, T. Coherent electronic coupling versus localization in individual molecular dimers. *Phys. Rev. Lett.* **2004**, *92*, 103001.

58.   Tinnefeld, P.; Weston, K. D.; Vosch, T.; Cotlet, M.; Weil, T.; Hofkens, J.; Müllen, K.; Schryver, F. C. de; Sauer, M. Antibunching in the Emission of a Single Tetrachromophoric Dendritic System. *J. Am. Chem. Soc.* **2002**, *124*, 14310–14311.

59.   Hofkens, J.; Cotlet, M.; Vosch, T.; Tinnefeld, P.; Weston, K. D.; Ego, C.; Grimsdale, A.; Müllen, K.; Beljonne, D.; Brédas, J. L.; Jordens, S.; Schweitzer, G.; Sauer, M.; Schryver, F. de. Revealing Competitive Forster-Type Resonance Energy-Transfer Pathways in Single Bichromophoric Molecules. *Proc. Natl. Acad. Sci. U.S.A.* **2003**, *100*, 13146–13151.

60.   Hübner, C. G.; Zumofen, G.; Renn, A.; Herrmann, A.; Müllen, K.; Basché, T. Photon Antibunching and Collective Effects in the Fluorescence of Single Bichromophoric Molecules. *Phys. Rev. Lett.* **2003**, *91*, 93903.

61.   Steiner, F.; Vogelsang, J.; Lupton, J. M. Singlet-Triplet Annihilation Limits Exciton Yield in Poly(3-Hexylthiophene). *Phys. Rev. Lett.* **2014**, *112*, 137402.

62.   Hedley, G. J.; Ruseckas, A.; Samuel, I. D. W. Light Harvesting for Organic Photovoltaics. *Chem. Rev.* **2017**, *117*, 796–837.

63.   Tinnefeld, P.; Hofkens, J.; Herten, D.-P.; Masuo, S.; Vosch, T.; Cotlet, M.; Habuchi, S.; Müllen, K.; Schryver, F. C. de; Sauer, M. Higher-Excited-State Photophysical Pathways in Multichromophoric Systems Revealed by Single-Molecule Fluorescence Spectroscopy. *ChemPhysChem* **2004**, *5*, 1786–1790.

64.   Abbe, E. Beiträge zur Theorie des Mikroskops und der mikroskopischen Wahrnehmung. *Archiv f. mikrosk. Anatomie* **1873**, *9*, 413–468.

65.   Plotegher, N.; Gratton, E.; Bubacco, L. Number and Brightness analysis of alpha-synuclein oligomerization and the associated mitochondrial morphology alterations in live cells. *Biochim. Biophys. Acta* **2014**, *1840*, 2014–2024.

66.   Nerreter, T.; Letschert, S.; Götz, R.; Doose, S.; Danhof, S.; Einsele, H.; Sauer, M.; Hudecek, M. Super-Resolution Microscopy Reveals Ultra-Low CD19 Expression on Myeloma Cells that Triggers Elimination by CD19 CAR-T. *Nat. Commun.* **2019**, *10*, 3137.

67.   Pape, J. K.; Stephan, T.; Balzarotti, F.; Büchner, R.; Lange, F.; Riedel, D.; Jakobs, S.; Hell, S. W. Multicolor 3D MINFLUX Nanoscopy of Mitochondrial MICOS Proteins. *Proc. Natl. Acad. Sci. U.S.A.* **2020**, *117*, 20607–20614.

68.   Maunz, P.; Moehring, D. L.; Olmschenk, S.; Younge, K. C.; Matsukevich, D. N.; Monroe, C. Quantum Interference of Photon Pairs from Two Remote Trapped Atomic Ions. *Nat. Phys.* **2007**, *3*, 538–541.

69.   Kolesov, R.; Xia, K.; Reuter, R.; Stöhr, R.; Zappe, A.; Meijer, J.; Hemmer, P. R.; Wrachtrup, J. Optical Detection of a Single Rare-Earth Ion in a Crystal. *Nat. Commun.* **2012**, *3*, 1029.

70.   Barros, H. G.; Stute, A.; Northup, T. E.; Russo, C.; Schmidt, P. O.; Blatt, R. Deterministic Single-Photon Source from a Single Ion. *New J. Phys.* **2009**, *11*, 103004.

71.   Lounis, B.; Moerner, W. E. Single Photons on Demand from a Single Molecule at Room Temperature. *Nature* **2000**, *407*, 491–493.

72.   Fleury; Segura; Zumofen; Hecht; Wild. Nonclassical Photon Statistics in Single-Molecule Fluorescence at Room Temperature. *Phys. Rev. Lett.* **2000**, *84*, 1148–1151.

73.   Ambrose, W. P.; Basché, T.; Moerner, W. E. Detection and Spectroscopy of Single Pentacene Molecules in a p-Terphenyl Crystal by Means of Fluorescence Excitation. *J. Chem. Phys.* **1991**, *95*, 7150–7163.

74.   Basché, T.; Moerner, W. E.; Orrit, M.; Talon, H. Photon Antibunching in the Fluorescence of a Single Dye Molecule Trapped in a Solid. *Phys. Rev. Lett.* **1992**, *69*, 1516–1519.

75.   Kurtsiefer, C.; Mayer, S.; Zarda, P.; Weinfurter, H. Stable solid-state source of single photons. *Phys. Rev. Lett.* **2000**, *85*, 290–293.

76.   Brouri, R.; Beveratos, A.; Poizat, J. P.; Grangier, P. Photon Antibunching in the Fluorescence of Individual Color Centers in Diamond. *Opt. Lett.* **2000**, *25*, 1294–1296.

77.   Brown, R. H.; Twiss, R. Q. LXXIV. A new type of interferometer for use in radio astronomy. *Phil. Mag. J. Sci.* **1954**, *45*, 663–682.

78.   Brown, R. H.; Twiss, R. Q. Correlation between Photons in two Coherent Beams of Light. *Nature* **1956**, *177*, 27–29.

79.   Brown, R. H.; Twiss, R. Q. A Test of a New Type of Stellar Interferometer on Sirius. *Nature* **1956**, *178*, 1046–1048.

80.   Ta, H.; Wolfrum, J.; Herten, D.-P. An extended scheme for counting fluorescent molecules by photon-antibunching. *Laser Phys.* **2010**, *20*, 119–124.

81.   Masuo, S.; Vosch, T.; Cotlet, M.; Tinnefeld, P.; Habuchi, S.; Bell, T. D. M.; Oesterling, I.; Beljonne, D.; Champagne, B.; Müllen, K.; Sauer, M.; Hofkens, J.; Schryver, F. C. de. Multichromophoric Dendrimers as Single-Photon Sources: A Single-Molecule Study. *J. Phys. Chem. B* **2004**, *108*, 16686–16696.

82.   Ta, H.; Kiel, A.; Wahl, M.; Herten, D.-P. Experimental Approach to Extend the Range for Counting Fluorescent Molecules Based on Photon-Antibunching. *Phys. Chem. Chem. Phys.* **2010**, *12*, 10295–10300.

83.   Kurz, A.; Schmied, J. J.; Grußmayer, K. S.; Holzmeister, P.; Tinnefeld, P.; Herten, D.-P. Counting Fluorescent Dye Molecules on DNA Origami by Means of Photon Statistics. *Small* **2013**, *9*, 4061–4068.

84.   Ta, H.; Keller, J.; Haltmeier, M.; Saka, S. K.; Schmied, J.; Opazo, F.; Tinnefeld, P.; Munk, A.; Hell, S. W. Mapping molecules in scanning far-field fluorescence nanoscopy. *Nat. Commun.* **2015**, *6*, 7977.

85.   Schedlbauer, J.; Scherf, U.; Vogelsang, J.; Lupton, J. M. Dynamic Quenching of Triplet Excitons in Single Conjugated-Polymer Chains. *J. Phys. Chem. Lett.* **2020**, *11*, 5192–5198.

86.   Chaudhuri, D.; Li, D.; Che, Y.; Shafran, E.; Gerton, J. M.; Zang, L.; Lupton, J. M. Enhancing long-range exciton guiding in molecular nanowires by H-aggregation lifetime engineering. *Nano Lett.* **2011**, *11*, 488–492.

87.   Shaw, P. E.; Ruseckas, A.; Samuel, I. D. W. Exciton Diffusion Measurements in Poly(3-hexylthiophene). *Adv. Mater.* **2008**, *20*, 3516–3520.

88.   Baldo, M. A.; Holmes, R. J.; Forrest, S. R. Prospects for electrically pumped organic lasers. *Phys. Rev. B* **2002**, *66*, 599.

89.   Bout, D. A. V.; Yip, W.-T.; Hu, D.; Fu, D.-K.; Swager, T. M.; Barbara, P. F. Discrete Intensity Jumps and Intramolecular Electronic Energy Transfer in the Spectroscopy of Single Conjugated Polymer Molecules. *Science* **1997**, *277*, 1074–1077.

90.   Lamb, D. C.; Schenk, A.; Röcker, C.; Nienhaus, G. U. Determining Chemical Rate Coefficients Using Time-Gated Fluorescence Correlation Spectroscopy. *J. Phys. Org. Chem.* **2000**, *13*, 654–658.

91.   Rothemund, P. W. K. Folding DNA to create nanoscale shapes and patterns. *Nature* **2006**, *440*, 297–302.

92.   Dey, S.; Fan, C.; Gothelf, K. V.; Li, J.; Lin, C.; Liu, L.; Liu, N.; Nijenhuis, M. A. D.; Saccà, B.; Simmel, F. C.; Yan, H.; Zhan, P. DNA origami. *Nat Rev Methods Primers* **2021**, *1*, 237.

93.   Vogelsang, J.; Cordes, T.; Forthmann, C.; Steinhauer, C.; Tinnefeld, P. Intrinsically Resolution Enhancing Probes for Confocal Microscopy. *Nano Lett.* **2010**, *10*, 672–679.

94.   Becker, K.; Lagoudakis, P. G.; Gaefke, G.; Höger, S.; Lupton, J. M. Exciton Accumulation in Pi-Conjugated Wires Encapsulated by Light-Harvesting Macrocycles. *Angew. Chem. Int. Ed.* **2007**, *46*, 3450–3455.

95.   Hell, S. W. Far-field optical nanoscopy. *Science* **2007**, *316*, 1153–1158.

96.   Niekamp, S.; Stuurman, N.; Vale, R. D. A 6-nm ultra-photostable DNA FluoroCube for fluorescence imaging. *Nat Methods* **2020**, *77*, 51.

97.   Valizadeh, A.; Mikaeili, H.; Samiei, M.; Farkhani, S. M.; Zarghami, N.; Kouhi, M.; Akbarzadeh, A.; Davaran, S. Quantum dots: Synthesis, bioapplications, and toxicity. *Nanoscale Res. Lett.* **2012**, *7*, 480.

98.   Nicoli, F.; Roos, M. K.; Hemmig, E. A.; Di Antonio, M.; Vivie-Riedle, R. de; Liedl, T. Proximity-Induced H-Aggregation of Cyanine Dyes on DNA-Duplexes. *J. Phys. Chem. B* **2016**, *120*, 9941–9947.

99.   Marmé, N.; Friedrich, A.; Denapaite, D.; Hakenbeck, R.; Knemeyer, J.-P. Single nucleotide polymorphism analysis using different colored dye dimer probes. *Chem. Phys. Lett.* **2006**, *428*, 440–445.

100.   Hernando, J.; van der Schaaf, M.; van Dijk, Erik M. H. P.; Sauer, M.; García-Parajó, M. F.; van Hulst, N. F. Excitonic Behavior of Rhodamine Dimers: A Single-Molecule Study. *J. Phys. Chem. A* **2003**, *107*, 43–52.

101.   Stangl, T.; Wilhelm, P.; Schmitz, D.; Remmerssen, K.; Henzel, S.; Jester, S.-S.; Höger, S.; Vogelsang, J.; Lupton, J. M. Temporal Fluctuations in Excimer-Like Interactions between π-Conjugated Chromophores. *J. Phys. Chem. Lett.* **2015**, *6*, 1321–1326.

102.   Schmied, J. J.; Gietl, A.; Holzmeister, P.; Forthmann, C.; Steinhauer, C.; Dammeyer, T.; Tinnefeld, P. Fluorescence and Super-Resolution Standards Based on DNA Origami. *Nat. Methods* **2012**, *9*, 1133–1134.

103.   Kim, B. S.-I.; Jin, Y.-J.; Lee, W.-E.; Byun, D. J.; Yu, R.; Park, S.-J.; Kim, H.; Song, K.-H.; Jang, S.-Y.; Kwak, G. Highly Fluorescent, Photostable, Conjugated Polymer Dots with Amorphous, Glassy-State, Coarsened Structure for Bioimaging. *Adv. Optical Mater.* **2015**, *3*, 78–86.

104.   Wu, C.; Bull, B.; Szymanski, C.; Christensen, K.; McNeill, J. Multicolor conjugated polymer dots for biological fluorescence imaging. *ACS nano* **2008**, *2*, 2415–2423.

105.   Genin, E.; Gao, Z.; Varela, J. A.; Daniel, J.; Bsaibess, T.; Gosse, I.; Groc, L.; Cognet, L.; Blanchard-Desce, M. „Hyper-bright" near-infrared emitting fluorescent organic nanoparticles for single particle tracking. *Adv. Mater.* **2014**, *26*, 2258-61, 2257.

106. Trofymchuk, K.; Reisch, A.; Didier, P.; Fras, F.; Gilliot, P.; Mely, Y.; Klymchenko, A. S. Giant light-harvesting nanoantenna for single-molecule detection in ambient light. *Nature photonics* **2017**, *11*, 657–663.

107. Matikonda, S. S.; Hammersley, G.; Kumari, N.; Grabenhorst, L.; Glembockyte, V.; Tinnefeld, P.; Ivanic, J.; Levitus, M.; Schnermann, M. J. Impact of Cyanine Conformational Restraint in the Near-Infrared Range. *J. Org. Chem.* **2020**, *85*, 5907–5915.

108. Butkevich, A. N.; Bossi, M. L.; Lukinavičius, G.; Hell, S. W. Triarylmethane Fluorophores Resistant to Oxidative Photobluing. *J. Am. Chem. Soc.* **2019**, *141*, 981–989.

109. Mujumdar, R. B.; Ernst, L. A.; Mujumdar, S. R.; Lewis, C. J.; Waggoner, A. S. Cyanine dye labeling reagents: Sulfoindocyanine succinimidyl esters. *Bioconjugate Chem.* **1993**, *4*, 105–111.

110. Condon, E. U. Nuclear Motions Associated with Electron Transitions in Diatomic Molecules. *Phys. Rev.* **1928**, *32*, 858–872.

111. Menzel, R.; Thiel, E. Intersystem crossing rate constants of rhodamine dyes: Influence of the amino-group substitution. *Chem. Phys. Lett.* **1998**, *291*, 237–243.

112. van de Linde, S.; Krstić, I.; Prisner, T.; Doose, S.; Heilemann, M.; Sauer, M. Photoinduced formation of reversible dye radicals and their impact on super-resolution imaging. *Photochem. Photobiol. Sci.* **2011**, *10*, 499–506.

113. Liphardt, B.; Liphardt, B.; Lüttke, W. Laser dyes III: Concepts to increase the photostability of laser dyes. *Opt. Commun.* **1983**, *48*, 129–133.

114. Nani, R. R.; Kelley, J. A.; Ivanic, J.; Schnermann, M. J. Reactive Species Involved in the Regioselective Photooxidation of Heptamethine Cyanines. *Chem. Sci.* **2015**, *6*, 6556–6563.

115. Song, L.; Varma, C. A.; Verhoeven, J. W.; Tanke, H. J. Influence of the triplet excited state on the photobleaching kinetics of fluorescein in microscopy. *Biophys. J.* **1996**, *70*, 2959–2968.

116. Rasnik, I.; McKinney, S. A.; Ha, T. Nonblinking and long-lasting single-molecule fluorescence imaging. *Nature methods* **2006**, *3*, 891–893.

117. Glembockyte, V.; Cosa, G. Redox-Based Photostabilizing Agents in Fluorescence Imaging: The Hidden Role of Intersystem Crossing in Geminate Radical Ion Pairs. *J. Am. Chem. Soc.* **2017**, *139*, 13227–13233.

118. Holzmeister, P.; Gietl, A.; Tinnefeld, P. Geminate Recombination as a Photoprotection Mechanism for Fluorescent Dyes. *Angew. Chem.* **2014**, *53*, 5685–5688.

119. JELLEY, E. E. Spectral Absorption and Fluorescence of Dyes in the Molecular State. *Nature* **1936**, *138*, 1009–1010.

120. Stern, O.; Volmer, M. Über die Abklingungszeit der Fluoreszenz. *Phys. Z.* **1919**, *20*, 183–188.

121. Scholes, G. D. Long-range resonance energy transfer in molecular systems. *Annu. Rev. Phys. Chem.* **2003**, *54*, 57–87.

122. Hellenkamp, B.; Schmid, S.; Doroshenko, O.; Opanasyuk, O.; Kühnemuth, R.; Rezaei Adariani, S.; Ambrose, B.; Aznauryan, M.; Barth, A.; Birkedal, V.; Bowen, M. E.; Chen, H.; Cordes, T.; Eilert, T.; Fijen, C.; Gebhardt, C.; Götz, M.; Gouridis, G.; Gratton, E.; Ha, T. *et al.* Precision and accuracy of single-molecule FRET measurements-a multi-laboratory benchmark study. *Nat. Methods* **2018**, *15*, 669–676.

123. Woller, J. G.; Hannestad, J. K.; Albinsson, B. Self-assembled nanoscale DNA-porphyrin complex for artificial light harvesting. *J. Am. Chem. Soc.* **2013**, *135*, 2759–2768.

124.   Hemmig, E. A.; Creatore, C.; Wünsch, B.; Hecker, L.; Mair, P.; Parker, M. A.; Emmott, S.; Tinnefeld, P.; Keyser, U. F.; Chin, A. W. Programming Light-Harvesting Efficiency Using DNA Origami. *Nano letters* **2016**, *16*, 2369–2374.

125.   Stangl, T.; Bange, S.; Schmitz, D.; Würsch, D.; Höger, S.; Vogelsang, J.; Lupton, J. M. Temporal switching of homo-FRET pathways in single-chromophore dimer models of π-conjugated polymers. *J. Am. Chem. Soc.* **2013**, *135*, 78–81.

126.   Hess, S. T.; Huang, S.; Heikal, A. A.; Webb, W. W. Biological and chemical applications of fluorescence correlation spectroscopy: A review. *Biochemistry* **2002**, *41*, 697–705.

127.   Seeman, N. C. Nucleic acid junctions and lattices. *J. Theor. Biol.* **1982**, *99*, 237–247.

128.   Douglas, S. M.; Marblestone, A. H.; Teerapittayanon, S.; Vazquez, A.; Church, G. M.; Shih, W. M. Rapid prototyping of 3D DNA-origami shapes with caDNAno. *Nucleic Acids Res.* **2009**, *37*, 5001–5006.

129.   Kramm, K.; Schröder, T.; Gouge, J.; Vera, A. M.; Gupta, K.; Heiss, F. B.; Liedl, T.; Engel, C.; Berger, I.; Vannini, A.; Tinnefeld, P.; Grohmann, D. DNA origami-based single-molecule force spectroscopy elucidates RNA Polymerase III pre-initiation complex stability. *Nat. Commun.* **2020**, *11*, 2828.

130.   Nickels, P. C.; Wünsch, B.; Holzmeister, P.; Bae, W.; Kneer, L. M.; Grohmann, D.; Tinnefeld, P.; Liedl, T. Molecular Force Spectroscopy with a DNA Origami-Based Nanoscopic Force Clamp. *Science* **2016**, *354*, 305–307.

131.   Sigl, C.; Willner, E. M.; Engelen, W.; Kretzmann, J. A.; Sachenbacher, K.; Liedl, A.; Kolbe, F.; Wilsch, F.; Aghvami, S. A.; Protzer, U.; Hagan, M. F.; Fraden, S.; Dietz, H. Programmable icosahedral shell system for virus trapping. *Nat. Mater.* **2021**, *15*, 373.

132.   Acuna, G. P.; Bucher, M.; Stein, I. H.; Steinhauer, C.; Kuzyk, A.; Holzmeister, P.; Schreiber, R.; Moroz, A.; Stefani, F. D.; Liedl, T.; Simmel, F. C.; Tinnefeld, P. Distance dependence of single-fluorophore quenching by gold nanoparticles studied on DNA origami. *ACS nano* **2012**, *6*, 3189–3195.

133.   Acuna, G. P.; Möller, F. M.; Holzmeister, P.; Beater, S.; Lalkens, B.; Tinnefeld, P. Fluorescence enhancement at docking sites of DNA-directed self-assembled nanoantennas. *Science* **2012**, *338*, 506–510.

134.   Raab, M.; Vietz, C.; Stefani, F. D.; Acuna, G. P.; Tinnefeld, P. Shifting molecular localization by plasmonic coupling in a single-molecule mirage. *Nat. Commun.* **2017**, *8*, 13966.

135.   Sternisha, S. M.; Mukherjee, P.; Alex, A.; Chaney, E. J.; Barkalifa, R.; Wan, B.; Lee, J. H.; Rico-Jimenez, J.; Žurauskas, M.; Spillman, D. R.; Sripada, S. A.; Marjanovic, M.; Arp, Z.; Galosy, S. S.; Bhanushali, D. S.; Hood, S. R.; Bose, S.; Boppart, S. A. Longitudinal monitoring of cell metabolism in biopharmaceutical production using label-free fluorescence lifetime imaging microscopy. *Biotechnol. J.* **2021**, *16*, e2000629.

136.   Vicidomini, G.; Moneron, G.; Han, K. Y.; Westphal, V.; Ta, H.; Reuss, M.; Engelhardt, J.; Eggeling, C.; Hell, S. W. Sharper low-power STED nanoscopy by time gating. *Nat. Methods* **2011**, *8*, 571–573.

137.   Enderlein, J.; Gregor, I. Using fluorescence lifetime for discriminating detector afterpulsing in fluorescence-correlation spectroscopy. *Rev. Sci. Instrum.* **2005**, *76*, 33102.

138.   Rüttinger, S.; Kapusta, P.; Patting, M.; Wahl, M.; Macdonald, R. On the Resolution Capabilities and Limits of Fluorescence Lifetime Correlation Spectroscopy (FLCS) Measurements. *J. Fluoresc.* **2010**, *20*, 105–114.

139.   Hedley, G. J.; Schröder, T.; Steiner, F.; Eder, T.; Hofmann, F. J.; Bange, S.; Laux, D.; Höger, S.; Tinnefeld, P.; Lupton, J. M.; Vogelsang, J. Picosecond Time-Resolved Photon Antibunching Measures Nanoscale Exciton Motion and the True Number of Chromophores. *Nat. Commun.* **2021**, *12*, 1327.

7 List of Abbreviations

2fFCS	Dual-Focus Fluorescence Correlation Spectroscopy
AA	Ascorbic Acid
APD	Avalanche Photodiode
bp	Base Pair
BSA	Bovine Serum Albumin
CoPS	Counting by Photon Statistics
CP	Conjugated Polymers
CRT	Correlation Relaxation Time
DBCO	Dibenzocyclooctyne
DNA	Deoxyribonucleic Acid
dsDNA	Double-Stranded Deoxyribonucleic Acid
FCCS	Fluorescence Cross-Correlation Spectroscopy
FCS	Fluorescence Correlation Spectroscopy
FLCS	Fluorescence Lifetime Correlation Spectroscopy
FLIM	Fluorescence Lifetime Imaging
FRET	Förster Resonance Energy Transfer
FRET-FCS	Förster Resonance Energy Transfer Fluorescence Correlation Spectroscopy
gSTED	gated Stimulated Emission Depletion
HBT	Hanbury Brown-Twiss
HOMO	Highest Occupied Molecular Orbital
IC	Internal Conversion
IRF	Instrument Response Function
ISC	Inter System Crossing
LUMO	Lowest Unoccupied Molecular Orbital
mcNP	Multichromophoric Nanoparticles

MV	Methyl Viologen
NADPH	Nicotinamide Adenine Dinucleotide Phosphate
PET	Photoinduced Electron Transfer
PIE	Pulsed Interleaved Excitation
PSM	Single Mode Fiber
psTRAB	Picosecond Time Resolved Antibunching
ROXS	Reducing and Oxidizing System
SDA	Singlet-Darkstate Annihilation
sg-FCS	Shrinking-Gate
SSA	Singlet-Singlet Annihilation
ssDNA	Single-Stranded Deoxyribonucleic Acid
STA	Singlet-Triplet Annihilation
TCSPC	Time Correlated Single Photon Counting
TQ	Trolox Quinine
TTA	Triplet-Triplet Annihilation
TX	Trolox

8 Acknowledgements

9 List of Publications

Peer-Reviewed Publications

1. Wang, D.; Vietz, C.; **Schröder, T**.; Acuna, G.; Lalkens, B.; Tinnefeld, P. A DNA Walker as a Fluorescence Signal Amplifier. *Nano Lett.* **2017**, *17*, 5368–5374.

2. Hellenkamp, B.; Schmid, S.; Doroshenko, O.; Opanasyuk, O.; Kühnemuth, R.; Rezaei Adariani, S.; Ambrose, B.; Aznauryan, M.; Barth, A.; Birkedal, V.; Bowen, M. E.; Chen, H.; Cordes, T.; Eilert, T.; Fijen, C.; Gebhardt, C.; Götz, M.; Gouridis, G.; Gratton, E.; Ha, T.; **Schröder, T** *et al.* Precision and accuracy of single-molecule FRET measurements-a multi-laboratory benchmark study. *Nat. Methods* **2018**, *15*, 669–676.

3. **Schröder, T**.; Scheible, M. B.; Steiner, F.; Vogelsang, J.; Tinnefeld, P. Interchromophoric Interactions Determine the Maximum Brightness Density in DNA Origami Structures. *Nano Lett.* **2019**, *19*, 1275–1281.

4. Kramm, K.; **Schröder, T**.; Gouge, J.; Vera, A. M.; Gupta, K.; Heiss, F. B.; Liedl, T.; Engel, C.; Berger, I.; Vannini, A.; Tinnefeld, P.; Grohmann, D. DNA origami-based single-molecule force spectroscopy elucidates RNA Polymerase III pre-initiation complex stability. *Nature communications* **2020**, *11*, 2828.

5. Hedley, G. J.; **Schröder, T**.; Steiner, F.; Eder, T.; Hofmann, F. J.; Bange, S.; Laux, D.; Höger, S.; Tinnefeld, P.; Lupton, J. M.; Vogelsang, J. Picosecond Time-Resolved Photon Antibunching Measures Nanoscale Exciton Motion and the True Number of Chromophores. *Nat. Commun.* **2021**, *12*, 1327.

6. Kamińska, I.; Bohlen, J.; Yaadav, R.; Schüler, P.; Raab, M.; **Schröder, T**.; Zähringer, J.; Zielonka, K.; Krause, S.; Tinnefeld, P. Graphene Energy Transfer for Single-Molecule Biophysics, Biosensing, and Super-Resolution Microscopy. *Adv. Mater.* **2021**, *33*, e2101099.

7. **Schröder, T**.; Bange, S.; Schedlbauer, J.; Steiner, F.; Lupton, J. M.; Tinnefeld, P.; Vogelsang, J. How Blinking Affects Photon Correlations in Multichromophoric Nanoparticles. *ACS nano* **2021**, *15*, 18037–18047.

8. Ochmann, S. E.; **Schröder, T**.; Schulz, C. M.; Tinnefeld, P. Quantitative Single-Molecule Measurements of Membrane Charges with DNA Origami. *Anal. Chem.* **2022**, 94, 2633–2640.

Manuscripts in preparation

9. Baumann, K. N.; **Schröder, T**.; Ciryam, P. S.; Morszy, D.; Tinnefeld, P.; Knowles, T. P. J.; Hernandez-Ainsa, S. A DNA-Liposome Composite Carrier for Triggered Release. *submitted to ACS Appl. Bio Mater.,* **2022**.

10. **Schröder, T**.; Bohlen, J.; Ochmann, S. E.; Schüler, P.; Krause, S.; Lamb, D. C.; Tinnefeld, P. Shrinking gate fluorescence correlation spectroscopy yields equilibrium constants and distinguishes photophysics from structural dynamics. *Submission pending due to consideration for a patent application,* **2022**.

11. Büber, E.; Franquelim, H.; **Schröder, T.**; Scheckenbach, M.; Dass, M.; Tinnefeld, P. A FRET based dynamic DNA origami tool for particle curvature sensing. *in preparation.*

Conferences and Presentations

09/2015	Poster presentation at PicoQuant's 21st Single Molecule Workshop: "Characterizing Dye Incorporation in DNA Origami", Berlin, Germany.
05-2017	Poster presentation at BraunschweigerJungChemikerTagung: "Approaching the Highest Brightness Density with DNA Origami", Braunschweig, Germany.
05-2017	Poster presentation at DNAtec Workshop: "Approaching the highest brightness density with DNA origami", Dresden, Germany.
09/2017	Oral presentation at PQ PicoQuant's 23rd Single Molecule Workshop: "Finding the Highest Labeling Density in DNA Origami", Berlin, Germany.
09/2019	Oral presentation at PicoQuant's 25th Single Molecule Workshop: "Following the Fate of Excitions in Multi-Chromophoric Nanoparticles", Berlin, Germany
09/2019	Oral Presentation at CeNS/CRC235 Workshop 'Evolving Nanosciences': "Following the Fate of Excitons in Densely Labeled Chromophoric Nanoparticles", Venice, Italy.
09/2021	Oral Presentation at PicoQuant's 26th Single Molecule Workshop: "Microtime Gating for Fluorescence Correlation Spectroscopy", Berlin, Germany.

Honors and Prizes

01/2017	Prize for the Master Degree of the Förderverein der Freunde des Instituts für Organische Chemie an der TU Braunschweig e.V.
09/2019	Award for the best student talk at PicoQuant's 25th Single Molecule Workshop in Berlin, Germany